

Electronic Thesis and Dissertation Repository

---

8-20-2020 2:30 PM

## Development of High-Performance All-Solid-State Batteries

Jianneng Liang, *The University of Western Ontario*

Supervisor: Sun, Xueliang, *The University of Western Ontario*

A thesis submitted in partial fulfillment of the requirements for the Doctor of Philosophy degree in Mechanical and Materials Engineering

© Jianneng Liang 2020

Follow this and additional works at: <https://ir.lib.uwo.ca/etd>



Part of the [Materials Science and Engineering Commons](#)

---

### Recommended Citation

Liang, Jianneng, "Development of High-Performance All-Solid-State Batteries" (2020). *Electronic Thesis and Dissertation Repository*. 7211.

<https://ir.lib.uwo.ca/etd/7211>

This Dissertation/Thesis is brought to you for free and open access by Scholarship@Western. It has been accepted for inclusion in Electronic Thesis and Dissertation Repository by an authorized administrator of Scholarship@Western. For more information, please contact [wlsadmin@uwo.ca](mailto:wlsadmin@uwo.ca).

## Abstract

All-solid-state batteries (ASSBs) with polyethylene oxide (PEO)-based solid polymer electrolytes (SPEs) or oxide-based solid-state electrolytes (SSEs) are promising candidates for electric vehicles application. However, ASSBs suffer from critical challenges including (i) low electrochemical oxidation window, (ii) poor interface contact, (iii) incompatibility between the SSE and electrode. This thesis, therefore, focuses on various strategies for addressing these problems and understanding the insight mechanisms.

To address the low oxidation window challenge of SPE, surface engineering method was used. The surface coating on  $\text{LiCoO}_2$ , and/or carbon particles with lithium tantalate was conducted. This study disclosed that carbon particles/SPE interface is detrimental to the electrochemical decomposition of SPE. Further, lithium niobium oxide engineering NMC811/SPE interface was done for improving the stability of NMC811 particles and alleviating the decomposition of SPE.

Moreover, the oxidation window of SPE was increased by engineering the end functional group of PEO. Stable performance ASSBs were obtained with the dimethylamine end group SPE. Besides, the binders' effect was studied. PEO binder are not practical for 4 V class cathodes because of its low oxidation window, while carboxyl-rich polymer binders have superior performance. Mechanism studies showed that they have higher voltage stability and work as a coating material to protect electrode/SPE interface.

The poor contact between oxide-based SSE and cathode particles was addressed with solution method synthesized  $\text{Li}_3\text{InCl}_6$  SSE. The incompatibility between NASICON SSEs and sulfur cathodes is tackled with ultra-thin  $\text{Al}_2\text{O}_3$  protection.

The discoveries of this thesis provide important guidance to design high performance, high energy density ASSBs.

## Keywords

All-solid-state batteries, solid-state electrolyte, interface, cathodes, binders.

## Summary for Lay Audience

Developing all-solid-state batteries (ASSBs) with nonflammable solid-state electrolytes (SSEs) is important for electric vehicle (EV) applications. However, the problems including (1) instability of solid polymer electrolytes (SPEs) at high voltage, (2) poor interfacial contact, and (3) side reactions at the electrode/SSE interface significantly restrict the development of ASSBs. Several methods were developed to address these problems, and their insight mechanism were investigated in this thesis.

To address the high voltage instability problem of SPEs, interface protection method was used. The interface between the  $\text{LiCoO}_2$  particles and SPE, the interface of carbon particles and SPE, are protected, respectively, with lithium tantalate. The results indicated carbon particles/SPE is detrimental to the decomposition of SPE. Ni-rich NMC811 cathode should be used for achieving high energy density ASSBs. However, both NMC811 and SPE are not stable at high voltage. The NMC811 electrode/SPE interface was engineered with lithium niobium oxide (LNO), as a result of this, the instability problem of NMC811 and the decomposition of SPE were alleviated with LNO protection.

Modifying the structure of the polymer chain was done by using dimethylformamide solvent to increase the high voltage stability of polymer. As a result of this, higher voltage stability of SPE and higher electrochemical performance of ASSBs were realized with this modified SPE.

In ASSBs, the most used binder is PEO which is not stable at high voltage, thus it is not suitable for high voltage ASSBs. Mechanism studies showed that carboxyl-rich polymer (CRP) binders are more stable at high voltage, therefore, they present better performance in ASSBs.

The poor contact between SSEs and cathodes was addressed by solution synthesized  $\text{Li}_3\text{InCl}_6$ . Mechanism studies showed that in-situ synthesized  $\text{Li}_3\text{InCl}_6$  realized intimately contacts between SSE and cathode. Side reaction between the oxide-based SSE and electrode was also addressed. The sulfur cathode can react with the Ti-containing NASICON SSE, resulting in SSE decomposition. With ultra-thin  $\text{Al}_2\text{O}_3$  protection, the stability of the NASICON SSE dramatically increased and the cycling performances of ASSBs were improved.

The discoveries of this thesis provide important guidance to design high performance, high energy density ASSBs.

## Co-Authorship Statement

1.

**Title:** Recent progress on solid-state hybrid electrolytes for solid-state lithium batteries

**Authors:** Jianneng Liang, Jing Luo, Qian Sun, Xiaofei Yang, Ruying Li, Xueliang Sun

The final version of this manuscript has been published in **Energy Storage Materials**, 2019, 21, 308-334. J. Liang written this review paper. All the authors contributed to designing, polishing, and modifying this paper.

2.

**Title:** Engineering the conductive carbon/PEO interface to stabilize solid polymer electrolytes for all-solid-state high voltage LiCoO<sub>2</sub> batteries

**Authors:** Jianneng Liang, Yipeng Sun, Yang Zhao, Qian Sun, Jing Luo, Feipeng Zhao, Xiaoting Lin, Xia Li, Ruying Li, Li Zhang, Shigang Lu, Huan Huang, Xueliang Sun

The final version of this manuscript has been published in **Journal of Materials Chemistry A**, 2020, 8, 2769-2776. J. Liang, Q. Sun and X. Sun conceived the idea and experiments; J. Liang conducted the electrode/SPE preparations, electrochemical performance testing, and SEM. Y. Zhao, F. Zhao and Y. Sun helped to conduct the ALD coating experiment. Y. Sun assisted in the synchrotron XAS measurement; J. Luo, X. Li, R. Li, X. Lin, L. Zhang, S. Lu and H. Huang participated in data analysis and discussion; J. Luo polished the manuscript; X. Sun supervised the overall project. All authors discussed the results and commented on the manuscript.

3.

**Title:** Stabilization of all-solid-state Li-S batteries with a polymer–ceramic sandwich electrolyte by atomic layer deposition

**Authors:** Jianneng Liang, Qian Sun, Yang Zhao, Yipeng Sun, Changhong Wang, Weihan Li, Minsi Li, Dawei Wang, Xia Li, Yulong Liu, Keegan Adair, Ruying Li, Li Zhang, Rong Yang, Shigang Lu, Huan Huang, Xueliang Sun

The final version of this manuscript has been published in **Journal of Materials Chemistry A**, 2018, 6, 23712-23719. J. Liang, Q. Sun and X. Sun conceived the idea and experiments; J. Liang carried out the synthesis and performed the materials characterization and electrochemical performance testing. Zhao and Y. Sun helped to conduct ALD coating experiments. C. Wang and Y. Liu helped with LATP solid-state electrolyte preparations; W. Li, M. Li and D. Wang assisted in the Synchrotron XPS measurements; X. Li, K. Adair, R. Li, L. Zhang, R. Yang, S. Lu and H. Huang participated in data analysis and discussion; X. Sun supervised the overall project. All authors discussed the results and commented on the manuscript.

4.

**Title:** Stabilizing and understanding the interface between nickel-rich cathode and PEO-based electrolyte by lithium niobium oxide coating for high-performance all-solid-state batteries

**Authors:** Jianneng Liang, Sooyeon Hwang, Shuang Li, Jing Luo, Yipeng Sun, Yang Zhao, Qian Sun, Weihan Li, Minsi Li, Mohammad Norouzi Banis, Xia Li, Ruying Li, Li Zhang, Shangqian Zhao, Shigang Lu, Huan Huang, Dong Su, Xueliang Sun

The final version of this manuscript has been published in **Nano Energy**, 2020, 105107. J. Liang and S. Hwang contributed equally to this work. J. Liang conceived and designed the experimental work. J. Liang and S. Hwang prepared the manuscript. S. Hwang, and S. Li, conducted FIB, TEM. Zhao and Y. Sun helped to conduct ALD coating experiment. W. Li, M. Li and M. N. Banis assisted in the Synchrotron XAS measurement; Q. Sun, J. Luo, X. Li, R. Li, L. Zhang, S. Lu, D. Su and H. Huang participated data analysis and discussion; J. Luo polished the manuscript; D. Su and X. Sun supervised the overall project. All authors discussed the results and commented on the manuscript.

5.

**Title:** A facile method for enhancing the electrochemical oxidation window of PEO-based solid-polymer electrolytes

**Authors:** Jianneng Liang, Andreas J. Achazi, Qian Sun, Keegan Adair, Yipeng Sun, Liam Israels, Ruying Li, Li Zhang, Shigang Lu, Huan Huang, Payam Kaghazchi, Xueliang Sun

The final version of this manuscript is to be submitted for polishing. J. Liang and A. J. Achazi attributed equally to the work. J. Liang conducted the synthesis of electrodes and SPEs, electrochemical performance testing, SEM, XAS and EIS testing. Andreas and Payam Kaghazchi designed and conducted theoretical calculations. K. Adair helped with the synchrotron testing. Q. Sun, K. Adaira, Y. Sun, L. Israels, R. Li, L. Zhang, S. Lu, H. Huang, and X. Sun participated in the data analysis and discussion. X. Sun and Payam Kaghazchi respectively supervised the experimental and simulations parts of the project. All authors discussed the results and commented on the manuscript.

6.

**Title:** Dramatically prolonged cycling life of 4 V all solid-state polymer batteries by alternating high voltage compatible binders

**Authors:** Jianneng Liang, Dachang Chen, Keegan Adair, Qian Sun, Nathaniel Graham Holmes, Yang Zhao, Yipeng Sun, Jing Luo, Ruying Li, Li Zhang, Shangqian Zhao, Shigang Lu, Huan Huang, Xiaoxing Zhang, Chandra Veer Singh, Xueliang Sun

The final version of this manuscript is to be submitted. J. Liang and D. Chen attributed equally to the work. J. Liang, Q. Sun and X. Sun conceived the idea and experiments; J. Liang and Q. Sun conducted the synthesis of electrodes and SPEs, electrochemical performance testing, SEM, XPS and synchrotron samples preparations. D. Chen and C. V. Singh designed and conducted theoretical calculations. K. Adair helped with the synchrotron testing. J. Luo, N. G. Holmes, Y. Zhao, Y. Sun, R. Li, X. L. Zhang, S. Lu, H. Huang and X. Zhang participated in the data analysis and discussion. X. Sun and C.V. Singh respectively supervised the experimental and simulations parts of the project. All authors discussed the results and commented on the manuscript.

7.



**Title:** In-situ synthesis of  $\text{Li}_3\text{InCl}_6$  halide solid-state electrolyte for addressing interfacial challenge in  $\text{LiCoO}_2/\text{garnet}$  solid-state batteries

**Authors:** Jianneng Liang, Jing Luo, Weihan Li, Junjie Li, Jiamin Fu, Jianwen Liang, Qian Sun, Liam Israels, Ruying Li, Shangqian Zhao, Li Zhang, Shigang Lu, Huan Huang, Xueliang Sun

The final version of this manuscript is to be submitted for polishing. J. Liang and J. Luo attributed equally to the work. J. Liang, J. Luo and X. Sun conceived the idea and experiments; J. Liang conducted the synthesis of electrodes and solid-state electrolytes, electrochemical performance testing, SEM, synchrotron samples preparations. J. Liang, J. Luo prepared the manuscript. W. Li, J. Li, J. Fu helped with the synchrotron testing. J. Luo, W. Li, J. Li, J. Fu, J. Liang, Q. Sun, L. Israels, R. Li, S. Zhao, L. Zhang, S. Lu, H. Huang, and X. Sun participated in the data analysis and discussion. X. Sun supervised the project. All authors discussed the results and commented on the manuscript.

8.

**Title:** Transition metal oxide cathode and solid-state electrolyte interfaces: challenges, design strategies and interface characterization

**Authors:** Jianneng Liang, Changhong Wang, Ruying Li, Xueliang Sun

The final version of this review paper is to be submitted for polishing. J. Liang and C. Wang attributed equally to the work. J. Liang and C. Wang written this review paper. R. Li participated in the discussion. X. Sun supervised the whole project. All the authors contributed to designing, polishing, and modifying this paper.

*When you know a thing, to hold that you know it; and when you do not know a thing,  
to allow that you do not know it - this is knowledge.*

*--Kongzi*

*知之为知之，不知为不知，是知也。*

*孔子*

## Acknowledgments

This Ph.D. work was conducted in Professor Xueliang (Andy) Sun's Nanomaterials and Energy Group at the University of Western Ontario (UWO). Here, it is my great honor to express my acknowledgements to everyone who has accompanied me, supported me and contributed to my Ph.D. work in the last five years.

Foremost, I would like to express my sincere gratitude to my supervisor Prof. X. Sun who did continuous favors and supports to my Ph.D. study and research. Prof. X. Sun is a Canada Research Chair in Development of Nanomaterials for Clean Energy, he is also a Fellow of the Royal Society of Canada and a Fellow of the Canadian Academy of Engineering. His patience, motivation, enthusiasm, and immense knowledge have deeply inspired me. He has guided me on how to conduct research during my Ph.D. study and taught me the essence of research work: solving the practical problem! He also did great efforts to supervise and lead my research work in the right direction. Without Dr. Sun's continuous support and encouragement, it would have been impossible for me to finish my Ph.D. work.

Besides my supervisor, I would like to thank my lab manager Ms. Ruying Li. Ms. Li really put in great efforts to maintain the organization of our lab and provide a comfortable, reliable and safe environment for us to conduct research and experiment. She not only helps in managing the lab but also takes significant concern in the daily life of our group members. If we have any difficulty in our life or study, we can seek help from her. With her great help in our lab, I can finish my Ph.D. work happily and comfortably.

My sincere thanks also go to examiners of my thesis defense, Prof. Yuan Yang from Engineering Department of Columbia University in the City of New York, Prof. Yining Huang from Chemistry Department of University of Western Ontario, Prof. Jun Yang from Mechanical and Materials Engineering Department of University of Western Ontario, and Prof. Hamidreza Abdolvand from Mechanical and Materials Engineering Department of University of Western Ontario, for their valuable and constructive suggestions and comments on my thesis. I would also like to thank my advisory committee members, Prof. Liying Jiang and Prof. Aaron Price, from the Mechanical and Materials Engineering Department of University of Western Ontario, for their valuable and critical advice towards my Ph.D. work and study.

Sincere thanks go to Canadian Light Source (CLS) and their scientists for their helps in synchrotron based XAS, XPS testing. Sincere thanks also go to Dong Su, Dr. Sooyeon Hwang, and Dr. Shuang Li, from Center for Functional Nanomaterials, Brookhaven National Laboratory, for their helps in HAADF-STEM, FIB characterizations and discussions. I would also like to acknowledge Prof. Chandra Veer Singh and Mr. Dachang Chen from University of Toronto, Prof. Payam Kaghazchi and Dr. Andreas J. Achazi from Forschungszentrum Jülich GmbH, Institute of Energy and Climate Research, Materials Synthesis and Processing (IEK-1) and University of South Dakota for their helps in first principle calculations and discussions.

I would like to also thank my colleagues at the University of Western Ontario. I would like to thank Joanna Blom, our department Graduate Coordinator, for her help in my Ph.D. study in the document work. I would also like to extend my appreciation to Dr. Qian Sun, Dr. Xia Li, Dr. Yang Zhao, and Dr. Yulong Liu the postdoctoral fellows in our group, who gave me plenty of guidance and inspiration in my research works. I would also like to thank Dr. Changtai Zhao, Dr. Xiaofei Yang, Dr. Biqiong Wang, Dr. Biwei Xaio, Dr. Weihan Li, Dr. Mohammad N. Banis, Dr. Hossein Yadegari, Dr. Jianwen Liang, Dr. Xiaona Li, Dr. Andrew Lushington, Dr. Dawei Wang, Dr. Zhongxin Song, Dr. Wei Xiao, Dr. Lei Zhang, Dr. Chuang Yu, Dr. Xulei Sui, Dr. Ruizhi Yu, Dr. Hui Duan, Dr. Changhong Wang, Dr. Sixu Deng, Dr. Fei Sun, Dr. Jiwei Wang, Dr. Xianqing Liang, Dr. Xiaohui Zhang, Mr. Yipeng Sun, Mr. Keegan Adair, Mr. Feipeng Zhao, Ms. Xiaoting Lin, Ms. Jing Luo, Mr. Junjie Li, Mr. Jiaming Fu, Mr. Tiansheng Mu, Mr. Dawei Wang, Mr. Gang Sun, Mr. Hanyu Huo, Mr. Kieran Doyle Davis, Mr. Nathaniel Holmes, Ms. Xuejie Gao, Ms. Minsi Li, Ms. Mengxue He, Ms. Yanxia Yuan, Mr. Liam Israels and other visiting scholars and students to our group. I am so happy and honored to work with this group of ambitious and enthusiastic people. You have made my life and research enjoyable and pleasant.

Many thanks to the funding support from the China Automotive Battery Research Institute, Natural Science and Engineering Research Council of Canada (NSERC), the Canada Research Chair Program (CRC), University of Western Ontario (UWO), China Scholarship Council (CSC), and MITACS Ph.D. program. Without their support, this work would not have been finished.

Last but not least, I would like to extend my most sincere gratitude to my parents Mr. Jinling Liang, Mrs. Qiongling Zou, my grandparents, my elder sister Ms. Fenfang Liang, and my younger brother Mr. Jianmin Liang. I would also like to thank my girlfriend who stays with me without any question and doubt for five years for supporting my Ph.D. study. It is impossible for me to finish the Ph.D. study without their understanding, supporting and encouragements. I love you all!

Gianneng Liang

University of Western Ontario

Aug. 22, 2020

# Table of Contents

Abstract.....	ii
Summary for Lay Audience.....	iv
Co-Authorship Statement.....	vi
Acknowledgments.....	xi
Table of Contents.....	xiv
List of Figures.....	xx
List of Abbreviations.....	xxx
List of Appendices.....	xxxiv
Chapter 1.....	1
1 Introduction.....	1
1.1 Lithium ion batteries: from liquid to solid.....	1
1.2 Challenges in solid-state lithium ion batteries.....	4
1.3 Thesis objectives.....	6
1.4 Thesis organizations.....	7
Reference.....	10
Chapter 2.....	12
2 Literature review.....	12
2.1 Solid-state electrolytes for solid-state lithium ion batteries.....	13
2.1.1 Solid polymer electrolytes.....	13
2.1.2 Oxide-based solid-state electrolyte.....	15
2.1.3 Sulfide-based solid-state electrolyte.....	19
2.1.4 Halide-based solid-state electrolyte.....	21
2.1.5 Hybrid solid-state electrolyte.....	22
2.2 Solutions for high-performance solid-state batteries.....	28

2.2.1	Solutions for solid-state lithium batteries with solid polymer electrolyte	29
2.2.2	Solutions for high-performance solid-state batteries with oxide-based solid-state electrolytes.....	39
2.2.3	Conclusion and perspectives.....	45
	Reference.....	49
Chapter 3	.....	61
3	Experimental methods and characterization techniques .....	61
3.1	Experimental methods .....	61
3.1.1	Preparation of PEO-based polymer electrolytes .....	61
3.1.2	Preparations of LiCoO <sub>2</sub> , Nickel-rich NMC811 cathode electrodes.....	62
3.1.3	Preparation of LATP and LLZO solid-state electrolyte .....	63
3.1.4	Preparation of Li <sub>3</sub> InCl <sub>6</sub> -LiCoO <sub>2</sub> composite cathode.....	63
3.1.5	Atomic layer deposition for interface engineering .....	64
3.2	Characterization techniques .....	64
3.2.1	Physical characterization methods .....	64
3.2.2	Electrochemical measurements.....	69
	References .....	71
Chapter 4	.....	72
4	Engineering the conductive carbon/PEO interface to stabilize solid polymer electrolytes for all-solid-state high voltage LiCoO <sub>2</sub> batteries .....	72
4.1	Introduction.....	73
4.2	Experimental .....	76
4.2.1	Preparation of LiCoO <sub>2</sub> electrode with/without ALD coating.....	76
4.2.2	Electrochemical performance testing.....	76
4.2.3	Materials characterization.....	77
4.3	Results and discussion .....	77
4.4	Conclusions.....	85

Acknowledgment .....	86
References .....	86
Supporting information .....	89
Chapter 5.....	99
5 Stabilizing and understanding the interface between Nickel-rich cathode and PEO-based electrolyte by lithium niobium oxide coating for high-performance all-solid-state batteries .....	99
5.1 Introduction.....	100
5.2 Experimental.....	102
5.2.1 Preparation of ALD LNO coating NMC811 electrodes .....	102
5.2.2 Electrochemical performance testing.....	102
5.2.3 Physical characterization .....	103
5.3 Results and discussion .....	103
5.4 Conclusions.....	113
Acknowledgement.....	114
References .....	114
Supporting information .....	118
Chapter 6.....	125
6 A facile method for enhancing the electrochemical oxidation window of PEO-based solid-polymer electrolytes.....	125
6.1 Introduction.....	126
6.2 Experimental.....	128
6.2.1 Preparation of PEO-based SPEs with different solvents .....	128
6.2.2 LiCoO <sub>2</sub> electrodes preparation.....	128
6.2.3 Electrochemical performance testing.....	128
6.2.4 Material characterizations .....	129
6.3 Results and discussion .....	129



6.4 Conclusion .....	136
Acknowledgements .....	136
References .....	136
Supporting information .....	139
Chapter 7.....	143
7 Dramatically prolonged cycling life of 4 V all solid-state polymer batteries by alternating high voltage compatible binders .....	143
7.1 Introduction.....	144
7.2 Experimental .....	146
7.2.1 LiCoO <sub>2</sub> electrodes and binder-AB composite electrode preparation.....	146
7.2.2 Electrochemical performance testing.....	146
7.2.3 Material characterizations .....	147
7.2.4 Theoretical method .....	147
7.3 Results and discussion .....	148
7.4 Conclusion .....	157
Acknowledgement.....	158
References .....	158
Supporting information .....	163
Chapter 8.....	172
8 In-situ synthesis of Li <sub>3</sub> InCl <sub>6</sub> halide solid-state electrolyte for addressing interfacial challenge in LiCoO <sub>2</sub> /garnet solid-state batteries.....	172
8.1 Introduction.....	173
8.2 Experimental .....	175
8.2.1 Preparation of LLZO solid-state electrolyte .....	175
8.2.2 Preparation of LIC-LCO-AB composite cathode on the surface of LLZO SSE.....	175
8.2.3 ASSLIB assembly.....	176

8.2.4	Material characterizations .....	176
8.3	Results and discussion .....	176
8.4	Conclusion .....	182
8.5	Acknowledgement .....	183
	References .....	183
	Supporting information .....	186
Chapter 9	.....	188
9	Stabilization of all-solid-state Li-S batteries with a polymer-ceramic sandwich electrolyte by atomic layer deposition .....	188
9.1	Introduction.....	189
9.2	Experimental .....	191
9.2.1	Preparation of NASICON-type solid-state electrolyte LATP for ALD coating.....	191
9.2.2	Preparation of the sulfur electrode .....	191
9.2.3	Preparation of fully reduced-LATP .....	192
9.2.4	Electrochemical characterization .....	192
9.2.5	Physical characterization .....	193
9.3	Results and discussion .....	193
9.4	Conclusions.....	202
	Acknowledgements .....	203
	References .....	203
	Supporting information .....	206
Chapter 10	.....	215
10	Conclusions and perspectives .....	215
10.1	Conclusion .....	216
10.2	Contribution to this field.....	219
10.3	Perspectives.....	220

Appendices.....	223
Curriculum Vitae .....	226

## List of Figures

Figure 1.1 Schematic diagram of a LIB. (Separator is eliminated in this schematic diagram)	2
Figure 1.2 Configuration of all-solid-state batteries (ASSBs).....	3
Figure 2.1 (a) Structure of a crystalline PEO-based SPE consisting of PEO and LiAsF <sub>6</sub> . Left, PEO chain axis is perpendicular to the page. Right, PEO chain axis is parallel to the page. Purple spheres, Li; white spheres, As; pink spheres, F; light green, carbon in PEO chain 1; dark green, oxygen in PEO chain 1. Light red, carbon in PEO chain 2; dark red, oxygen in PEO chain 2. Hydrogens are not shown. <sup>4</sup> (b) Temperature dependent ionic conductivity of PEO-based SPEs. <sup>21</sup> (c) The electrochemical stable window of a PEO-based SPE is only 3.8 V. <sup>28</sup> (d)-(g) X-ray tomography slices show the evolution of Li dendrite formation in SPE and their 3-dimensional (3D) reconstructions diagrams (h). <sup>22</sup> .....	15
Figure 2.2 The crystalline structures of (a) NASICON, (b) Garnet, and (c) Perovskite SSEs. <sup>52</sup> Time-of-flight secondary ion mass spectroscopy (TOF-SIMS) study of LiCoO <sub>2</sub> /LLZO interface: (d) SEM image of a LiCoO <sub>2</sub> /LLZO interface and elemental distributions of (e) Al <sup>+</sup> , (f) Zr <sup>+</sup> , (g) La <sup>+</sup> , and (h) Co <sup>+</sup> ; color scales show the concentrations of each ion where the upper color represent higher concentrations. <sup>53</sup> (i) Scanning electron microscopy (SEM) image showing the poor contact between NASICON SSE and Li <sub>2</sub> MnO <sub>4</sub> . <sup>54</sup> (j) X-ray photoelectron spectroscopy (XPS) study on the reduction of Ti <sup>4+</sup> in LATP by lithium metal anode. <sup>55</sup> .....	18
Figure 2.3 Crystal structure of LGPS sulfide-based SSE; (b) one dimensional view of LGPS framework; (c) Lithium ion conduction pathways in LGPS; zigzag conduction pathways along the c-axis are indicated. <sup>61</sup> (d) Crystal structure of Li <sub>9.54</sub> Si <sub>1.74</sub> P <sub>1.44</sub> S <sub>11.7</sub> Cl <sub>0.3</sub> ; (e) nuclear distributions of Li atoms in Li <sub>9.54</sub> Si <sub>1.74</sub> P <sub>1.44</sub> S <sub>11.7</sub> Cl <sub>0.3</sub> at 25 °C. (f) Comparison on ionic conductivities of the LGPS family, Li <sub>9.6</sub> P <sub>3</sub> S <sub>12</sub> and Li <sub>9.54</sub> Si <sub>1.74</sub> P <sub>1.44</sub> S <sub>11.7</sub> Cl <sub>0.3</sub> . <sup>64</sup> (g) The first principles calculation for the phase equilibria of LGPS during lithiation and delithiation process, where it shows the stable window of LGPS is 1.71 - 2.14 V. <sup>43</sup> The equilibrium lithium concentrations predicted by the conventional model. (h) and the calculation model (i). (j) The equilibrium lithium concentrations predicted by calculation model at the initial stage of charging for the LCO/LPS interface. <sup>73</sup> (k) Capacity lose at the initial charge/discharge	

cycle and the loss of interfacial contact between cathode particles and a sulfide-based SSE.<sup>76</sup>  
..... 20

Figure 2.4 The composite electrolytes of (a) ceramic in polymer and (b) polymer in ceramic. Lithium dendrite growth mechanism of (c) ‘polymer in ceramic’ with SPE filled in 5 μm size of LLZTO garnet SSE, (d) ‘ceramic in polymer’ with 200 nm size of LLZTO garnet SSE filled in SPE and (e) sandwich type composite electrolyte with ‘ceramic in polymer’ composite electrolyte at the Li/‘polymer in ceramic’ composite electrolyte interface.<sup>116</sup> ..... 26

Figure 2.5 Comparison on ionic conductivities of different types of SSEs including NASICON-type, garnet-type, perovskite-type, sulfide-based SSEs, SPE, and hybrid electrolytes with composite structure. Hybrid electrolytes show comparable ionic conductivities to other individual SSEs.<sup>126</sup> ..... 28

Figure 2.6 Strategies for designing a high ionic conductivity hybrid electrolyte. (a) Size and concentration effects on the ionic conductivity of PEO-LLZO hybrid electrolytes.<sup>110</sup> (b) Comparison of the lithium ion transport pathways in hybrid electrolytes with nanowire or particle LLTO fillers.<sup>105</sup> Reproduced with permission. (c) Vertically aligned lithium ion transporting channels to enhance the ionic conductivity.<sup>99</sup> (d) Creating a 3D ionic conducting ceramic network for enhancing the ionic conductivity of a hybrid electrolyte.<sup>109</sup> (e) Plasticizer additives to increase the RT ionic conductivity of a hybrid electrolyte.<sup>144</sup> ..... 33

Figure 2.7 (a) Synthesis process of 3D garnet SSE framework for reinforcing the SPE. (b) comparison of lithium symmetric cells performance with garnet-SPE composite electrolyte and 3D garnet SSE framework reinforced SPE.<sup>149</sup> (c) Electrochemical behavior of lithium metal electrodes in SPEs with different salts. Galvanostatic cycling of lithium symmetric cells at 0.1 mA/cm<sup>2</sup> (half cycle time 2 h) at 70 °C. (d) and (e) Schematic illustration of the reaction mechanisms for the electrolytes containing LiN<sub>3</sub> and LiNO<sub>3</sub> additives, respectively.<sup>157</sup> (f) Schematic illustration of Al<sub>2</sub>O<sub>3</sub> coated lithium metal anode for SPE symmetric cells. (g) Electrochemical behavior of lithium metal electrodes in SPEs with different thickness of Al<sub>2</sub>O<sub>3</sub> coating.<sup>164</sup> ..... 36

Figure 2.8 (a) TEM images of (a) noncoated LiCoO<sub>2</sub> and (b) Al<sub>2</sub>O<sub>3</sub> coated LiCoO<sub>2</sub> particle. (c) comparison of cycling performance of noncoated LiCoO<sub>2</sub> and Al<sub>2</sub>O<sub>3</sub> coated LiCoO<sub>2</sub> in

solid polymer batteries.<sup>29</sup> (d) Schematic illustration of double layer structure SPE for SSLIBs. (e) Charge/discharge profile of SSLIB with double layer structure SPE. (f) Comparison of cycling performance of SSLIBs with different structure SPEs. (g) Rate performance of SSLIB with double layer structure SPE. (h) Comparison of impedance curves of SSLIB with double layer structure SPE and with single PEO-based SPE before and after cycling.<sup>32</sup> ..... 39

Figure 2.9 (a) SEM images of the garnet SSE/lithium metal interface without ALD Al<sub>2</sub>O<sub>3</sub> coating (left) and with ALD Al<sub>2</sub>O<sub>3</sub> coating (right). The insets are photos of melted lithium metal on top of the garnet SSEs surfaces. An intimate contact between lithium metal and SSE was achieved with ALD Al<sub>2</sub>O<sub>3</sub> coating. (b) Comparison of the impedances of symmetrical lithium cells with garnet SSEs with/without ALD Al<sub>2</sub>O<sub>3</sub> coating. The inset is the enlarged EIS curve of symmetrical lithium cells with garnet SSEs with ALD Al<sub>2</sub>O<sub>3</sub> coating where a very small impedance is presented.<sup>169</sup> (c) Cycling performance of bare LATP/lithium symmetric cell at a current density of 0.01 mA/cm<sup>2</sup>. A significant increase of overpotential is observed. (d) Cycling performance of ALD Al<sub>2</sub>O<sub>3</sub> coating LATP/lithium symmetric cell at a current density of 0.01 mA/cm<sup>2</sup>; The potential profile is quite stable with ALD coating.<sup>55</sup> .. 41

Figure 2.10 (a) Schematic diagram shows the co-sintering process to construct a SSLIB with oxide-based SSE. Left, mixture of LLZO particles, LCO particle, Li<sub>2.3</sub>C<sub>0.7</sub>B<sub>0.3</sub>O<sub>3</sub> sintering additive on the top of LLZO SSE pellet. Right, co-sintering this pellet at 700 °C to obtain an intimate SSE/cathode interface. (b) Cycling performance at RT of the SSLIB obtained from (c), lithium metal was used as anode.<sup>175</sup> (c) Schematic diagrams show the structure of SSLIBs with dense SSE (left) and porous structure SSE (right). (d) Surface SEM image of porous structure SSE pellet. (e) Comparison of SSLIBs performances with dense SSE and porous structure SSE.<sup>176</sup> ..... 43

Figure 2.11 Configurations showing the poor contact between oxide-based SSE and cathode, anode electrodes. (b) After adding small amount of liquid electrolyte, the interface is well wetted, realizing an uniform Li<sup>+</sup> flux. (c) Comparison on the performance of the LiFePO<sub>4</sub> LIBs with different amounts of liquid-based electrolyte in the LATP/electrode.<sup>183</sup> (d) The configuration of a SSLIB with a SPE-oxide sandwich hybrid electrolyte and the molecule structure of the SPE. Electric potential profile across (e) a SPE-oxide sandwich electrolyte

and (f) a single SPE; (g) Comparison of the performances of the SSLBs with single layer SPE and SPE-oxide sandwich electrolyte at 0.2 C, 0.5 C and 0.6 C. <sup>184</sup> .....	45
Figure 3.1 (a) Teflon container on the subtract of the stirrer. (b) Teflon evaporating dish ....	62
Figure 3.2 (a) A pair of zirconia vessels (out-shell with stainless steel), (b) Ball mill machine for rotating the zirconia vessels. (c) High temperature Muffle furnace for SSEs sintering....	63
Figure 3.3 (a) Photo image of FE-SEM Hitachi S-4800, (b) Schematic diagram shows the working principle of FE-SEM. <sup>1</sup> .....	65
Figure 3.4 (a) Photo image of Raman spectroscopy, (b) Schematic diagram shows the working principle of Raman spectroscopy. <sup>2</sup> .....	66
Figure 3.5 (a) Photo image of Bruker D8 Advance Diffractometer XRD system; (b) Schematic illustration of Bragg's Law. ....	67
Figure 3.6 (a) Schematic diagram of a synchrotron radiation facility; (b) The dipole radiation pattern of an electron moving in a circular orbit at a low speed ( $\beta = v/c \ll 1$ ); (c) The narrow cone radiation pattern of an electron moving in a circular orbit at high speed ( $\beta = v/c \approx 1$ ); (d) Schematic illustration of the collection of synchrotron radiation through a horizontal slit; <sup>4</sup> (e) The summaries of the interaction mechanisms between X-rays and an atom. <sup>5</sup> .....	69
Figure 3.7 Photo image of a group of Land 2001A Battery Test System. Each unit has 8 independent channels for battery testing.....	70
Figure 3.8 Photo image of A multichannel potentiostat 3/Z (VMP3) coupling with an oven for temperature variation testing.....	71
Figure 4.1 Schematic diagram showing the working mechanism of ALD coating for enabling stable, high voltage solid polymer electrolyte-based lithium ion batteries. The decomposition of SPEs on (a) unprotected LiCoO <sub>2</sub> electrode and (b) electrode with protected LiCoO <sub>2</sub> particles (LCO-coating), and the working mechanism of (c) protected electrode (LCO+CB-coating) in ASSLBs after extensive charge/discharge cycles. Conductive carbon can accelerate the decomposition of SPEs at high voltage, and thus, the protection of the	

carbon/SPE interface is very important for stabilizing high voltage solid-state lithium ion batteries. .... 75

Figure 4.2 (a) A TEM image of the 10 cycles of ALD LTO (thickness is ~5 nm) coating on LiCoO<sub>2</sub> particles and its (b) schematic diagram of the LiCoO<sub>2</sub> electrode with the LCO-coating where conductive carbon is not protected. (c) A SEM image in backscattered electron mode of the 20 cycles of ALD LTO (thickness is ~10 nm) coating on both conductive carbon and LiCoO<sub>2</sub> particles from the LCO+CB-coating sample after focused ion beam (FIB) cutting, and its (d) schematic diagram showing the LiCoO<sub>2</sub> electrode where both LiCoO<sub>2</sub> and conductive carbon are protected. The binder is omitted in the schematic diagrams. .... 78

Figure 4.3 Charge/discharge profiles of ASSLBs with (a) bare LiCoO<sub>2</sub> electrode, (b) LCO-coating protected electrode, and (c) LCO+CB-coating protected electrode at 0.2C and 60 °C. Corresponding (d) cycling performance, (e) rate performance, and (f) long-term cycling performance after rate performance testing for ASSLBs with different LiCoO<sub>2</sub> electrodes at 60 °C. .... 81

Figure 4.4 EIS spectra of ASSLBs with (a) bare LiCoO<sub>2</sub> electrode, (b) LCO-coating protected LiCoO<sub>2</sub> electrode, and (c) LCO+CB-coating protected LiCoO<sub>2</sub> electrode after 10, 20, and 30 cycles of charge/discharge. The inset tables show the critical frequency values on top of the high frequency semi-circle (Fa) and low frequency semi-circle (Fc) at different cycles of charge/discharge, respectively. (d) The equivalent circuit for fitting the EIS spectra. .... 83

Figure 4.5 (a) Comparison of the linear sweep voltammogram of the Li/SPE/PEO-carbon composite cell and Li/SPE/PEO-LTO@carbon composite cell (scan rate = 0.3 mV/s, from OCV to 4.5 V vs. Li/Li<sup>+</sup>). Comparison of the XAS Co K-edge spectra of unprotected LiCoO<sub>2</sub> before and after 5 cycles of charge/discharge in ASSLBs in the discharge state in terms of (b) TEY mode and (c) FLY mode. .... 85

Figure 5.1 (a) schematically showing the ALD-LNO coating on NMC811 electrode. (b) TEM image of ALD- LNO coated cathode active material particle. Comparison of Nb L<sub>3</sub>-edge XAS between ALD-LNO and standard LiNbO<sub>3</sub> sample at (c) TEY and (d) FLY. .... 104



Figure 5.2 Discharge voltage profiles of (a) Li/SPE/bare NMC811 SSB and (b) Li/SPE/ALD-LNO coated NMC811 SSB after different cycles. (c) The midpoint voltage evolution the two SSBs over 200 cycles. (d) Comparison of long cycling performance of the Li/SPE/bare NMC811 SSB and the Li/SPE/ALD-LNO coated NMC811 SSB. The cycling performance was evaluated by galvanostatic discharge/charge cycling at a current of 0.2 C at 60 °C. (e) Comparison of the first-cycle Coulombic efficiency and average Coulombic efficiency of 200 cycles for the SSBs with or without ALD-LNO coating. (f) Comparison of the energy density of 4 V class cathodes in SSBs with dry SPE published in different years at the first cycle, and (g) the energy density after different cycles.<sup>15,16,20,21,23,29-37</sup> The energy density was calculated based on the cathode only due to the limited data about the thicknesses/weights of anode and SPE. .... 106

Figure 5.3 SEM images of (a) a NMC811 secondary particle after 50 cycles of charge/discharge and corresponding (b) HAADF image and STEM-EDX mappings. (c) ALD-LNO coated NMC811 particles after 50 cycles of charge/discharge and (d) HAADF image and STEM-EDX mappings. Scale bars are 2 μm for (a) and (c), 400 nm for (b) and (d). .... 108

Figure 5.4 Ni L<sub>3</sub>-edge synchrotron-based XAS at TEY mode (a, b) and FLY mode (c, d) for bare NMC811 and ALD-LNO coated NMC811 electrodes before/after 5 charge/discharge cycle at discharge state. (b), (d) Normalized peak A intensity in comparison with varied peak B intensity. .... 110

Figure 5.5 XPS C 1s spectra of (a) bare NMC811 electrode, (b) bare NMC811 electrode after 5 charge/discharge cycles at the discharge state, and (c) ALD-LNO coated NMC811 electrode after 5 charge/discharge cycles at the discharge state. (d) XPS spectrum of Nb 3d of ALD-LNO coated NMC811 electrode after 5 charge/discharge cycles at discharge state... 112

Figure 5.6 Schematically showing the ALD-LNO coating effect on the NMC811 SSBs with PEO-based SPE. (a) bare NMC811 particle. Crack emerged in the NMC811 particle after cycling, along with oxygen released, triggering the severe chemical decomposition of SPE.<sup>46</sup> The decay of NMC811 particle, chemical decomposition of SPE and the electrochemical decomposition of SPE result in an unstable CEI in SSBs; (b) ALD-LNO coated NMC811

particle. ALD-LNO coated NMC811 particle preserves structural integrity and without/with less oxygen release, and alleviated SPE decomposition. .... 112

Figure 6.1 (a) Comparison of TGA for DMF-PEOSPE and AN-PEOSPE. (b), (c) The comparison of thicknesses of AN-PEOSPE (b) and DMF-PEOSPE (c) with the same weight and same size. (d) Temperature dependent ionic conductivity of DMF-PEOSPE and AN-PEOSPE. (e) and (f) The optical images of AN-PEOSPE (e) and DMF-PEOSPE (f). .... 130

Figure 6.2 (a) CV cures, (b) Charge/discharge profile, and long cycling performance of Li/SPE/LiCoO<sub>2</sub> ASSLIBs with AN-PEOSPE and DMF-PEOSPE. All Li/SPE/LiCoO<sub>2</sub> ASSLIBs were tested at 60 °C. .... 131

Figure 6.3 (a) LSV studies of DMF-PEOSPE and AN-PEOSPE (from OCV to 6 V vs.Li/Li<sup>+</sup>). (b) 1H NMR spectrum for DMF-PEOSPE and AN-PEOSPE and (c) the enlarge area of 1H NMR spectrum from 1.5 to 4 ppm. Schematically diagram and Gibbs energies for breaking the c-c bond in (d) H<sub>3</sub>CO-[-CH<sub>2</sub>-CH<sub>2</sub>-O-]<sub>4</sub>-CH<sub>3</sub><sup>+</sup> cation and (c) [(H<sub>3</sub>C)<sub>2</sub>N-[-CH<sub>2</sub>-CH<sub>2</sub>-O-]<sub>4</sub>-CH<sub>2</sub>-CH<sub>2</sub>-N(CH<sub>3</sub>)<sub>2</sub>]<sup>+</sup> cation. White sphere: H; grey sphere: C; red sphere: O and blue sphere: N. .... 133

Figure 6.4 Co L-edge XAS in (a) TEY and (b) FLY modes. EIS spectra for Li/SPE/LiCoO<sub>2</sub> ASSLIBs with SPE prepared by (c) AN and (d) DMF. EIS spectra were collected at 4.2 V charging state ..... 135

Figure 7.1 Electrochemical performance of ASSPBs. The charge/discharge voltage profiles of (a) PEO-LCO, (b) CMC-LCO within the first 100 cycles. (c) The average coulombic efficiency of ASSPBs with different binders after 1000 cycles. (d) Cycle performance of ASSPBs with different binders. (e) Capacity retention of ASSPBs with PEO and CMC as the binders after 1000 cycles. Capacity retention is calculated as a percentage of the capacity over the third cycle discharge capacity. (DC: Discharge Capacity, CE: Coulombic Efficiency) All batteries were tested at 60 °C with a voltage cut off of 2.7-4.2 V, and a current density of 0.1 C for the first two cycles and 0.4 C for the remainder of the cycling. .... 149

Figure 7.2 (a) O K-edge XAS at TEY mode and (b) FLY mode for different LCO electrode samples. SEM images for (c) PEO-LCO, (d) CMC-LCO and (e) Na-alginate-LCO electrode. (f) Schematic diagrams for the binding capability of PEO (f) and CRP binders (g). ..... 152

Figure 7.3 XPS results of C1s from (a) PEO-LCO electrode surface and (b) CMC-LCO electrode surface before and after cycling in SPB for 5 cycling (discharge state); XPS results of O1s from (a) PEO-LCO electrode surface and (b) CMC-LCO electrode surface before and after cycling in SPB for 5 cycling (discharge state). ..... 154

Figure 7.4 Synchrotron-based XAS of the Co L-edge at discharge state with (a) TEY detection and (b) FLY detection for LCO particles, PEO-LCO electrodes and CMC-LCO electrodes before and after 5 cycles at full discharge state. .... 155

Figure 7.5 (a) Adsorption energy comparison with the same molar quantity and (b) mass quantity (g). Optimized geometric structure and adsorption energy comparison (c) PEO dipolymer, (d) PVDF (dipolymer), (e) CMC monomer and (f) Sodium alginate monomer on  $\text{LiCoO}_2$  (001). ..... 157

Figure 8.1 Schematic diagram shows processes of making LIC-LCO-AB composite cathode at the surface of garnet LLZO SSE surface. The carbon black powders are omitted. .... 177

Figure 8.2 SEM images of cross-section of (a) LIC-LCO-AB composite electrode on the surface of LLZO at low magnitude (b) EDX spectrum of cross-section LIC-LCO-AB composite electrode at low magnitude (c). (d)-(h) elemental EDX mapping of O, Zr, La, Co, and Cl respectively. Scale bare: 100 $\mu\text{m}$  for (a), 50 $\mu\text{m}$  for (c). ..... 178

Figure 8.3 (a) EIS spectrum of ASSLIBs with 30 %, 40 % and 50 %  $\text{Li}_3\text{InCl}_6$  in LCO composite electrode. (b) charge/discharge profiles of ASSLIBs with 30 %, 40 % and 50 %  $\text{Li}_3\text{InCl}_6$  in LCO composite electrode at 0.1 C. (c) charge/discharge profiles of ASSLIBs with 40 %  $\text{Li}_3\text{InCl}_6$  in LCO composite cathode with different LCO active materials loading at 0.1 C. (d) Cycling performance of ASSLIB with 4 mg/cm<sup>2</sup> loading of LCO at 0.1 C. All the batteries were tested at 60 °C because a dry PEO-based SPE was used at Lithium anode side for reducing the interface resistance between lithium and garnet SSE..... 180

Figure 8.4 Synchrotron based XAS results from Five samples including pristine LLZO powders, pristine  $\text{Li}_3\text{InCl}_6$  powders, LLZO- $\text{Li}_3\text{InCl}_6$  mixture powders, LLZO- $\text{Li}_3\text{InCl}_6$  mixture powders with 200 °C treatment and in-situ synthesis of  $\text{Li}_3\text{InCl}_6$  on the LLZO powders at 200 °C. (a) La  $L_3$ -edge XAS spectra; (b) Zr  $L_3$ -edge XAS spectra; (c) In  $L_3$ -edge XAS spectra and (d) Cl K-edge XAS spectra. .... 182

Figure 9.1 (a) A schematic diagram showing the preparation of an ALD coated LATP SSE and the configuration of ASSLSBs. (b) XRD patterns of LATP with different numbers of ALD coating cycles. (c) Temperature dependent ionic conductivity of the PEO-based SPE and PLP sandwich-type hybrid electrolyte. .... 194

Figure 9.2 Cyclic voltammetry curves of a (a) PEO SPE Li-S battery, (b) ASSLSB with a PLP sandwich electrolyte and (c) ASSLSB with 10 cycles of ALD-PLP. Charge/discharge potential profiles of ASSLSB (d) with a PEO SPE, (e) with a PLP SSE and (f) with 10 cycles of ALD-PLP SSE; (g) cycling performance of Li-S batteries with different electrolytes and its corresponding coulombic efficiency (h). All cycling was performed at a current density of 0.1C (1C = 1670 mAh/g) and 60 °C. .... 196

Figure 9.3 Cross sectional SEM images of (a) pristine LATP, (b) bare LATP after 100 charge/discharge cycles, (c) 5 cycles of ALD coated LATP after 100 charge/discharge cycles, (d) 10 cycles of ALD coated LATP after 100 charge/discharge cycles, (e) 20 cycles of ALD coated LATP after 100 charge/discharge cycles, and (f) 50 cycles of ALD coated LATP after 100 charge/discharge cycles. The red dotted lines indicate the cross section of the LATP side at the cathode interface. Scale bar: 20  $\mu\text{m}$ . (g) Comparison of the XRD patterns of LATP after sintering and LATP with different cycle numbers of ALD coating after 100 charge/discharge cycles in ASSLSBs. The XRD peaks corresponding to the reduced LATP phase are highlighted. .... 199

Figure 9.4 Ti 1s XPS of (a) bare LATP, (b) 5 cycles ALD-LATP, (c) 10 cycles of ALD-LATP and (d) 20 cycles of ALD-LATP after 100 charge/discharge cycles in ASSLSBs. All XPS studies were conducted on the LATP surface facing the sulfur cathode. .... 201

Figure 9.5 Magnified schematic diagram showing (a) bare LATP (top) and the reduction of LATP upon cycling (bottom), and (b) protection of the bulk LATP by ALD before (top) and

after (bottom) cycling. The cell configurations of (c) Li/PEO/S ASSLSB, (d) Li/PLP/S ASSLSB, and (e) Li/ALD-PLP/S ASSLSB..... 202

## List of Abbreviations

**3D:** three-dimensional

### A

**AB:** Acetylene black

**AC:** Alternating current

**ALD:** Atomic layer deposition

**ASSB:** All-solid-state battery

**ASSLB:** All-solid-state lithium battery

**ASSLIB:** All-solid-state lithium ion battery

**ASSLPB:** All-solid-state lithium polymer battery

**ASSLSB:** All-solid-state lithium sulfur battery

### C

**CE:** Coulombic efficiency

**CLS:** Canadian Light Sources

**cryo-TEM:** Transmission electron cryomicroscopy

**CSC:** China Scholarship Council

**CV:** Cyclic Voltammetry

### D

**DEC:** diethyl carbonate

**DFT:** Density function theory

## **E**

**EDC:** ethylene carbonate (DEC)

**EDX:** Energy-dispersive X-ray spectroscopy

**EIS:** Electrochemical impedance spectroscopy

**EMC:** ethylmethyl carbonate

**EO:** ethylene oxide

**EVs:** Electric vehicles

## **F**

**FTIR:** Fourier-transformed infrared spectroscopy

**FLY:** Fluorescence yield

## **G**

**GPE:** Gel polymer electrolyte

## **H**

**HAADF:** High-angle annular dark-field imaging

**HOMO:** Highest occupied molecular orbital

**HXMA:** Hard X-ray MicroAnalysis

## **I**

**ICE:** Initial coulombic efficiency

## **L**

**LCO:** LiCoO<sub>2</sub>

**LFP:**  $\text{LiFePO}_4$

**LIB:** Lithium ion battery

**Li-S battery:** Lithium sulfur battery

**LUMO:** Lowest unoccupied molecular orbital

## **M**

**MLD:** Molecular layer deposition

**MS:** Mass spectrometry

**MW:** Molecular weight

## **N**

**NMC:** Lithium nickel manganese cobalt oxide

**NMP:** N-Methyl-2-pyrrolidone

**NMR:** Nuclear Magnetic Resonance

**NSERC:** National science & engineering research center

## **P**

**PEG:** Polyethylene glycol

**PEO:** Polyethylene oxide

**PVDF:** Polyvinylidene fluoride

## **R**

**RIXS:** Resonant inelastic X-ray scattering

## **S**



**SEI:** Solid electrolyte interphase

**SEM:** Scanning electron microscopy

**SGM:** Spherical Grating Monochromator beamline in Canadian Light Sources

**SPE:** Solid polymer electrolyte

**SPB:** Solid polymer battery

**SSE:** solid state electrolyte

**STEM:** Scanning transmission electron microscopy

**SXRMB:** Soft X-ray microcharacterization beamline

## **T**

**TEY:** Total electron yield

**TEM:** Transmission electron microscopy

**TGA:** Thermogravimetric analysis

## **U**

**UWO:** University of Western Ontario

## **X**

**XAS:** X ray absorption spectroscopy

**XPS:** X ray photoelectron spectroscopy

**XRD:** X ray diffraction

## List of Appendices

Appendix A: Permission from Royal Society of Chemistry (RSC) For Published Article on Journal of Materials Chemistry A.....	223
Appendix B: Permission from Elsevier for Published Article on Energy Storage Materials. .....	224
Appendix C: Permission from Elsevier for Published Article on Nano Energy.....	225

# Chapter 1

## 1 Introduction

### 1.1 Lithium ion batteries: from liquid to solid

Energy risk due to the exhaustion of fossil fuels and environmental air pollution related to modern transportation systems, force the research and development of green and regenerated energies. As the promising candidates for green and regenerated energies, wind power, hydropower, solar energy, nuclear energy etc. have been widely studied and applied for driving our society forward. However, due to the large-scale equipment, time limitation and location limitation, suitable energy storage systems/devices must be developed for convenient and effective application of these green and regenerated energies.

Lithium ion batteries (LIBs), as promising candidates for small and large-scale energy storage systems have received tremendous research interests in the past five decades due to their stable cycling performance and high energy density. In 1991, Sony first commercialized lithium ion batteries with twice the energy density than that of nickel-cadmium or nickel-metal hydride batteries, in terms of both weight and volume.<sup>1</sup> Nowadays, LIBs have been widely applied portable devices such as in cellphones, airpods, laptops, and electric vehicles (EVs), as well as in satellites. As a result of the wide application of LIBs, the 2019 Nobel Prize in Chemistry was awarded jointly to three scientists who have worked on LIBs for several decades and made a big contribution to the development of LIBs.<sup>2</sup>

A practical LIB typically consists of four functional components, the cathode, anode, separator and electrolyte. **Figure 1.1** presents schematically the structure and the working mechanism of LIBs. Cathodes and anodes are typical layered structure materials and undergo an intercalation/deintercalation process of lithium ions during the charge/discharge process. Specifically, during the discharge process, lithium ions deintercalate from the graphite anode, travel through the electrolyte, and intercalate into the layered  $\text{LiMO}_2$  ( $M = \text{Co}, \text{Mn}, \text{Ni}$ ) cathode material. The electrons flow via the external

circuit to power the device. During the charge process, the process mentioned above reverses.

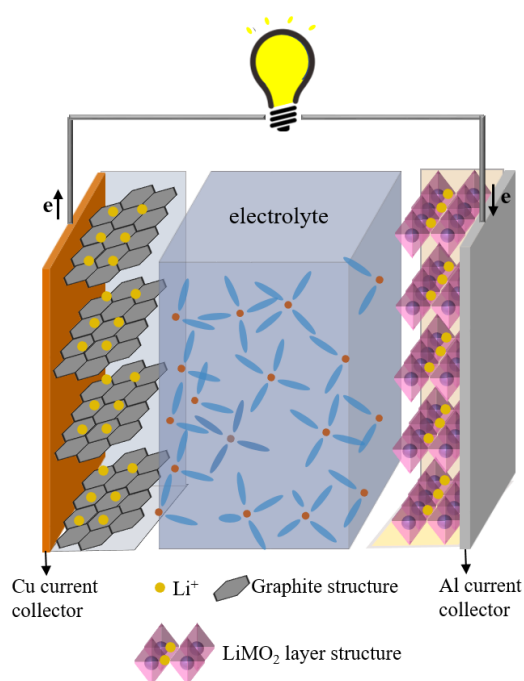


**Figure 1.1** Schematic diagram of a LIB. (Separator is eliminated in this schematic diagram)

To pursue high performance and high energy density of LIBs, a variety of anode materials and cathode materials have been developed and investigated. For anode materials, the most popular and commercialized anode is graphite, which attracted plenty of research interests due to its long cycling stability and reliability. However, its specific capacity is relatively low, which makes it not a suitable anode material for high energy density LIBs, for the application in EVs with the long driving distance. Therefore, novel and higher energy density anodes were studied by scientists and researchers in the past several decades. As successful examples, silicon (Si) and lithium metal are two promising candidates for anode materials in high energy density LIBs. Si anode has very high specific capacity over 4200 mAh/g, which is more than 10 times higher than that of a graphite anode.<sup>3</sup> Lithium metal anodes also can deliver a high specific capacity over 3800 mAh/g, with a lowest electrochemical potential of -3.04 V versus the standard hydrogen electrode.<sup>4</sup> However, there are still many challenges, such as the volume expansion and lithium dendrite formation that need to be addressed before commercializing Si anodes and lithium metal

anodes.<sup>3-6</sup> For the cathode materials,  $\text{LiCoO}_2$  is one of the earliest cathode materials for LIBs.<sup>7</sup> Later on,  $\text{LiFePO}_4$  was discovered to be a high-performance cathode material for LIBs, with high specific capacity and high rate performance.<sup>8</sup>

Energy density of LIBs is calculated based on capacity multiplied by voltage. Therefore, to further enhance the energy density of LIBs, higher specific capacity or higher voltage cathode materials must be applied. To achieve this goal, novel cathode materials such as layered structure Ni-rich  $\text{LiNi}_x\text{Mn}_y\text{Co}_{1-x-y}\text{O}_2$ , layered structure Li-rich  $\text{LiNi}_x\text{Mn}_y\text{Co}_{1-x-y}\text{O}_2$  and spinel structure  $\text{LiMn}_2\text{O}_4$  were developed. Though these cathodes can deliver high energy density, their chemical/electrochemical stabilities and electrochemical performances are still far away from satisfied for commercial LIBs. To overcome these challenges, most of the research works in the past 20 years were dedicated to enhancing these cathode material's performances by surface coating, element doping, structure design, binder selection and electrolyte selection/modification.<sup>9-13</sup>

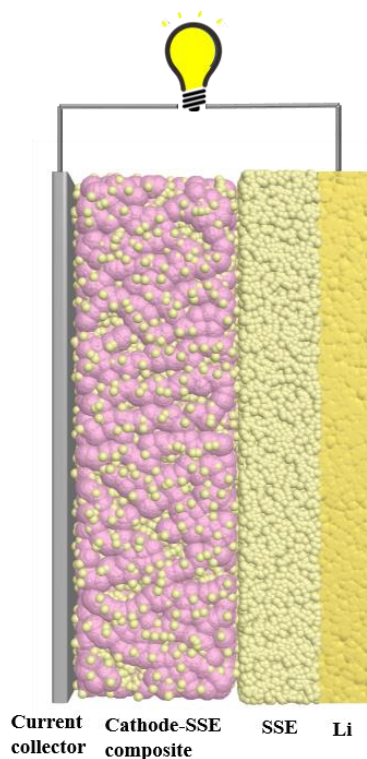


**Figure 1.2** Configuration of all-solid-state batteries (ASSBs).

However, commercial LIBs using liquid organic electrolyte suffer from serious safety issues. Liquid organic electrolyte is flammable, which has a low boiling point and a low flash point.<sup>14</sup> The overheating, short-circuiting or another accident will lead to the fire and even explosion of LIBs. The safety issues are more critical when LIBs were applied in EVs. Therefore, to make LIBs safer and more reliable, flammable liquid organic electrolyte must be eliminated. Developing All-solid-state LIBs (ASSLIBs) is the perfect solution for safe LIBs. The confabulation of an ASSLIB is shown in **Figure 1.2**. The basic working mechanism of ASSLIBs does not change, but the liquid electrolyte and separator are replaced by a solid-state electrolyte (SSE), to avoid the direct contact between anode and cathode. Due to the better safety of ASSLIBs, lithium metal anode can be used in ASSLIBs, leading to higher energy density. Also, ASSLIBs package can be designed as bipolar structure, which can reduce the weight of out-shell, current collector and thus increase the energy density. With such advantages, ASSLIBs have received a great amount of research attention from academia and industry.

## 1.2 Challenges in solid-state lithium ion batteries

Though ASSLIBs are safer and expected to be able to deliver higher energy density, there is still a long way to go for ASSLIBs before being a practically applicable product. The key challenges of ASSLIBs come from the problems of SSEs. A high performance SSE applied in ASSLIBs should include the properties: (i) high total (bulk and grain boundary)  $\text{Li}^+$  ion conductivity over a wide temperature range, (ii) wide electrochemical stable window to couple with lithium metal anodes and high voltage cathodes, (iii) chemically and mechanically compatible interfaces with anode and cathode, (iv) chemically stable in ambience environment, and (v) low interfacial resistance toward electrodes. Unfortunately, none of the SSEs developed today can meet all these criterions. Five main challenges stand in SSEs' way to high performance ASSLIBs.

### i) Poor ionic conductivity

The ionic conductivities of SSEs are relatively low. Compared to the liquid organic electrolyte whose ionic conductivity is over  $10^{-2}$  S/cm, most of the SSEs such as polymer electrolytes, oxide-based SSEs and halide-based SSEs, have an ionic conductivity range of

$10^{-5}$  to  $10^{-3}$  S/cm.<sup>15-17</sup> Only a few sulfide-based SSEs, such as  $\text{Li}_{10}\text{GeP}_2\text{S}_{12}$  and  $\text{Li}_{9.54}\text{Si}_{1.74}\text{P}_{1.44}\text{S}_{11.7}\text{Cl}_{0.3}$ , can reach the level of  $10^{-2}$  S/cm.<sup>18, 19</sup> The poor ionic conductivity of SSEs will decrease the rate performance of SSLIBs and also limit the released capacity.

#### ii) Mismatch problem

The mismatch problem of SSE/electrode interface will deteriorate the electrochemical performance of ASSLIBs. The solid-state nature and rigid property of SSEs result in the poor contact with the solid-state electrodes, especially for the particle types of electrode materials. Without intimate contact between SSEs and electrodes,  $\text{Li}^+$  ions cannot transfer from the SSE to the electrodes; thus, electrochemical reaction cannot happen.

#### iii) Incompatibility between SSE and electrode materials

The SSE and electrode may be incompatible with each other. The chemical/electrochemical reactions arise when SSE and electrode materials are integrated together, resulting in the formation of a solid electrolyte interphase (SEI). This interphase may not be a good  $\text{Li}^+$  ion conductor, which contributes to high interfacial resistance. Sometimes these chemical/electrochemical reactions will propagate into the bulk of materials and are not only limited at the interface. This will degrade the performance of SSEs and electrodes.

#### iv) Space-charge layer

The space-charge layer formation at the SSE and cathode interface will also lead to high interfacial resistance. The formation of a space-charge layer is due to the different chemical potentials between two contacted materials, and the atoms or electrons are unable to migrate to establish local charge neutrality. The space-charge layer is not a good  $\text{Li}^+$  ion conductivity layer, thus, resulting in poor  $\text{Li}^+$  ion migration and high interfacial resistance.

#### v) Lithium dendrite formation

The application of a lithium metal anode in ASSLIBs will result in the formation of lithium dendrites. Generally speaking, lithium dendrite growth is regarded as a self-enhanced process. The dendrite lithium can attract more lithium ions to deposit, due to the higher

electric fields, as a result of the high curvature structure of the dendrite shape. This can lead to continuous lithium dendrite growth. The formation of lithium dendrites will finally lead to the short circuit of ASSLIBs, leading to batteries failing and safety issues.

To overcome abovementioned challenges in ASSLIBs, many strategies and approaches including interface engineering, SSE modification, electrode design etc. were proposed and studied. Great progress has been achieved. In Chapter 2, the details of these solutions will be introduced and discussed.

### 1.3 Thesis objectives

All-solid-state lithium batteries (ASSLBs) have been widely regarded as the promising candidate for the application in EVs. However, the challenges including (i) low electrochemical oxidation window, (ii) mismatch problem, (iii) incompatibility between the SSE and electrode material problems have significantly restricted the application of ASSLBs. The existing research focus in ASSLBs are mainly divided into 3 categories (1) synthesizing high performance SSEs, (2) addressing the interface problems between SSEs and electrode for high performance ASSLBs, (3) understanding the interface behavior in ASSLBs. In the past five years, the author has devoted significant efforts to develop different solutions from interface modification, electrolyte modification and electrode design to stabilize the SSE and electrode interface for achieving high performance and high energy density all-solid-state lithium batteries, and using advanced characterization techniques to understanding the interface behavior in ASSLBs. The major research objectives are listed below:

#### Part. 1 Solid-state electrolyte/electrode interfaces engineering to address the interfacial reaction problems for high energy density ASSLBs

- i) To stabilize the performance of high voltage  $\text{LiCoO}_2$  coupled with polyethylene oxide (PEO) based solid polymer electrolytes (SPEs), coating with an atomic layer deposition (ALD) derived lithium tantalate on the  $\text{LiCoO}_2$  electrode was studied. The interface modification of  $\text{LiCoO}_2$  particles/SPE interface, carbon black particles/SPE interface,



as well as engineering both  $\text{LiCoO}_2$  and carbon black particles (electrode surface)/SPE, will be studied and compared.

- ii) To enable high performance Ni-rich  $\text{LiNi}_{0.8}\text{Mn}_{0.1}\text{Co}_{0.1}\text{O}_2$  (NMC811) ASSLIBs with PEO-based SPEs, ALD derived lithium niobium oxide was applied as a protected layer for not only stabilizing the NMC811 cathode, but also inhibiting the decomposition of the SPE at high voltage.
- iii) To address the incompatibility (side-reaction) between a Ti-containing NASICON SSE and sulfur cathode,  $\text{Al}_2\text{O}_3$  was coated on the surface of the SSE as a protected layer. The thickness of coating and understanding of surface/interface chemistry will be studied and established.

#### Part. 2 Electrolyte modification for high energy density ASSLIBs

- i) To enhance the electrochemical stability of PEO-based SPEs at high voltage, for 4 V class ASSLIBs, the PEO polymer was modified with a stable functional group. The mechanism of the modified SPE will be studied and discussed.

#### Part. 3 Electrode design for high performance ASSLIBs

- i) To develop high performance and long cycling life ASSLIBs, the binder effects were studied. The carboxyl-rich polymer binders, including sodium alginate (Na-alginate) and sodium carboxymethyl cellulose (CMC), show more stable performance in 4 V class ASSLIBs. The mechanism of binders will be investigated and discussed.
- ii) To develop an all ceramic ASSLIB with oxide-based SSE and  $\text{LiCoO}_2$  cathode, the in-situ formation of  $\text{Li}_3\text{InCl}_6$  (LIC) SSE at the oxide-based SSE/ $\text{LiCoO}_2$  interface is studied. The contents of LIC in LIC- $\text{LiCoO}_2$  composite cathodes will be studied and the performance of ASSLIBs will be evaluated.

## 1.4 Thesis organizations

This thesis consists of ten chapters (two introductory chapters, one experimental chapter, six article chapters, and one conclusion chapter) and is organized according to the

requirements on “Integrated-Article” form, as outlined in the Thesis Regulation Guide by the School of Graduate and Postdoctoral Studies (SGPS) of the University of Western Ontario. The contents of the thesis are organized as follows:

**Chapter 1** briefly introduces the current status of research on liquid organic electrolyte-based LIBs and ASSLIBs and summarizes the challenges in ASSLIBs and the solutions for addressing these challenges.

**Chapter 2** gives a detailed introduction into the current status of research surrounding ASSLIBs. The advantages and challenges for different SSEs are summarized. The approaches for tackling the challenges in ASSLIBs with SPEs and oxide-based SSEs are also discussed. Finally, the future work in this field is proposed.

**Chapter 3** describes the details about the experimental methods and analytical apparatus used in the work of this thesis.

**Chapter 4** studies the coating effects on electrode surfaces, active material particles surfaces and conductive carbon particles surfaces, on the performance enhancement in high voltage ASSLIBs. The electrochemical performance results disclosed that conductive carbon/SPE interfaces are detrimental to high voltage ASSLIBs. Interface engineering between conductive carbon and SPE interfaces can help to improvement the stability of SPE at high voltage.

**Chapter 5** further explores the interface engineering effect between Ni-rich NMC811 cathodes and SPEs. The instability of Ni-rich cathodes and the electrochemical decomposition of SPEs are two main reasons for the poor cycling performance of ASSLIBs. However, the oxygen release from layered structure NMC811 cathodes may also initiate the chemical decomposition of SPEs. Mechanism studies showed that with the ALD derived LNO coating on the NMC811 cathode electrode surface, the stability of the NMC811 cathode was improved and thus reduced the oxygen release. At the same time, the low electronic conductive LNO can effectively inhibit the electrochemical decomposition of SPEs. As a result of this, the electrochemical performance of ASSLIBs significantly improved.

**Chapter 6** describes a facile method for enhancing the electrochemical oxidation window of PEO-based SPEs. Specifically, this method is to tailor the end functional group of the PEO polymer chain to enhance its electrochemical stability. NMR studies showed that end methylene group in regular PEO polymer was replaced by a dimethylamine group due to the reaction between PEO and dimethylformamide solvent at 70 °C. Mathematical modeling resulting indicates that the Gibbs energy for breaking C-C bond in the dimethylamine end group PEO is higher than that in the methylene end group PEO. Thus, the high voltage stability of the SPE is increased. Therefore, 4 V class ASSLIBs with this SPE present better performance.

**Chapter 7** investigates the binder effects in 4 V class ASSLIBs. It is found that carboxyl-rich polymer (CRP) binders are superior to PEO and PVDF binders for 4 V class ASSLIBs. With a CRP binder, 4 V class ASSLIBs can be cycled 1000 times with a capacity retention of 60%; 10 times higher than that of a PEO binder. Mechanism studies have indicated that CRP binders are high voltage stable, and they work as coating materials for preventing the electrochemical decomposition of SPE at high voltage.

**Chapter 8** develops a new co-sintering assistance for building oxide based ASSLIBs. Oxide based ASSLIBs suffer from the mismatch problem, which impedes their ability to attain good electrochemical performance. By applying a low sintering temperature and high ionic conductive halide SSE  $\text{Li}_3\text{InCl}_6$ , the mismatch issue between the LLZO garnet SSE and  $\text{LiCoO}_2$  cathode is solved. This results in a 129.2 mAh/g discharge capacity from the ASSLIB; comparable to that (132 mAh/g) obtained from the liquid based LIB. The content of AB,  $\text{Li}_3\text{InCl}_6$  and the loading of active materials are also studied. The interfacial stability between LLZO and  $\text{Li}_3\text{InCl}_6$  is also investigated. This work provides a new approach for building oxide based ASSLIBs, which will trigger more related studies in this field.

**Chapter 9** develops a high performance ASSLSB with the protection of ALD coating on the SSE/cathode interface. ASSLSBs are a promising candidate for next generation energy storage devices due to their high energy density and the abundance of sulfur. However, the intermediate discharge product, polysulfide, is reductant to the LATP SSE. Therefore, an

ultrathin ALD derived  $\text{Al}_2\text{O}_3$  coating is used to prevent the reduction of LATP SSE in ASSLSBs. With as thin as 1 nm of  $\text{Al}_2\text{O}_3$  coating, the electrochemical performance of ASSLSBs greatly improved.

**Chapter 10** summarizes the results, conclusions and contributions of the thesis work. Some personal opinions, perspectives, and suggestions for future developments of ASSLIBs and/or ASSLBs are also illustrated.

## Reference

1. A. Yoshino, *Angew. Chem. Int. Ed.*, 2012, 51, 5798-5800.
2. The Nobel Prize in Chemistry 2019. NobelPrize.org. Nobel Media AB 2020. Wed. 12 Feb 2020. <<https://www.nobelprize.org/prizes/chemistry/2019/summary/>>
3. X. Su, Q. Wu, J. Li, X. Xiao, A. Lott, W. Lu, B. W. Sheldon and J. Wu, *Adv. Energy Mater.*, 2014, 4, 1300882.
4. D. Lin, Y. Liu and Y. Cui, *Nat. Nanotech.*, 2017, 12, 194-206.
5. M. Ge, X. Fang, J. Rong and C. Zhou, *Nanotechnology*, 2013, 24, 422001.
6. X.-B. Cheng, R. Zhang, C.-Z. Zhao and Q. Zhang, *Chem. Rev.*, 2017, 117, 10403-10473.
7. K. Mizushima, P. C. Jones, P. J. Wiseman and J. B. Goodenough, *Solid State Ionics*, 1981, 3-4, 171-174.
8. Y.-H. Huang and J. B. Goodenough, *Chem. Mater.*, 2008, 20, 7237-7241.
9. B. Xiao and X. Sun, *Adv. Energy Mater.*, 2018, 8, 1802057.
10. L. Liang, W. Zhang, F. Zhao, D. K. Denis, F. u. Zaman, L. Hou and C. Yuan, *Adv. Mater. Interfaces*, 2020, 7, 1901749.
11. N. P. W. Pieczonka, V. Borgel, B. Ziv, N. Leifer, V. Dargel, D. Aurbach, J.-H. Kim, Z. Liu, X. Huang, S. A. Krachkovskiy, G. R. Goward, I. Halalay, B. R. Powell and A. Manthiram, *Adv. Energy Mater.*, 2015, 5, 1501008.
12. C. Zhang, *Nat. Energy*, 2019, 4, 350-350.
13. S. Chen, K. Wen, J. Fan, Y. Bando and D. Golberg, *J. Mater. Chem. A*, 2018, 6, 11631-11663.
14. S. Hess, M. Wohlfahrt-Mehrens and M. Wachtler, *J. Electrochem. Soc.*, 2015, 162, A3084-A3097.

15. F. Croce, G. B. Appetecchi, L. Persi and B. Scrosati, *Nature*, 1998, 394, 456-458.
16. V. Thangadurai, S. Narayanan and D. Pinzaru, *Chem. Soc. Rev.*, 2014, 43, 4714-4727.
17. X. Li, J. Liang, N. Chen, J. Luo, K. R. Adair, C. Wang, M. N. Banis, T.-K. Sham, L. Zhang, S. Zhao, S. Lu, H. Huang, R. Li and X. Sun, *Angew. Chem. Int. Ed.*, 2019, 58, 16427-16432.
18. N. Kamaya, K. Homma, Y. Yamakawa, M. Hirayama, R. Kanno, M. Yonemura, T. Kamiyama, Y. Kato, S. Hama, K. Kawamoto and A. Mitsui, *Nat. Mater.*, 2011, 10, 682-686.
19. Y. Kato, S. Hori, T. Saito, K. Suzuki, M. Hirayama, A. Mitsui, M. Yonemura, H. Iba and R. Kanno, *Nat. Energy*, 2016, 1, 16030.

## Chapter 2

### 2 Literature review

Herein, the literatures about SSEs and ASSLIBs will be reviewed. Different types of SSEs including SPEs, oxide-based SSEs, sulfide-based SSEs, halide-based SSEs and hybrid electrolytes will be introduced and discussed. The solutions for addressing the challenges in ASSLIBs with SPEs and oxide-based SSEs will be summarized.

---

Note: some parts of this chapter have been published in **Energy Storage Materials**, 2019, 21, 308-334.

## 2.1 Solid-state electrolytes for solid-state lithium ion batteries

The SSEs for ASSLIBs must have very good  $\text{Li}^+$  ion conduction with an ionic conductivity over  $10^{-4}$  S/cm at the working environment. The candidate materials which have the properties to conduct  $\text{Li}^+$  ion include polymer-lithium salt complexes (e.g. SPE), crystallized lithium containing oxide materials, sulfide materials, halide materials and other materials, like nitride, hydride. Different types of SSEs related to their advantages/disadvantages and challenges will be discussed in this chapter.

### 2.1.1 Solid polymer electrolytes

In 1973, the discovery of ionic conductive complexes between polyethylene oxide (PEO) and alkali metal salts by Wright et al.<sup>1</sup> opened up a new direction for SSE research. Generally speaking, a good SPE consists of a high dielectric host polymer, complexed with a lithium salt with a low lattice energy (**Figure 2.1a** shows the structure of a SPE with PEO complexing with  $\text{LiAsF}_6$ ). Polymers with polar functional groups are chosen to facilitate the dissociation and transport of alkali ions; salts with high ionization ability are selected. Among all SPEs, PEO-based SPEs are most widely studied<sup>2-10</sup> due to their excellent salt-solvating ability and interfacial compatibility with electrodes. Moreover, ASSLIBs with a  $\text{LiFePO}_4$  cathode, a Li metal anode and a polyether based SPE, show excellent cycling performance at elevated temperature.<sup>10</sup> They have been commercialized in the electric car model, Bolloré Bluecar, to provide 30 KWh electricity, with a driving range of 250 km. Other host polymer candidates including polyacrylonitrile (PAN),<sup>11-13</sup> poly(methylmethacrylate) (PMMA),<sup>14,15</sup> poly(vinylidene fluoride-co-hexafluoropropylene) (PVDF-HFP)<sup>16,17</sup> and poly(propylene carbonate) (PPC),<sup>18,19</sup> as well as poly(ethylene carbonate) (PEC)<sup>20</sup>, have also received increasing research interest lately for potential application in ASSLIBs.

However, the ionic conductivity of PEO-based SPEs is in the range of  $10^{-7}$ - $10^{-5}$  S/cm at RT (**Figure 2.1b**)<sup>2-4,21</sup>, which falls short of the requirement of ASSLIBs for operating at a wide temperature range. Moreover, due to the poor mechanical strength of the polymer matrix, SPEs suffer from the lithium dendrite formation problem.<sup>22</sup> Lithium dendrite growth at a

Li/SPE/Li symmetrical cell had been observed using the X-ray tomography technique (**Figure 2.1d-h**).<sup>22,23</sup> The results show that the defect of the lithium anode surface plays a key role in the nucleation of Li dendrites. N.S. Schauer et al. investigated the temperature influence on the Li dendrite formation in SPEs. At a higher temperature (over 105 °C), significant dendrite growth was observed and caused failure of the cell, while under a lower temperature (lower than 90 °C), Li dendrite growth was prohibited.<sup>23</sup> These results can be illustrated as that: at higher temperature, the SPE is melting, so they have lower mechanical strength compared at lower temperature, therefore, lithium dendrite formed at high temperature while inhibited at lower temperature. Thus, to prevent growth of lithium dendrites, a high shear modulus is required for SPEs. As proposed by Monroe and J. Newman, if the shear modulus of SPE is higher than that of lithium metal, the dendrite growth can be inhibited.<sup>24-27</sup>

Another challenge is the electrochemical oxidation of SPEs at high voltages, which seriously restrict their applications in high energy density ASSLIBs.<sup>28</sup> The instability of SPEs under high voltage makes the SPE/cathode interface a big challenge in high energy density ASSLIB systems. PEO-based SPEs are known to be electrochemically stable under 3.8 V (vs. Li/Li<sup>+</sup>) (**Figure 2.1c**), so they are relatively stable towards LiFePO<sub>4</sub> cathode that has a charging plateau at about 3.4 V.<sup>10</sup> However, PEO-based SPEs fail to deliver good performance in ASSLIBs with a high voltage (>4 V) cathode such as LiCoO<sub>2</sub>.<sup>29</sup> To improve the stability of SPEs at high voltage, interfacial coating and double layer SPE approaches have been developed.<sup>29-32</sup>



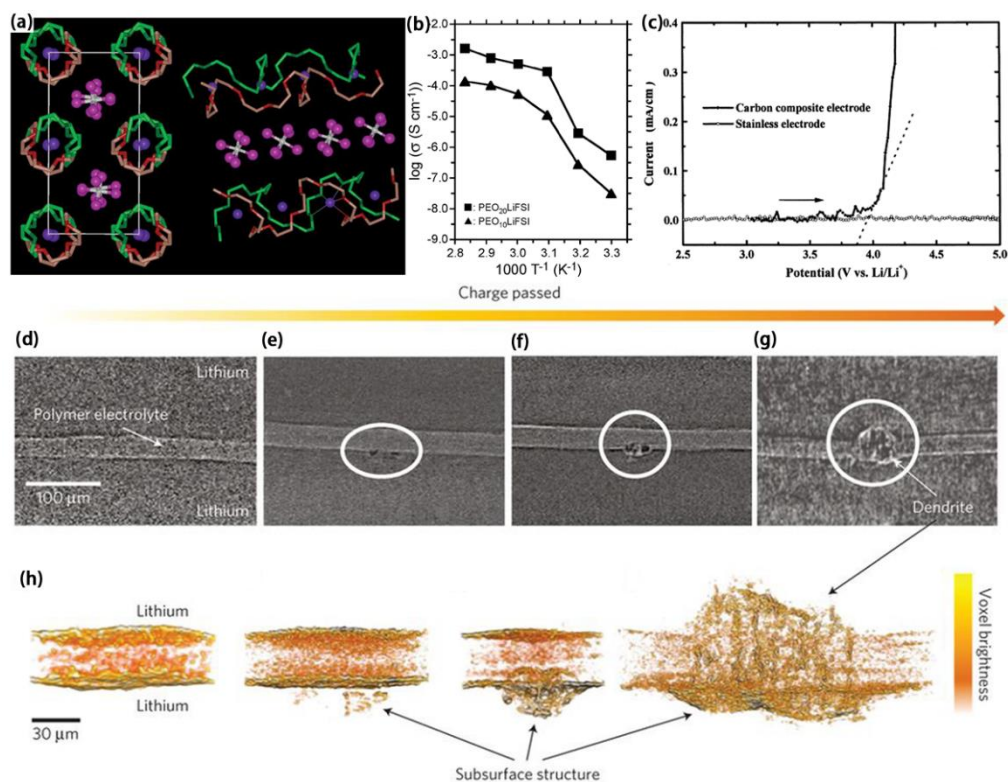


**Figure 2.1** (a) Structure of a crystalline PEO-based SPE consisting of PEO and LiAsF<sub>6</sub>. Left, PEO chain axis is perpendicular to the page. Right, PEO chain axis is parallel to the page. Purple spheres, Li; white spheres, As; pink spheres, F; light green, carbon in PEO chain 1; dark green, oxygen in PEO chain 1. Light red, carbon in PEO chain 2; dark red, oxygen in PEO chain 2. Hydrogens are not shown.<sup>4</sup> (b) Temperature dependent ionic conductivity of PEO-based SPEs.<sup>21</sup> (c) The electrochemical stability window of a PEO-based SPE is only 3.8 V.<sup>28</sup> (d)-(g) X-ray tomography slices show the evolution of Li dendrite formation in SPE and their 3-dimensional (3D) reconstruction diagrams (h).<sup>22</sup>

### 2.1.2 Oxide-based solid-state electrolyte

NASICON-type, perovskite-type, and garnet-type SSEs are the most popular oxide-based SSEs and have demonstrated feasibilities for ASSLIBs. Their intrinsic advantages, such as high ionic conductivity and air stability properties, make them attractive in the applications of ASSLIBs. Categorized by different structures, the oxide-based SSEs exhibit different ionic conductivities and chemical properties and face different challenges in the application of ASSLIBs. Representative examples will be discussed in this section.

NASICON-type SSEs; the name was given to a sodium superionic conductor  $\text{NaM}_2(\text{PO}_4)_3$  ( $\text{M} = \text{Ge}, \text{Ti}, \text{Zr}$ ), have the crystalline NASICON framework. The NASICON framework consists of corner sharing  $\text{PO}_4$  tetrahedra and  $\text{MO}_6$  ( $\text{M} = \text{Ge}, \text{Ti}, \text{Zr}$ ) octahedra forming a 3D network structure.<sup>33</sup>  $\text{Na}^+$  ions are located on interstitial sites and transported along the  $c$  axis.<sup>34</sup> By replacing  $\text{Na}^+$  with  $\text{Li}^+$ , NASICON-type SSEs become  $\text{Li}^+$  ion conductors without the change of the NASICON crystal structure (**Figure 2.2a**). Currently, the most popular NASICON-type SSEs are  $\text{Li}_{1+x}\text{Al}_x\text{Ti}_{2-x}(\text{PO}_4)_3$  (LATP) and  $\text{Li}_{1+x}\text{Al}_x\text{Ge}_{2-x}(\text{PO}_4)_3$  (LAGP), which are obtained by partial Al substitution of Ti or Ge, in  $\text{LiTi}_2(\text{PO}_4)_3$  and  $\text{LiGe}_2(\text{PO}_4)_3$ , respectively. The highest ionic conductivity of NASICON-type SSEs reported to date at RT are in the range of  $10^{-3}$  to  $10^{-2}$  S/cm,<sup>34</sup> which is almost comparable to that of liquid-based electrolytes. However, the rigid nature of NASICON-type SSEs makes it challenging to achieve good interface with the electrodes. Another challenge is that the Ti-containing LATP can react with reductants such as lithium metal (**Figure 2.2j**) and polysulfides, seriously restricting its application in high energy density ASSLIBs.

Garnet-type SSEs have a general chemical formula of  $\text{A}_3\text{B}_2(\text{XO}_4)_3$  ( $\text{A} = \text{Ca}, \text{Mg}, \text{Y}, \text{La}$  et al.  $\text{B} = \text{Al}, \text{Fe}, \text{Ga}, \text{Ge}, \text{Mn}, \text{Ni}$  or  $\text{V}$ ;  $\text{X} = \text{Si}, \text{Ge}, \text{Al}$ ), where A, B, and X have eight, six, and four oxygen coordinated cation sites in a crystalline face-center-cubic structure.<sup>35</sup> The crystalline structure of cubic phase garnet-type SSEs is shown in **Figure 2.2b**. In cubic phase garnet SSE, Li are located at Li1 (24d) and Li2 (48g/96h) sites. The studies of garnet-type SSEs cover  $\text{Li}_3$ -type  $\text{Li}_3\text{Ln}_3\text{Te}_2\text{O}_{12}$  ( $\text{Ln} = \text{Y}, \text{Pr}, \text{Nd}, \text{Sm-Lu}$ ),<sup>36</sup>  $\text{Li}_5$ -type  $\text{Li}_5\text{La}_3\text{M}_2\text{O}_{12}$  ( $\text{M} = \text{Nb}, \text{Ta}$ ),<sup>37</sup>  $\text{Li}_6$ -type  $\text{Li}_6\text{Ala}_2\text{M}_2\text{O}_{12}$  ( $\text{A} = \text{Mg}, \text{Ca}, \text{Sr}, \text{Ba}$ ),<sup>38</sup> and  $\text{Li}_7$ -type  $\text{Li}_7\text{La}_3\text{X}_2\text{O}_{12}$  ( $\text{X} = \text{Zr}, \text{Sn}, \text{Ta}$ ).<sup>39</sup> The first three garnet SSEs have relatively low RT ionic conductivity ( $\sim 10^{-5}$  S/cm), while  $\text{Li}_7\text{La}_3\text{Zr}_2\text{O}_{12}$  (LLZO) possesses relatively high ionic conductivity ( $10^{-4}$ - $10^{-3}$  S/cm). Therefore, research interests are mostly dedicated in LLZO and its derivatives with different elemental doping.<sup>40-42</sup> Garnet-type SSEs are also attractive for their wide electrochemical window and superior stability towards lithium metal anodes.<sup>43</sup> LLZO has two different phases, a lower ionic conductive tetragonal phase and a higher ionic conductive cubic phase. Cubic phase LLZO is more desirable for practical applications, but it usually requires very high sintering temperature to obtain the cubic phase.<sup>39</sup> The  $\text{Li}^+/\text{H}^+$  exchange,<sup>44</sup> upon exposure to moisture, can cause  $\text{LiOH}$ ,  $\text{Li}_2\text{CO}_3$  formation on the LLZO surface, leading to additional problems such as poor lithium wettability and poor

ionic conductivity. Even though LLZO is known to have a high ionic conductivity and stability towards lithium metal anodes, the Li dendrite problem<sup>45,46</sup> and interfacial mismatch issue, due to the rigid properties, remain challenging for garnet-type SSEs. LLZO and electrodes also suffer from the interphase problem. The interphase problem, due to side reactions or elemental diffusion at the interface between the oxide-based SSE and cathode have been reported. At the LiCoO<sub>2</sub>/LLZO interface, Co undergoes mutual diffusion with Zr and La (**Figure 2.2d-h**), forming an interphase with low ionic conductivity (i.e. high interfacial resistance).

Perovskite-type SSEs, with a structure of ABO<sub>3</sub> (A = Ca, Sr, La; B = Al, Ti), were first reported as an oxygen ion conductor.<sup>47</sup> After aliovalent substitution of both metal ions in A-sites, with a formula of Li<sub>3x</sub>La<sub>2/3-x</sub>TiO<sub>3</sub> (**Figure 2.2c**), a Li<sup>+</sup> ion conductor is obtained with a high bulk ionic conductivity over 10<sup>-3</sup> S/cm at RT.<sup>48</sup> Unfortunately, the high grain boundary resistance, high interfacial resistance, and poor compatibility of Ti<sup>4+</sup> with the lithium metal anode, restrict their wide application in ASSLIBs.

Overall, oxide-based SSEs have relatively high ionic conductivity and chemical stability at ambient. Oxide-based SSEs have the highest Young's modulus among all types of SSEs. The Young's moduli for LATP, garnet-type SSE LLZO, and perovskite-type SSE are 115 GPa,<sup>49</sup> 150 GPa,<sup>50</sup> and 203 GPa,<sup>51</sup> respectively. This high elastic modulus could be beneficial for suppressing lithium dendrite formation if engineered properly, but it may result in the mismatch problem towards electrodes if the SSE has too high elastic modulus. **Figure 2.2i** shows the mismatch problem between NASICON SSEs and electrodes, where a big gap is present at the interface and laminating happens, which results in high interfacial resistance and poor electrochemical performance.

In summary, interfacial mismatch and the lithium dendrite problem are the key challenges for oxide-based SSEs and more research efforts are required in this area. The strategies for these interfacial problems include (i) solidifying melting state lithium on SSEs to ensure intimate contact, (ii) co-sintering active materials and SSEs with a sintering additive, and (iii) creating a porous structure SSE to increase the contact area between electrode materials and SSEs. It is believed that engineering the interface with a soft and high ionic

conductive layer between the SSE and electrodes may be a good strategy to tackle the challenges for ASSLIBs with oxide-based SSEs. The details of these solutions will be discussed in the section 2.2.

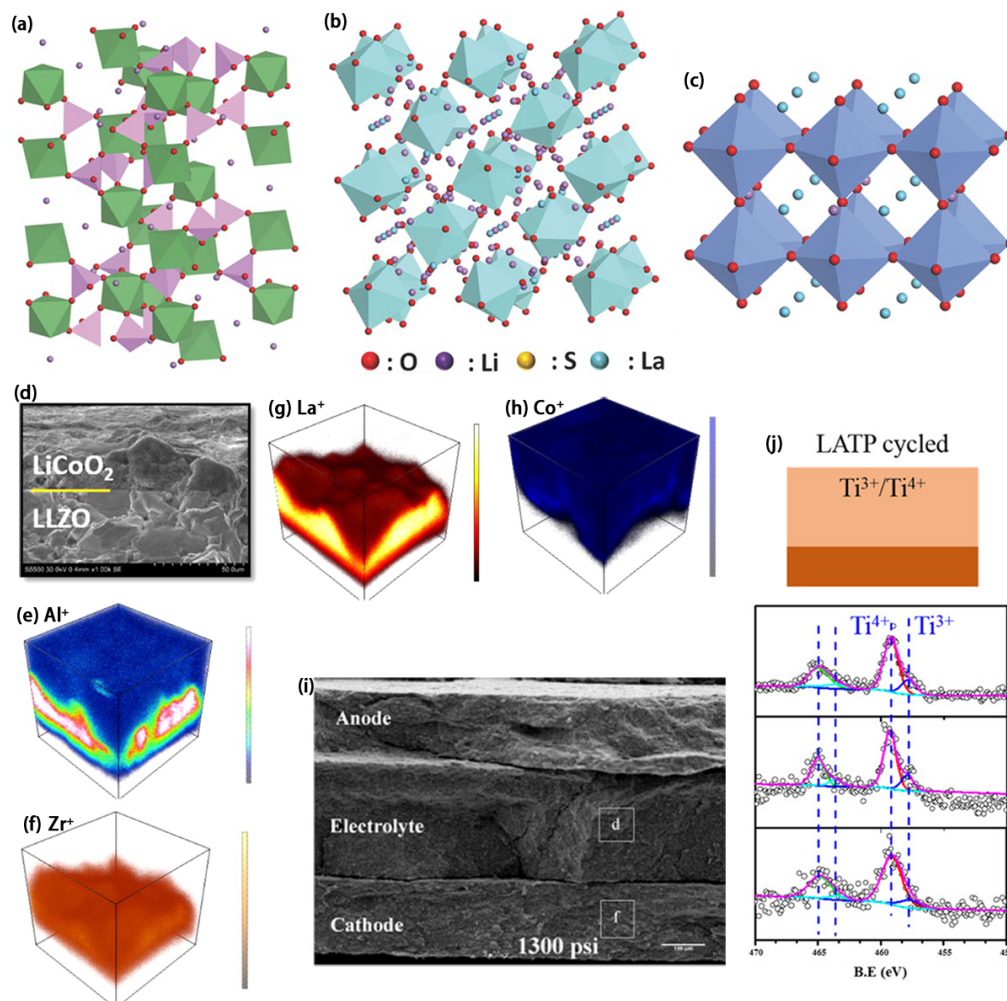


**Figure 2.2** The crystalline structures of (a) NASICON, (b) Garnet, and (c) Perovskite SSEs.<sup>52</sup> Time-of-flight secondary ion mass spectroscopy (TOF-SIMS) study of LiCoO<sub>2</sub>/LLZO interface: (d) SEM image of a LiCoO<sub>2</sub>/LLZO interface and elemental distributions of (e) Al<sup>+</sup>, (f) Zr<sup>+</sup>, (g) La<sup>+</sup>, and (h) Co<sup>+</sup>; color scales show the concentrations of each ion where the upper color represents higher concentrations.<sup>53</sup> (i) Scanning electron microscopy (SEM) image showing the poor contact between NASICON SSE and Li<sub>2</sub>MnO<sub>4</sub>.<sup>54</sup> (j) X-ray photoelectron spectroscopy (XPS) study on the reduction of Ti<sup>4+</sup> in LATP by lithium metal anode.<sup>55</sup>

### 2.1.3 Sulfide-based solid-state electrolyte

Sulfide-based SSEs can be categorized by amorphous, crystalline, and glass-ceramic sulfide SSEs. The representative amorphous sulfide-based SSEs are  $x\text{Li}_2\text{S}\cdot(1-x)\text{P}_2\text{S}_5$  and  $x\text{Li}_2\text{S}\cdot(1-x)\text{SiS}_2$  systems. Both systems present an RT ionic conductivity over  $10^{-4}$  S/cm.<sup>56,57</sup> Crystalline sulfide-based SSE  $\text{Li}_3\text{PS}_4$  was first reported by Tachez et al.<sup>58</sup> Later, Kanno's group reported a thio-LISICON type SSE, produced by replacing  $\text{O}^{2-}$  of the LISICON [ $\text{Li}_{14}\text{Zn}(\text{GeO}_4)_4$ ] family, with  $\text{S}^{2-}$ .<sup>59</sup> The replacement leads to a higher ionic conductivity at RT, because  $\text{S}^{2-}$  has a larger ionic radius, higher polarizability, and lower electronegativity than  $\text{O}^{2-}$ . The replacement of  $\text{O}^{2-}$  by  $\text{S}^{2-}$  lowers the binding of  $\text{Li}^+$  in the crystal framework and enlarges the ion transport channel, thus enhancing the ionic conductivity.<sup>55</sup> Most of the reported crystalline sulfide-based SSEs have an ionic conductivity over  $10^{-4}$  S/cm at RT.<sup>60-63</sup> Glass-ceramic sulfide-based SSEs are prepared by crystallization of glass-state SSEs. Glass-ceramic SSEs based on  $x\text{Li}_2\text{S}\cdot(1-x)\text{P}_2\text{S}_5$  have received tremendous research attentions, especially after the discovery of  $\text{Li}_{10}\text{GeP}_2\text{S}_{12}$  (LGPS) (**Figure 2.3a-c**) families and their derivations, such as  $\text{Li}_{9.54}\text{Si}_{1.74}\text{P}_{1.44}\text{S}_{11.7}\text{Cl}_{0.3}$  (**Figure 2.3d-f**),<sup>61,64,65</sup> which both exhibit ionic conductivities over  $10^{-2}$  S/cm at RT.

The high RT ionic conductivity and relatively soft mechanical properties of sulfide-based SSEs make them promising candidates for the application in ASSLIBs. ASSLIBs with a sulfide-based SSE can be fabricated by simply cold pressing without high temperature co-sintering. However, sulfide-based SSEs suffer from serious instability issues with lithium metal anodes and the conventional cathode materials, which significantly hinder their practical applications in ASSLIBs. The side reaction behaviors between electrodes and sulfide-based SSEs have received much research attention.<sup>43,66-70</sup> The electrochemical stability window of different types of sulfide-based SSEs were evaluated by theoretical calculations (**Figure 2.3g**) and experimental characterizations,<sup>43,66,70,71</sup> where they showed that the sulfide-based SSEs have a narrow electrochemical stability window. In-situ XPS was performed to clarify the interfacial chemistry between sulfide-based SSEs and lithium metal, which confirmed the decomposition products of  $\text{Li}_3\text{P}$ ,  $\text{Li}_2\text{S}$ , and Li-Ge alloy at the interface.<sup>69</sup> The decomposed products have low ionic conductivities and thus introduce high interfacial resistance.

Considering the interface between sulfide-based SSEs and cathodes, the electrochemical instability problem and the formation of space-charge layer (SCL) seriously hinder the application of sulfide-based SSEs. The instability between sulfide-based SSEs and cathode materials, such as  $\text{LiCoO}_2$ , were studied by theoretical calculation and transmission electron microscopy (TEM), confirming the side-reaction products of  $\text{Li}_2\text{S}$ ,  $\text{CoS}_3$  and  $\text{Co}(\text{PO}_3)_2$  at the interface, which cause high interfacial resistance.<sup>68,72</sup> SCL is typically formed at the interface between sulfide-based SSEs and  $\text{LiCoO}_2$ , due to the chemical potential difference between them (Figure 2.3h-j).<sup>73</sup> The high resistance of SCL significantly lowers the capacity and rate performance of ASSLIBs. Interfacial engineering by an oxide material coating layer such as  $\text{Al}_2\text{O}_3$ ,  $\text{Li}_4\text{Ti}_5\text{O}_{12}$ , and  $\text{LiNbO}_3$ , has been demonstrated as an effective way to inhibit the side-reactions and SCL formation.<sup>73-75</sup>

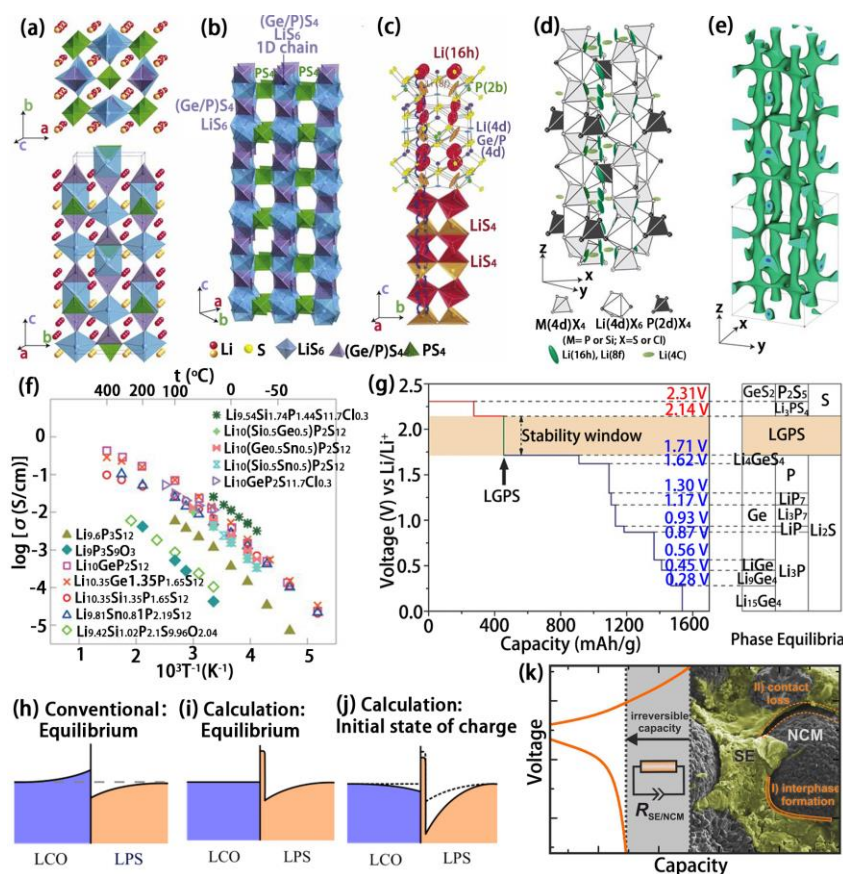


**Figure 2.3** Crystal structure of LGPS sulfide-based SSE; (b) one dimensional view of LGPS framework; (c) Lithium ion conduction pathways in LGPS; zigzag conduction pathways along the c-axis are indicated.<sup>61</sup> (d) Crystal structure of  $\text{Li}_{9.54}\text{Si}_{1.74}\text{P}_{1.44}\text{S}_{11.7}\text{Cl}_{0.3}$ ;

(e) nuclear distributions of Li atoms in  $\text{Li}_{9.54}\text{Si}_{1.74}\text{P}_{1.44}\text{S}_{11.7}\text{Cl}_{0.3}$  at 25 °C. (f) Comparison on ionic conductivities of the LGPS family,  $\text{Li}_{9.6}\text{P}_3\text{S}_{12}$  and  $\text{Li}_{9.54}\text{Si}_{1.74}\text{P}_{1.44}\text{S}_{11.7}\text{Cl}_{0.3}$ .<sup>64</sup> (g) The first principles calculation for the phase equilibria of LGPS during the lithiation and delithiation process, where it shows the stable window of LGPS is 1.71 - 2.14 V.<sup>43</sup> The equilibrium lithium concentrations predicted by the conventional model. (h) and the calculation model (i). (j) The equilibrium lithium concentrations predicted by the calculation model at the initial stage of charging for the LCO/LPS interface.<sup>73</sup> (k) Capacity loss at the initial charge/discharge cycle and the loss of interfacial contact between cathode particles and a sulfide-based SSE.<sup>76</sup>

Even though sulfide-based SSEs are relatively soft compared to oxide-based SSEs, sulfide-based SSEs still experience the mismatch problem. Their poor flexibility still makes it difficult to buffer the volume change of the electrode materials during charge and discharge; the loss of intimate contact between the SSE and cathode particles eventually deteriorates the performance of the ASSLIBs (**Figure 2.3k**).<sup>76</sup> Therefore, understanding the mechanical properties of SSEs and controlling the mechanical properties of SSEs to ensure good contact between the SSE and active materials are as important as preventing the SSE/electrode interfacial side-reaction, for building a high performance ASSLIB.

#### 2.1.4 Halide-based solid-state electrolyte

In the 1970s, W. Weppner et al. first reported the halide-based SSE,  $\text{LiAlCl}_4$ , which has ionic conductivity of  $1 \times 10^{-6}$  S/cm.<sup>77</sup> After that, only a few reports studied new types of halide-based SSEs.<sup>78-80</sup> Though the ionic conductivities of these reported halide-based SSEs were relatively low, researchers are still persistent in their search for a high ionic conductivity halide-based SSE for ASSLIBs. This is because halide-based SSE have a stable interface with the cathode, which make them superior to sulfide-based SSE. And halide-based SSE are mechanically soft, which make them superior to the rigid oxide-based SSEs. Luckily, in 2018, T Asano et al. successfully enhanced the ionic conductivity of halide-based SSEs,  $\text{Li}_3\text{YCl}_6$  and  $\text{Li}_3\text{YBr}_6$ , to  $10^{-3}$  s/cm, by the high energy ball milling synthesis method. Moreover, 4 V class  $\text{LiCoO}_2$  ASSLIBs with  $\text{Li}_3\text{YCl}_6$  halide SSEs showed very stable cycling performance. Inspired by this work, there is a great trend in synthesis novel high ionic conductivity halide-based SSEs for ASSLIBs.<sup>81-85</sup> X. Li et al. prepared a

$\text{Li}_3\text{InCl}_6$  halide-based SSE by solution method, using water as the solution, which has an ionic conductivity of  $2.03 \times 10^{-3}$  S/cm.<sup>85</sup> The as-prepared  $\text{Li}_3\text{InCl}_6$  halide-based SSE also shows good air stability performance, which is superior over the sulfide-based SSE in terms of air stability.<sup>81</sup> Halide-based SSEs with aliovalent substitution was studied by L. Nazar's group, who used Zr to dope  $\text{Li}_3\text{MCl}_6$  ( $\text{M} = \text{Y}, \text{Er}$ ) to enhanced its ionic conductivity to  $1.4 \times 10^{-3}$  S/cm. The Zr doped halide-based SSE also shows very good performance in  $\text{LiCoO}_2$  ASSLIBs.

Though halide-based SSEs have very good compatibility with cathode materials, high ionic conductivity at RT, and facile fabrication process for ASSLIBs, their compatibility with lithium metal anodes and other anodes such as graphite, indium and silicon, is very poor. All the reported ASSLIBs performed with halide-based SSEs must use a layer of sulfide-based SSE at the anode side to avoid the direct contact between the halide-based SSE and anode. This will satisfy the energy density of the SSLIBs. Thereafter, the synthesis of both anode stable and cathode stable halide-based SSEs, aliovalent substitution of halide-based SSE, and using protected lithium anodes for halide-based SSEs, are the main future research directions.

## 2.1.5 Hybrid solid-state electrolyte

### 2.1.5.1 Insulating fillers in SPEs

Hybrid electrolytes, rationally combining two or more types of SSEs with complementary advantages, are promising for building feasible ASSLIBs. Coupling desired soft electrolytes and stiff inorganic SSEs can ensure good electrode wettability, high ionic conductivity, and high mechanical strength to prevent lithium dendrite formation at the same time. Before wide development of the hybrid electrolyte concept, composite electrolytes with insulating fillers and a SPE matrix had received much research attention. The insulating fillers in the composite electrolytes can improve the ionic conductivity to some extent. In the early 1980s,  $\alpha\text{-Al}_2\text{O}_3$  was introduced to a SPE for the first time. The insulating fillers are shown to be able to improve the ionic conductivity by almost two orders of magnitude, to  $10^{-5}$  S/cm at RT.<sup>86,87</sup> Thereafter, other different metal oxides such as  $\text{TiO}_2$ ,<sup>88-89</sup>  $\text{ZrO}_2$ ,<sup>90,91</sup> and  $\text{SiO}_2$ <sup>90,92,93</sup> have been widely studied in composite electrolytes.



Besides metal oxides fillers, metal organic framework (MOF) with a coordination network composed of central metal ions and organic ligands, exhibiting properties of both inorganic and organic materials, are proposed as unique fillers. In comparison with the traditional inorganic fillers, MOFs not only possess some similar properties to metal oxide fillers, such as high thermal stability, large surface area, and abundant Lewis-acid sites, but also have easily modified organic functional groups for improving the ionic conductivity and interfacial compatibility as well.<sup>94,95</sup> Based on the above advantages, C. Yuan et al., dispersed MOF-5 nanoparticles into a PEO electrolyte. As a result, improved interfacial stability and an ionic conductivity of  $3.16 \times 10^{-5}$  S/cm at 25 °C were obtained.<sup>96</sup> Besides, several different kinds of MOFs such as Al(BTC) and MIL-53(Al), with similar roles, were proposed to improve ionic conductivity.<sup>97,98</sup> In order to compensate for the decreased ionic conductivity resulting from the aggregation of high surface energy of MOFs fillers, Z. Wang et al. linked the MOF nanoparticles to the flexible polymer chains by the one-pot UV photopolymerization method. Benefitting from the uniformly dispersed MOF fillers via chemical bonding, a ionic conductivity of  $4.31 \times 10^{-5}$  S/cm at 30 °C was achieved.<sup>95</sup> Despite the improved ionic conductivity, mechanical properties, and interfacial compatibility by adding these insulating fillers, the relatively low ionic conductivity level of  $10^{-5}$  S/cm at RT still cannot meet the practical demands for ASSLIBs.

#### 2.1.5.2 Polymer-oxide SSE hybrid electrolyte

Considering aforementioned inorganic fillers are ionic insulator, which significantly limits further improvements of the ionic conductivity. A composite electrolyte, with an oxide-based SSE mixed with a SPE, is discussed in this part. The combination of a SPE and an oxide-based SSE can realize mechanical flexibility, high ionic conductivity, good wettability to electrodes, good mechanical properties, no Li dendrites, and an enhanced electrochemical stability window at the same time. This type of composite electrolyte can be classified as ‘ceramic in polymer’ and ‘polymer in ceramic’ according to the contents of the ceramic fillers (**Figure 2.4a-b**). Many recent studies focus on enhancing the ionic conductivity of SPEs by adding oxide-based SSE fillers. NASICON-type SSEs, including LATP and LAGP, have been reported.<sup>99-103</sup> The inorganic SSE fillers can not only reduce the crystallinity of the polymer matrix but also possibly provide extra ion transporting

pathways. Y. Wang et al. systematically studied the effect of the incorporation of LATP fillers in a PEO-LATP hybrid electrolyte. They found that increasing the LATP content can decrease the melting temperature ( $T_m$ ) of the PEO complex. Scanning electron microscopy (SEM) analysis showed there is decrease of size of the PEO spherulites after addition of LATP fillers. An ionic conductivity of  $1.167 \times 10^{-3}$  S/cm at 60 °C was achieved with 15 wt.% LATP fillers at an EO/Li<sup>+</sup> ratio of 8.<sup>101</sup>

Since LATP suffers from the Ti<sup>4+</sup> reduction problem when it is in contact with a lithium metal anode, LAGP of the same structure but without Ti<sup>4+</sup>, also received much research attention in composite electrolytes. Y. Zhao et al. had studied the influence of size and concentration of LAGP on the ionic conductivity of the PEO-LAGP-LiTFSI hybrid electrolyte. With different sizes of LAGP fillers, the hybrid electrolyte achieved optimal ionic conductivities with 15-20 wt.% of LAGP. For example, the ionic conductivity of PEO-LAGP-LiTFSI was optimized to  $6.76 \times 10^{-4}$  S/cm at 60 °C with 20 wt.% nano-sized LAGP.<sup>104</sup> Enhanced ionic conductivity with perovskite-type SSE fillers in a SPE matrix was also observed.<sup>105</sup> Y. Cui's group synthesized a nanowire shape of LLTO and incorporated it into a PAN-LiClO<sub>4</sub> SPE. They found that with 15 wt.% nanowire LLTO fillers, the hybrid electrolyte PAN-LLTO-LiClO<sub>4</sub> exhibited a RT ionic conductivity of  $2.4 \times 10^{-4}$  S/cm.

Similar to other oxide-based SSEs, the garnet type SSE LLZO has high ionic conductivity at RT, as well as good electrochemical, chemical, and thermal stability. But unlike the LATP containing an unstable Ti<sup>4+</sup> constituent, LLZO possesses superior electrochemical stability towards lithium metal anodes.<sup>70,106</sup> Consequently, LLZO fillers are expected to not only improve the ionic conductivity but also further improve the stability of hybrid electrolytes at the interface with lithium metal anodes.<sup>107</sup> The reported data shows that SPE-LLZO hybrid electrolytes with different polymer-to-filler ratios had a wide range of ionic conductivities from  $10^{-6}$  to  $10^{-4}$  S/cm at RT. While an RT ionic conductivity of  $10^{-6}$  S/cm order of PEO-LiTFSI SPE filled in LLZO (70 wt.%) was reported by M. Keller et al.,<sup>108</sup> an RT ionic conductivity of  $10^{-4}$  S/cm of PEO-LLZO hybrid electrolytes was also reported by L. Hu' group<sup>109</sup> and J. Zhang et al.<sup>110</sup> In the latter two cases, the reasons for the

higher ionic conductivities are probably because of the usage of the 3 dimensional (3D) LLZO framework and ultra-small (~40 nm) size of LLZO as the fillers.

In addition to the wide application of PEO-based SPEs in hybrid electrolytes, polymer electrolytes based on other polymer structures, such as polyvinylidene fluoride (PVDF), PVDF-HFP, and polyethylene carbonate (PEC), also received much research attention for constructing hybrid electrolytes due to their unique properties, such as high mechanical strength and a high lithium transference number.<sup>19,111-115</sup> However, additional solvent, liquid electrolyte, or combination with other SSEs are required to achieve feasible battery performance in these systems. The PVDF-LLZO hybrid electrolyte reported by X. Zhang et al. exhibited a high ionic conductivity of  $5 \times 10^{-4}$  S/cm at 25 °C, but the residual DMF solvent, remaining from the preparation process, was found in the hybrid electrolyte, according to their thermogravimetric analysis (TGA) results. The DMF content could have played an important role in the high ionic conductivity and battery performance at RT. LiCoO<sub>2</sub> batteries with this PVDF-LLZO hybrid electrolyte exhibited excellent cycling performance and rate performance, delivering a discharge capacity of 130 mAh/g at 4 C rate, which is overcomparable to that of liquid electrolyte systems.<sup>112</sup> C. Sun's group reported a PVDF-HFP-LLZO hybrid electrolyte with RT ionic conductivity of  $1.23 \times 10^{-6}$  S/cm, which was increased to  $1.1 \times 10^{-4}$  S/cm with the addition of a 20  $\mu$ L liquid electrolyte.<sup>115</sup> The LiFePO<sub>4</sub> battery with the PVDF-HFP-LLZO-liquid hybrid electrolyte presented excellent electrochemical performance at RT. L. Fan's group reported a PEC-LLZO hybrid electrolyte prepared by a solution casting method, which had an ionic conductivity of  $5.24 \times 10^{-5}$  S/cm at 55 °C. This PEC-LLZO hybrid electrolyte presented much better thermal stability compared to a commercial Celgard separator and rendered a stable flexible ASSLIB at elevated temperature.<sup>111</sup>

'Polymer in ceramic' composite electrolytes have high mechanical strength which is good at dendrite suppression. However, poor interfacial contact with electrodes results in high interfacial resistance. 'Ceramic in polymer' composite electrolytes have better interfacial contact with electrodes, but their strength is not enough for dendrite suppression. The design using a 'polymer in ceramic' composite electrolyte as the main ionic conductor and separator and 'ceramic in polymer' composite electrolyte as the interface, to ensure

intimate contact with the lithium anode, can render a long cycling performance, dendrite free ASSLIB (Figure 2.4c-e).<sup>116</sup>

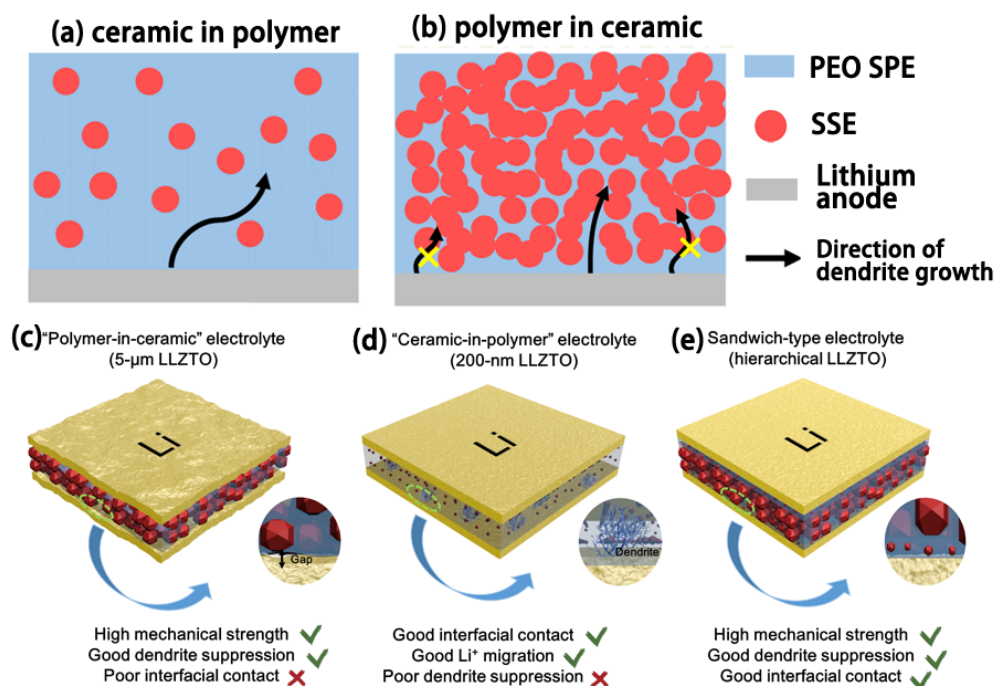


**Figure 2.4** The composite electrolytes of (a) ceramic in polymer and (b) polymer in ceramic. Lithium dendrite growth mechanism of (c) 'polymer in ceramic' with SPE filled in 5  $\mu\text{m}$  size of LLZTO garnet SSE, (d) 'ceramic in polymer' with 200 nm size of LLZTO garnet SSE filled in SPE and (e) sandwich type composite electrolyte with 'ceramic in polymer' composite electrolyte at the Li/'polymer in ceramic' composite electrolyte interface.<sup>116</sup>

### 2.1.5.3 Polymer-sulfide composite electrolytes

Sulfide-based SSEs have much higher ionic conductivities at RT than oxide-based SSEs, some of which are even comparable to liquid electrolytes.<sup>61</sup> Therefore, it is attractive to combine sulfide-based SSEs with SPEs to achieve decent ionic conductivity and mechanical properties. X. Xu's group reported an improved ionic conductivity, enlarged electrochemical window, and stabilized electrolyte/Li interface hybrid electrolyte consisting of LGPS and PEO-LITFSI SPE. In addition, the succinonitrile doping further increased the RT ionic conductivity of this hybrid electrolyte.<sup>117</sup> Another type of sulfide-

based SSE, containing  $\text{Li}_2\text{S}$ ,  $\text{P}_2\text{S}_5$  and  $\text{P}_2\text{O}_5$ ,  $\text{Li}_3\text{PS}_4$ , has also been reported to complex with PEO-based SPE.<sup>118,119</sup> Similar to the insulating fillers and oxide-based SSE filler, the enhancement in the ionic conductivity and interfacial stability toward the lithium metal anode was also achieved after adding sulfide-based SSEs into the SPE.

To address the instability of sulfide-based SSEs in air and to enhance its flexibility, integrating SPEs into a sulfide-based SSE matrix is a strategy ('polymer in ceramic'). Sulfide-based SSEs have a Young's modulus in the range of 14-37 GPa. Although the values are lower than that of oxide-based SSEs ( $\sim 150$  GPa),<sup>120,121</sup> the sulfide-based SSEs are still rigid and brittle, resulting in high grain boundary resistance and high interfacial resistance towards electrodes. The rigid property cannot accommodate the volume change of electrodes during the charge/discharge process. To address these problems, a SPE, whose elastic modulus is around 20 MPa, three orders of magnitude lower than that of sulfide-based SSE,<sup>122</sup> is introduced to improve flexibility and enhance the ambient stability of the sulfide-based SSE. However, the incorporation of a low ionic conductive SPE into a sulfide-based SSE matrix will sacrifice the high ionic conductivity. For example, incorporation of 1 wt.% - 5 wt.% comb shaped polymer (poly(oxyethylene)s with tri(oxyethylene)s as side chains (this polymer has the molecule structure of  $-(\text{CH}_2\text{CH}_2\text{O})_l-(\text{CH}_2\text{CHO}-(\text{CH}_2\text{O}(\text{CH}_2\text{CH}_2\text{O})_3\text{CH}_3))_m)_p-$ ,  $l = 81$ ,  $m = 19$ ) complexing with  $\text{LiClO}_4$  into a  $95(0.6\text{Li}_2\text{S}\cdot 0.4\text{SiS}_2)\cdot 5\text{Li}_4\text{SiO}_4$  (mol%) sulfide-based SSE resulted in an ionic conductivity of  $\sim 10^{-5}$  S/cm at  $60^\circ\text{C}$ , which is almost 10 times lower than that of the bulk sulfide-based SSE, despite enhancing the flexibility of the SSE.<sup>123</sup> Thus, SPEs with high ionic conductivities are preferred. PFPE (hydroxy-terminated perfluoropolyether polymer) random copolymers-based SPEs with an ionic conductivity over  $10^{-4}$  S/cm at RT are favorable.<sup>124</sup> I. Villaluenga et al. integrated 23 wt.% of PFPE-LITFSI SPE into a sulfide-based SSE ( $75\text{Li}_2\text{S}\cdot 25\text{P}_2\text{S}_5$ ) matrix to fill up the gaps in the sulfide-based SSE pellets obtained from the cold press process. Significantly faster ion transport and lower grain boundary resistance were achieved in this hybrid electrolyte by the compact packing. They also developed a method to calculate the ionic conductivity,  $\sigma_{\text{calc}}$ , of the hybrid electrolyte, by the following equation (**Eq. (2.1)**) (ignoring any tortuosity):

$$\sigma_{\text{calc}} = \varphi_{\text{sulfide}} * \sigma_{\text{sulfide}} + \varphi_{\text{PFPE}} * \sigma_{\text{PFPE}} \quad \text{Eq. (2.1)}$$

where  $\phi_{\text{sulfide}}$  and  $\phi_{\text{PFPE}}$  are the volume fractions of the sulfide-based SSE and PFPE-LITFSI SPE;  $\sigma_{\text{sulfide}}$  and  $\sigma_{\text{PFPE}}$  are the corresponding ionic conductivities. The calculated values were in good consistence with the experimental values. The as-prepared hybrid electrolyte achieved an ionic conductivity over  $10^{-4}$  S/cm at 30 °C.<sup>125</sup>

In a short summary, the ionic conductivities of each individual SSE and composite hybrid electrolytes are compared in **Figure 2.5**. From this figure, it is clear that the reported hybrid electrolytes have comparable ionic conductivities to the individual SSEs such as oxide-based SSEs, SPE and sulfide-based SSEs.

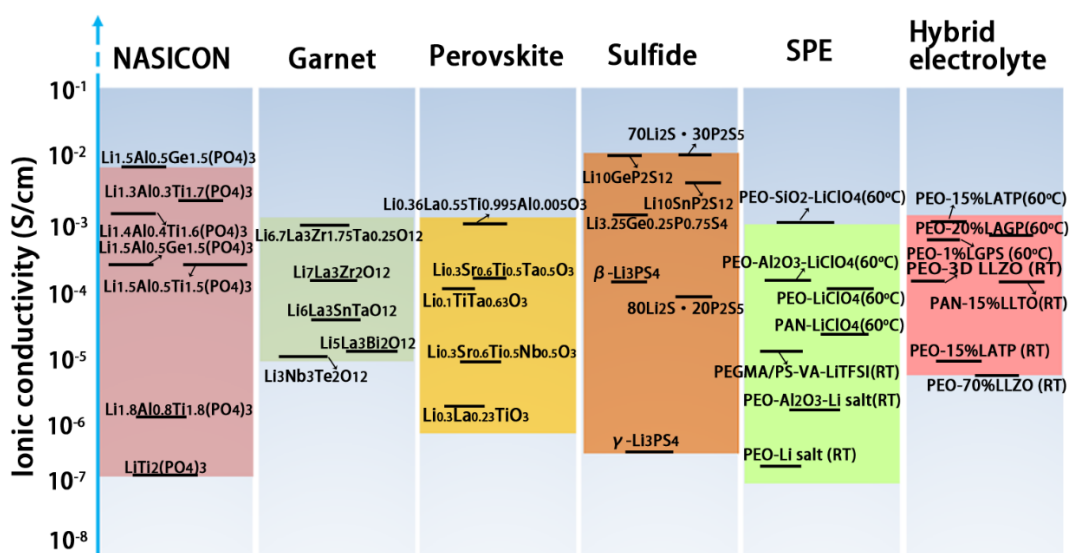


**Figure 2.5** Comparison on ionic conductivities of different types of SSEs including NASICON-type, garnet-type, perovskite-type, sulfide-based SSEs, SPE, and hybrid electrolytes with composite structure. Hybrid electrolytes show comparable ionic conductivities to other individual SSEs.<sup>126</sup>

## 2.2 Solutions for high-performance solid-state batteries

To address the challenges in SSBs, many approaches have been developed and have accomplished great progress. In this chapter, different strategies for the challenges including (i) low ionic conductivity, (ii) the mismatch problem, and (iii) the incompatibility problem, will be summarized and discussed.

## 2.2.1 Solutions for solid-state lithium batteries with solid polymer electrolyte

### 2.2.1.1 Improving the ionic conductivity of solid polymer electrolyte

In the past two decades, many efforts have been dedicated to study the mechanism of insulating fillers (e.g.  $\text{Al}_2\text{O}_3$ ,  $\text{TiO}_2$ ,  $\text{SiO}_2$ ) in improving the ionic conductivity of composite electrolytes. The improvements due to insulating ceramic fillers were proposed by the following mechanisms: (i) the fillers physically interrupt and suppress the crystallinity of the polymer; (ii) Lewis acid-base type surface interactions between the filler surface and polymer chains kinetically inhibit the crystallization of polymer chains; (iii) Lewis acid-base interactions at the interface between the fillers' surface and the SPE provide preferential pathways for  $\text{Li}^+$  ion conduction; (iv) Lewis acid-base type surface interactions with the lithium salt facilitate the dissociation of the salt.<sup>127-132</sup> In addition to the above-mentioned filler effects, the inorganic SSE filler bulk can also serve as extra  $\text{Li}^+$  ion conduction channels, showing advantages over the insulating fillers.<sup>108,133</sup> Therefore, SSE fillers are preferred when designing a high ionic conductive composite electrolyte. In this chapter, focusing on the ionic conductivity enhancement for hybrid electrolytes, effects of size, concentration, and shape of the SSE fillers, as well as plasticizer effects, will be discussed.

#### i) Size and concentration of fillers

For insulating fillers, such as  $\text{TiO}_2$ ,  $\text{Al}_2\text{O}_3$  and  $\text{SiO}_2$ , smaller size is preferred. Nano-sized fillers with high specific surface areas are able to provide strong interaction with the polymer chains and lithium salts. Ceramic fillers interrupt the long-range order of polymer chains and thus increase the percentage of amorphous phase. The effect is more significant when the size of fillers is close to the chain length of the polymer.<sup>134</sup> M. Dissanayake et al. had systematically studied the effects of  $\text{Al}_2\text{O}_3$  filler size and concentration on conductivities in a PEO- $\text{LiCF}_3\text{SO}_3$  (LiTf) SPE.<sup>128</sup> They found that the smaller size of the fillers led to a higher ionic conductivity. The optimal ionic conductivity achieved with 5.8 nm size  $\text{Al}_2\text{O}_3$  fillers was one order of magnitude higher than that with 10  $\mu\text{m}$  size fillers.

They believed that the smaller sized  $\text{Al}_2\text{O}_3$  fillers have higher surface areas which are beneficial to the favorable surface interactions.

The effects of size and concentration of LLZO SSE fillers in a PEO polymer matrix was systematically studied by J. Zhang et al.<sup>110</sup> In the study, PEO-LLZO hybrid electrolytes were prepared without any lithium salts. They believed that  $\text{Li}^+$  near the LLZO particle surface can be influenced by the PEO polymer. As a consequence, lithium vacancies on the LLZO grain surface are created. The surface Li vacancies of LLZO provide sites for  $\text{Li}^+$  transfer. As a result, both high ionic conductivity of LLZO particles and the surface vacancies contributed to the overall conductivity enhancement of the hybrid electrolyte. The percolation effect was considered to play an important role in improving ionic conductivity. **Figure 2.6a** shows the ionic conductivities of PEO-LLZO hybrid electrolytes with different sizes of LLZO fillers and different concentrations. With the size of 40 nm, 400 nm and 10  $\mu\text{m}$  LLZO fillers, the conductivities were optimized at 12.7, 15.1, and 21.1 vol.%, respectively. The highest ionic conductivity of PEO-LLZO composite electrolyte at 30 °C can be over  $10^{-4}$  S/cm with 12.7 vol.% 40 nm LLZO fillers. Y. Zhao et al. also studied the effects of LAGP filler size and concentration on ionic conductivity for PEO-LAGP-LITFSI composite electrolytes.<sup>104</sup> With different sizes of LAGP fillers, the conductivities were optimized with 15-20 wt.% LAGP fillers. For example, with 20 wt.% nano-size LAGP fillers, the hybrid electrolytes exhibited the highest ionic conductivity of  $6.76 \times 10^{-4}$  S/cm at 60 °C.

## ii) Shape of fillers

Depending on the  $\text{Li}^+$  ion conduction mechanism, the shape of SSE fillers can be an important factor effecting the ionic conductivity of composite electrolytes. For insulating ceramic fillers, the conductivity improvement mainly relies on the interactions of their surface groups with the surrounding polymer chains and lithium salts. As long as the insulating fillers have high surface area, allowing effective surface interactions, the particular shape of insulating fillers is not of importance. Particle shape of insulating fillers are most commonly used in this case since the variety of metal oxides such as nano-size  $\text{Al}_2\text{O}_3$ ,  $\text{SiO}_2$ , and  $\text{TiO}_2$  particles with different surface groups are easily accessible.<sup>2,135-138</sup>



Additionally, besides surface interactions between fillers and polymer and lithium salts, ionic conducting SSE fillers can provide additional Li<sup>+</sup> ion pathways within the fillers, hence particular interconnecting structures can be designed to maximize ionic conductivity and minimize the grain boundary. In addition to commercial and home-made nano-size SSE particles,<sup>104</sup> novel shapes of nanowire (random or vertically aligned) and 3D network structures have been rationally designed and synthesized for hybrid electrolytes.<sup>99,105,109</sup>

One dimensional LLTO nanowire fillers can be prepared by electrospinning polyvinylpyrrolidone polymer fiber that contain Li, La, and Ti salts and subsequent calcination at 600-900 °C in air for 2 h.<sup>105</sup> The nanowire fillers were applied in a PAN-LiClO<sub>4</sub> based hybrid electrolyte in comparison with LLTO nanoparticle fillers. As schematically shown in **Figure 2.6b**, the interconnecting nanowires provide a network for fast Li<sup>+</sup> ion conduction, while the Li<sup>+</sup> ion pathway is intermittent through the discrete particles. The nanowire LLTO fillers enabled significantly higher ionic conductivity than nanoparticle LLTO fillers with the same concentration. With 15 wt.% LLTO nanowire fillers, an ionic conductivity over 10<sup>-4</sup> S/cm was achieved at 20 °C.

Simply mixing the inorganic SSE particles and SPE, where the SPE is a continuous phase and the inorganic SSE is a dispersed phase, is the most common method to prepare composite electrolytes. However, the Li<sup>+</sup> ion can only transfer within SPE rather than from high conductive inorganic SSE particle to another, which significantly decreased the capability of SSE fillers. In this consideration, 3D continuous inorganic conductive frameworks were developed for shortening the Li<sup>+</sup> ion transport pathway and to further enhance the ionic conductivity. A vertically aligned LATP, fabricated via an ice-template method, and filling with PEO-based SPE had been reported by Y. Yang's group (**Figure 2.6c**). The vertical structure of LATP is expected to provide a fast-ionic conductive channel in the composite electrolyte, thus, the result showed that a high ionic conductivity of 5.2×10<sup>-5</sup> S/cm at RT was achieved.<sup>99</sup> L. Hu's group developed a 3D Li<sup>+</sup> ion conducting network with garnet-type SSE LLZO to provide continuous channels for Li<sup>+</sup> ion conduction in a PEO matrix (**Figure 2.6d**).<sup>109,139</sup> The RT ionic conductivity of this composite electrolyte was up to 2.5×10<sup>-4</sup> S/cm, which was among the highest reported ionic conductivities for polymer-oxide hybrid electrolytes.<sup>109</sup> As a proof of concept, a continuous

Li<sup>+</sup> ion conducting network can effectively improve the RT ionic conductivity of polymer-oxide hybrid electrolytes.

### iii) Adding plasticizers

Besides tuning the shapes and properties of fillers, composite electrolytes can be tailored for higher ionic conductivity by adding plasticizers (Figure 2.6e). Plasticizers can be low-molar-mass organics, organic solvents or ionic liquids (ILs). The working principle of plasticizers is to increase the content of amorphous phase of the polymer and improve segmental motion; at the same time, plasticizers promote the dissociation of lithium salt and thus increase the number of effective charge carriers.<sup>140-142</sup> Succinonitrile (SN) is a good example of a plasticizer which remains a plastic crystal under RT. Importantly, composites of SN and lithium salts have very high RT ionic conductivity (in the order of 10<sup>-4</sup> S/cm). Studies show that incorporating just a small amount of SN (9 wt.%) into a PEO-LAGP-LiClO<sub>4</sub> hybrid electrolyte can significantly improve the RT ionic conductivity from 3.0×10<sup>-5</sup> to 1.1 10<sup>-4</sup> S/cm. Using this hybrid electrolyte, ASSLIBs with a LiFePO<sub>4</sub> cathode delivered satisfying discharge capacity at 0.2 C and 0.5 C under 25 °C.<sup>103</sup>

Using liquid organic electrolytes as plasticizers is also a very popular method to enhance the ionic conductivity and ensure complete wetting of electrodes for RT SSBs' functionality.<sup>102</sup> Hybrid electrolytes of P(VdF-co-HFP)-LAGP-carbonate liquid electrolyte and P(VdF-co-HFP)-LLTO-carbonate liquid electrolyte had been reported by Seul-Ki Kim et al. and Hang T. T. Le et al. respectively. Both hybrid electrolytes presented good electrochemical performance in RT SSBs.<sup>102,143</sup>

In summary, the influences of the size, concentration, and shape of the SSEs' fillers in composite hybrid electrolytes are critical for the enhancement of the ionic conductivity of hybrid electrolytes. Small size and interconnected shape of SSE fillers are favorable. The presence of plasticizers in composite electrolytes can also enhance the ionic conductivity because it can lower the crystallinity of polymer and promote the dissociation of lithium salt.

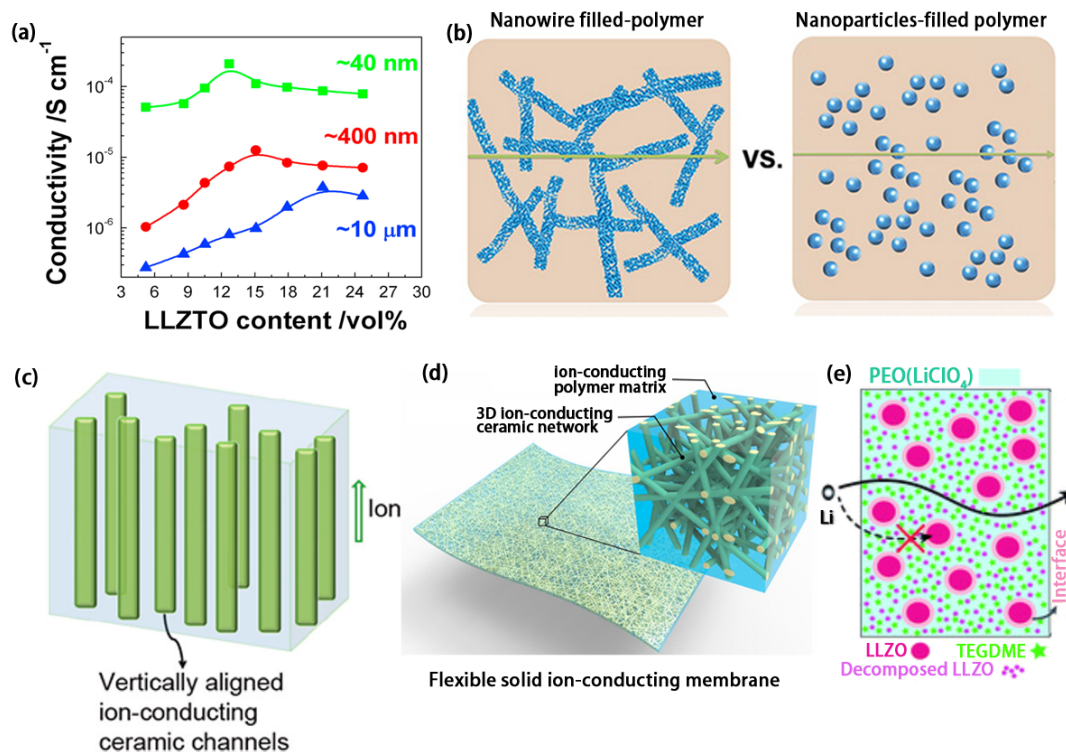


**Figure 2.6** Strategies for designing a high ionic conductivity hybrid electrolyte. (a) Size and concentration effects on the ionic conductivity of PEO-LLZO hybrid electrolytes.<sup>110</sup> (b) Comparison of the lithium ion transport pathways in hybrid electrolytes with nanowire or particle LLTO fillers.<sup>105</sup> Reproduced with permission. (c) Vertically aligned lithium ion transporting channels to enhance the ionic conductivity.<sup>99</sup> (d) Creating a 3D ionic conducting ceramic network for enhancing the ionic conductivity of a hybrid electrolyte.<sup>109</sup> (e) Plasticizer additives to increase the RT ionic conductivity of a hybrid electrolyte.<sup>144</sup>

### 2.2.1.2 Solutions for lithium dendrite formation

#### i) Enhancing the mechanical strength of solid polymer electrolytes

Lithium dendrite formation in SPEs is believed to be due to the poor mechanical strength of the SPE. Therefore, enhancing the mechanical strength of SPEs can physically prevent lithium dendrite formation in SPE based lithium batteries. The strategies for enhancing the mechanical strength of SPEs include (1) adding fillers into the polymer metric; (2) using high mechanical strength of framework to support the SPE and (3) synthesizing the cross-linked polymer electrolyte. For the first approach, oxide-based SSEs are a good choice as

the fillers for reinforcing the SPEs. A successful sample was demonstrated by F. Chen et al. who used LLZO particles as the fillers in a PEO-based SPE, and improved the cycling performance of a lithium symmetric cell.<sup>145</sup> Using LATP and MOFs as the fillers for reinforcing SPEs have also been reported, and both presented excellent dendrite free cycling performance.<sup>146,147</sup>

For the second approach, the strength framework supports, such as polymer separator, glass fiber, and 3D lithium ion conductor oxide-based SSEs, have been tried in reinforcing the SPEs. J. Wu et al. had used a 5  $\mu\text{m}$  thick polyethylene separator as a support and filled with PEO-based SPE to make thin film high strength polymer electrolyte. The as-prepared SPE showed excellent cycling performance in lithium symmetric cells, with 1500 h charge/discharge without short circuit at a current density of 0.1  $\text{mA}/\text{cm}^2$  and a capacity of 0.1  $\text{mAh}/\text{cm}^2$ .<sup>148</sup> X. Guo's group had prepared a 3D garnet SSE framework via the polymeric sponge method. Then, this 3D garnet SSE framework was immersed into a PEO-based SPE solution to obtain a hybrid electrolyte. This hybrid electrolyte had very good electrochemical performance in lithium symmetric cells and SSLBs (**Figure 2.7a,b**).<sup>149</sup>

For the third approach, the cross-linking of polymer has higher Young's module than that of single chain structure polymer, so they exhibit better dendrite inhibit capability. The successful demonstrations of this concept were done by Q. Lu et al.<sup>150</sup> and H. Liao et al.<sup>151</sup> who used a novel initiator free, one pot synthesis strategy based on a ring opening polymerization reaction, to prepare high mechanical strength cross-linked polymer electrolytes for dendrite free lithium metal batteries.

## ii) Salt effects

PEO or EO containing polymers have great capacity to complex with salts that have high ionization ability. SPEs are the mixture consisting of polymer metric and dissociated lithium salt. The salt plays an important role in the formation of the solid electrolyte interphase in ASSLIBs. Therefore, by adjusting the content of salt in SPEs, the formation of the SEI layer can be controlled. Based on this mechanism, the salt effect in liquid organic electrolytes for lithium metal batteries have been widely studied. Salts such as  $\text{CsPF}_6$ , LiFSI, LiODFB etc. have been studied in improving dendrite free lithium metal batteries

with liquid organic electrolytes.<sup>152-155</sup> Similar to the effects in liquid batteries, the salts in SPE based lithium metal batteries also showed a big influence in the dendrite formation. X. Yang et al. added CsClO<sub>4</sub> salt in PEO-based SPE and studied the effect of Cs<sup>+</sup> on inhibiting lithium dendrite growth. It is proposed that Cs<sup>+</sup> can form a positively charged electrostatic shield around the initial lithium tips. This can force further deposition of lithium to adjacent regions of the anode and result in a dendrite-free lithium deposition.<sup>156</sup> The effects of LiN<sub>3</sub> and LiNO<sub>3</sub> salt additives in PEO-based SPE were studied by G. Eshetu et al.<sup>157</sup>, who found that LiN<sub>3</sub> is a good additive for the formation of a compact and highly conductive passivation layer on the lithium metal anode, which therefore avoids dendrite formation (**Figure 2.7c-e**).

### iii) Interface engineering

The lithium plating and stripping processes happen at the surface of the lithium metal anode; thus, the surface structure and chemical properties are important for dendrite free lithium metal batteries. To adjust the chemical properties of the lithium metal anode, surface coating is one of the promising methods. There are tremendous works reporting the surface coating of lithium metal for dendrite free liquid organic batteries. The coating materials, ranging from metal oxides,<sup>158,159</sup> polymers,<sup>160</sup> and metal sulfides<sup>161</sup> to nitrides<sup>162</sup> and halides<sup>163</sup>, have been tried in lithium batteries to avoid the dendrite growth. In the lithium metal batteries with SPEs, coating strategy also works effectively. L. Wang et al. applied ALD deposited Al<sub>2</sub>O<sub>3</sub> to protect lithium metal and applied it in the SPEs lithium batteries. With a 20 nm thick Al<sub>2</sub>O<sub>3</sub> coating, a lithium symmetric cell had a cycle life of 660 h at a current density of 0.1 mA/cm<sup>2</sup>. (**Figure 2.7f,g**)<sup>164</sup>

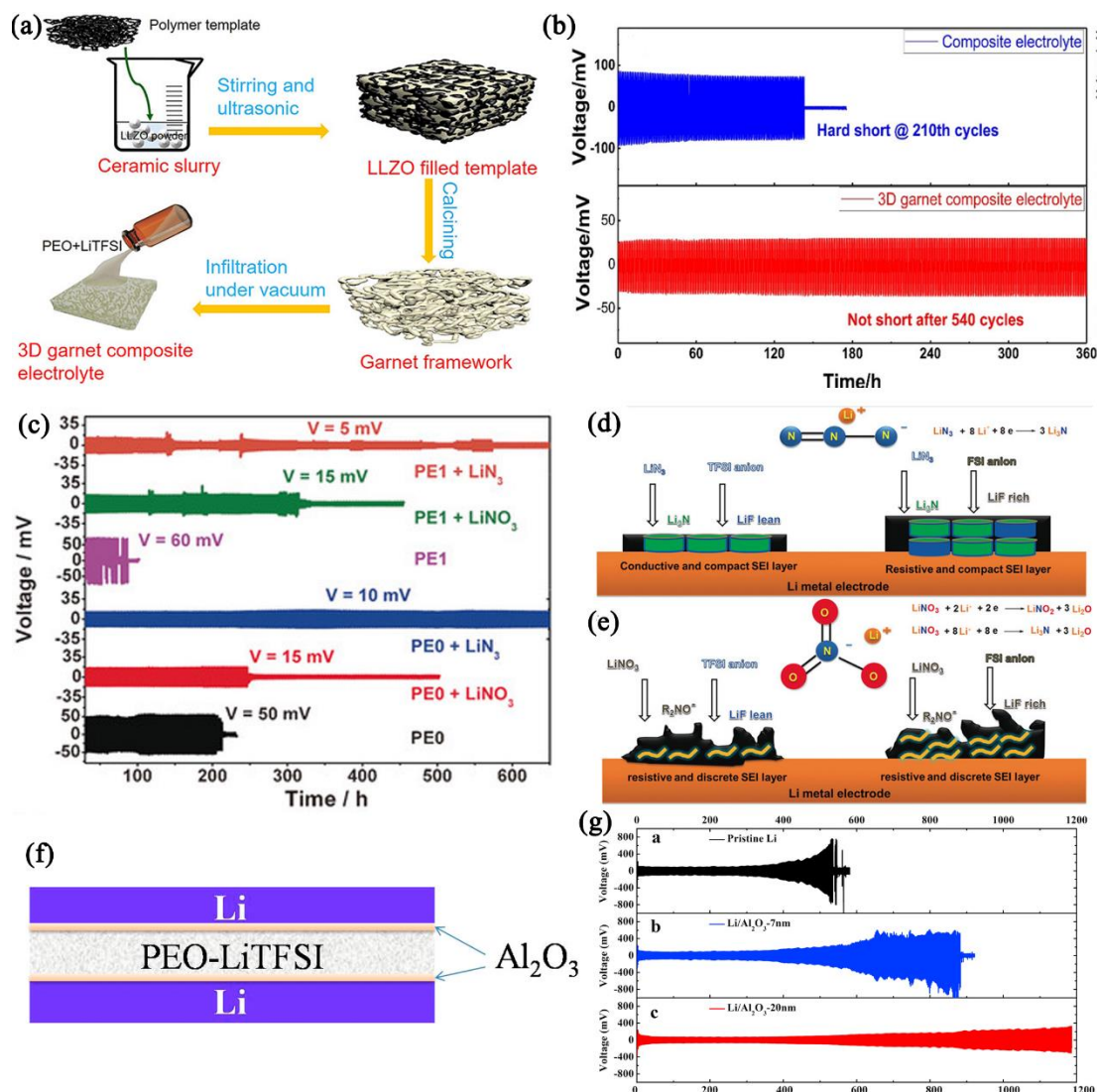


**Figure 2.7** (a) Synthesis process of 3D garnet SSE framework for reinforcing the SPE. (b) comparison of lithium symmetric cells performance with garnet-SPE composite electrolyte and 3D garnet SSE framework reinforced SPE.<sup>149</sup> (c) Electrochemical behavior of lithium metal electrodes in SPEs with different salts. Galvanostatic cycling of lithium symmetric cells at 0.1 mA/cm<sup>2</sup> (half cycle time 2 h) at 70 °C. (d) and (e) Schematic illustration of the reaction mechanisms for the electrolytes containing LiN<sub>3</sub> and LiNO<sub>3</sub> additives, respectively.<sup>157</sup> (f) Schematic illustration of Al<sub>2</sub>O<sub>3</sub> coated lithium metal anode for SPE symmetric cells. (g) Electrochemical behavior of lithium metal electrodes in SPEs with different thickness of Al<sub>2</sub>O<sub>3</sub> coating.<sup>164</sup>

### 2.2.1.3 Solution for low electrochemical stability window

SPEs have a low electrochemical stability window, which is the main reason for their poor performance in high voltage ASSLIBs. For PEO-based SPEs, it is well accepted that their oxidation windows are lower than 3.8 V vs. Li/Li<sup>+</sup>,<sup>28</sup> which means SPEs will be oxidized when the ASSLIBs are charged to over 3.8 V. The decomposed products of the SPEs will form the unstable CEI in the cathode interface, resulting in high interfacial resistance. Therefore, the challenges of the low electrochemical oxidation windows of SPEs must be addressed for high energy density ASSLIBs application.

#### i) Interface engineering

To avoid the decomposition of SPEs, artificial CEI can be designed to enhance the stability of the electrolyte/cathode interface according to the theory proposed by J. B. Goodenough et al.<sup>165</sup> who proposed that a cathode, with a electrochemical potential below the highest occupied molecular orbital (HOMO) of the electrolyte, will oxidize the electrolyte, unless a passivation layer blocks electron transfer from the electrolyte HOMO to the cathode. The artificial CEI can work as such a passivation layer, therefore preventing the decomposition of the SPE.

To fabricate the artificial CEI, coating with an inert material at the cathode particles is the most popular way. In 2005, S. Seki et al had tried to coat Li<sub>3</sub>PO<sub>4</sub> on the surface of LiCoO<sub>2</sub> particles for coupling with SPE. The results showed that Li<sub>3</sub>PO<sub>4</sub> coating can improve the SPE/cathode interfacial stability and improve the cycling performance of solid polymer batteries.<sup>31</sup> Similarly, using Al<sub>2</sub>O<sub>3</sub> as the coating material for engineering the SPE/LiCoO<sub>2</sub> interface was studied by H. Miyashiro et al. and similar results as Li<sub>3</sub>PO<sub>4</sub> coating was obtained (**Figure 2.8a-c**).<sup>29</sup>

Polymer material as the coating layer was also studied by G. Cui's group who used poly(ethyl  $\alpha$ -cyanoacrylate) (PECA) to protect the SPE/LiCoO<sub>2</sub> interface for enhancing the cycling performance of 4 V class solid polymer batteries. However, they proposed that PECA coating prevents the decomposition of lithium salt in the SPE rather than prevents the decomposition of the PEO polymer metric.<sup>30</sup>

Oxide-based SSE LATP, as the coating material for engineering the SPE/LiCoO<sub>2</sub> interface, have also been studied by H. Li's group. LATP SSE has a high oxidation window of up to 4.3 V according to the theoretical calculation, it has high ionic conductivity of over 10<sup>-3</sup> S/cm at RT. Therefore, it should be a good coating material for ASSLIBs. H. Li's group applied a solution-based synthesis method to coat a 20 nm thick layer of LATP on the LiCoO<sub>2</sub> particles. The as-coated LiCoO<sub>2</sub> cathode exhibited stable cycling performance in solid polymer batteries, demonstrating that LATP coating has great capacity to stabilize the SPE/cathode interface.<sup>166</sup>

Even though the as mentioned coating methods can improve the performance of solid polymer batteries at high voltage, the improvement is minor and the performances of SSBs are still far from practical application.

#### ii) Double layer solid polymer electrolyte

Since the coating strategy can only improve the performance of high voltage solid polymer batteries slightly, double layer structure of SPEs was developed. Double layer SPEs have two layers of SPEs in solid polymer batteries, with one anode stable SPE and one cathode stable (high voltage stable) SPE (**Figure 2.8d**). Based on this strategy, W. Zhou et al. used a PEO-based SPE for the anode layer and poly(N-methyl-malonic amide) SPE for the cathode layer to fabricate a SSLIB with a LiCoO<sub>2</sub> cathode and lithium metal anode. A capacity retention of 91.2% after 100 cycles of charge/discharge was achieved with such a structure of batteries (**Figure 2.8e-h**).<sup>32</sup> In another study by G. Cui's group, a multi-layer of PEO-based SPEs with different lithium salt in different layer was investigated and it is regarded as the double layer SPEs. At the cathode side, a PEO-based SPE with LiTFFPB salt was used and LiTFSI+5% LiTFFPB salts were used for the anode side of the SPE. With such a design, solid polymer batteries with Ni-rich cathodes delivered higher stable cycling performances compared to the single salt of PEO-based SPEs.<sup>167</sup>

Double layer structure SPEs seem to have better cycling performance compared to the reported coating methods. However, double layer structure SPEs may increase the thickness of the SPE and sacrifice the energy density of solid polymer batteries. Also,



double layer structure SPEs will increase one more interface between different SPEs, which may increase the overall resistance of the cell.

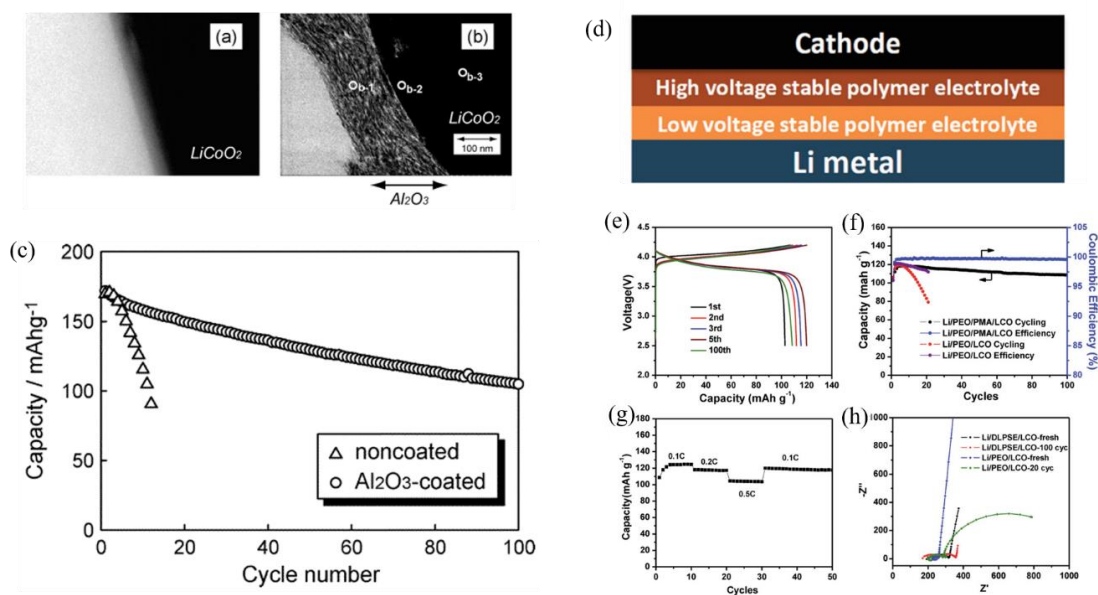


**Figure 2.8** (a) TEM images of (a) noncoated LiCoO<sub>2</sub> and (b) Al<sub>2</sub>O<sub>3</sub> coated LiCoO<sub>2</sub> particle. (c) comparison of cycling performance of noncoated LiCoO<sub>2</sub> and Al<sub>2</sub>O<sub>3</sub> coated LiCoO<sub>2</sub> in solid polymer batteries.<sup>29</sup> (d) Schematic illustration of double layer structure SPE for ASSLIBs. (e) Charge/discharge profile of ASSLIB with double layer structure SPE. (f) Comparison of cycling performance of ASSLIBs with different structure SPEs. (g) Rate performance of ASSLIB with double layer structure SPE. (h) Comparison of impedance curves of ASSLIB with double layer structure SPE and with single PEO-based SPE before and after cycling.<sup>32</sup>

## 2.2.2 Solutions for high-performance solid-state batteries with oxide-based solid-state electrolytes

Oxide-based SSEs are promising SSEs for ASSLIBs due to their air stability and high ionic conductivity. Unfortunately, their rigid properties make it difficult to realize an intimate contact and good binding with the electrode interface. To address this challenge, several strategies were developed.

### 2.2.2.1 Oxide-based solid-state electrolytes with lithium anode interface

In terms of oxide-based SSE/lithium interfaces, different types of oxide-based SSEs have different challenges. For garnet SSE LLZO, the problem is only the mismatch issue, since LLZO is high stable towards lithium metal. However, for  $\text{Ti}^{4+}$  containing oxide-based SSEs, such as LATP and LLTO, not only the mismatch problem, but also the reduction of  $\text{Ti}^{4+}$  by lithium metal matters. Therefore, for addressing these challenges, different approaches were studied.

Melting lithium metal to its liquid state, then solidifying it at the surface of oxide-based SSEs is the most popular method to fabricate oxide-based SSE/lithium interfaces. Melting lithium metal onto the oxide-based SSE surface, instead of simply pressing a lithium metal foil to the SSE, can achieve a matching interface. Molten lithium metal has high fluidity which can fill the gaps of the uneven SSE surface and enable intimate interfacial contact. However, garnet-type SSEs may have poor wettability to molten lithium, namely “lithiophobic” (**Figure 2.9a** left). Thus, surface coatings including  $\text{Al}_2\text{O}_3$ , ZnO, Ge, etc. on SSEs can enable good lithium wettability, namely “lithiophilic” coatings (**Figure 2.9a** right).<sup>168-170</sup> For example, L. Hu's group<sup>169</sup> dramatically reduced the contact angle between molten lithium and a garnet-type SSE and reduced the RT interfacial resistance of from  $1710 \Omega/\text{cm}^2$  to  $1 \Omega/\text{cm}^2$  via a thin layer of  $\text{Al}_2\text{O}_3$  coating on the garnet-type SSE via atomic layer deposition (ALD) (**Figure 2.9b**). The lithium symmetric cell, with an  $\text{Al}_2\text{O}_3$  coated garnet SSE, presented excellent plating/stripping performance over 90 h with negligible increase of overpotential at a current density of  $0.2 \text{ mA}/\text{cm}^2$ . To turn the lithiophobic lithium anode to a lithiophilic lithium anode, making lithium-based alloy can be another way. Y. Lu et al. used an Li-Al alloy as the anode material for garnet SSEs. They found that Al will spontaneously permeate into LLZO and construct a robust Al enriched SEI by the reaction between Li-Al alloy and LLZO, realizing a low SSE/anode interfacial impedance below  $1 \Omega/\text{cm}^2$ .<sup>171</sup>

$\text{Ti}^{4+}$  in LATP or LLTO can be easily reduced by the lithium metal anode (**Figure 2.2j**) resulting in a phase change of the SSE, which decreases ionic conductivity and increases electronic conductivity. This kind of highly electronic conductive interphase is particularly

prone to exacerbate Li dendrite growth.<sup>172,173</sup> Our group has demonstrated a thin layer of  $\text{Al}_2\text{O}_3$  coating on the LATP surface to prevent  $\text{Ti}^{4+}$  reduction in LATP, significantly enhancing the stability of LATP towards the lithium metal anode (**Figure 2.9c,d**).<sup>55</sup>

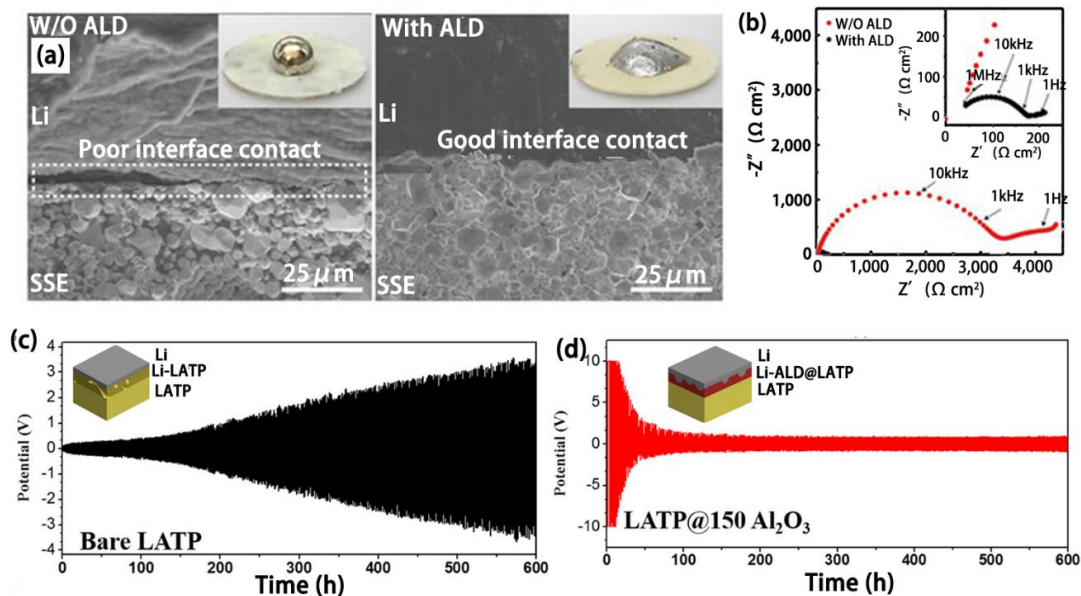


**Figure 2.9** (a) SEM images of the garnet SSE/lithium metal interface without ALD  $\text{Al}_2\text{O}_3$  coating (left) and with ALD  $\text{Al}_2\text{O}_3$  coating (right). The insets are photos of melted lithium metal on top of the garnet SSE surfaces. An intimate contact between lithium metal and SSE was achieved with ALD  $\text{Al}_2\text{O}_3$  coating. (b) Comparison of the impedances of symmetrical lithium cells with garnet SSEs with/without ALD  $\text{Al}_2\text{O}_3$  coating. The inset is the enlarged EIS curve of symmetrical lithium cells with garnet SSEs with ALD  $\text{Al}_2\text{O}_3$  coating where a very small impedance is presented.<sup>169</sup> (c) Cycling performance of bare LATP/lithium symmetric cell at a current density of  $0.01 \text{ mA/cm}^2$ . A significant increase of overpotential is observed. (d) Cycling performance of ALD  $\text{Al}_2\text{O}_3$  coating LATP/lithium symmetric cell at a current density of  $0.01 \text{ mA/cm}^2$ ; The potential profile is quite stable with ALD coating.<sup>55</sup>

### 2.2.2.2 Oxide-based solid-state electrolytes with cathode particles interface

Oxide-based SSE/cathode interfaces are one of the most challenging problems for ASSLIBs. Though the melting strategy of lithium metal anode is workable for addressing

the SSE/lithium interface problem, it is not suitable for engineering the interface with the cathode because of the high melting points of SSEs and cathodes. Moreover, a cathode is a heterogeneous structure containing nano-size or micro-size active material particles and nano-size conductive carbon and/or polymer binders. The stiff and rough morphology of cathodes makes the mismatch problem even more prominent. Alternatively, a feasible method is co-sintering oxide-based SSEs and cathode materials together with a low-melting-point SSE as a sintering additive to promote the sintering process at a relatively low temperature to avoid side reactions. Ohta et al. developed a solid-state LiCoO<sub>2</sub> battery with LLZO as the SSE and LiBO<sub>3</sub> as the sintering additive and lowered the co-sintering temperature to 700 °C. This LiCoO<sub>2</sub> SSB delivered a discharge capacity of 85 mAh/g in a charge/discharge voltage window of 3.0 - 4.05 V (vs. Li/Li<sup>+</sup>).<sup>174</sup> A similar study by C. Wang's group used Li<sub>2.3</sub>C<sub>0.7</sub>B<sub>0.3</sub>O<sub>3</sub> as the sintering additive to construct an all ceramic ASSLIB with excellent cycling performance (**Figure 2.10a,b**).<sup>175</sup> Creating porous structured SSEs, to enlarge the contact area between the SSE and electrode materials, is another strategy to realize ASSLIBs with oxide-based SSEs (**Figure 2.10e-g**).<sup>176</sup> The flat surface of SSEs usually have point contact with electrode particles. By creating a porous structure, electrode particles can fill the porous and enlarge the contact area between the SSE and electrode, thus, reducing the interfacial resistance. The ASSLIBs with normal, flat LLZO SSEs, cannot deliver any capacity, while with the porous structure LLZO, ASSLIBs can obtain good electrochemical performance (**Figure 2.10g**).

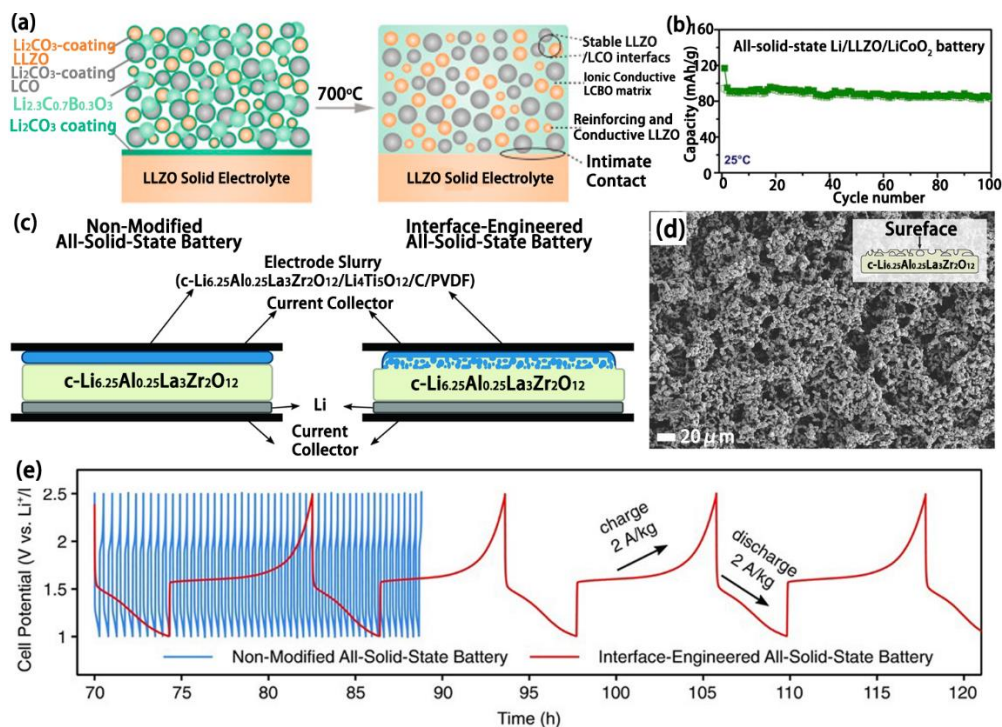


**Figure 2.10** (a) Schematic diagram shows the co-sintering process to construct an ASLIB with oxide-based SSE. Left, mixture of LLZO particles, LCO particle,  $\text{Li}_{2.3}\text{C}_{0.7}\text{B}_{0.3}\text{O}_3$  sintering additive on the top of LLZO SSE pellet. Right, co-sintering this pellet at  $700^\circ\text{C}$  to obtain an intimate SSE/cathode interface. (b) Cycling performance at RT of the ASLIB obtained from (a), lithium metal was used as anode.<sup>175</sup> (c) Schematic diagrams show the structure of ASLIBs with flat SSE (left) and porous structure SSE (right). (d) Surface SEM image of porous structure SSE pellet. (e) Comparison of ASLIBs' performances with dense SSE and porous structure SSE.<sup>176</sup>

Even though the SSE/cathode interfacial mismatch problem can be partially addressed by the co-sintering method,<sup>53, 174,177, 178</sup> or creating porous structure SSEs, to enlarge the contact area between the SSE and electrode materials,<sup>176,179</sup> the volume change of electrode materials during charge/discharge will still lead to loss of contact between SSEs and electrode materials, due to the stiff nature of SSEs.<sup>180-182</sup> Therefore, hybrid electrolytes with an oxide-based SSE as the main lithium ion conductor and a liquid organic electrolyte or a soft SPE layer at the interface between the cathode and oxide-based SSE, can be a practical solution for this issue. Our group comprehensively studied the amount of liquid electrolyte used to address the cathode and LATP SSE interface mismatch issue (**Figure**

**2.11a-c).**<sup>183</sup> The results showed that adding as little as 2  $\mu\text{L}$  of liquid electrolyte at the  $\text{LiFePO}_4$  cathode/LATP interface can enable the battery operation at RT with a discharge capacity of 125 mAh/g at 1 C and 98 mAh/g at 4 C. Interestingly, excess liquid electrolyte showed no further contribution to the electrochemical performance enhancement. Such a small amount of liquid electrolyte will be completely absorbed by the electrode and will be free of leakage concerns.

J. B. Goodenough et al. have studied the electrochemical properties of SPE-oxide sandwich hybrid electrolytes. **Figure 2.11e** and **f** propose the electric potential profiles across a sandwich hybrid electrolyte and a single SPE in a  $\text{LiFePO}_4$  cell. Due to redistribution of charge carriers in different conductors (including anode, SPE, oxide-based SSE, and cathode), an electric double layer was created at the interface between two conductors, causing an electric field (i.e. potential difference) at the interface. In a single SPE cell, a strong electric field, generated at the anode/SPE interface, can reduce the lowest unoccupied molecular orbital energy of the SPE related to the Fermi energy of lithium, and thus facilitates the decomposition of the SPE.<sup>184</sup> In contrast, the overall electric field across the sandwich electrolyte is interrupted by the oxide-based SSE interlayer (**Figure 2.11f**). The oxide-based SSE can block the passage of the salt anions and increase the lithium ion transference number,  $t_{\text{Li}^+}$ . Reduced electric field at the anode/SPE interface helps to stabilize the SPE. The intimate contact between the lithium anode and SPE also provides an unformal lithium ion flux that mitigates lithium dendrite formation. As a result, all solid-state  $\text{LiFePO}_4$  batteries with a SPE/LATP/SPE hybrid electrolyte showed significantly improved cycling performance compared to the single layer SPE-based  $\text{LiFePO}_4$  batteries (**Figure 2.11g**).<sup>184</sup>

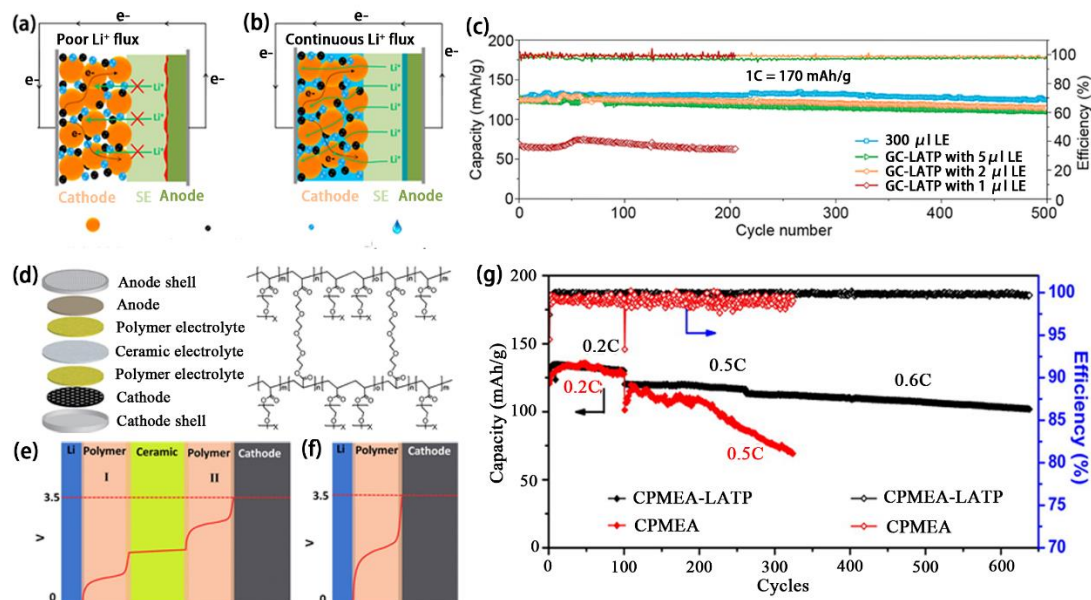


**Figure 2.11** Configurations showing the poor contact between oxide-based SSE and cathode, anode electrodes. (b) After adding small amount of liquid electrolyte, the interface is well wetted, realizing an uniform Li<sup>+</sup> flux. (c) Comparison on the performance of the LiFePO<sub>4</sub> LIBs with different amounts of liquid-based electrolyte in the LATP/electrode.<sup>183</sup> (d) The configuration of ASSLIB with a SPE-oxide sandwich hybrid electrolyte and the molecule structure of the SPE. Electric potential profile across (e) a SPE-oxide sandwich electrolyte and (f) a single SPE; (g) Comparison of the performances of the ASSLIBs with single layer SPE and SPE-oxide sandwich electrolyte at 0.2 C, 0.5 C and 0.6 C.<sup>184</sup>

### 2.2.3 Conclusion and perspectives

SSEs are essential elements to the development of ASSLIBs, serving as both separators and ionic conductors. SPEs, oxide-based SSEs, and sulfide-based SSEs and halide-based SSEs are typical categories of common SSEs for ASSLIBs, inheriting different pros and cons. SPEs usually have good flexibility and softness that enable low interfacial resistance towards electrodes, but the low ionic conductivity at RT, lithium dendrite formation and relatively narrow electrochemical stability window, limit their practical applications. Oxide-based and sulfide-based SSEs exhibit relatively high ionic conductivities at RT compared to SPEs, but the rigid and brittle properties cause difficulties in maintaining sufficient contact with electrodes. Halide-based SSEs have good compatibility with high

voltage cathodes, but their stability with anodes is very poor. Hybrid electrolyte rational combinations of liquid electrolyte, SPE, and inorganic SSEs is a promising SSE to maximize the advantages and compensate the disadvantages of each constituent.

Interfacial problems between SSEs and electrodes are the key issues for ASSLIBs. Mismatch, incompatibility, SCL, and lithium dendrite formation are common interfacial problems. Lithium dendrite formation in SPEs can be addressed by enhancing the mechanical strength of the SPE, by adjusting the salt contents in the SPEs and by interface engineering of the SPE/Li interface. To stabilize the SPE/cathode interface in high voltage ASSLIBs, coating with inert materials and using double layer SPEs are the two effective strategies. Mismatch between SSE and electrode materials is the main challenge for oxide-based SSEs due to their rigid properties. Hence, using a molten lithium to solidify on the surface of oxide-based SSEs is a good approach since molten lithium has great capacity to flow and fill the uneven surface of rigid oxide-based SSEs. However, the surface of SSE may be lithiophobic. Therefore, surface coating and making Li-metal alloy anode to adjust the lithiophobic properties to lithiophilic are necessary for intimate contact between the lithium anode and oxide-based SSE. However, the molten strategy is not capable for addressing the oxide-based SSE and cathode interface. Thus, applying a low melting point of SSE for co-sintering the cathode materials together with oxide-based SSEs to realize the intimate contact is one of the approaches. Another way is to take advantage of liquid electrolytes or SPEs which have good contact ability with solid materials to bind the cathode and oxide-based SSE together to achieve a good oxide-based SSE/cathode interface. However, this method must apply liquid electrolytes, which are flammable, or SPEs, which will increase the weight of the SSE and create additional interface resistance.

Although significant progress has been achieved in ASSLIBs, there are still challenges to be overcome for the development of practical ASSLIBs. Deeper understandings of different SSEs in terms of ionic conduction mechanisms, the origin of chemical and electrochemical instabilities, and possible interface modifications need to be obtained in the future. For practical ASSLIBs to be applied in EVs, the energy density and working temperature are the major concerns. Potential research efforts and solutions are proposed as follows:



- i) Understanding the lithium ion transport mechanisms in SSEs is important for the development of advanced SSEs. Advanced characterization techniques, such as NMR, STXM (synchrotron scanning transmission X-ray microscopy)<sup>185</sup> and neutron diffraction<sup>186</sup>, are powerful tools for lithium ion transport mechanism studies. In particular, in-situ analyses on lithium ion transport across SSE and electrode interfaces are vital for understanding the electrochemical reaction and performance limitation; more studies are expected to be done in this field.
  
- ii) In order to achieve high energy density for practical ASSLIBs, it is necessary to minimize the weight percentage of SSEs and maximize the active materials content. Theoretical calculations pointed out that the thickness of SPEs should be below 90  $\mu\text{m}$  to achieve a comparable energy density to liquid-based lithium batteries.<sup>187</sup> For oxide-based SSEs such as LLZO, due to its higher mass density, they need to be 4 times thinner for a comparable energy density.<sup>188</sup> Therefore, more research efforts should focus on advanced fabrication techniques, such as sputtering,<sup>189</sup> tape casting<sup>190</sup> and 3D printing<sup>191,192</sup>, to prepare thin SSEs. Meanwhile, high active materials loading for high energy density could lead to poor electronic and ionic conduction problems, which are more serious in ASSLIBs. Novel electrode designs with high electronic and ionic conductivity are crucial for practical ASSLIBs.
  
- iii) In order to boost the energy density of ASSLIBs for EV applications, implementation of high voltage and high capacity cathodes are necessary. However, most of the SSEs, such as PEO-based SPEs and sulfide-based SSEs, are not stable at high voltage (e.g. > 4.0 V). There is an urgent need for developing high voltage stable SSEs for high energy density ASSLIBs. Composite electrolytes with an enhanced electrochemical stability window compared to bare SPEs can be superior SSE candidates for high energy density ASSLIBs. Halide-based SSEs have high electrochemical oxidation windows would be another choice. On the other hand, engineering the SSE/active materials interface with an artificial SEI can enhance the interfacial stability, which have been extensively studied in SPE and sulfide-based ASSLIBs.<sup>28-30,74,193</sup> However, the performance is still far away from practical applications. More investigations on interfacial engineering using advanced coating techniques are desired for further enhancing the performance

of ASSLIBs. Atomic layer deposition (ALD) and molecule layer deposition (MLD), the powerful techniques for fabricating conformal coatings with controlled thickness, are perfect tools.<sup>194,195</sup> Another ultimate approach for high voltage ASSLIBs is the pursuit of high voltage stable SSEs. PEO-based SPEs and sulfide-based SSEs are reported to have low electrochemical oxidation windows, while halide-based SSEs, especially fluoride-based SSEs, possess a high electrochemical oxidation voltage. Implementing halide-based SSEs or searching for other high voltage stable SSEs are an important direction for practical and high energy density ASSLIBs.

- iv) Implementing sulfur cathodes is another approach for obtaining high energy density ASSLBs, based on the high theoretical specific capacity of 1672 mAh/g for sulfur. However, there are still many challenges that need to be overcome, including the incompatibility between sulfur cathodes and SSEs, polysulfide shuttling effects, the volumetric expansion, and the poor ionic/electronic conductivities of sulfur and discharge products. Mechanism studies and the innovative sulfur cathode designs are urgent for developing high performance ASSLBs.
- v) The mechanical properties of the SSEs have great influence on the SSBs' performance. To achieve a practical SSB, a SSE with suitable mechanical properties to accommodate the volumetric expansion of active materials and maintain intimate SSE/active materials contact is critical. Up to date, tremendous research work was dedicated to understanding the basic mechanical properties of available SSEs. In the future, inspiring studies on controlling the mechanical properties of the SSEs or developing new SSEs with suitable mechanical properties should receive more attention. Hybrid electrolytes with polymer-inorganic composite is a favorable strategy to tune the mechanical properties of SSEs. Hybrid electrolytes shall play an important role in practical SSBs
- vi) The working temperature range of SSEs is important for ASSLIBs. Although the thermal properties of SSEs are much better than conventional liquid electrolytes, most SSEs have not yet achieved practical performance for ASSLIBs at low temperature. The development of SSEs with a high ionic conductivity and a low activation energy,

as well as designs of novel electrode structures for good electronic/ionic conductivities are highlighted directions.

vii) The SSE/active materials interface is the most important topic in ASSLIBs. The understanding of the interfacial ion transport would be helpful for developing high-performance ASSLIBs. Advanced characterization techniques such as NMR, synchrotron radiation-based X-ray techniques (XAS, STXM, X-ray computed tomography), HR-TEM, Rutherford backscattering spectroscopy, etc., are very powerful tools for studying the interfacial engineering mechanism and interfacial ions transport. Especially, in-situ study at the interface shall give fundamental understandings and guidance for interfacial engineering designs.<sup>196-199</sup>

## Reference

1. D. Fenton, J. Parker, P. Wright, *Polymer* 1973, 14, 589.
2. F. Croce, G. Appetecchi, L. Persi, B. Scrosati, *Nature*, 1998, 394 456–458.
3. G.S. MacGlashan, Y.G. Andreev, P.G. Bruce, *Nature*, 1999, 398, 792–794.
4. Z. Gadjourova, Y.G. Andreev, D.P. Tunstall, P.G. Bruce, *Nature*, 2001, 412, 520–523.
5. K. Zaghib, K. Kinoshita, *J. Power Sources*, 2004, 125, 214–220.
6. K. Zaghib, Y. Choquette, A. Guerfi, M. Simoneau, A. Belanger, M. Gauthier, *J. Power Sources*, 1997, 68, 368–371.
7. K. Zaghib, M. Simoneau, M. Armand, M. Gauthier, *J. Power Sources*, 1999, 81, 300–305.
8. H. Marceau, C.-S. Kim, A. Paolella, S. Ladouceur, M. Lagace, M. Chaker, A. Vijh, A. Guerfi, C.M. Julien, A. Mauger, M. Armand, P. Hovington, K. Zaghib, *J. Power Sources*, 2016, 319, 247–254.
9. J.-C. Daigle, A. Vijh, P. Hovington, C. Gagnon, J. Hamel-P<sup>^</sup>quet, S. Verreault, N. Turcotte, D. Clement, A. Guerfi, K. Zaghib, *J. Power Sources*, 2015, 279, 372–383.
10. P. Hovington, M. Lagace, A. Guerfi, P. Bouchard, A. Mauger, C. Julien, M. Armand, K. Zaghib, *Nano Lett.*, 2015, 15, 2671–2678.
11. Y. Chen, Y. Chuang, J. Su, H. Yu, Y. Chen-Yang, *J. Power Sources*, 2011, 196, 2802–2809.

12. C. Yang, H. Ywi Chen, F. Lin, C. Chen, *Solid State Ionics*, 2002, 150, 327–335.
13. H. Choe, B. Carroll, D. Pasquariello, K. Abraham, *Chem. Mater.*, 1997, 9, 369–379.
14. H.-W. Chen, T.-P. Lin, F.-C. Chang, *Polymer*, 2002, 43, 5281–5288.
15. S. Ahmad, T. Saxena, S. Ahmad, S. Agnihotry, *J. Power Sources*, 2006, 159, 205–209.
16. D. Saikia, A. Kumar, *Electrochim. Acta*, 2004, 49, 2581–2589.
17. R. Miao, B. Liu, Z. Zhu, Y. Liu, J. Li, X. Wang, Q. Li, *J. Power Sources*, 2008, 184, 420–426.
18. D. Zhou, R. Zhou, C. Chen, W.-A. Yee, J. Kong, G. Ding, X. Lu, *J. Phys. Chem. B*, 2013, 117, 7783–7789.
19. J. Zhang, X. Zang, H. Wen, T. Dong, J. Chai, Y. Li, B. Chen, J. Zhao, S. Dong, J. Ma, *J. Mater. Chem. A*, 2017, 5, 4940–4948.
20. L. Meabe, T.V. Huynh, N. Lago, H. Sardon, C. Li, L.A. O'Dell, M. Armand, M. Forsyth, D. Mecerreyes, *Electrochim. Acta*, 2018, 264, 367–375.
21. Y. Tominaga, K. Yamazaki, *Chem. Commun.*, 2014, 50, 4448–4450.
22. K.J. Harry, D.T. Hallinan, D.Y. Parkinson, A.A. MacDowell, N.P. Balsara, *Nat. Mater.*, 2014, 13, 69–73.
23. N.S. Schauer, K.J. Harry, D.Y. Parkinson, H. Watanabe, N.P. Balsara, *J. Electrochem. Soc.*, 2015, 162, A398–A405.
24. P. Barai, K. Higa, V. Srinivasan, *Phys. Chem. Chem. Phys.*, 2017, 19, 20493–20505.
25. R. Khurana, J.L. Schaefer, L.A. Archer, G.W. Coates, *J. Am. Chem. Soc.*, 2014, 136, 7395–7402.
26. A. Mauger, M. Armand, C. Julien, K. Zaghbi, *J. Power Sources*, 2017, 353, 333–342.
27. C. Monroe, J. Newman, *J. Electrochem. Soc.*, 2005, 152, A396–A404.
28. Y. Xia, T. Fujieda, K. Tatsumi, P.P. Prosini, T. Sakai, *J. Power Sources*, 2001, 92, 234–243.
29. H. Miyashiro, Y. Kobayashi, S. Seki, Y. Mita, A. Usami, M. Nakayama, M. Wakihara, *Chem. Mater.*, 2005, 17, 5603–5605.
30. J. Ma, Z. Liu, B. Chen, L. Wang, L. Yue, H. Liu, J. Zhang, Z. Liu, G. Cui, *J. Electrochem. Soc.*, 2017, 164, A3454–A3461.

31. S. Seki, Y. Kobayashi, H. Miyashiro, Y. Mita, T. Iwahori, *Chem. Mater.*, 2005, 17, 2041–2045.
32. Zhou, W., Wang, Z., Pu, Y., Li, Y., Xin, S., Li, X., Chen, J., Goodenough, J. B., *Adv. Mater.*, 2019, 31, 1805574.
33. C.R. Mariappan, C. Yada, F. Rosciano, B. Roling, *J. Power Sources*, 2011, 196, 6456–6464.
34. B. Kumar, D. Thomas, J. Kumar, *J. Electrochem. Soc.*, 2009, 156, A506–A513.
35. V. Thangadurai, S. Narayanan, D. Pinzaru, *Chem. Soc. Rev.*, 2014, 43, 4714–4727.
36. M.P. O'Callaghan, D.R. Lynham, E.J. Cussen, G.Z. Chen, *Chem. Mater.*, 2006, 18, 4681–4689.
37. V. Thangadurai, H. Kaack, W.J. Weppner, *J. Am. Ceram. Soc.*, 2003, 86, 437–440.
38. V. Thangadurai, W. Weppner, *J. Am. Ceram. Soc.*, 2005, 88, 411–418.
39. R. Murugan, V. Thangadurai, W. Weppner, *Angew. Chem. Int. Ed.*, 2007, 46, 7778–7781.
40. D. Rettenwander, G.n. Redhammer, F. Preishuber-Pflügl, L. Cheng, L. Miara, R. Wagner, A. Welzl, E. Suard, M.M. Doeff, M. Wilkening, J. Fleig, G. Amthauer, *Chem. Mater.*, 2016, 28, 2384–2392.
41. R. Jalem, M. Rushton, W. Manalastas Jr., M. Nakayama, T. Kasuga, J.A. Kilner, R.W. Grimes, *Chem. Mater.*, 2015, 27, 2821–2831.
42. D. Wang, G. Zhong, W.K. Pang, Z. Guo, Y. Li, M.J. McDonald, R. Fu, J.-X. Mi, Y. Yang, *Chem. Mater.*, 2015, 27, 6650–6659.
43. F. Han, Y. Zhu, X. He, Y. Mo, C. Wang, *Adv. Energy Mater.*, 2016, 6, 1501590.
44. L. Truong, V. Thangadurai, *Chem. Mater.*, 2011, 23, 3970–3977.
45. Y. Ren, Y. Shen, Y. Lin, C.-W. Nan, *Electrochem. Commun.*, 2015, 57, 27–30.
46. L. Porz, T. Swamy, B.W. Sheldon, D. Rettenwander, T. Frömmling, H.L. Thaman, S. Berendts, R. Uecker, W.C. Carter, Y.M. Chiang, *Adv. Energy Mater.*, 2017, 7, 1701003.
47. T. Takahashi, H. Iwahara, *Energy Convers.*, 1971, 11, 105–111.
48. Y. Inaguma, C. Liqun, M. Itoh, T. Nakamura, T. Uchida, H. Ikuta, M. Wakihara, *Solid State Commun.*, 1993, 86, 689–693.
49. S.D. Jackman, R.A. Cutler, *J. Power Sources*, 2012, 218, 65–72.

50. S. Yu, R.D. Schmidt, R. Garcia-Mendez, E. Herbert, N.J. Dudney, J.B. Wolfenstine, J. Sakamoto, D.J. Siegel, *Chem. Mater.*, 2016, 28, 197–206.
51. K.G. Schell, F. Lemke, E.C. Bucharsky, A. Hintennach, M. Hoffmann, *J. Mater. Sci.*, 2017, 52, 2232–2240.
52. Y. Liu, P. He, H. Zhou, *Adv. Energy Mater.*, 2018, 8, 1701602.
53. K. Park, B.-C. Yu, J.-W. Jung, Y. Li, W. Zhou, H. Gao, S. Son, J.B. Goodenough, *Chem. Mater.*, 2016, 28, 8051–8059.
54. N.M. Asl, J. Keith, C. Lim, L. Zhu, Y. Kim, *Electrochim. Acta*, 2012, 79, 8–16.
55. Y. Liu, Q. Sun, Y. Zhao, B. Wang, P. Kaghazchi, K.R. Adair, R. Li, C. Zhang, J. Liu, L.-Y. Kuo, Y. Hu, T.-K. Sham, L. Zhang, R. Yang, S. Lu, X. Song, X. Sun, *ACS Appl. Mater. Interfaces*, 2018, 10, 31240–31248.
56. A. Hayashi, S. Hama, H. Morimoto, M. Tatsumisago, T. Minami, *J. Am. Ceram. Soc.*, 2001, 84, 477–479.
57. S. Kondo, K. Takada, Y. Yamamura, *Solid State Ionics*, 1992, 53, 1183–1186.
58. M. Tachez, J.-P. Malugani, R. Mercier, G. Robert, *Solid State Ionics*, 1984, 14, 181–185.
59. R. Kanno, T. Hata, Y. Kawamoto, M. Irie, *Solid State Ionics*, 2000, 130, 97–104.
60. R. Kanno, M. Murayama, *J. Electrochem. Soc.*, 2001, 148, A742–A746.
61. N. Kamaya, K. Homma, Y. Yamakawa, M. Hirayama, R. Kanno, M. Yonemura, T. Kamiyama, Y. Kato, S. Hama, K. Kawamoto, A. Mitsui, *Nat. Mater.*, 2011, 10, 682–686.
62. M. Murayama, N. Sonoyama, A. Yamada, R. Kanno, *Solid State Ionics*, 2004, 170, 173–180.
63. X. Yao, D. Liu, C. Wang, P. Long, G. Peng, Y.-S. Hu, H. Li, L. Chen, X. Xu, *Nano Lett.*, 2016, 16, 7148–7154.
64. Y. Kato, S. Hori, T. Saito, K. Suzuki, M. Hirayama, A. Mitsui, M. Yonemura, H. Iba, R. Kanno, *Nat. Energy*, 2016, 1, 16030.
65. A. Kuhn, O. Gerbig, C. Zhu, F. Falkenberg, J. Maier, B.V. Lotsch, *Phys. Chem. Chem. Phys.*, 2014, 16, 14669–14674.
66. Y. Zhu, X. He, Y. Mo, *ACS Appl. Mater. Interfaces*, 2015, 7, 23685–23693

67. C. Wang, Y. Zhao, Q. Sun, X. Li, Y. Liu, J. Liang, X. Li, X. Lin, R. Li, K.R. Adair, L. Zhang, R. Yang, S. Lu, X. Sun, *Nano Energy*, 2018, 53, 168–174.
68. W.D. Richards, L.J. Miara, Y. Wang, J.C. Kim, G. Ceder, *Chem. Mater.*, 2015, 28, 266–273.
69. S. Wenzel, S. Randau, T. Leichtweiß, D.A. Weber, J. Sann, W.G. Zeier, J.r. Janek, *Chem. Mater.*, 2016, 28, 2400–2407.
70. Y. Zhu, X. He, Y. Mo, *J. Mater. Chem. A*, 2016, 4, 3253–3266.
71. F. Han, T. Gao, Y. Zhu, K.J. Gaskell, C. Wang, *Adv. Mater.*, 2015, 27, 3473–3483.
72. A. Sakuda, A. Hayashi, M. Tatsumisago, *Chem. Mater.*, 2009, 22, 949–956.
73. J. Haruyama, K. Sodeyama, L. Han, K. Takada, Y. Tateyama, *Chem. Mater.*, 2014, 26, 4248–4255.
74. J.H. Woo, J.E. Trevey, A.S. Cavanagh, Y.S. Choi, S.C. Kim, S.M. George, K.H. Oh, S.-H. Lee, *J. Electrochem. Soc.*, 2012, 159, A1120–A1124.
75. N. Ohta, K. Takada, L. Zhang, R. Ma, M. Osada, T. Sasaki, *Adv. Mater.*, 2006, 18, 2226–2229.
76. R. Koerver, I. Aygün, T. Leichtweiß, C. Dietrich, W. Zhang, J.O. Binder, P. Hartmann, W.G. Zeier, J.r. Janek, *Chem. Mater.*, 2017, 29, 5574–5582.
77. W. Weppner and R. Huggins, *J. Electrochem. Soc.*, 1977, 124, 35.
78. H. Lutz, W. Schmidt and H. Haeuseler, *J. Phys. Chem. Solids*, 1981, 42, 287-289.
79. H. Lutz, Z. Zhang and A. Pfitzner, *Solid State Ionics*, 1993, 62, 1-3.
80. W. Schmidt and H. Lutz, *Berichte der Bunsengesellschaft für physikalische Chemie*, 1984, 88, 720-723.
81. X. Li, J. Liang, J. Luo, M. Norouzi Banis, C. Wang, W. Li, S. Deng, C. Yu, F. Zhao, Y. Hu, T.-K. Sham, L. Zhang, S. Zhao, S. Lu, H. Huang, R. Li, K. R. Adair and X. Sun, *Energy Environ. Sci.*, 2019, 12, 2665-2671.
82. K.-H. Park, K. Kaup, A. Assoud, Q. Zhang, X. Wu and L. F. Nazar, *ACS Energy Lett.*, 2020, 5, 2, 533-539.
83. Z. Xu, X. Chen, K. Liu, R. Chen, X. Zeng and H. Zhu, *Chem. Mater.*, 2019, 31, 7425-7433.
84. S. Wang, Q. Bai, A. M. Nolan, Y. Liu, S. Gong, Q. Sun and Y. Mo, *Angew. Chem. Int. Ed.*, 2019, 58, 8039-8043.

85. X. Li, J. Liang, N. Chen, J. Luo, K. R. Adair, C. Wang, M. N. Banis, T.-K. Sham, L. Zhang, S. Zhao, S. Lu, H. Huang, R. Li and X. Sun, *Angew. Chem. Int. Ed.*, 2019, 58, 16427-16432.
86. J.E. Weston, B.C.H. Steele, *Solid State Ion*, 1982, 7, 75–79.
87. F. Croce, L. Persi, F. Ronci, B. Scrosati, *Solid State Ionics*, 2000, 135, 47–52.
88. C.W. Lin, C.L. Hung, M. Venkateswarlu, B.J. Hwang, *J. Power Sources*, 2005, 146, 397–401.
89. S. Jayanthi, K. Kulasekarapandian, A. Arulsankar, K. Sankaranarayanan, B. Sundaresan, *J. Compos. Mater.*, 2015, 49, 1035–1045.
90. O. Sheng, C. Jin, J. Luo, H. Yuan, C. Fang, H. Huang, Y. Gan, J. Zhang, Y. Xia, C. Liang, W. Zhang, X. Tao, *J. Mater. Chem. A*, 2017, 5, 12934–12942.
91. K. Liu, F. Ding, Q.W. Lu, J.Q. Liu, Q.Q. Zhang, X.J. Liu, Q. Xu, *Solid State Ionics*, 2016, 289, 1–8.
92. A.M. Stephan, T.P. Kumar, M.A. Kulandainathan, N.A. Laksh, *J. Phys. Chem. B*, 2009, 113, 1963–1971.
93. J.L. Schaefer, D.A. Yanga, L.A. Archer, *Chem. Mater.*, 2013, 25, 834–839.
94. H. Huo, B. Wu, T. Zhang, X. Zheng, L. Ge, T. Xu, X. Guo, X. Sun, *Energy Storage Mater.*, 2019, 18, 59–67
95. Z. Wang, S. Wang, A. Wang, X. Liu, J. Chen, Q. Zeng, L. Zhang, W. Liu, L. Zhang, *J. Mater. Chem. A*, 2018, 6, 17227–17234.
96. C. Yuan, J. Li, P. Han, Y. Lai, Z. Zhang, J. Liu, *J. Power Sources*, 2013, 240, 653–658.
97. C. Gerbaldi, J.R. Nair, M.A. Kulandainathan, R.S. Kumar, C. Ferrara, P. Mustarellic, A.M. Stephan, *J. Mater. Chem. A*, 2014, 2, 9948–9954.
98. K. Zhu, Y. Liu, J. Liu, *RSC Adv.*, 2014, 4, 42278–42284.
99. H. Zhai, P. Xu, M. Ning, Q. Cheng, J. Mandal, Y. Yang, *Nano Lett.*, 2017, 17, 3182–3187.
100. Y.J. Wang, Y. Pan, L. Wang, M.J. Pang, L. Chen, *J. Appl. Polym. Sci.*, 2006, 102, 4269–4275.
101. Y.J. Wang, Y. Pan, D. Kim, *J. Power Sources*, 2006, 159, 690–701.



102. S.-K. Kim, Y.-C. Jung, D.-H. Kim, W.-C. Shin, M. Ue, D.-W. Kim, *J. Electrochem. Soc.*, 2016, 163, A974–A980.
103. Y.-C. Jung, M.-S. Park, C.-H. Doh, D.-W. Kim, *Electrochim. Acta*, 2016, 218, 271–277.
104. Y. Zhao, Z. Huang, S. Chen, B. Chen, J. Yang, Q. Zhang, F. Ding, Y. Chen, X. Xu, *Solid State Ionics*, 2016, 295, 65–71.
105. W. Liu, N. Liu, J. Sun, P.-C. Hsu, Y. Li, H.-W. Lee, Y. Cui, *Nano Lett.*, 2015, 15, 2740–2745.
106. S. Ohta, T. Kobayashi, T. Asaoka, *J. Power Sources*, 2011, 196, 3342–3345.
107. J.H. Choi, C.H. Lee, J.H. Yu, C.H. Doh, S.M. Lee, *J. Power Sources*, 2015, 274, 458–463.
108. M. Keller, G.B. Appetecchi, G.-T. Kim, V. Sharova, M. Schneider, J. Schuhmacher, A. Roters, S. Passerini, *J. Power Sources*, 2017, 353, 287–297.
109. K.K. Fu, Y. Gong, J. Dai, A. Gong, X. Han, Y. Yao, C. Wang, Y. Wang, Y. Chen, C. Yan, Y. Li, E.D. Wachsman, L. Hu, *Proc. Natl. Acad. Sci. U.S.A.*, 2016, 113, 7094–7099.
110. J. Zhang, N. Zhao, M. Zhang, Y. Li, P.K. Chu, X. Guo, Z. Di, X. Wang, H. Li, *Nano Energy*, 2016, 28, 447–454.
111. Z. He, L. Chen, B. Zhang, Y. Liu, L.-Z. Fan, *J. Power Sources*, 2018, 392, 232–238.
112. X. Zhang, T. Liu, S. Zhang, X. Huang, B. Xu, Y. Lin, B. Xu, L. Li, C.-W. Nan, Y. Shen, *J. Am. Chem. Soc.*, 2017, 139, 13779–13785.
113. J. Yu, S.C.T. Kwok, Z. Lu, M.B. Effat, Y.-Q. Lyu, M.M.F. Yuen, F. Ciucci, *Chemelectrochem*, 2018, 5, 2873–2881.
114. K. Kimura, H. Matsumoto, J. Hassoun, S. Panero, B. Scrosati, Y. Tominaga, *Electrochim. Acta*, 2015, 175, 134–140.
115. W. Zhang, J. Nie, F. Li, Z.L. Wang, C. Sun, *Nano Energy*, 2018, 45, 413–419.
116. H. Huo, Y. Chen, J. Luo, X. Yang, X. Guo, X. Sun, *Adv. Energy Mater.*, 2019, 9, 1804004.
117. Y. Zhao, C. Wu, G. Peng, X. Chen, X. Yao, Y. Bai, F. Wu, S. Chen, X. Xu, *J. Power Sources*, 2016, 301, 47–53.

118. Z. Zhang, Y. Zhao, S. Chen, D. Xie, X. Yao, P. Cui, X. Xu, *J. Mater. Chem. A*, 2017, 5, 16984–16993.
119. S. Chen, J. Wang, Z. Zhang, L. Wu, L. Yao, Z. Wei, Y. Deng, D. Xie, X. Yao, X. Xu, *J. Power Sources*, 2018, 387, 72–80.
120. A. Sakuda, A. Hayashi, Y. Takigawa, K. Higashi, M. Tatsumisago, *J. Ceram. Soc. Jpn.*, 2013, 121, 946–949.
121. J. Wolfenstine, J.L. Allen, J. Sakamoto, D.J. Siegel, H. Choe, *Ionics*, 2018, 24, 1271–1276.
122. S. Bi, C.N. Sun, T.A. Zawodzinski, F. Ren, J.K. Keum, S.K. Ahn, D. Li, J. Chen, *J. Polym. Sci., Part B: Polym. Phys.*, 2015, 53, 1450–1457.
123. S. Kohjiya, T. Kitade, Y. Ikeda, A. Hayashi, A. Matsuda, M. Tatsumisago, T. Minami, *Solid State Ionics*, 2002, 154, 1–6.
124. D.H. Wong, J.L. Thelen, Y. Fu, D. Devaux, A.A. Pandya, V.S. Battaglia, N.P. Balsara, J.M. DeSimone, *Proc. Natl. Acad. Sci. U.S.A.*, 2014, 111, 3327–3331.
125. I. Villaluenga, K.H. Wujcik, W. Tong, D. Devaux, D.H. Wong, J.M. DeSimone, N.P. Balsara, *Proc. Natl. Acad. Sci. U.S.A.*, 2016, 113, 52–57.
126. J. Liang, J. Luo, Q. Sun, X. Yang, X. Sun, *Energy Storage Mater.*, 2019, 21, 308–334
127. M. Murayama, N. Sonoyama, A. Yamada, R. Kanno, *Solid State Ionics*, 2004, 170, 173–180.
128. M. Dissanayake, P. Jayathilaka, R. Bokalawala, I. Albinsson, B.-E. Mellander, *J. Power Sources*, 2003, 119, 409–414.
129. F. Croce, L. Persi, B. Scrosati, F. Serraino-Fiory, E. Plichta, M. Hendrickson, *Electrochim. Acta*, 2001, 46, 2457–2461.
130. Z. Wang, X. Huang, L. Chen, *Electrochem. Solid State Lett.*, 2003, 6, E40–E44.
131. J. Shin, S. Passerini, *J. Electrochem. Soc.*, 2004, 151, A238–A245.
132. G. Appetecchi, F. Croce, L. Persi, F. Ronci, B. Scrosati, *Electrochim. Acta*, 2000, 45, 1481–1490.
133. J. Zheng, M. Tang, Y.Y. Hu, *Angew. Chem.*, 2016, 128, 12726–12730.
134. W. Gang, J. Roos, D. Brinkmann, F. Capuano, F. Croce, B. Scrosati, *Solid State Ionics*, 1992, 53, 1102–1105.

135. D. Lin, W. Liu, Y. Liu, H.R. Lee, P.-C. Hsu, K. Liu, Y. Cui, *Nano Lett.*, 2015, 16, 459–465.
136. S.K. Fullerton-Shirey, J.K. Maranas, *J. Phys. Chem. C*, 2010, 114, 9196–9206.
137. E.M. Masoud, A.A. El-Bellihi, W.A. Bayoumy, M.A. Mousa, *J. Alloy. Comp.*, 2013, 575, 223–228.
138. P. Sun, Y.H. Liao, X.Y. Luo, Z.H. Li, T.T. Chen, L.D. Xing, W.S. Li, *RSC Adv.*, 2015, 5, 64368–64377.
139. H. Xie, C. Yang, K. Fu, Y. Yao, F. Jiang, E. Hitz, B. Liu, S. Wang, L. Hu, *Adv. Energy Mater.*, 2018, 8, 1703474.
140. Y.-T. Kim, E.S. Smotkin, *Solid State Ionics*, 2002, 149, 29–37.
141. S. Ibrahim, M.R. Johan, *Int. J. Electrochem. Sci.*, 2011, 6, 5565–5587.
142. H. Huo, N. Zhao, J. Sun, F. Du, Y. Li, X. Guo, *J. Power Sources*, 2017, 372, 1–7.
143. H.T. Le, D.T. Ngo, R.S. Kalubarme, G. Cao, C.-N. Park, C.-J. Park, *ACS Appl. Mater. Interfaces*, 2016, 8, 20710–20719.
144. J. Zheng, H. Dang, X. Feng, P.-H. Chien, Y.-Y. Hu, *J. Mater. Chem. A*, 2017, 5, 18457–18463.
145. F. Chen, D. Yang, W. Zha, B. Zhu, Y. Zhang, J. Li, Y. Gu, Q. Shen, L. Zhang and D. R. Sadoway, *Electrochim. Acta*, 2017, 258, 1106-1114.
146. L. Liu, L. Chu, B. Jiang and M. Li, *Solid State Ionics*, 2019, 331, 89-95.
147. J.-F. Wu and X. Guo, *J. Mater. Chem. A*, 2019, 7, 2653-2659.
148. Wu, J., Rao, Z., Cheng, Z., Yuan, L., Li, Z., Huang, Y., *Adv. Energy Mater.* 2019, 9, 1902767.
149. Z. Li, W-X. Sha, X. Guo, *ACS Appl. Mater. Interfaces* 2019, 11, 26920–26927
150. Q. Lu, Y.-B. He, Q. Yu, B. Li, Y. V. Kaneti, Y. Yao, F. Kang and Q.-H. Yang, *Adv. Mater.*, 2017, 29, 1604460.
151. H. Liao, H. Chen, F. Zhou, Z. Zhang and H. Chen, *J. Power Sources*, 2019, 435, 226748.
152. F. Ding, W. Xu, G. L. Graff, J. Zhang, M. L. Sushko, X. Chen, Y. Shao, M. H. Engelhard, Z. Nie, J. Xiao, X. Liu, P. V. Sushko, J. Liu and J.-G. Zhang, *J. Am. Chem. Soc.*, 2013, 135, 4450-4456.

153. R. Miao, J. Yang, X. Feng, H. Jia, J. Wang and Y. Nuli, *J. Power Sources*, 2014, 271, 291-297.
154. F. Wu, Q. Zhu, R. Chen, N. Chen, Y. Chen, Y. Ye, J. Qian and L. Li, *J. Power Sources*, 2015, 296, 10-17.
155. X.-B. Cheng, R. Zhang, C.-Z. Zhao, F. Wei, J.-G. Zhang and Q. Zhang, *Adv. Sci.*, 2016, 3, 1500213.
156. X. Yang, Q. Sun, C. Zhao, X. Gao, K. Adair, Y. Zhao, J. Luo, X. Lin, J. Liang, H. Huang, L. Zhang, S. Lu, R. Li and X. Sun, *Energy Storage Mater.*, 2019, 22, 194-199.
157. G. G. Eshetu, X. Judez, C. Li, O. Bondarchuk, L. M. Rodriguez-Martinez, H. Zhang and M. Armand, *Angew. Chem. Int. Ed.*, 2017, 56, 15368-15372
158. L. Chen, J. G. Connell, A. Nie, Z. Huang, K. R. Zavadil, K. C. Klavetter, Y. Yuan, S. Sharifi-Asl, R. Shahbazian-Yassar, J. A. Libera, A. U. Mane and J. W. Elam, *J. Mater. Chem. A*, 2017, 5, 12297-12309.
159. N.-W. Li, Y.-X. Yin, C.-P. Yang and Y.-G. Guo, *Adv. Mater.*, 2016, 28, 1853-1858.
160. J. Lopez, A. Pei, J. Y. Oh, G.-J. N. Wang, Y. Cui and Z. Bao, *J. Am. Chem. Soc.*, 2018, 140, 11735-11744.
161. J. Liang, X. Li, Y. Zhao, L. V. Goncharova, G. Wang, K. R. Adair, C. Wang, R. Li, Y. Zhu, Y. Qian, L. Zhang, R. Yang, S. Lu and X. Sun, *Adv. Mater.*, 2018, 30, 1804684.
162. Y. Li, Y. Sun, A. Pei, K. Chen, A. Vailionis, Y. Li, G. Zheng, J. Sun and Y. Cui, *ACS Cent. Sci.*, 2018, 4, 97-104.
163. Z. Peng, N. Zhao, Z. Zhang, H. Wan, H. Lin, M. Liu, C. Shen, H. He, X. Guo, J.-G. Zhang and D. Wang, *Nano Energy*, 2017, 39, 662-672.
164. L. Wang, L. Zhang, Q. Wang, W. Li, B. Wu, W. Jia, Y. Wang, J. Li and H. Li, *Energy Storage Mater.*, 2018, 10, 16-23.
165. J. B. Goodenough and Y. Kim, *Chem. Mater.*, 2010, 22, 587-603.
166. Q. Yang, J. Huang, Y. Li, Y. Wang, J. Qiu, J. Zhang, H. Yu, X. Yu, H. Li and L. Chen, *J. Power Sources*, 2018, 388, 65-70.
167. C. Wang, T. Wang, L. Wang, Z. Hu, Z. Cui, J. Li, S. Dong, X. Zhou and G. Cui, *Adv. Sci.*, 2019, 6, 1901036.

168. W. Luo, Y. Gong, Y. Zhu, Y. Li, Y. Yao, Y. Zhang, K.K. Fu, G. Pastel, C.F. Lin, Y. Mo, E.D. Wachsman, L. Hu, *Adv. Mater.*, 2017, 29, 1606042.
169. X. Han, Y. Gong, K.K. Fu, X. He, G.T. Hitz, J. Dai, A. Pearse, B. Liu, H. Wang, G. Rubloff, Y. Mo, V. Thangadurai, E.D. Wachsman, L. Hu, *Nat. Mater.*, 2017, 16, 572–579.
170. C. Wang, Y. Gong, B. Liu, K. Fu, Y. Yao, E. Hitz, Y. Li, J. Dai, S. Xu, W. Luo, E.D. Wachsman, L. Hu, *Nano Lett.*, 2016, 17, 565–571.
171. Y. Lu, X. Huang, Y. Ruan, Q. Wang, R. Kun, J. Yang and Z. Wen, *J. Mater. Chem. A*, 2018, 6, 18853-18858.
172. F. Han, A.S. Westover, J. Yue, X. Fan, F. Wang, M. Chi, D.N. Leonard, N.J. Dudney, H. Wang, C. Wang, *Nat. Energy*, 2019, 4, 187–196.
173. Y. Song, L. Yang, W. Zhao, Z. Wang, Y. Zhao, Z. Wang, Q. Zhao, H. Liu, F. Pan, *Adv. Energy Mater.*, 2019, 12, 1900671.
174. S. Ohta, S. Komagata, J. Seki, T. Saeki, S. Morishita, T. Asaoka, *J. Power Sources*, 2013, 238, 53–56.
175. F. Han, J. Yue, C. Chen, N. Zhao, X. Fan, Z. Ma, T. Gao, F. Wang, X. Guo, C. Wang, *Joule*, 2018, 2, 497–508.
176. J. Van Den Broek, S. Afyon, J.L. Rupp, *Adv. Energy Mater.*, 2016, 6, 1600736.
177. S. Ohta, J. Seki, Y. Yagi, Y. Kihira, T. Tani, T. Asaoka, *J. Power Sources*, 2014, 265, 40–44.
178. M. Shoji, H. Munakata, K. Kanamura, *Front. Energy Res.*, 2016, 4, 32.
179. K.K. Fu, Y. Gong, G.T. Hitz, D.W. McOwen, Y. Li, S. Xu, Y. Wen, L. Zhang, C. Wang, G. Pastel, J. Dai, B. Liu, H. Xie, Y. Yao, E.D. Wachsman, L. Hu, *Energy Environ. Sci.*, 2017, 10, 1568–1575.
180. R. Koerver, W. Zhang, L. de Biasi, S. Schweidler, A. Kondrakov, S. Kolling, T. Brezesinski, P. Hartmann, W. Zeier, J. Janek, *Energy Environ. Sci.*, 2018, 11, 2142–2158.
181. H. Huo, J. Sun, X. Meng, M. He, N. Zhao, X. Guo, *J. Power Sources*, 2018, 383, 150–156.
182. X. Yao, N. Huang, F. Han, Q. Zhang, H. Wan, J.P. Mwizerwa, C. Wang, X. Xu, *Adv. Energy Mater.*, 2017, 7, 1602923.

183. C. Wang, Q. Sun, Y. Liu, Y. Zhao, X. Li, X. Lin, M.N. Banis, M. Li, W. Li, K.R. Adair, D. Wang, J. Liang, R. Li, L. Zhang, R. Yang, S. Lu, X. Sun, *Nano Energy*, 2018, 48, 35–43.
184. W. Zhou, S. Wang, Y. Li, S. Xin, A. Manthiram, J.B. Goodenough, *J. Am. Chem. Soc.*, 2016, 138, 9385–9388.
185. W.C. Chueh, F. El Gabaly, J.D. Sugar, N.C. Bartelt, A.H. McDaniel, K.R. Fenton, K.R. Zavadil, T. Tyliszczak, W. Lai, K.F. McCarty, *Nano Lett.*, 2013, 13, 866–872.
186. M. Yashima, M. Itoh, Y. Inaguma, Y. Morii, *J. Am. Chem. Soc.*, 2005, 127, 3491–3495.
187. C. Li, H. Zhang, L. Otaegui, G. Singh, M. Armand, L.M. Rodriguez-Martinez, *J. Power Sources*, 2016, 326, 1–5.
188. M. Keller, A. Varzi, S. Passerini, *J. Power Sources*, 2018, 392, 206–225.
189. Y. Hamon, A. Douard, F. Sabary, C. Marcel, P. Vinatier, B. Pecquenard, A. Levasseur, *Solid State Ionics*, 2006, 177, 257–261.
190. R.A. Jonson, P.J. McGinn, *Solid State Ionics*, 2018, 323, 49–55.
191. D.W. McOwen, S. Xu, Y. Gong, Y. Wen, G.L. Godbey, J.E. Gritton, T.R. Hamann, J. Dai, G.T. Hitz, L. Hu, *Adv. Mater.*, 2018, 30, 1707132.
192. X. Gao, Q. Sun, X. Yang, J. Liang, A. Koo, W. Li, J. Liang, J. Wang, R. Li, F.B. Holness, A.D. Price, S. Yang, T.-K. Sham, X. Sun, *Nano Energy*, 2019, 56, 595–603.
193. N. Ohta, K. Takada, I. Sakaguchi, L. Zhang, R. Ma, K. Fukuda, M. Osada, T. Sasaki, *Electrochem. Commun.*, 2007, 9, 1486–1490.
194. Y. Zhao, X. Sun, *ACS Energy Lett.*, 2018, 3, 899–914.
195. Y. Zhao, K. Zheng, X. Sun, *Joule*, 2018, 2, 1–22.
196. F. Lin, Y. Liu, X. Yu, L. Cheng, A. Singer, O.G. Shpyrko, H.L. Xin, N. Tamura, C. Tian, T.-C. Weng, X.-Q. Yang, Y.S. Meng, D. Nordlund, W. Yang, M.M. Doeff, *Chem. Rev.*, 2017, 117, 13123–13186.
197. J. Lu, T. Wu, K. Amine, *Nat. Energy*, 2017, 2, 17011.
198. Y. Yang, X. Liu, Z. Dai, F. Yuan, Y. Bando, D. Golberg, X. Wang, *Adv. Mater.*, 2017, 29, 1606922.
199. X. Li, H.Y. Wang, H. Yang, W. Cai, S. Liu, B. Liu, *Small Methods*, 2018, 2, 1700395.

## Chapter 3

### 3 Experimental methods and characterization techniques

In this chapter, the experimental details in the preparations of SPEs, oxide-based SSEs, and electrodes will be illustrated. The characterization techniques that have been used during the mechanism studies will also be introduced.

#### 3.1 Experimental methods

##### 3.1.1 Preparation of PEO-based polymer electrolytes

Polyethylene oxide (PEO, MW 600000) and LiClO<sub>4</sub> (purity, 99.9%) were carefully dried before using. 0.093 g of LiClO<sub>4</sub> was first dissolved in acetonitrile (AN) and stirred over 5 h in a Teflon container (**Figure 3.1a**). Then 0.6 g of PEO was added to the solution and stirred overnight. The resulting homogeneous mixture, containing PEO-LiClO<sub>4</sub>, was coated onto a Teflon evaporating dish (**Figure 3.1b**) and dried at 60 °C for 24 h in vacuum to obtain the PEO-based SPE membrane. The thickness of the SPE is 70 ± 10 μm.

PEO-based SPE with garnet SSE particle fillers were prepared by the same method. 0.24g of LLZO was added into 50 mL of AN and mixed by ultrasonication for 5 h. Then, 1.2 g of PEO and 0.19 g of LiClO<sub>4</sub> were added into the mixture and stirred overnight at room temperature. This homogeneous mixture was cast onto a Teflon substrate and dried at room temperature overnight, to slowly evaporate the AN, followed by vacuum drying at 60 °C for 2 days. The obtained PEO-LiClO<sub>4</sub>-LLZO SPE membrane was immediately transferred to an Ar-filled glovebox and rested over 3 days.

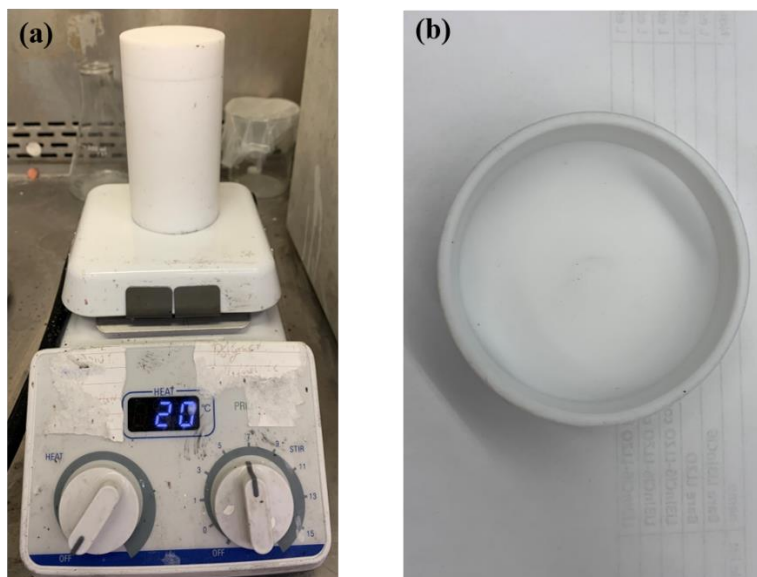


**Figure 3.1** (a) Teflon container on the substrate of the stirrer. (b) Teflon evaporating dish

### 3.1.2 Preparations of $\text{LiCoO}_2$ , Nickel-rich NMC811 cathode electrodes

$\text{LiCoO}_2$  electrodes were prepared by mixing 80 wt. %  $\text{LiCoO}_2$  particles, 10 wt. % carbon-black (Acetylene Black), 10 wt.% binder (PEO, PVDF, Na-alginate, CMC,) and a certain amount solvent to form slurry. The solvent for PEO binder is acetonitrile (AN), for PVDF is N-methylpyrrolidinone (NMP), and for Na-alginate and carboxymethyl cellulose (CMC) is water. Doctor blade casting method was used to coat the slurry on the carbon coated Al foil. The PEO-LCO, Na-alginate-LCO, and CMO-LCO electrodes were dried at 60 °C in a vacuum oven for 12 h and the PVDF-LCO electrode was dried at 100 °C in a vacuum oven for 12 h, to obtain the LCO electrode with different binders. Another  $\text{LiCoO}_2$  electrode were prepared by mixing 90 wt. % of  $\text{LiCoO}_2$  particles, 6 wt. % carbon-black (Acetylene Black), 4 wt.% PVDF with NMP, following by doctor blade casting the slurry on the Al foil. Then the electrode was dried at 100 °C in a vacuum oven, for 12 h, to obtain the 90 % LCO electrode. A similar process was used to prepare the NMC811 cathode electrode by just replacing the LCO powders with NMC powders.



### 3.1.3 Preparation of LATP and LLZO solid-state electrolyte

NASICON-type SSE  $\text{Li}_{1.4}\text{Al}_{0.4}\text{Ti}_{1.6}(\text{PO}_4)_3$  (LATP) was synthesized by a solid-state reaction method. Stoichiometric amounts of  $\text{Li}_2\text{CO}_3$ ,  $\text{Al}_2\text{O}_3$ ,  $\text{TiO}_2$ , and  $\text{NH}_4\text{H}_2\text{PO}_4$  were first mixed using a ball milling method, at 300 rpm for 5 h in a zirconia vessel (**Figure 3.2a**) with zirconia balls. Then the mixed powders were calcined at 700 °C for 2 h in a Muffle furnace (**Figure 3.2c**). The obtained powders were ground with polyvinyl alcohol (PVA) as the binder before being pressed into 1.2 cm diameter pellets at 300 MPa. The as-pressed pellets were calcined at 900 °C for 6 h in a Muffle furnace to get LATP SSE pellets.

LLZO powders with the molecular formula of  $\text{Li}_{6.4}\text{La}_3\text{Zr}_{1.4}\text{Ta}_{0.6}\text{O}_{12}$ , was purchased from Shanghai, China. LLZO powders were ground with polyvinyl alcohol (PVA) as the binder before being pressed into 1.2 cm diameter pellets at 250 MPa. The as-pressed LLZO pellets were calcined at 1200 °C for 6 h to get LLZO SSE pellets.



**Figure 3.2** (a) A pair of zirconia vessels (out-shell with stainless steel), (b) Ball mill machine for rotating the zirconia vessels. (c) High temperature Muffle furnace for SSE sintering.

### 3.1.4 Preparation of $\text{Li}_3\text{InCl}_6\text{-LiCoO}_2$ composite cathode

The  $\text{Li}_3\text{InCl}_6\text{-LiCoO}_2$  (LIC-LCO) composite cathode was prepared by dissolving 12.72 mg  $\text{LiCl}$  and 29.38 mg  $\text{InCl}_3 \cdot 4\text{H}_2\text{O}$  in a certain volume of water-ethanol (1:1) solution, which resulted in 34.83 mg of LIC. Then LCO powders and Acetylene black (AB) powders were added into the solution. The weight ratio of LIC-LCO-CB was set at 30:60:10, 40:50:10, 50:40:10 for different composite electrodes. Then, the mixture was dropped on the surface

of the LLZO SSE. The loading of LCO was controlled by controlling the volume of mixture using a Pipette. After evaporating the solvent at RT, the samples were transferred to a high vacuum oven at 80 °C for 12 h. Then, the temperature was shifted to 200 °C for 5 h and cooled down spontaneously to RT. After the temperature cooled down to RT, the samples were taken out and transferred into a glovebox for battery assembling.

### 3.1.5 Atomic layer deposition for interface engineering

Atomic layer deposition (ALD) is a chemical reaction deposition process. Compared to traditional vapor phase methods, such as chemical vapor depositions (CVD) and physical vapor depositions (PVD), ALD is a surface-controlled process where the growth of the film is dictated by two self-limited gas-solid surface reactions. ALD techniques depend primarily on binary reaction sequences, in which two reactions occur on the surface. And it can deposit a wide range of binary inorganic compounds, including metal oxide, metal nitrides, metal sulfides and mixed metal oxide. Due to its versatile properties, ALD has been one of the most rapidly developing thin film deposition techniques in the past decade, attracting increasing attention in different applications, ranging from electronic devices to energy storage systems. The ALD technique shows unique properties, including excellent uniformity and conformity, atomic scale and stoichiometric deposition, and low growth temperatures, which makes it a promising and powerful technique for interfacial engineering in ASSLIBs.

## 3.2 Characterization techniques

### 3.2.1 Physical characterization methods

#### i) FE-SEM and EDX

The morphologies of the samples were observed using field emission scanning electron microscopes (FE-SEM) (Hitachi S-4800 as shown in **Figure 3.3**). The FE-SEM was operated at 5 kV to observe morphologies of samples. The FE-SEM was coupled with an EDX which can disclose important information of elemental distribution. FE-SEM is a microscope technique that uses electrons as a medium rather than light(photon). These electrons are emitted by a field emission source and then they are accelerated by a high

electrical field. These electrons are called primary electrons, which are focused and deflected by the lenses to obtain a narrow scan beam. This narrow scan beam bombards the sample, resulting in the secondary electrons from each spot of the sample. According to the angle and velocity of these secondary electrons, the surface structure of the sample is determined. The electron detector can catch the secondary electrons to produce a signal, which is amplified and transformed to a video scan image or a digital image. When the sample is bombarded by the electron beam, electrons are ejected from the atoms of the sample's surface, which results in electron vacancies. The electron vacancies are then filled by the electron from a higher state, and then an X-ray is emitted to balance the energy difference between these two electrons' states. The X-ray energy is characteristic of the element from which it was emitted. By applying a detector to measure the relative abundance of emitted X-rays versus their energy, the elements' distribution of the sample can be identified; this is how EDX works.

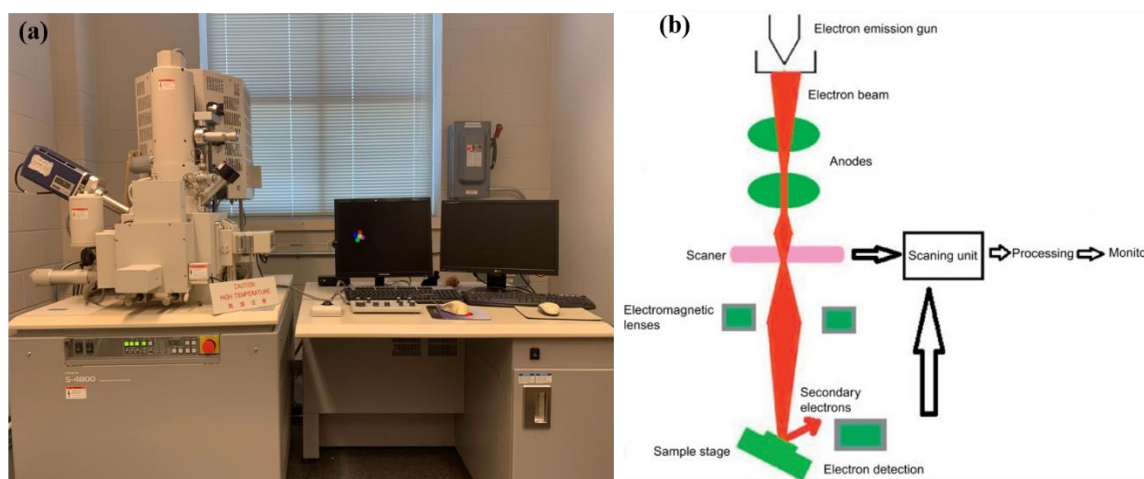


**Figure 3.3** (a) Photo image of FE-SEM Hitachi S-4800, (b) Schematic diagram shows the working principle of FE-SEM.<sup>1</sup>

## ii) Raman spectroscopy

The working principle of Raman spectroscopy is based on the interaction between photons and matter (molecules). When the photons (light) shoot on molecules, the light is scattered. However, it is not that every scattered photon can maintain the same frequency with the incident photons, there are some scattered photons that have different frequency, which is

the result of the interaction between the oscillation of light and molecular vibration, this is called Raman scattering phenomenon, named because of its discoverer, Sir C.V. Raman. A Raman spectroscopy system usually includes four major components: (1) laser system, (2) light collection optics, (3) filter or spectrophotometer, (4) detector (**Figure 3.4b**). A lens is used for collecting the reflecting light, followed by a filter separating the Raman scatterings from the incident light. The Raman scattering light then go through the monochromator and detector, which can identify their frequency. A certain type of molecular structure or chemical bonds have a certain frequency resulting from the interaction with light, which then can reveal chemical information from the sample.

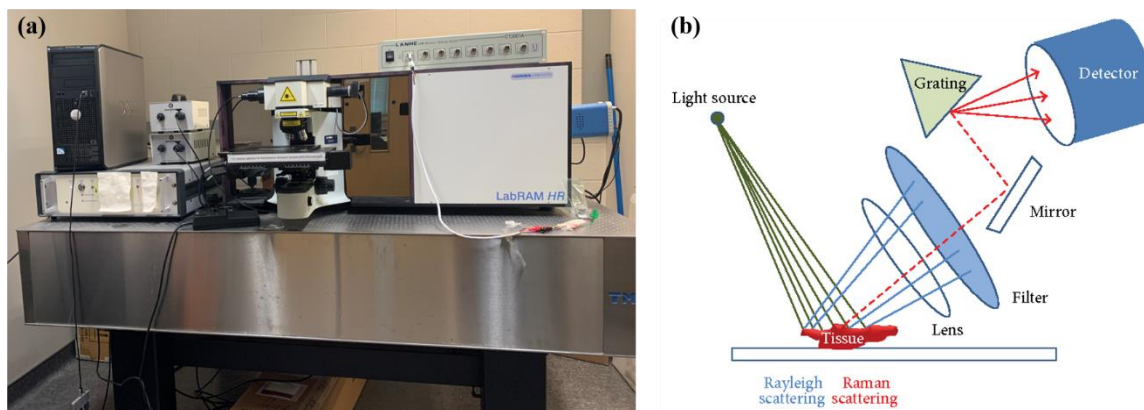


**Figure 3.4** (a) Photo image of a Raman spectroscopy machine, (b) Schematic diagram shows the working principle of Raman spectroscopy.<sup>2</sup>

### iii) XRD

Crystalline materials have atoms that are arranged to repeat periodically. When the X-ray is directed at a crystalline material, it might be diffracted. If the wavelength of the incident X-ray satisfies Bragg's Law,<sup>3</sup>  $n\lambda = 2d \sin\theta$ , the diffracted X-ray will resonate and form constructive interference. Due to the random orientated crystalline material powders, it is necessary to scan the powders through a range of  $2\theta$  angles, to obtain all possible diffraction directions of the lattice. Each crystalline material has its unique d-spacing, which result in unique X-ray diffraction (XRD) spectrum. Therefore, XRD can identify the crystalline material by comparing the sample's spectrum to the standard spectrum from the database.

An X-ray diffraction machine typically consists of three basic elements, (i) X-ray tube, (ii) sample holder and (iii) X-ray detector. The X-ray is generated by the X-ray tube, by heating a filament to generate electrons which are then accelerated by a voltage. The accelerated electrons bombard a target material (usually Cu) to produce characteristic X-rays. Then the X-rays are collimated and directed onto the sample, the detector records the diffracted X-rays. The sample or the detector will be rotated from 0 degrees to 90 degrees, to monitor the change of the diffraction pattern. Once the angle satisfies the Bragg Equation, constructive interference occurs and a peak in intensity occurs. A detector records and processes this X-ray signal and converts the signal to a count rate, which is then output to a device, such as a printer or computer monitor.

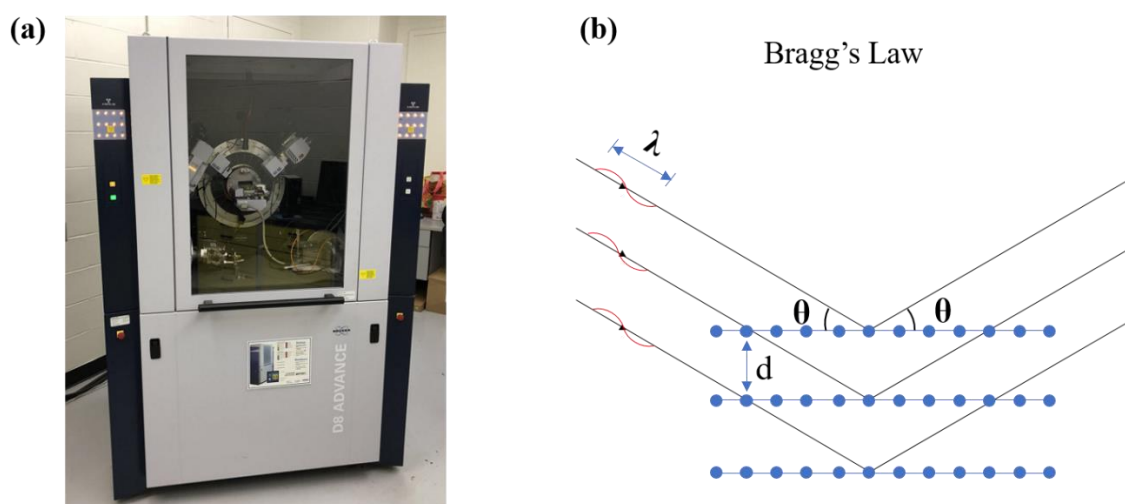


**Figure 3.5** (a) Photo image of Bruker D8 Advance Diffractometer XRD system; (b) Schematic illustration of Bragg's Law.

#### iv) Synchrotron radiation

Synchrotron radiation is generated when the electrons or the charged particles that have a velocity close to the speed of light, are forced to change the direction of their motion or magnitude of speed under the magnetic fields. The generation of synchrotron radiation has two conditions, the closed speed of light of the charged particles and changing the velocity of the charged particles. Based on these principles, human beings can produce synchrotron radiation using a machine, which is called a storage ring (**Figure 3.6a**). In the storage ring,

the electrons are generated and firstly accelerated by a linear accelerator (called ‘Linac’) to a high speed. Then they are further accelerated in the booster ring to higher the speed (close to the speed of light) before they are injected in the storage ring. The whole system is highly evacuated to ensure none of the energy of the electrons is lost due to collision with other particles. There are radio frequency (RF) cavities in the storage ring, which can compensate the energy loss of electrons due to the emitting of synchrotron radiation and they can accelerate the velocity of electrons if it is needed. Storage rings consist of an array of bending magnets (BM) for focusing and bending the electron beam, usually connected by straight linear sections for experimental purpose.

When the electrons have a low speed ( $v \ll c$ ,  $c$  is the speed of light), its emitted pattern is similar to that of an oscillating dipole, with its maximum of intensity in the direction perpendicular to the acceleration direction and it does not depend on the speed (**Figure 3.6b**). But when the velocity of electrons is close to the speed of light, due to the relativistic effect, the emitted pattern is thus compressed into a narrow cone in the direction of motion, which results in an emission tangential to the particle orbit (**Figure 3.6c**). As such, the radiation (X-ray) can be collected for experimental purposes through a horizontal slit (S) of width,  $w$ , at a distance,  $D$  from the electron orbit. By applying the collected tunable energy of X-rays, a variety of experiments can be conducted based on the theories of the interaction between X-rays and matter, such as photoelectric effect, Auger electron, Compton scattering, Rayleigh scattering, and X-ray fluorescence, X-ray diffraction, etc. (**Figure 3.6e**). Different effects can disclose different information of the atoms. Therefore, synchrotron radiation is a very powerful technique for materials characterizations.

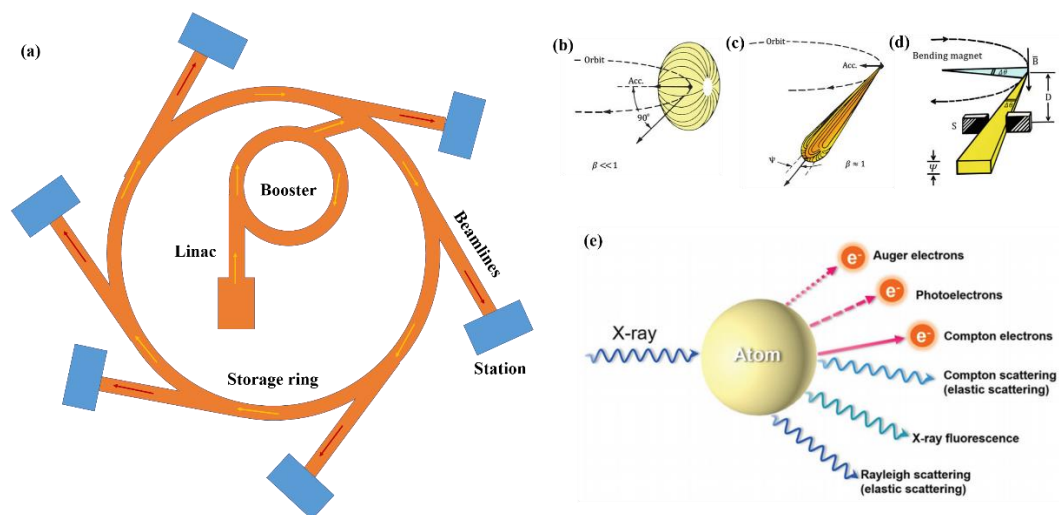


**Figure 3.6** (a) Schematic diagram of a synchrotron radiation facility; (b) The dipole radiation pattern of an electron moving in a circular orbit at a low speed ( $\beta = v/c \ll 1$ ); (c) The narrow cone radiation pattern of an electron moving in a circular orbit at high speed ( $\beta = v/c \approx 1$ ); (d) Schematic illustration of the collection of synchrotron radiation through a horizontal slit;<sup>4</sup> (e) The summaries of the interaction mechanisms between X-rays and an atom.<sup>5</sup>

### 3.2.2 Electrochemical measurements

#### i) Land 2001A Battery Test System

The electrochemical performances of the batteries were evaluated by the Land 2001A Battery Test System. The Land 2001A Battery Test System is designed for energy storage materials research and various battery tests. They can be programmed to run automatic, constant current charge and discharge tests, as well as cycle life tests. With current/voltage custom-built (current ranges from 1 mA to 5 A, voltage ranges from 5 V to 15 V), the battery test systems can run precise battery charge/discharge tests in most cases of coin cell tests/half-cell tests, pouch cell tests, and cylindrical cell tests. The control software has a friendly interface, which means new users can operate it with minimal training.



**Figure 3.7** Photo image of a group of Land 2001A Battery Test Systems. Each unit has 8 independent channels for battery testing.

ii) CV and EIS measurement

Cyclic voltammetry (CV) and electrochemical impedance spectroscopy (EIS) experiments are conducted in a multichannel potentiostat 3/Z (VMP3) device. CV is an electrochemical tool that can measure the current change in a battery/cell with the change of voltage. It is conducted by scanning the potential of a working electrode and measuring the resulting current. It can reflect the potentials of the redox reaction taking place in the system.

EIS is an electrochemical technique that applies a small amplitude, alternating current signal, to probe the impedance properties of an electrochemical cell. By scanning over a wide range of frequencies (typically from MHz to mHz) of the alternating current signal, the impedances at different frequencies are recorded, thus, an EIS spectrum is obtained.





**Figure 3.8** Photo image of A multichannel potentiostat 3/Z (VMP3) coupling with an oven for temperature variation testing.

## References

1. D. Semnani, in *Electrospun Nanofibers*, ed. M. Afshari, Woodhead Publishing, 2017, DOI: <https://doi.org/10.1016/B978-0-08-100907-9.00007-6>, pp. 151-180.
2. K. H. Hun. "Endoscopic Raman Spectroscopy for Molecular Fingerprinting of Gastric Cancer: Principle to Implementation." *BioMed research international*, 2015.
3. W.H. Bragg; W.L. Bragg, "The Reflexion of X-rays by Crystals". *Proc. R. Soc. Lond. A.* 1913, 88 (605), 428–38.
4. A. Balerna and S. Mobilio, in *Synchrotron radiation*, Springer, 2015, pp. 3-28.
5. X. Chen, J. Song, X. Chen and H. Yang, *Chem. Soc. Rev.*, 2019, 48, 3073-3101.

## Chapter 4

### 4 Engineering the conductive carbon/PEO interface to stabilize solid polymer electrolytes for all-solid-state high voltage LiCoO<sub>2</sub> batteries

ASSLIBs are promising energy storage devices for application in electric transportation and large-scale energy storage systems. Polyethylene oxide (PEO)-based solid polymer electrolytes (SPEs) are attractive SSEs for ASSLIBs due to their high ionic conductivity, light weight, and low cost. However, the low electrochemical oxidation potential window of PEO seriously restricts its implementation with high voltage cathodes for high energy density ASSLIBs. Effective interfacial engineering between high voltage cathodes and SPEs can be a solution. Most of the reported conventional cathode protection approaches have been focused only on building coating layers on active material particles, which, however, can be insufficient because the conductive carbon is able to accelerate the decomposition of SPEs. In this work, atomic layer deposition (ALD) coating on the electrode, instead of active material particles, realizes a unique method to protect the cathode/SPE interface. As a successful example, a thin ALD-derived lithium tantalate coating on the high voltage LiCoO<sub>2</sub> electrode demonstrated good compatibility with PEO-based SPEs, significantly enhancing the cycling performance of the ASSLIBs. The inner mechanism is attributed to the fact that the protection of the conductive carbon/SPE interface helps reduce the electrochemical oxidation of PEO-based SPEs. This work shall give new insights for the interfacial engineering of high voltage cathodes and SPEs.

---

Note: this work has been published.

**J. Liang**, Y. Sun, Y. Zhao, Q. Sun, J. Luo, F. Zhao, X. Lin, X. Li, R. Li, L. Zhang, S. Lu, H. Huang, and X. Sun, *J. Mater. Chem. A*, 2020, 8, 2769-2776

## 4.1 Introduction

All solid-state lithium ion batteries (ASSLIBs) are promising candidates for application in electric vehicles (EVs) and other large-scale energy storage systems due to their high energy density and enhanced safety. Feasible solid-state electrolytes (SSEs) are a key component to realize ASSLIBs. Among all the solid-state lithium ion conductors, SSE systems including solid polymer electrolytes (SPEs), oxide-based SSEs, sulfide-based SSEs, and hybrid electrolytes received the most research interest.<sup>1-4</sup> To realize the practical applications of ASSLIBs, the following challenges of SSEs must be addressed: (i) high interfacial resistance, (ii) low ionic conductivity, (iii) narrow electrochemical window, and (iv) instability with electrodes.<sup>2,5,6</sup>

SPEs based on polyethylene oxide (PEO) and lithium salt complexes are promising candidates for ASSLIBs, owing to their high ionic conductivity at elevated temperature and low interfacial resistance toward electrodes. More importantly, PEO is commercially available, low cost, light weight, and environmentally friendly.<sup>6</sup> However, (1) the low ionic conductivity at room temperature,<sup>6-8</sup> (2) the susceptibility to lithium dendrites,<sup>9</sup> and (3) the instability at high voltage<sup>10</sup> of PEO-based SPEs are the main issues that hinder their wide applications in ASSLIBs.

Tremendous research efforts have been dedicated to address challenges (1) and (2) in recent years. For example, Cui's group enhanced the RT ionic conductivity of PEO-based SPEs from  $10^{-7}$  S/cm to  $4.4 \times 10^{-5}$  S/cm by in situ formation of nanosized SiO<sub>2</sub> particle fillers in the PEO matrix.<sup>8</sup> Hu's group created a 3D garnet-type SSE nanofiber network for PEO to form a hybrid electrolyte that has an ionic conductivity of  $2.5 \times 10^{-4}$  S/cm at RT.<sup>11</sup> Plenty of studies applying inorganic SSE fillers in the PEO matrix to enhance the RT ionic conductivity of PEO-based SPEs have also been reported.<sup>12,13</sup> On the other hand, many studies were reported to address the lithium dendrite formation problem in all-solid-state lithium batteries (ASSLBs) with PEO-based SPEs.<sup>11-14</sup> For example, Zhao et al. prepared a LLZO-PEO hybrid electrolyte for ASSLBs and they proposed that anions were tethered in the hybrid electrolyte by the polymer matrix and ceramic fillers, which results in a uniform distribution of space charges and lithium ions, thus, resulting in dendrite-free lithium deposition.<sup>14</sup>

However, the issue of the instability of PEO-based SPEs at high voltage (challenge (3)) received little research attention. The instability of PEO at high voltage makes it challenging to couple with high voltage cathodes such as LiCoO<sub>2</sub>. Even though PEO-based SPEs show excellent stability with LiFePO<sub>4</sub> cathode with charge voltage below 4 V (vs. Li/Li<sup>+</sup>),<sup>15</sup> the limited theoretical energy density of LiFePO<sub>4</sub> restrains its further application in future electric transportation. Alternatively, layer structured oxide cathodes such as LiCoO<sub>2</sub> have a high specific capacity and high charge/discharge voltage, which makes them promising candidates for high energy density ASSLIBs. Since the practical capacity of LiCoO<sub>2</sub> is positively related to the charge cut-off voltage, a high charge cut-off voltage is required for high-energy-density applications.<sup>16</sup> However, charge cut-off voltage over 4.5 V remains a challenge for PEO-based SPEs due to the decomposition of PEO-based SPEs at high voltage.<sup>17-19</sup>

One solution to enable PEO-based SPE coupling with high voltage LiCoO<sub>2</sub> is interfacial engineering of SPEs and the LiCoO<sub>2</sub> active material interface with coating layers. Coatings on LiCoO<sub>2</sub> particles with Al<sub>2</sub>O<sub>3</sub>,<sup>19</sup> Li<sub>3</sub>PO<sub>4</sub>,<sup>18</sup> poly(ethylcyanoacrylate) (PECA),<sup>20</sup> and Li<sub>1.4</sub>Al<sub>0.4</sub>Ti<sub>1.6</sub>(PO<sub>4</sub>)<sub>3</sub> (LATP)<sup>21</sup> have been reported to improve solid-state batteries performances. However, most of these previous studies only studied the coating effect on the active material/SPE interface while the conductive carbon/SPE interface is ignored. Unfortunately, conductive carbon has been proved to be able to accelerate the decomposition of SSEs including PEO-based SPEs, oxide-based SSEs and sulfide-based SSEs.<sup>10,22,23</sup> Thus, the detrimental effect of conductive carbon on the PEO-based SPE cannot be neglected in high voltage ASSLIBs. Therefore, systematic studies on the effects of coatings on active material particles versus on the whole electrodes (i.e. covering both active material and conductive carbon) are important to disclose the interfacial engineering mechanism and can provide us with helpful insights for future high energy density ASSLIBs designs.

Herein, atomic layer deposition (ALD), as an emerging technique, which is capable of depositing uniform and conformal thin films with precise thickness control by self-limited chemical reactions, is chosen for realizing active material particle coating and whole electrode coating because the ALD process can be carried out at a low temperature

compared to other chemical/physical deposition techniques such as chemical vapor deposition (CVD), physical vapor deposition (PVD), sol-gel methods, etc. Thus, ALD can be non-destructive to electrode components (cathode particles and conductive carbon). In this study, ALD derived lithium tantalate protective coatings are demonstrated to stabilize the interface between PEO-based SPEs and  $\text{LiCoO}_2$  electrodes at high voltage (4.5 V vs.  $\text{Li}/\text{Li}^+$ ). Effects of coatings on the  $\text{LiCoO}_2$  particles, the whole electrode, and conductive carbon particles are compared. The results show that the coating on  $\text{LiCoO}_2$  particles cannot improve the performance of ASSLIBs, while the coating on electrode sheets (coating on both  $\text{LiCoO}_2$  particles and carbon particles) shows significant enhancement in cycling performance, the same as the coating on conductive carbon particles. The working mechanism of the ALD coating is illustrated in **Figure 4.1**. These results highlight that a suitable coating approach is critical in preventing the electrochemical oxidation of PEO-based SPEs at high voltage for the stabilization of the high voltage performance of ASSLIBs.

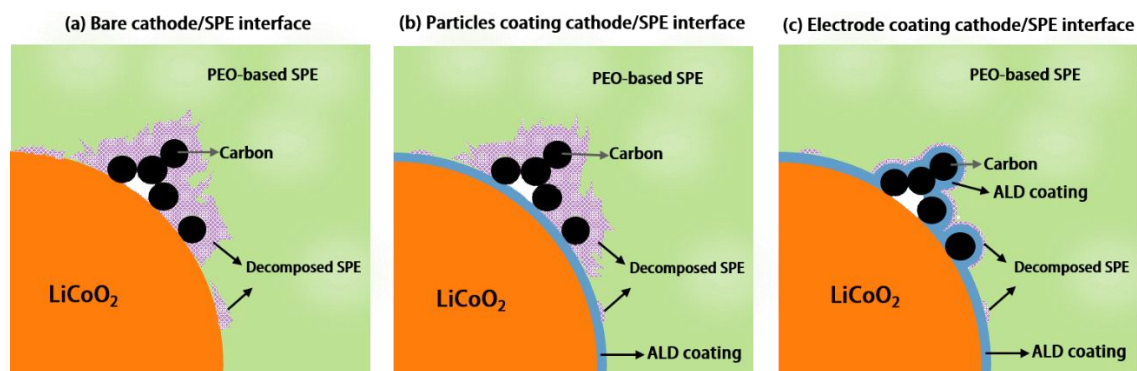


**Figure 4.1** Schematic diagram showing the working mechanism of ALD coating for enabling stable, high voltage solid polymer electrolyte-based lithium ion batteries. The decomposition of SPEs on (a) unprotected  $\text{LiCoO}_2$  electrode and (b) electrode with protected  $\text{LiCoO}_2$  particles (LCO-coating), and the working mechanism of (c) protected electrode (LCO+CB-coating) in ASSLIBs after extensive charge/discharge cycles. Conductive carbon can accelerate the decomposition of SPEs at high voltage, and thus, the protection of the carbon/SPE interface is very important for stabilizing high voltage solid-state lithium ion batteries.

## 4.2 Experimental

### 4.2.1 Preparation of LiCoO<sub>2</sub> electrode with/without ALD coating

Bare LiCoO<sub>2</sub> electrodes were prepared by mixing 90 wt% of LiCoO<sub>2</sub> particles, 6 wt% carbon-black (acetylene black) and 4 wt% poly(vinylidene) fluoride binder in the N-methylpyrrolidinone (NMP) solvent. The slurry was coated on Al foil by a doctor blade method. The electrode was obtained after drying in a vacuum oven at 120 °C overnight. The loading of LiCoO<sub>2</sub> was around 1.5-2 mg/cm<sup>2</sup>. The obtained bare LiCoO<sub>2</sub> electrode was used directly for electrode coating. ALD LTO coatings on LiCoO<sub>2</sub> particles or electrodes followed a previously reported ALD procedure from our group.<sup>24</sup> Briefly, the LTO coatings were deposited using an ALD reactor (Savannah 100, Cambridge Nanotechnology Inc., USA) by alternatively pulsing lithium tert-butoxide, tantalum(V) ethoxide and H<sub>2</sub>O at 235 °C.

### 4.2.2 Electrochemical performance testing

All solid-state LiCoO<sub>2</sub> batteries were assembled in 2032 type coin cells in an argon-filled glove box (Vacuum Atmosphere Company, moisture and oxygen level less than 1 ppm). The LiCoO<sub>2</sub> electrodes and lithium foil were used as the working electrode and the counter electrode, respectively. The PEO-LiClO<sub>4</sub>-LLZTO SPE was used as both the separator and lithium ion conductor. No additional solvent or liquid electrolyte was applied into the LiCoO<sub>2</sub> ASSLBs. Galvanostatic charge/discharge was performed between 2.7 and 4.5 V in a 60 °C oven using a LAND battery tester. The ASSLBs were rested at 60 °C oven 30 h before testing. For LiCoO<sub>2</sub> batteries with liquid electrolyte, 2032 type coin cells were assembled with a liquid electrolyte containing 1 M LiPF<sub>6</sub> in ethylene carbonate (EC):ethylmethyl carbonate (EMC):diethyl carbonate (DEC) solvents with a volume ratio of 1:1:1, using a Celgard separator. Cyclic voltammetry of the LiCoO<sub>2</sub> batteries was performed between 2.7 and 4.5 V (vs. Li/Li<sup>+</sup>) at 60 °C. Linear sweep voltammetry of Li/SPE/PEO-carbon cells was conducted at an open-circuit voltage of 4.5 V on a versatile multichannel potentiostat 3/Z (VMP3). PEO-carbon composite electrodes consisted of 70 wt.% PEO and 26 wt.% carbon-black (with/without LTO coating) and 4 wt.% LiClO<sub>4</sub> was used as the working electrode. Electrochemical impedance spectroscopy (EIS) was

performed on a versatile multichannel potentiostat 3/Z (VMP3) by applying an AC voltage with 10 mV amplitude in the frequency range from 500 kHz to 0.01 Hz.

### 4.2.3 Materials characterization

The morphology of the samples was characterized using a Hitachi S-4800 field emission scanning electron microscope (FE-SEM) equipped with an energy dispersive X-ray spectrometer (EDX). FIB was conducted in a LEO (Zeiss) 1540XB FIB/SEM machine. Mass spectrometry was conducted on a Shimadzu GCMS-QP2010 gas chromatograph/mass spectrometer. X-ray absorption spectroscopy (XAS) measurements using total electron yield (TEY) and fluorescence yield (FLY) modes at the Co K-edge were performed at the Canadian light source (CLS) at the Soft X-ray Micro-characterization Beamline (SXRMB) with a photon energy range of 1.7-10 keV utilizing a Si (111) crystal monochromator.

## 4.3 Results and discussion

Cathodes were prepared with  $\text{LiCoO}_2$  particles, carbon black (acetylene black), and a poly(vinylidene) fluoride binder at a weight ratio of 90:6:4. Using the advanced ALD technique, the lithium tantalate (LTO) coating was deposited on either the  $\text{LiCoO}_2$  particles before electrode preparation (coating on  $\text{LiCoO}_2$  active materials, referred to as LCO-coating) or on the electrode surface after casting and drying (coating on the electrode, referred to as LCO+CB-coating) or on the carbon black particles before electrode preparation (coating on CB particles, referred to as CB-coating). **Figure S4.1a-c** show the scanning electron microscopy (SEM) images of a pristine  $\text{LiCoO}_2$  electrode, an electrode with ALD LTO coated  $\text{LiCoO}_2$  particles (LCO-coating), and an ALD LTO coated electrode (LCO+CB-coating). The three electrodes with or without these two types of coatings show a very similar morphology, indicating that the ALD LTO coatings were conformal and non-destructive. The LCO-coating did not alter the distribution of the conductive carbon on the electrode surface, nor did LCO+CB-coating. In addition, from the SEM images, one can easily find that the electrode/SPE interface actually has a large proportion of the conductive carbon/SPE interface since carbon black is uniformly distributed/covered on the  $\text{LiCoO}_2$  particle surface.

Transmission electron microscopy (TEM), SEM and energy-dispersive X-ray spectroscopy (EDX) analyses were used to confirm the deposition of the ALD coatings on active materials and the electrode (**Figure 4.2** and **S4.2-S4.5**). **Figure 4.2a** shows the TEM image of the ALD coating on  $\text{LiCoO}_2$  particle and the schematic illustration of the LCO-coating electrode is presented in **Figure 4.2b**. Differently, the ALD LTO coated electrode (LCO+CB-coating) shows a coating on both carbon black and  $\text{LiCoO}_2$  particles (**Figure 4.2c**). The EDX mapping results in **Figure S4.3** confirm that ALD LTO is deposited on both the CB and LCO particle surface for the LCO+CB-coating electrode. This type of electrode structure is schematically illustrated in **Figure 4.2d**. Hereby, two types of protective coverages are established: (I) partial protection between the  $\text{LiCoO}_2$ /SPE interface only and (II) full protection on the entire electrode covering both  $\text{LiCoO}_2$  and conductive carbon. The electrochemical performance will be compared systematically.

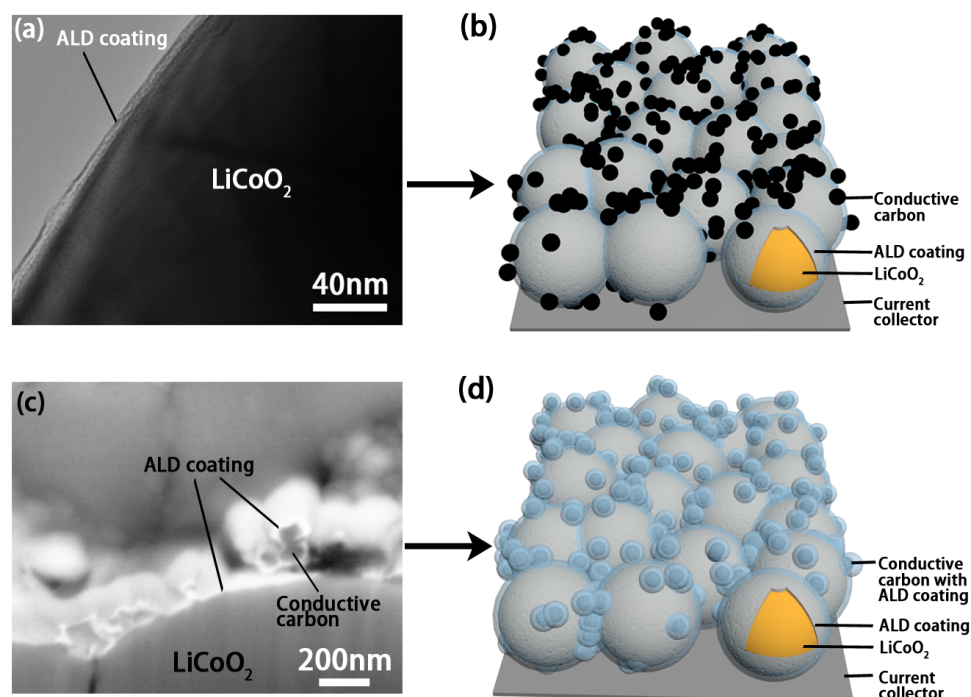


**Figure 4.2** (a) A TEM image of the 10 cycles of ALD LTO (thickness is  $\sim 5$  nm) coating on  $\text{LiCoO}_2$  particles and its (b) schematic diagram of the  $\text{LiCoO}_2$  electrode with the LCO-coating where conductive carbon is not protected. (c) A SEM image in backscattered electron mode of the 20 cycles of ALD LTO (thickness is  $\sim 10$  nm) coating on both conductive carbon and  $\text{LiCoO}_2$  particles from the LCO+CB-coating sample after focused



ion beam (FIB) cutting, and its (d) schematic diagram showing the LiCoO<sub>2</sub> electrode where both LiCoO<sub>2</sub> and conductive carbon are protected. The binder is omitted in the schematic diagrams.

Cyclic voltammetry (CV) was performed to study the electrochemical process of LiCoO<sub>2</sub> ASSLIBs with different coatings. For comparison, CV of a regular LiCoO<sub>2</sub> battery with a commercial carbonate-based liquid electrolyte was conducted for a comprehensive understanding. As shown in **Figure S4.6a**, the anodic peaks corresponded to the Li<sup>+</sup> extraction process, and the cathodic peaks were related to the Li<sup>+</sup> insertion process. There are three pairs of peaks which correspond to three oxidation/reduction couples. The redox pair at 4.07/3.74 V is the result of the conversion between Co<sup>3+</sup> and Co<sup>4+</sup> for the first-order phase transformation between two hexagonal phases.<sup>25</sup> The other two pairs of anodic/cathodic peaks are related to the order-disorder phase transformation between hexagonal and monoclinic phases.<sup>26-28</sup> In contrast, in ASSLIBs, the three pairs of redox peaks are combined into a pair of broad peaks for all three cells with a bare LiCoO<sub>2</sub> electrode, electrodes with LCO-coating protection and LCO+CB-coating protection (**Figure S4.6b-d**). This is probably because of the sluggish Li<sup>+</sup> transport in SPEs and electrodes that broadens the peaks related to the first-order phase transformation reaction, overlapping the other weak peaks. Nevertheless, the ASSLIBs with different cathodes still exhibit obvious difference in electrochemical behaviors. For the ASSLIB with the bare LiCoO<sub>2</sub> electrode, an anodic peak and a cathodic peak are observed with decreasing peak current intensities and increase in overpotentials over the three scans (**Figure S4.6b**). This is a typical indication of decay in electrochemical redox reversibility. The decrease in peak current intensities and increase in overpotentials also occur in the ASSLIB with LCO-coating protection (**Figure S4.6c**). As a conclusion, LCO-coating protection is insufficient in preventing the reversibility decay. In great contrast, instead of a decrease in peak current intensities and increase in overpotentials, the slight increase in peak current intensities and the decrease in overpotentials indicate a more reversible electrochemical process of the LCO+CB-coating protected electrode (**Figure S4.6d**).

The electrochemical performances of ASSLIBs with different protection coverages were characterized at 60 °C. First, the coating thickness is optimized. Different cycles of ALD

LTO were conducted on LCO-coating and LCO+CB-coating electrodes and their results are presented in **Figure S4.7**. Clearly, the ALD LTO coating thicknesses were optimized to 10 ALD cycles for LCO-coating protection and 20 ALD cycles for LCO+CB-coating protection.

The ASSLIBs performances with optimized ALD coating thickness for bare, LCO-coating, and LCO+CB coating are compared in **Figure 4.3**. Consistent with the CV results, observable voltage polarization along with serious capacity fading is already observed during the first 20 cycles of galvanostatic testing at 0.2C for both ASSLIBs with a bare  $\text{LiCoO}_2$  electrode (**Figure 4.3a**) or LCO-coating protected electrode (**Figure 4.3b**). This is possibly due to the severe decomposition of PEO-based SPEs at high voltage that increases the interfacial resistance. Even though the LCO-coating protection can protect the  $\text{LiCoO}_2$ /SPE interface, the conductive carbon was still in direct contact with the SPE.

In contrast, much smaller polarization increase is observed for the ASSLIB with the LCO+CB-coating protected electrode (**Figure 4.3c**). The discharge capacities are also relatively stable compared to the other two cells without protection or only with LCO-coating protection. Thus, the protection on the carbon/SPE interface is evidently very important.

The dramatically different effects between LCO-coating and LCO+CB-coating protections on the electrochemical performance can be further verified by cycling performance and rate performance. Under the optimized conditions, ASSLIBs with LCO+CB-coating protection demonstrate substantially enhanced performance over the ASSLIBs without protection or with LCO-coating protection (**Figure 4.3d-f**). While all three ASSLIBs deliver a similar initial discharge capacity around 170-177 mAh/g, a retaining capacity of 110.4 mAh/g at 100th cycles for the ASSLIB with the LCO+CB-coating protected electrode is significantly higher than the remaining capacity of  $\sim 71$  mAh/g for the other two ASSLIBs (**Figure 4.3d**). As shown in **Figure 4.3e**, LCO+CB-coating protection also markedly enhanced the rate performance at lower current densities of up to 0.6 C. However, at a higher current density, a higher capacity is achieved for the LCO-coating electrode. The reason can be possibly attributed to the higher lithium ion diffusion in the LCO-coating

electrode compared to that of the bare and LCO+CB coating electrodes. In the LCO-coating electrode, LCO particles are totally coated with LTO, which is a good lithium ion conductor, while in the LCO+CB-coating protected electrode, only part of LCO particles are exposed for ALD LTO deposition. Therefore, the lithium ion diffusion of the LCO-coating protected electrode is better than that of the LCO+CB-coating protected electrode (**Figure S4.8**) and bare electrode. At high current density, lithium ion diffusion becomes a determining step for the redox reaction. Thus, the electrode with higher  $\text{Li}^+$  ion diffusion can deliver a higher capacity.

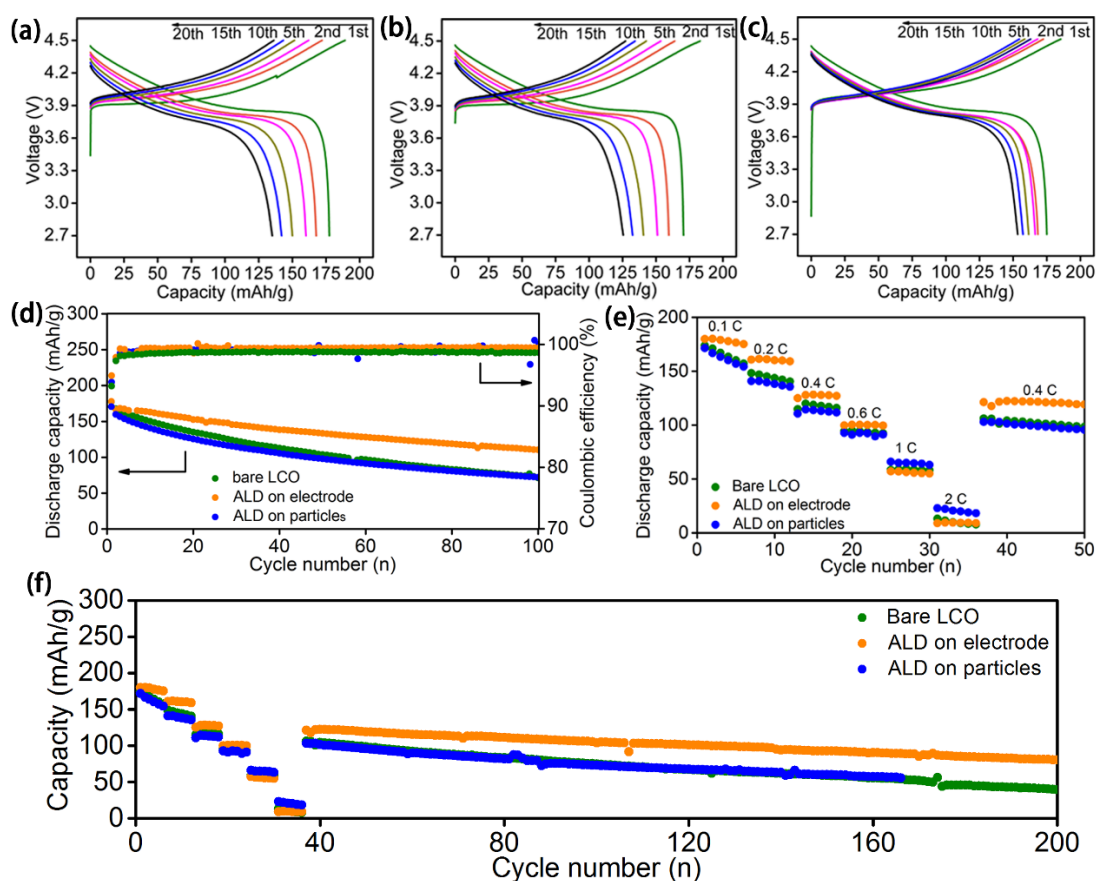


**Figure 4.3** Charge/discharge profiles of ASSLIBs with (a) bare LiCoO<sub>2</sub> electrode, (b) LCO-coating protected electrode, and (c) LCO+CB-coating protected electrode at 0.2C and 60 °C. Corresponding (d) cycling performance, (e) rate performance, and (f) long-term cycling performance after rate performance testing for ASSLIBs with different LiCoO<sub>2</sub> electrodes at 60 °C.

LCO+CB-coating protection also can improve the initial coulombic efficiency and subsequent average coulombic efficiency. The initial coulombic efficiencies for the ASSLBs with a bare LiCoO<sub>2</sub> electrode, LCO-coating protection, and LCO+CB-coating protection electrodes are 93.8%, 93.2%, and 94.9%, respectively; the subsequent average coulombic efficiencies are 99.0%, 98.6%, and 99.3% in order. The LCO-coating protection electrode actually shows barely any improvement over the bare LiCoO<sub>2</sub> electrode, indicating the protection of only LiCoO<sub>2</sub> particles is not enough in PEO-based ASSLBs. The higher coulombic efficiency by LCO+CB-coating protection indicates reduced decomposition of the PEO-based SPE during high voltage charge/discharge cycles in ASSLBs.

Electrochemical impedance spectroscopy (EIS) was conducted to study the evolution of interfacial resistance in the LiCoO<sub>2</sub> ASSLBs upon cycling (**Figure 4.4**). The three ASSLBs without coating or with LCO-coating or with LCO+CB-coating present EIS spectra with a similar shape but different evolution trends. There are two semicircles with one at high frequency and one at low frequency. **Figure 4.4d** shows the equivalent circuit for fitting these EIS spectra.  $R_e$  is the impedance from the SPE,  $R_a$  is the interfacial impedance between the lithium anode and SPE, and CPE1 is its corresponding constant phase element.  $R_c$  is the interfacial impedance between the cathode and SPE, and CPE2 is its corresponding constant phase element.<sup>18</sup> All ASSLIBs show relatively stable anode/SPE interfacial resistance with similar values, while dramatic difference is present at the cathode/SPE interfaces. For the bare LiCoO<sub>2</sub> ASSLIB (**Figure 4.4a**), a significant increase in the cathode/SPE interfacial resistance is observed over 30 cycles, enlarging from 1338  $\Omega$  at the 10th cycle to 1843  $\Omega$  at the 20th cycle to 2891  $\Omega$  at the 30th cycle. Similarly, consistent with the electrochemical performance, a significant increase in the cathode/SPE interfacial resistance is also observed in the ASSLIB with LCO-coating protection (**Figure 4.4b**). The increase in cathode/SPE interfacial resistance can be attributed to the accumulation of insulating SPE decomposition products, which can block the Li<sup>+</sup> ion transportation at the interface. In contrast, the cathode/SPE interfacial impedance of the ASSLIB with LCO+CB-coating protection is stabilized to  $\sim 920 \Omega$  after 30 cycles, confirming the stable SPE/cathode interface enabled by the ALD LTO coating on the

electrode. The EIS results strongly support the superior effects of ALD LTO protection for high-voltage ASSLIBs.

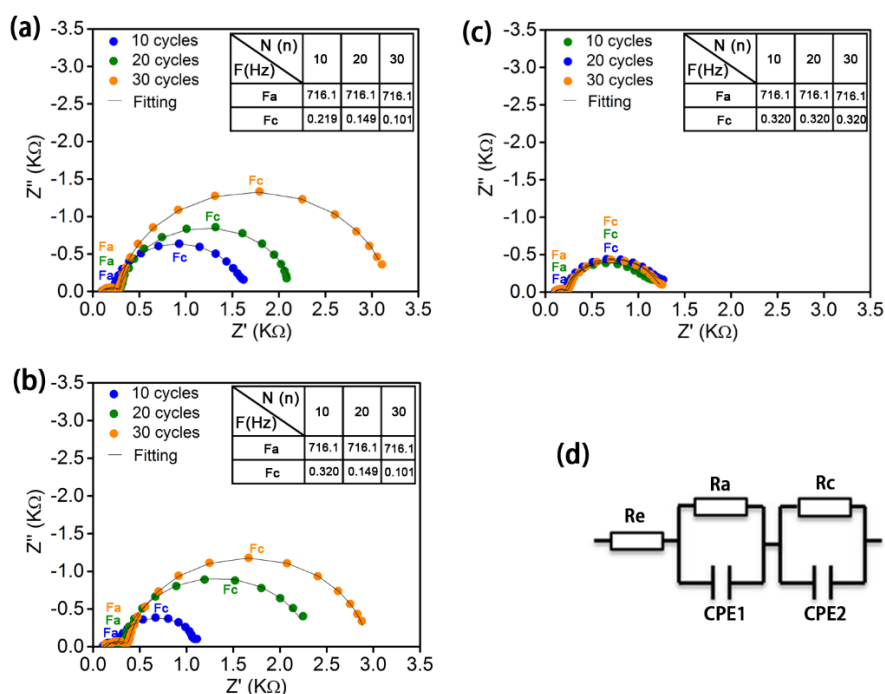


**Figure 4.4** EIS spectra of ASSLIBs with (a) bare LiCoO<sub>2</sub> electrode, (b) LCO-coating protected LiCoO<sub>2</sub> electrode, and (c) LCO+CB-coating protected LiCoO<sub>2</sub> electrode after 10, 20, and 30 cycles of charge/discharge. The inset tables show the critical frequency values on top of the high frequency semi-circle (Fa) and low frequency semi-circle (Fc) at different cycles of charge/discharge, respectively. (d) The equivalent circuit for fitting the EIS spectra.

To confirm that the conductive carbon/SPE interface is important for the ASSLIB performance enhancement, an ASSLIB with a CB-coated electrode (an electrode with bare LiCoO<sub>2</sub> and LTO coated CB) was assembled and studied. The results are presented in **Figure S4.10**. It shows that LTO coating on carbon particles can also enhance the cycling performance of the ASSLIB, and its cycling performance is very similar to that of LCO+CB coated ASSLIBs.

Why is the conductive carbon/SPE interface so critical? It is well known that the electrochemical oxidation potential of PEO-based SPEs is around 3.8 V vs. Li/Li<sup>+</sup>

according to the linear sweep voltammetry method using a PEO-carbon composite electrode.<sup>10</sup> Conventionally, it has been reported that electronic conductive additives (usually carbon black) play an important role in realizing completely utilization of electrode active materials for batteries, because the occurrence of electrochemical reactions requires both electrons and  $\text{Li}^+$  ions. However, in ASSLIBs with  $\text{Li}^+$  ion conductive SSEs, the presence of conductive carbons could also trigger irreversible decomposition of the SSEs,<sup>23</sup> leading to low coulombic efficiency and performance decay.

Even conductive carbon black particles occupy a low weight content in the electrodes. The large volume fraction of carbon black and resulted the large proportion of the carbon/SPE interface among the cathode/SPE interface cannot be neglected (**Figure S4.1a-c**). This could explain the similar performance of ASSLIBs with the bare  $\text{LiCoO}_2$  electrode and LCO-coating electrode, whereas the carbon black particles are in direct contact with the SPE in either case. The linear sweep voltammetry results of carbon-SPE composite electrodes with or without ALD LTO coating also confirmed the importance of the carbon/SPE interface. As shown in **Figure 4.5a**, the overshooting current approaching 4.5 V is observed for the bare carbon-PEO electrode, which indicates the serious decomposition of PEO at 4.5 V. In contract, this overshooting current is significantly reduced by the ALD LTO coated conductive carbon. As supported by the mass spectrometry results in **Figure S4.11b**, the significant signals from decomposed SPE products are presented in the bare carbon-PEO electrode. However, with the ALD LTO coating on carbon, the signals from the decomposed SPE are reduced (**Figure S4.11c**), which demonstrates the excellent capability of LTO in stabilizing the carbon/SPE interface at high voltage. This may be the reason why the protection of the conductive carbon/SPE interface can achieve such a significant enhancement in electrochemical performance.

Why does the LCO-coating electrode show almost no enhancement? It is possible that  $\text{LiCoO}_2$  active materials are stable and further ALD protection cannot enhance their stability in our study. This conclusion is supported by the X-ray absorption spectroscopy (XAS) of the unprotected  $\text{LiCoO}_2$  electrodes before and after cycling with the PEO-based SPE. The Co K-edge XAS results for  $\text{LiCoO}_2$  electrodes before and after 5 charge/discharge cycles at the discharge state in ASSLIBs showed almost no difference

under both total electron yield (TEY) mode (**Figure 4.5b**) and fluorescence yield (FLY) mode (**Figure 4.5c**). TEY mode provides surface chemical information up to several nanometers, and FLY mode reveals bulk chemical information. The XAS results indicated that the  $\text{LiCoO}_2$  active materials are relatively stable from the surface to bulk upon cycling in PEO-based ASSLBs. This is also supported by the stable cycling performance of the  $\text{LiCoO}_2$  battery with a carbonate-based liquid electrolyte (**Figure S4.12**). Since  $\text{LiCoO}_2$  is stable during charge/discharge processes, it is reasonable that the ALD LTO coating on  $\text{LiCoO}_2$  particles (LCO-coating protection) showed little effect while the ALD LTO coating on the electrode (LCO+CB-coating protection) achieved significant enhancement.

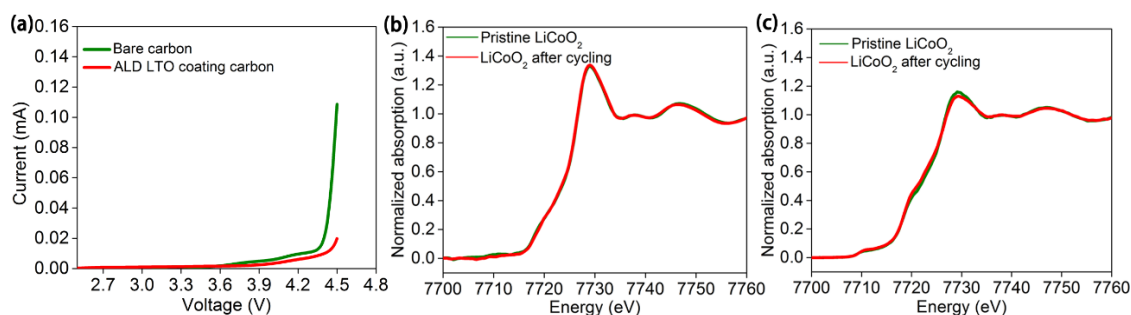


**Figure 4.5** (a) Comparison of the linear sweep voltammogram of the Li/SPE/PEO-carbon composite cell and Li/SPE/PEO-LTO@carbon composite cell (scan rate = 0.3 mV/s, from OCV to 4.5 V vs.  $\text{Li/Li}^+$ ). Comparison of the XAS Co K-edge spectra of unprotected  $\text{LiCoO}_2$  before and after 5 cycles of charge/discharge in ASSLBs in the discharge state in terms of (b) TEY mode and (c) FLY mode.

## 4.4 Conclusions

The effects of ALD lithium tantalate coatings on cathode active material particles, carbon black particles and the electrode surface were studied systematically for enhancing the high-voltage performance of PEO-based ASSLBs. Using stable  $\text{LiCoO}_2$  particles as an example for a high voltage cathode up to 4.5 V, we demonstrated the importance of the protection on the conductive carbon/SPE interface. It is found that interfacial protection covering the carbon/SPE interface is very important to stabilize the PEO-based SPE at high voltage and enhance the cycling performance of ASSLBs. Significantly improved cycling performance and rate performance were demonstrated in ASSLBs with simple 20 ALD

cycles of lithium tantalate coating on the electrode surface. This study sheds light on the rational design of protective coatings for the polymer electrolyte-electrode interface to enhance the high voltage performance of ASSLIBs.

## Acknowledgment

This work was supported by China Automotive Battery Research Institute, the Natural Sciences and Engineering Research Council of Canada (NSERC), the Canada Research Chair Program (CRC), the Canadian Light Source (CLS) and the University of Western Ontario.

## References

1. A. Manthiram, X. Yu and S. Wang, *Nat. Rev. Mater.*, 2017, 2, 16103.
2. C. Sun, J. Liu, Y. Gong, D. P. Wilkinson and J. Zhang, *Nano Energy*, 2017, 33, 363-386.
3. J. Liang, Q. Sun, Y. Zhao, Y. Sun, C. Wang, W. Li, M. Li, D. Wang, X. Li and Y. Liu, *J. Mater. Chem. A*, 2018, 6, 23712-23719.
4. J. Liang, J. Luo, Q. Sun, X. Yang, R. Li and X. Sun, *Energy Storage Mater.*, 2019, 21, 308-334.
5. V. Thangadurai, S. Narayanan and D. Pinzarú, *Chem. Soc. Rev.*, 2014, 43, 4714-4727.
6. L. Long, S. Wang, M. Xiao and Y. Meng, *J. Mater. Chem. A*, 2016, 4, 10038-10069.
7. F. Croce, G. Appetecchi, L. Persi and B. Scrosati, *Nature*, 1998, 394, 456.
8. D. Lin, W. Liu, Y. Liu, H. R. Lee, P.-C. Hsu, K. Liu and Y. Cui, *Nano Lett.*, 2015, 16, 459-465.
9. K. J. Harry, D. T. Hallinan, D. Y. Parkinson, A. A. MacDowell and N. P. Balsara, *Nat. Mater.*, 2014, 13, 69.
10. Y. Xia, T. Fujieda, K. Tatsumi, P. P. Prosini and T. Sakai, *J. Power Sources*, 2001, 92, 234-243.
11. K. K. Fu, Y. Gong, J. Dai, A. Gong, X. Han, Y. Yao, C. Wang, Y. Wang, Y. Chen and C. Yan, *Proc. Natl. Acad. Sci. U.S.A.*, 2016, 113, 7094-7099.



12. J. Zhang, N. Zhao, M. Zhang, Y. Li, P. K. Chu, X. Guo, Z. Di, X. Wang and H. Li, *Nano Energy*, 2016, 28, 447-454.
13. C. Yang, B. Liu, F. Jiang, Y. Zhang, H. Xie, E. Hitz and L. Hu, *Nano Res.*, 2017, 10, 4256-4265.
14. C.-Z. Zhao, X.-Q. Zhang, X.-B. Cheng, R. Zhang, R. Xu, P.-Y. Chen, H.-J. Peng, J.-Q. Huang and Q. Zhang, *Proc. Natl. Acad. Sci. U.S.A.*, 2017, 114, 11069-11074.
15. P. Hovington, M. Lagacé, A. Guerfi, P. Bouchard, A. Mauger, C. Julien, M. Armand and K. Zaghib, *Nano Lett.*, 2015, 15, 2671-2678.
16. L. Wang, B. Chen, J. Ma, G. Cui and L. Chen, *Chem. Soc. Rev.*, 2018, 47, 6505-6602.
17. K. Nie, Y. Hong, J. Qiu, Q. Li, X. Yu, H. Li and L. Chen, *Front. Chem.*, 2018, 6, 616.
18. S. Seki, Y. Kobayashi, H. Miyashiro, Y. Mita and T. Iwahori, *Chem. Mater.*, 2005, 17, 2041-2045.
19. H. Miyashiro, Y. Kobayashi, S. Seki, Y. Mita, A. Usami, M. Nakayama and M. Wakihara, *Chem. Mater.*, 2005, 17, 5603-5605.
20. J. Ma, Z. Liu, B. Chen, L. Wang, L. Yue, H. Liu, J. Zhang, Z. Liu and G. Cui, *J. Electrochem. Soc.*, 2017, 164, A3454-A3461.
21. Q. Yang, J. Huang, Y. Li, Y. Wang, J. Qiu, J. Zhang, H. Yu, X. Yu, H. Li and L. Chen, *J. Power Sources*, 2018, 388, 65-70.
22. F. Han, Y. Zhu, X. He, Y. Mo and C. Wang, *Adv. Energy Mater.*, 2016, 6, 1501590.
23. W. Zhang, T. Leichtweiß, S. P. Culver, R. Koerver, D. Das, D. A. Weber, W. G. Zeier and J. r. Janek, *ACS Appl. Mater. Interfaces*, 2017, 9, 35888-35896.
24. J. Liu, M. N. Banis, X. Li, A. Lushington, M. Cai, R. Li, T.-K. Sham and X. Sun, *J. Phys. Chem. C*, 2013, 117, 20260-20267.
25. Y. Gu, D. Chen, X. Jiao and F. Liu, *J. Mater. Chem.*, 2007, 17, 1769-1776.
26. K. Dokko, S. Horikoshi, T. Itoh, M. Nishizawa, M. Mohamedi and I. Uchida, *J. Power Sources*, 2000, 90, 109-115.
27. J. N. Reimers and J. Dahn, *J. Electrochem. Soc.*, 1992, 139, 2091-2097.
28. X. Li, J. Liu, X. Meng, Y. Tang, M. N. Banis, J. Yang, Y. Hu, R. Li, M. Cai and X. Sun, *J. Power Sources*, 2014, 247, 57-69.

29. D. Zhang, H. Yan, Z. Zhu, H. Zhang and J. Wang, *J. Power Sources*, 2011, 196, 10120-10125.
30. K. Karthik and R. Murugan, *J. Solid State Electrochem.*, 2018, 22, 2989-2998.
31. X.-L. Wang, A. Mei, M. Li, Y.-H. Lin and C.-W. Nan, *J. Appl. Phys.*, 2007, 102, 054907.

## Supporting information

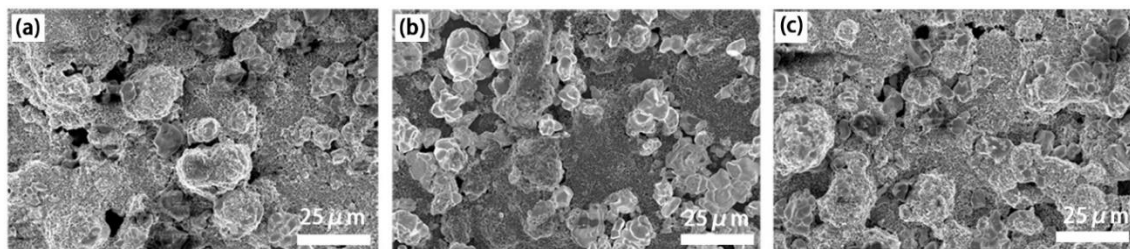


**Figure S4.1** SEM images of (a) bare LCO electrode, (b) electrode with ALD LTO coated  $\text{LiCoO}_2$  particles (LCO-coating protection) and (c) ALD LTO coated electrode (LCO+CB-coating protection).

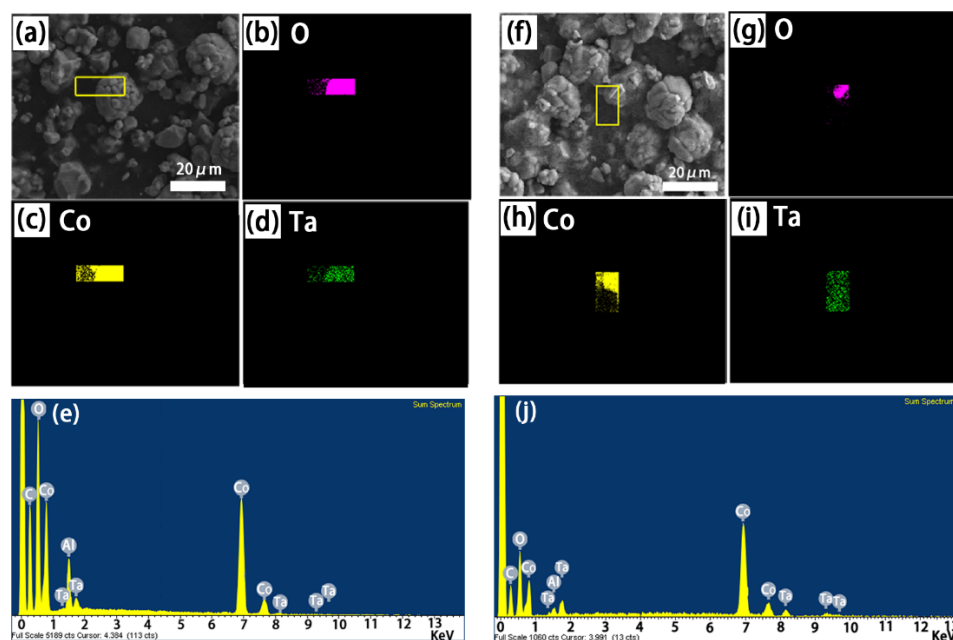


**Figure S4.2** (a) SEM image and EDX mappings of selected area for electrode with 50 cycles ALD LTO coated  $\text{LiCoO}_2$  particles (LCO-coating protection) and its corresponding (b) O mapping, (c) Co mapping, (d) Ta mapping and the corresponding EDX spectrum (e). (f) SEM image and EDX mappings of selected area for 50 cycles ALD LTO coated electrode (LCO+CB-coating protection) and its corresponding (g) O mapping, (h) Co mapping, (i) Ta mapping and the corresponding EDX spectrum (j).

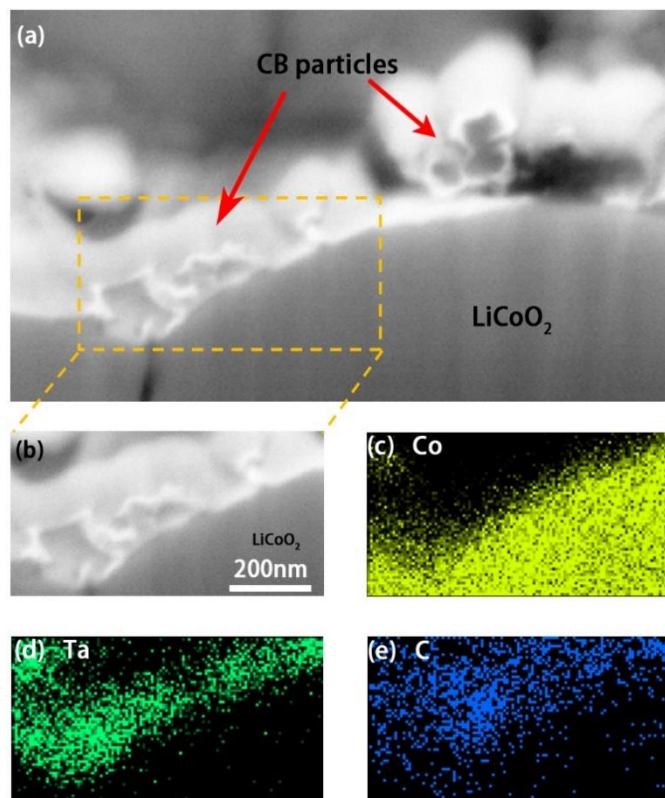


**Figure S4.3** (a) Cross-section view of SEM image of  $\text{LiCoO}_2$  particle covered with carbon black particles with LTO coating. (b) The selected area for EDX mapping and its corresponding element distribution of (c) Co, (d) Ta, (e) C.

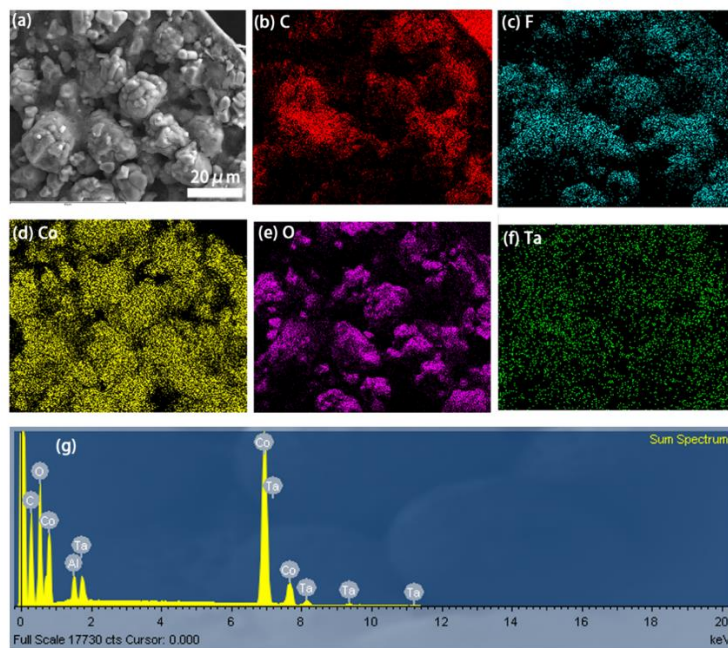


**Figure S4.4** SEM image and EDX mappings of ALD LTO coated LiCoO<sub>2</sub> electrode. (a) SEM image; EDX mappings of (b) C, (c) F, (d) Co, (e) O, and (f) Ta elements. (g) Corresponding EDX spectrum.

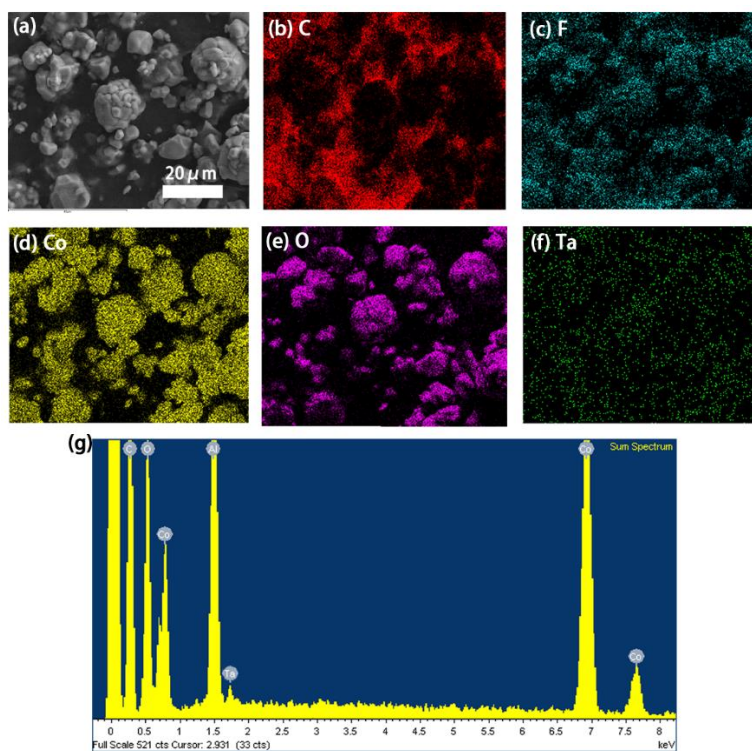


**Figure S4.5** SEM image and EDX mappings of the electrode with ALD LTO coated LiCoO<sub>2</sub> particles. (a) SEM image; EDX mappings of (b) C, (c) F, (d) Co, (e) O, and (f) Ta elements. (g) Corresponding EDX spectrum.

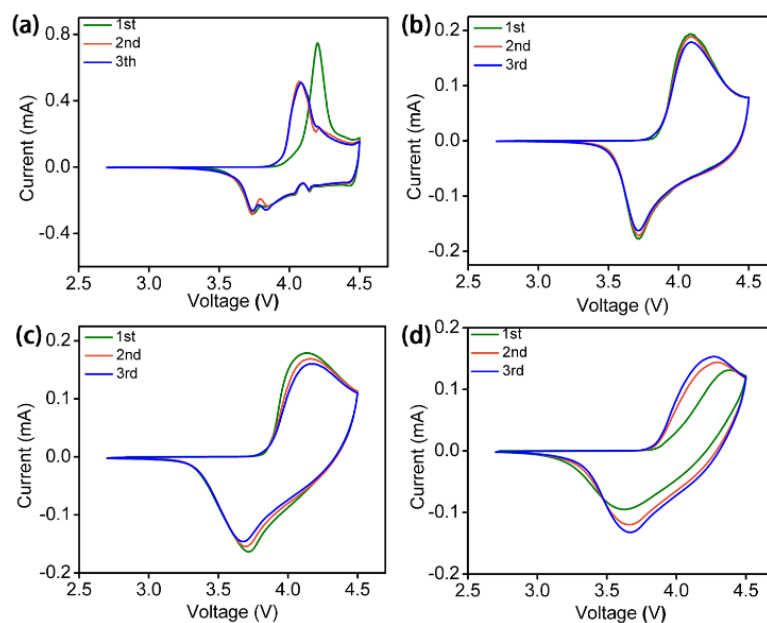


**Figure S4.6** CV of (a) liquid electrolyte-based LiCoO<sub>2</sub> battery, ASSLIBs with (b) bare LiCoO<sub>2</sub>, (c) LiCoO<sub>2</sub> particles coating and (d) LiCoO<sub>2</sub> electrode coating. All batteries were tested at 60°C.

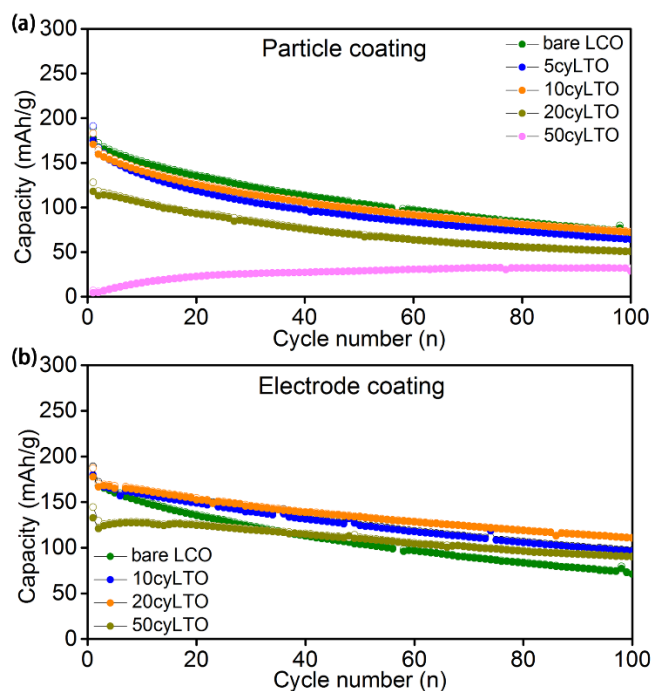


**Figure S4.7** The influences of ALD coating thickness on the performances of ASSLIBs with (a) particles coating and (b) electrode coating.

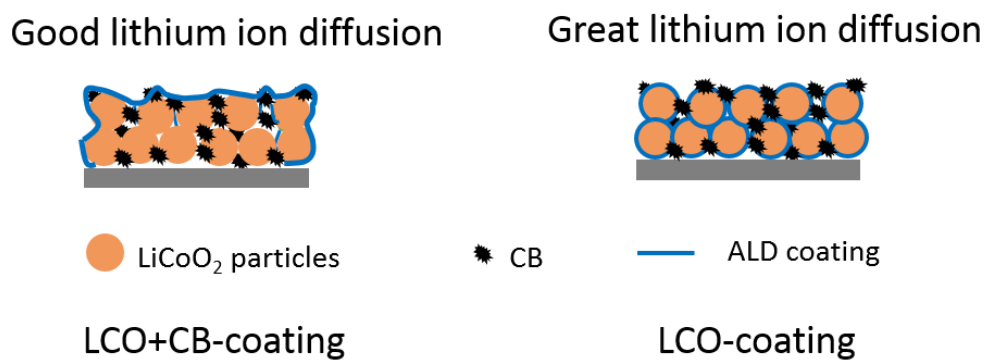


**Figure S4.8** Comparison of ALD coating in LCO+CB-coating electrode and LCO-coating electrode. A better lithium ion diffusion can be achieved in LCO-coating electrode.

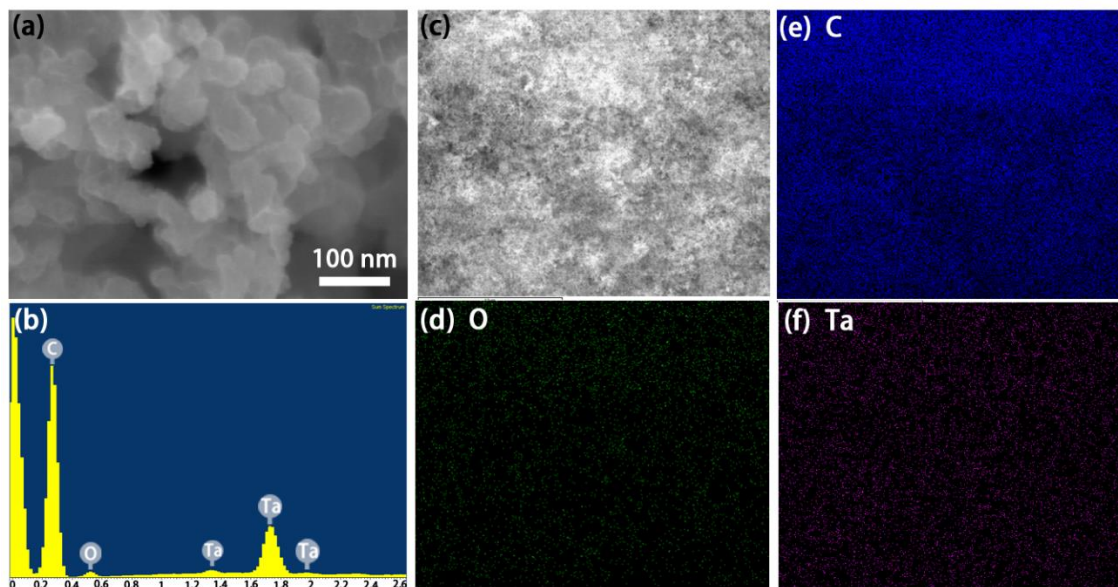


**Figure S4.9** (a) SEM image of carbon black particles with ALD-LTO coating. (b) EDX spectrum of carbon black particles with ALD-LTO coating; (c) corresponding SEM image of EDX mapping area; (d) corresponding O distribution; (e) corresponding C distribution; (f) corresponding Ta distribution.

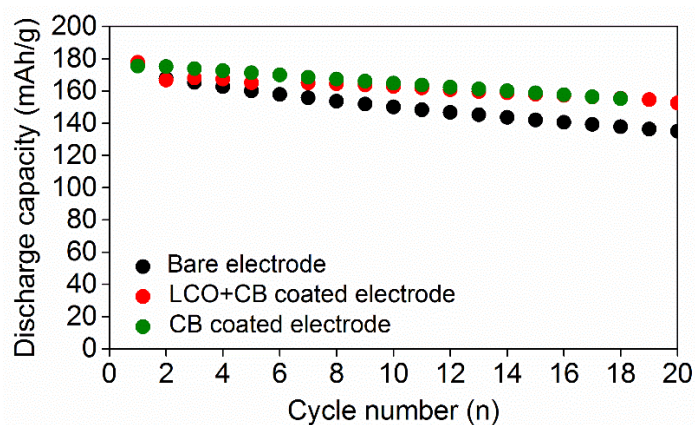


**Figure S4.10** Comparison of cycling performance of the batteries with bare  $\text{LiCoO}_2$  electrode, LCO+CB coated electrode and CB coated  $\text{LiCoO}_2$  electrode.



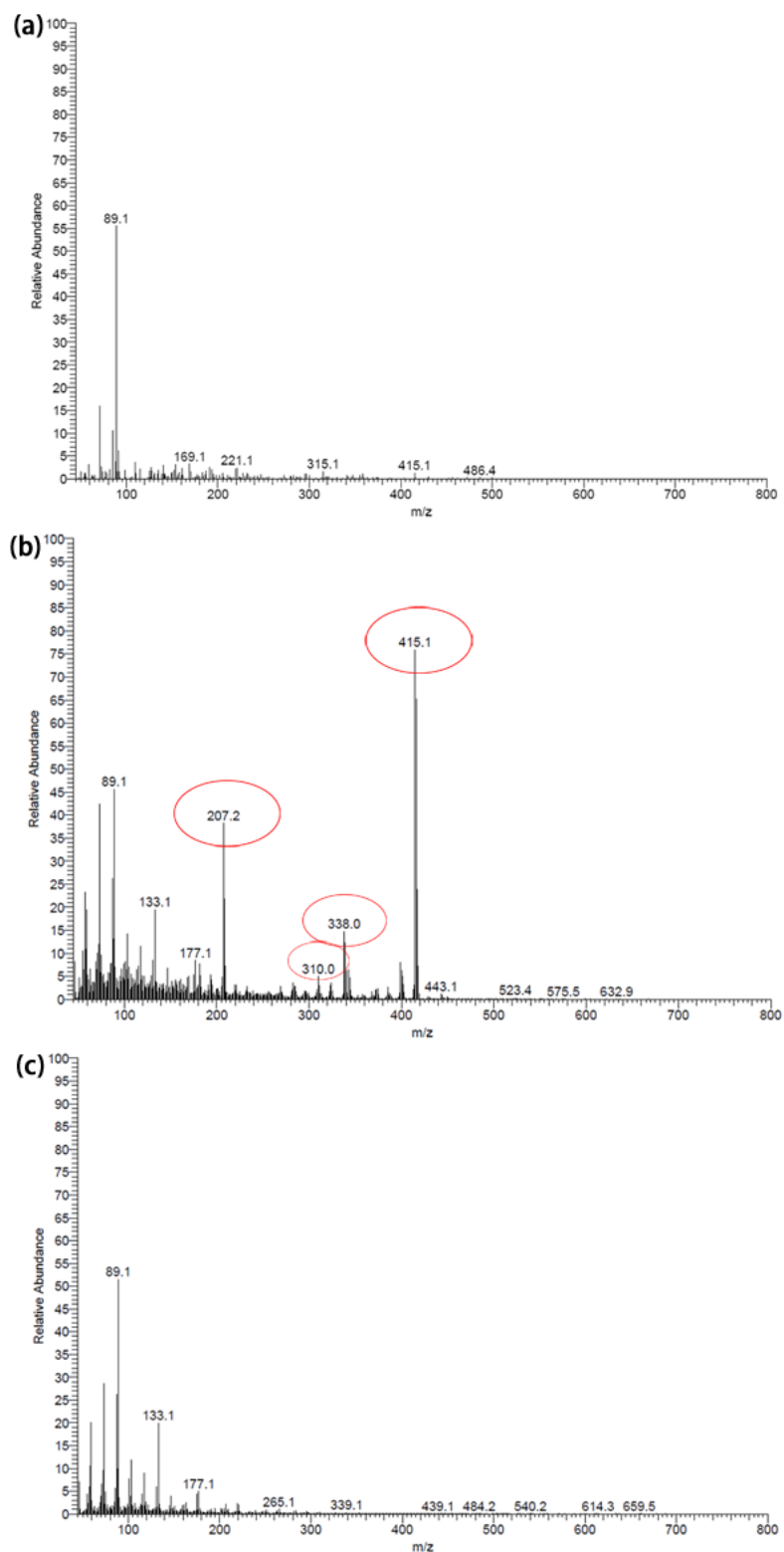


**Figure S4.11** The mass spectrometry (MS) results. (a) Pristine PEO-based SPE. (b) PEO-carbon composite after charging to 4.5 V and holding for 20 h; the red circles point out the

signals related to the decomposition of PEO-based SPE. (c) PEO-ALD LTO carbon composite after charging to 4.5 V and holding for 20 h. Compared with the plot of pristine PEO-based SPE, the additional peaks marked by red circle and the increased intensities of light MS peaks suggested the partial depolymerization of PEO under high voltage, while this phenomenon is not so clear for PEO-ALD LTO carbon composite, suggesting that the decomposition of PEO can be restricted.

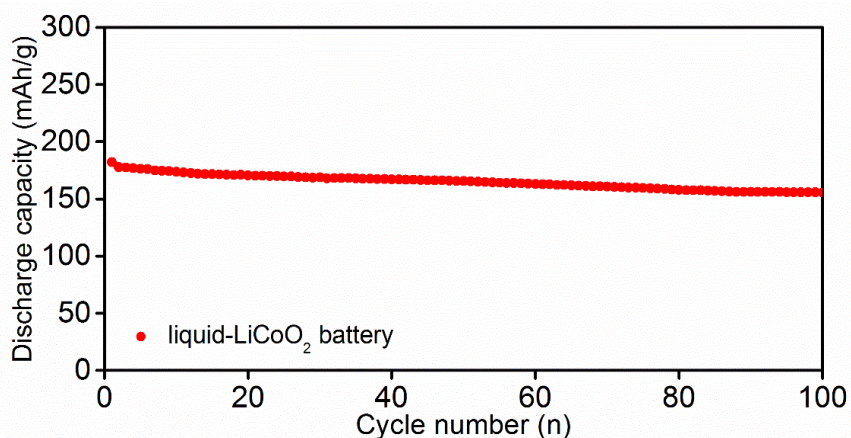


**Figure S4.12** Cycling performance of  $\text{LiCoO}_2$  battery with carbonate-based liquid electrolyte. The charge/discharge voltage window is from 2.7 - 4.5 V. The stable performance indicates the  $\text{LiCoO}_2$  particles are stable. The protection may not be so critical for performance enhancement. Thus, the capacity decay of the  $\text{LiCoO}_2$  ASSLIB is the contribution of the decomposition of SPE.

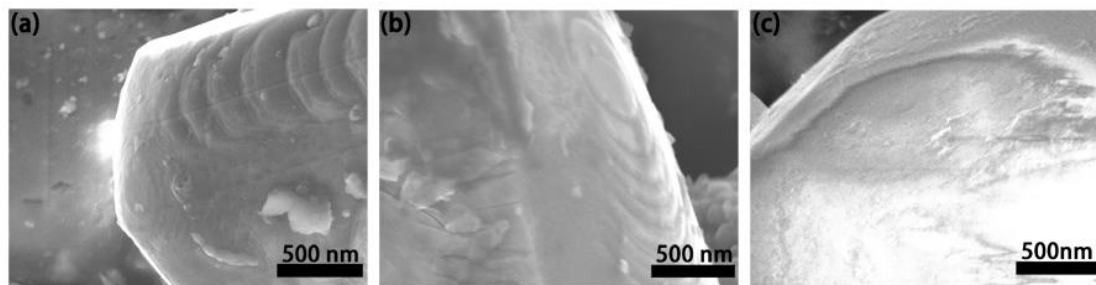


**Figure S4.13** SEM images of  $\text{LiCoO}_2$  particles collected from ASSLBs with (a) bare electrode, (b) LCO-coating protection, and (c) LCO+CB-coating protection after 200 cycles.

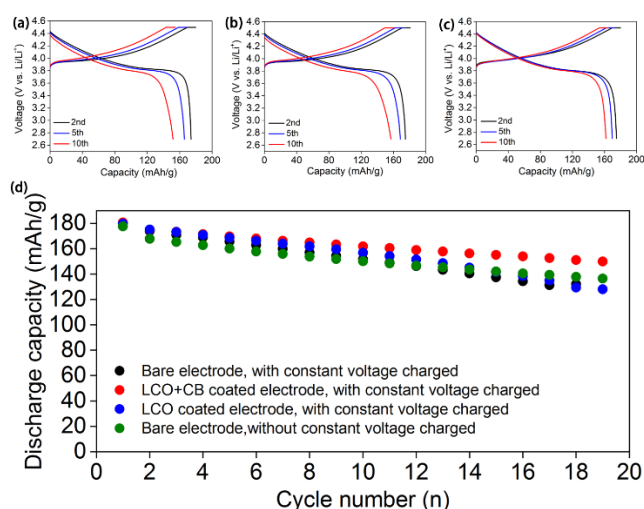


**Figure S4.14** Charge/discharge profiles of ASSLBs with (a) bare  $\text{LiCoO}_2$  electrode, (b) LCO-coating protection electrode, and (c) LCO+CB-coating protection electrode at 0.2 C and 60 °C with constant voltage charge step. (d) Comparison of discharge capacity of ASSLIBs with different electrodes.

**Table S4.1** Comparisons of dry polyethylene-based SPE all-solid-state  $\text{LiCoO}_2$  batteries performance.

Testing temperature [°C]	Charge voltage cut-off [V]	Discharge capacity at 1st cycles [mAh/g]	Discharge capacity at different cycles [mAh/g, cycle number]	Average capacity decay per cycles (mAh/g)	Refs.
80	4.45	172.8	67, 75	1.4	20
80	4.2	148	124, 30	0.8	29

60	4.4	172	101, 100	0.71	19
60	4.4	174	134, 20	2	18
25	4.2	146	120, 30	0.87	30
80	4.2	120	/	/	31
<b>60</b>	<b>4.5</b>	<b>177</b>	<b>110.4, 100</b>	<b>0.56</b>	<b>This work</b>

---

Note: The capacity decay is calculated based on the second cycle capacity.

## Chapter 5

### 5 Stabilizing and understanding the interface between Nickel-rich cathode and PEO-based electrolyte by lithium niobium oxide coating for high-performance all-solid-state batteries

In previous chapter, interface engineering between high voltage  $\text{LiCoO}_2$  electrode and SPE was studied. The ALD-derived lithium tantalate coating shows significant improvement of the electrochemical performance of ASSLIBs. To pursuit a higher energy density of ASSLIB, a higher energy density cathode, Nickel-rich lithium nickel manganese cobalt oxide  $\text{LiNi}_{0.8}\text{Mn}_{0.1}\text{Co}_{0.1}\text{O}_2$  (NMC811) cathode, should be used as the cathode materials in ASSLIBs.

However, the low electrochemical oxidation window of PEO-based SPE and the instability of NMC811 at the charge/discharge process seriously restrict the battery performance. Herein, a high voltage stable solid-state electrolyte layer lithium niobium oxide (LNO) is coated on the NMC811 electrode surface by atomic layer deposition for stabilizing NMC811-based solid polymer batteries. Electrochemical tests show that LNO coating can stabilize the NMC811 active materials and mitigate the decomposition of SPE upon the cycling process, maintaining a discharge capacity of 175.5 mAh/g after 50 cycles. Mechanism studies by SEM, STEM, XAS, and XPS disclose that the uncoated NMC811 suffers from chemomechanical degradations along with oxygen release triggering the decomposition of SPE, which results in an unstable cathodic electrolyte interphase. With LNO coating, chemomechanical degradations and oxygen release of NMC811 are inhibited and the decomposition of SPE is mitigated. This work renders a stable and high-performance high energy density SSB for high voltage application, which paves the way toward next-generation ASSLIBs.

---

**J. Liang**,<sup>#</sup> S. Hwang,<sup>#</sup> S. Li, J. Luo, Y. Sun, Y. Zhao, Q. Sun, W. Li, M. Li, M. N. Banis, X. Li, R. Li, L. Zhang, S. Zhao, S. Lu, H. Huang, D. Su,<sup>\*</sup> and X. Sun<sup>\*</sup>, **Nano Energy**, 2020, 105107.

<sup>#</sup> J. Liang and S. Hwang contributed equally to this work.

## 5.1 Introduction

The rapid development of electric transportation and grid-scale energy storage systems require the batteries with high energy density and reliable safety properties.<sup>1-3</sup> However, conventional lithium-ion batteries (LIBs) with liquid electrolyte cannot meet this requirement due to its potential safety issues such as leakage of liquid electrolyte, fire and even explosion if batteries are short-circuit or over-heat. Compared to conventional LIBs, solid-state batteries (SSBs) with solid-state electrolytes (SSEs) have received more and more research attentions due to their improved safety. Among the SSEs, poly(ethylene oxide) (PEO)-based solid polymer electrolyte (SPE) is one of the most promising candidate for the applications in high energy density SSBs because of its high ionic conductivity and low interfacial resistance toward electrodes, along with its low mass density, low cost, facile fabrication process, and environmental-friendly properties.<sup>4</sup> In addition, to achieve high energy density SSBs, cathodes with high specific capacity or/and high discharge voltage are favorable. Therefore, many novel lithium transition metal oxide cathodes such as lithium nickel oxide, lithium manganese oxide, and lithium nickel manganese cobalt oxide (NMC), with higher theoretical specific capacity were developed and received plenty of research concerns.<sup>5-12</sup> Among these cathode materials, Ni-rich lithium nickel manganese cobalt oxide, such as  $\text{LiNi}_{0.8}\text{Co}_{0.1}\text{Mn}_{0.1}\text{O}_2$  (NMC811), is one of the most promising candidates for the near future application in electric transportation.

However, the incorporation of PEO-based SPE and Nickel-rich NMC cathode experiences serious challenges. Firstly, the electrochemical oxidation voltage of PEO-based SPE is lower than 4 V vs.  $\text{Li}/\text{Li}^+$ .<sup>13</sup> Although PEO-based SPE can deliver a good performance in  $\text{LiFePO}_4$  SSB in a voltage window of 2.5 - 4.0 V,<sup>14</sup> its performance in 4 V class cathode such as  $\text{LiCoO}_2$  and Nickel-rich cathode is still very poor.<sup>15,16</sup> At high charge voltage of 4.3 V requested by NMC811 electrode, a serious decomposition of PEO-based SPE will happen. The second challenge roots from the instability of Ni-rich NMC811 cathode that causes problems including voltage fading, transition metal dissolution, surface reconstruction, and chemomechanical degradations upon cycling, significantly hindering the wide applications of Ni-rich NMC811 cathode in SSBs.<sup>7,10,12,17-19</sup>

To enhance the stability of PEO-based SPE at high voltage for coupling with high voltage and high specific capacity cathode materials, protecting the SPE/active material interface with an inert coating layer is proved to be an effective strategy.<sup>15,20-22</sup> Another approach is applying stable lithium salts for complexing with PEO-based polymer to stabilize the cathodic electrolyte interphase for enhancing the performance of high voltage solid polymer batteries.<sup>23,24</sup>

As for enhancing the stability of Ni-rich NMC cathodes, surface coating<sup>7,12,25</sup> and element doping<sup>26,27</sup> are two main strategies. For example, NMC cathode with  $\text{Li}_3\text{PO}_4$  surface coating was presented with significant improvement in the electrochemical performance due to the effects of  $\text{Li}_3\text{PO}_4$  coating in avoiding the liquid electrolyte induced corrosion of the NMC particle grain boundary and maintaining the structural stability of NMC particles.<sup>12</sup> Therefore, from the perspective of stabilizing SPE and stabilizing Ni-rich NMC cathode simultaneously, coating NMC811 electrode sheet with a  $\text{Li}^+$  ion conducting layer can not only maintain the stability of NMC811 cathode but also protect the SPE from the decomposition at high voltage.

Herein, an atomic layer deposition (ALD) derived lithium niobium oxide (LNO) solid-state electrolyte thin film is applied to tailor the interface between NMC811 cathode electrode and PEO-based SPE. The LNO coating layer is demonstrated to not only stabilize the NMC811 particles under high temperature and high-voltage cycling but also reduce the decomposition of PEO-based SPE. As a result, even though the specific discharge capacity of the bare NMC811 SSB dramatically drops from 204.8 mAh/g to 73.9 mAh/g in 50 cycles, ALD LNO coated NMC811 SSB maintains a high specific discharge capacity of 175.5 mAh/g after 50 cycles, showing significant improvement in the electrochemical performance. Mechanism studies by Scanning electron microscopy (SEM), scanning transmission electron microscopy (STEM), synchrotron based X-ray absorption spectroscopy (XAS), and X-ray photo spectroscopy (XPS) suggest that the uncoated NMC811 suffers from chemomechanical degradations along with oxygen release triggering the decomposition of SPE, which results in an unstable cathodic electrolyte interphase and serious decay in electrochemical performance, while with LNO coating,

chemomechanical degradations and oxygen release are inhibited and the decomposition of SPE is mitigated, rendering a high performance high energy density SSBs.

## 5.2 Experimental

### 5.2.1 Preparation of ALD LNO coating NMC811 electrodes

Bare NMC811 electrodes were prepared as followed: Firstly, 80 wt. % of NMC811 particles, 10 wt. % carbon-black (Acetylene Black) and 10 wt.% PVDF binder were mixed together in the NMP solvent. Secondly, the mixture was coated on Al foils that serves as the current collector by doctor blade method. Third, NMC811 electrode was dried in a vacuum at 100 °C for 24 h. ALD LiNbO<sub>x</sub> (LNO) coating NMC811 electrode was prepared by directly coating LNO on the bare NMC811 electrodes in an ALD reactor (Savannah 100, Cambridge Nanotechnology Inc., USA). Lithium tert-butoxide [LiOtBu, (CH<sub>3</sub>)<sub>3</sub>COLi, Alfa Aesar, >99.9%] and niobium ethoxide [Nb(OEt)<sub>5</sub>, Et = -CH<sub>2</sub>CH<sub>3</sub>, Strem Chemicals Inc., >99.9%] and H<sub>2</sub>O were used as the precursors and the deposition temperature was set as 235 °C.

### 5.2.2 Electrochemical performance testing

All solid-state NMC811 batteries were assembled in the 2032 type coin cells in an argon filled glove box (Vacuum Atmosphere Company, moisture and oxygen level less than 1 ppm). The PEO-based SPE was used as both separator and lithium ion conductor. Lithium metal was used as counter electrode and the NMC811 electrode was applied as the working electrode. Not any solvent or liquid electrolyte was added into NMC811 SSBs. Charge/discharge characteristics were tested between 2.8 and 4.3 V in a 60 °C oven using a LAND Battery Tester, the batteries were kept at 60 °C over 30 h before testing. CV of the NMC811 batteries were tested between 2.8 and 4.3 V (vs. Li/Li<sup>+</sup>) at 60 °C. Electrochemical impedance spectroscopy (EIS) was performed on the versatile multichannel potentiostat 3/Z (VMP3) by applying an AC voltage of 10 mV amplitude in the 500 kHz to 0.01 Hz frequency range.



### 5.2.3 Physical characterization

A Hitachi S-4800 field emission scanning electronic microscopy (FE-SEM), equipped with energy dispersive X-ray spectroscopy (EDX) was used to study the morphologies and the composition of the NMC811 cathode before and after charge/discharge cycles. Synchrotron X-ray absorption were carried out at the Canadian Light Source (CLS). X-ray photoelectron spectroscopy was conducted by ESCALAB 250 spectrometer, Perkin-Elmer. Cross-sectional TEM samples were prepared by focused ion beam method using Thermo-Fisher Helios Nanolab DualBeam. HAADF-STEM images and STEM-EDX elemental maps were acquired with Thermo-Fischer Talos F200X at an accelerating voltage of 200 kV.

## 5.3 Results and discussion

ALD derived LNO (ALD-LNO) was deposited directly on the surface of NMC811 electrode using Savannah 100 ALD system following the method that we reported previously.<sup>28</sup> **Figure 5.1a** schematically shows the process of ALD coating on NMC811 cathode electrode. The growth rate of ALD-LNO is 0.2 nm/cycle.<sup>28</sup> TEM image in **Figure 5.1b** presents the NMC811 particle with 50 cycles of ALD-LNO coating, where the thickness of LNO is around 10 nm. SEM coupled with energy-dispersive X-ray (EDX) confirmed the coverage of ALD-LNO coating on NMC811 electrode surface (**Figure S5.2** and **Figure S5.3**) as indicated by the uniform Nb mapping. Synchrotron based XAS at Nb L3-edge was used to characterize the chemical environment of the ALD-LNO. **Figure 5.1c-d** are the XAS spectra collected under total electron yield (TEY) and fluorescence yield (FLY) mode, respectively. TEY mode collected the information from the top few nanometers of the sample surface, while FLY mode was considered to reflect the bulk property. Both the edge position and spectral features of the ALD-LNO spectra are highly relevant to those of standard LiNbO<sub>3</sub> in TEY and FLY modes. The ALD-LNO and the standard LiNbO<sub>3</sub> samples showed the same peak A position at 2372.8 eV without energy shift, which indicated the same oxidation state of Nb in ALD-LNO as in the standard LiNbO<sub>3</sub> sample (Nb<sup>5+</sup>). Peak B was related to the ligand field splitting of d-orbitals originating from the local coordination structure of Nb<sup>5+</sup>.<sup>28</sup> The minor shift of peak B in ALD-LNO compared to standard LiNbO<sub>3</sub> sample indicating that there was difference of

the local coordination of  $\text{Nb}^{5+}$  in ALD-LNO, which was possibly original from the ALD synthesis process. ALD-LNO is amorphous while standard  $\text{LiNbO}_3$  is crystalline, the atom or electron surround Nb is different in these two sample. For ALD-LNO, the Nb  $L_3$ -edge XAS spectra were almost the same in FLY and TEY modes (**Figure S5.4b**). This was due to the intrinsic thin film property of ALD-LNO, which resulted in minor difference in bulk and surface properties since the thickness of 50 cycles of ALD-LNO is only around 10 nm.

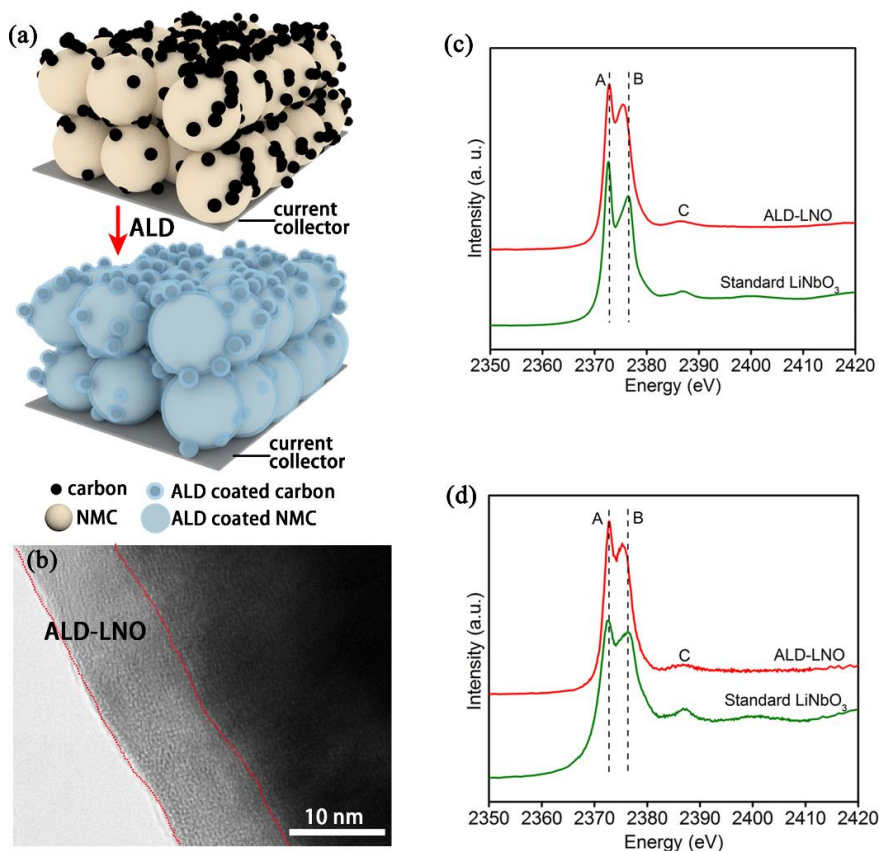


**Figure 5.1** (a) schematically showing the ALD-LNO coating on NMC811 electrode. (b) TEM image of ALD-LNO coated cathode active material particle. Comparison of Nb  $L_3$ -edge XAS between ALD-LNO and standard  $\text{LiNbO}_3$  sample at (c) TEY and (d) FLY.

The discharge/charge cycling stability of the SSBs with bare NMC811 cathode or ALD-LNO coated NMC811 cathode were evaluated at a current density of 0.2 C at 60 °C. The results are presented in **Figure 5.2**. The ALD-LNO coating thickness was optimized based on galvanostatic cycling performance (**Figure S5.5**). The NMC811 electrodes with 20-100 cycles of ALD-LNO coatings all showed significantly improved stability compared to the

bare NMC811 electrode, where 50 cycles of ALD-LNO coating delivered the highest specific discharge capacity. The lowered specific capacity by a thick ALD-LNO coating (100 cycles) was probably due to the restricted ionic/electronic transport through the coating. As a comparison to electrode coating, ALD coating on NMC811 particles only is also study, the results are shown in **Figure S5.6**, where it indicates that particles coating has little improvement in electrochemical performance but not as superior as electrode coating. Therefore, ALD-LNO coating of 50 cycles was chosen for further studies. **Figure 5.2a** and **b** are the discharge voltage profiles of the SSBs using bare NMC811 and ALD-LNO coated NMC811 cathodes, respectively. Clearly, the bare NMC811 SSB showed obvious capacity fading along with enlarging overpotential upon cycling, which suggested the continuous formation of the cathodic electrolyte interphase (CEI) and the decay of the NMC811 active materials. In contrast, the SSB with ALD-LNO coated NMC811 electrode demonstrated stable cycling performance with good capacity retention, which indicated a favorable CEI. The evolutions of the midpoint voltage of these two SSBs over 200 charge/discharge cycles are compared in **Figure 5.2c**. At the initial cycle, the midpoint voltage of both SSBs were similar around 3.78 V. However, after 200 cycles, the midpoint voltage of the bare NMC811 SSB dramatically faded to 3.02 V while the ALD-LNO coated NMC811 SSB still maintained a high midpoint voltage of 3.52 V. The stabilization of discharge voltage by the ALD-LNO coating is beneficial for preserving high energy density.

The long cycling stabilities of the NMC811 SSBs with or without ALD-LNO coating are compared in **Figure 5.2d**. The specific discharge capacity of the bare NMC811 SSB dramatically decreased from 204.8 to 73.9 mAh/g (i.e. 63.9% loss in capacity) within only 50 cycles. However, the ALD-LNO coated NMC811 SSB can maintained a high specific discharge capacity of 175.5 mAh/g after 50 cycles with 84.1 % capacity retention. At 200 cycles, the ALD-LNO coated NMC811 SSB delivered about 5 times higher discharge capacity than the SSB without coating. Meanwhile, the ALD-LNO coated NMC811 SSB showed a high average Coulombic efficiency of 99.2 % over 200 cycles, which was significantly higher than 92.3 % of the bare NMC811 SSB (**Figure 5.2e**). This result again indicated a more stable cathodic interface between the PEO-based SPE and the ALD-LNO NMC811 electrode than the non-coated electrode. The energy density of the as-studied

NMC811 SSB is compared to the energy densities of SSBs with dry polymer electrolytes from other reported works and the results are shown in **Figure 5.2f,g**. Clearly, our SSB has the highest energy density compared to the previous studies not only for the first cycle but also for the extensive cycles.

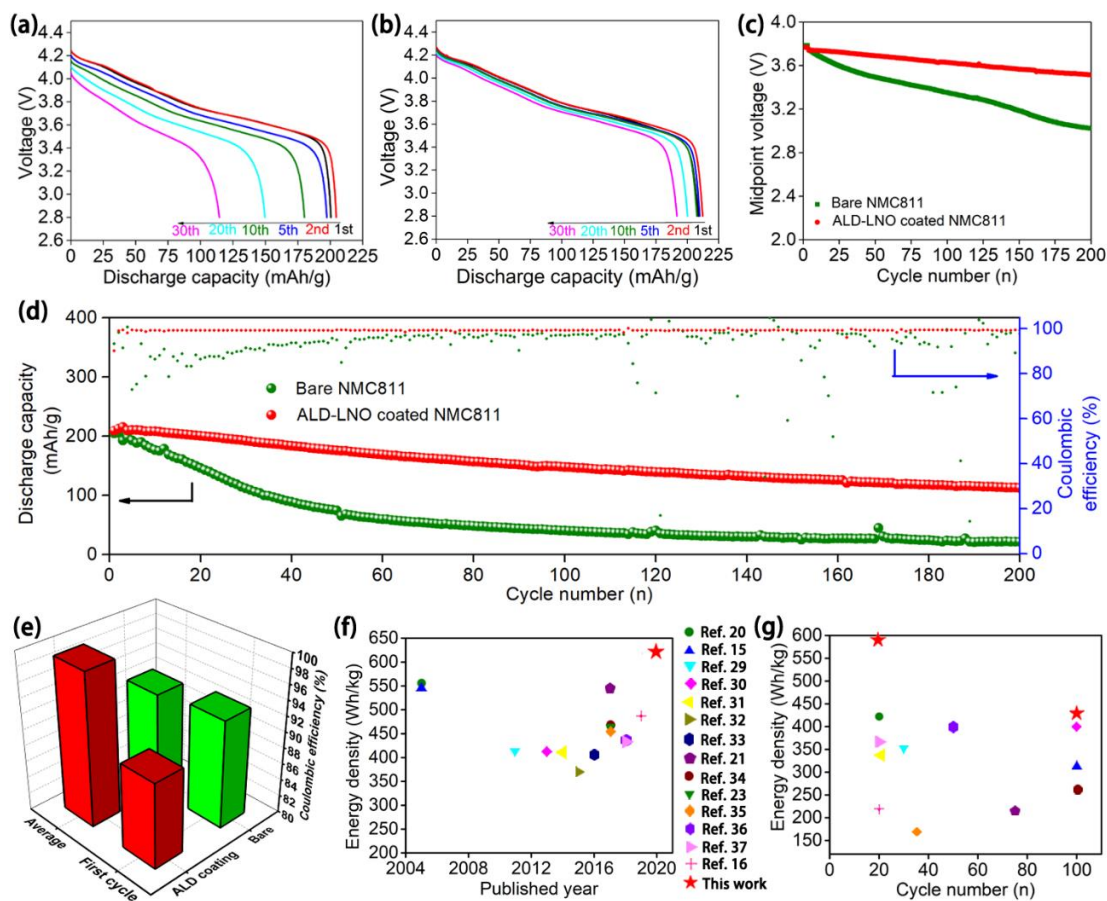
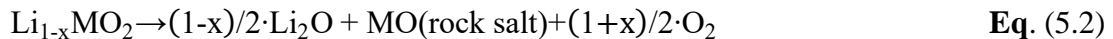
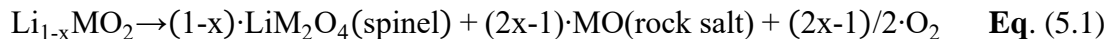


**Figure 5.2** Discharge voltage profiles of (a) Li/SPE/bare NMC811 SSB and (b) Li/SPE/ALD-LNO coated NMC811 SSB after different cycles. (c) The midpoint voltage evolution of the two SSBs over 200 cycles. (d) Comparison of long cycling performance of the Li/SPE/bare NMC811 SSB and the Li/SPE/ALD-LNO coated NMC811 SSB. The cycling performance was evaluated by galvanostatic discharge/charge cycling at a current of 0.2 C at 60 °C. (e) Comparison of the first-cycle Coulombic efficiency and average Coulombic efficiency of 200 cycles for the SSBs with or without ALD-LNO coating. (f) Comparison of the energy density of 4 V class cathodes in SSBs with dry SPE published in different years at the first cycle, and (g) the energy density after different

cycles.<sup>15,16,20,21,23,29-37</sup> The energy density was calculated based on the cathode only due to the limited data about the thicknesses/weights of anode and SPE.

Ni-rich NMC811 cathode materials are well known to be unstable upon charging/discharging cycles not only at liquid-based batteries but also in solid-state polymer batteries.<sup>12,16</sup> The performance fading of Ni-rich cathode materials is intimately related to the chemomechanical degradation such as the crack<sup>12,16,38</sup> and the surface reconstruction.<sup>10</sup> The role of ALD-LNO coating in enhancing the cycling stability of NMC811 electrodes in PEO based SSBs was studied comprehensively by focused ion beam (FIB), STEM, SEM, synchrotron based XAS.

The cycled NMC811 particles were collected from SSBs and cut by FIB for structural and morphological analyses. STEM image and corresponding EDX elemental mappings for the bare NMC811 are shown in **Figure 5.3a-d**. The bare NMC811 particle exhibited severe intergranular and intragranular cracks after 50 charge/discharge cycles in SSBs at 60 °C (**Figure 5.3a** and **b**), which is consistent with the reported results.<sup>16,39</sup> The significant mechanical cracks were possibly a combined consequence of the internal pressure resulting from material phase heterogeneity and oxygen release.<sup>39</sup> The deep delithiation and lithiation processes under 60 °C can trigger the surface phase reconstruction by the transition of the layered structure to spinel phases and rock-salt phases with the release of oxygen (**Eq. 5.1, 5.2**).<sup>39</sup>



Where M = Mn, Co, and Ni, and x is the extracted lithium ( $0 < x < 1$ ).

The intercalation/deintercalation of NMC811 resulting in inhomogeneous lithium distribution causes mismatched chemical strain, leading to stress concentration near the crack tip and grain boundary. The released oxygen was trapped in the cracking gap, resulting in big driving force for intergranular/intragranular cracking. Surprisingly, with ALD-LNO coating, surface chemistry of NMC811 is changed and the surface phase reconstruction process is inhibited. As a result, no intergranular or intragranular cracks

were found (**Figure 5.3c** and d), indicating that ALD-LNO coating can significantly enhance the stability of NMC811 cathode particles during long charge/discharge cycles. Presumably, the ALD-LNO coating inhibited the surface phase reconstruction for the formation of spinel and rock-salt phases, eliminated the chemical strain caused by inhomogeneous lithium distribution and the oxygen release, maintaining grain boundary contact, thus enhancing the cycling stability of SSBs. Similar results were obtained from SEM observations (**Figure S5.7**).

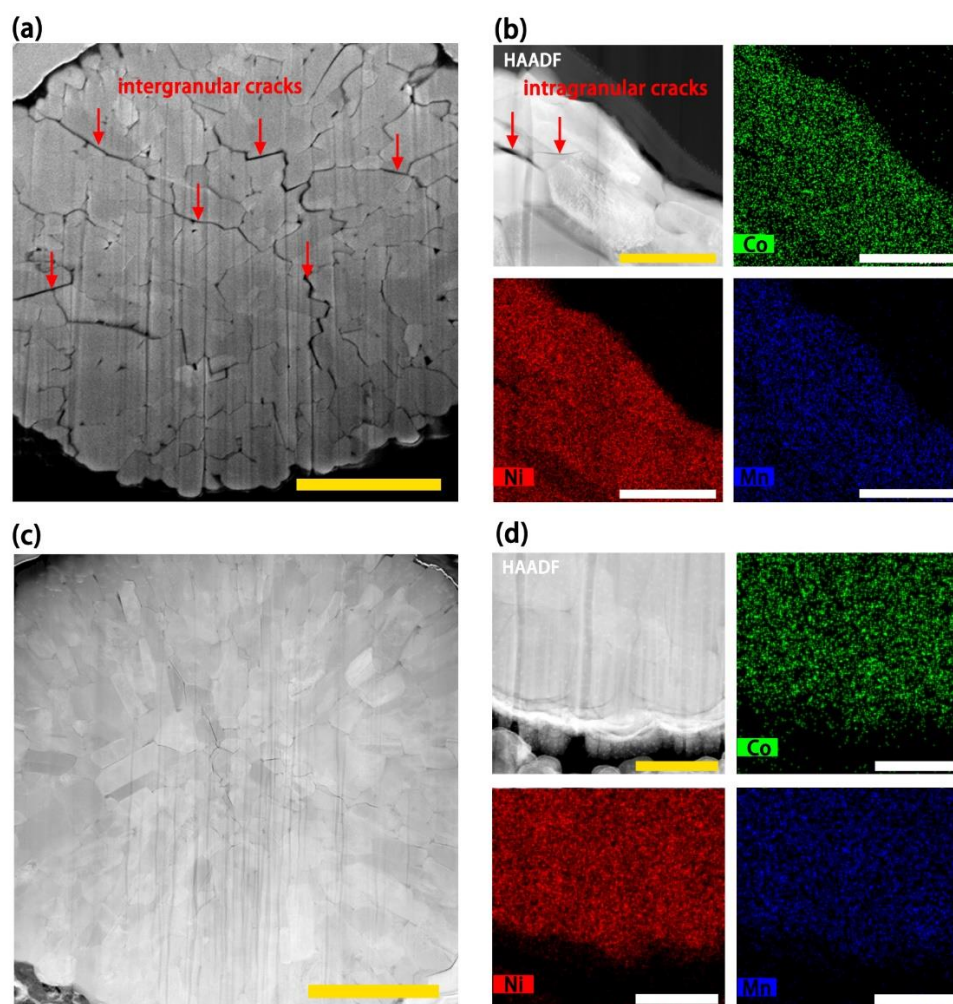


**Figure 5.3** STEM image of (a) a NMC811 secondary particle after 50 cycles of charge/discharge and corresponding (b) STEM-HAADF image and STEM-EDX mappings. (c) ALD-LNO coated NMC811 particles after 50 cycles of charge/discharge and

(d) STEM-HAADF image and STEM-EDX mappings. Scale bars are 2  $\mu\text{m}$  for (a) and (c), 400 nm for (b) and (d).

Synchrotron-based soft XAS was conducted to study the variation of surface chemical properties of NMC811 after charge/discharge and the results are presented in **Figure 5.4**. Spectra were collected at two detection modes (TEY and FYL) simultaneously on the pristine electrode surface and cycled electrodes surfaces with or without ALD-LNO coating at discharge state. The valence state of the Ni can be evaluated by the ratio of two splits (low energy state and high energy state, which are marked as peaks A and B, respectively in **Figure 5.4a, b**) of  $L_3$  edge in the Ni L-edge XAS spectra.<sup>40,41</sup> The ratio of B/A is positively related to the Ni valence state. **Figure 5.4a** and c are the Ni L-edge XAS TEY and FLY spectra of bare NMC811, ALD-LNO coated NMC811, bare NMC811 after cycling and ALD-LNO coated NMC811 electrodes after cycling at SSBs with PEO-based SPE, respectively. The spectra exhibited similar features in TEY and FLY modes. However, the ratio of B/A of  $L_3$  splits were clearly different among these samples as shown in **Figure 5.4b** and d. For TEY information (**Figure 5.4b**), the bare NMC811 sample showed the lowest B/A value indicating low oxidation of Ni in pristine NMC811. For bare NMC811 electrode after cycling at the discharge state, the B/A ratio showed a significant increase compared to that of pristine NMC811 sample, indicating the Ni oxidation state is higher than that of pristine NMC811. In other word, there is higher Ni oxidation state phases such as spinel  $\text{LiM}_2\text{O}_4$ , or  $\text{NiO}_2$  formation at the surface of particle, consistent with the surface phase reconstruction result from STEM studies. The ALD-LNO coated NMC811 showed very high B/A ratio, which was probably due to the interaction between NMC811 particle surface and ALD precursor ( $\text{H}_2\text{O}$ ). While NMC811 electrode with ALD-LNO coating shows less increase in the B/A ratio after cycling at discharge state compared to bare NMC811 electrode after cycling, which means ALD-LNO coating can enhance the reversibility of NMC811 particles. For FLY information, the bare NMC811 electrode, LNO coating NMC811 electrode and ALD-LNO coated NMC811 electrode after cycling at discharge state showed almost the same vale of B/A ratio (**Figure 5.4d**), which means ALD-LNO coating material only interact with NMC811 particles surface not into the bulk, and ALD-LNO coated NMC811 electrode showed high reversibility in the bulk NMC811 particle during charge/discharge cycling. Differently, bare NMC811 electrode after cycling

presented much higher B/A ratio compared to pristine NMC 811 electrode, which indicated poor reversibility of bare NMC811 cathode upon cycling not only at the surface but also in the bulk.

In summary, STEM, SEM, and XAS analyses disclosed the instability of NMC811 electrode in PEO-based SSBs, but the ALD-LNO coating can effectively enhance stability of NMC811 upon long cycles. Co and Mn XAS under FLY mode were also obtained (**Figure S5.8-S5.9**). The Co and Mn XAS spectra of these four samples showed no obvious difference. These results are consistent with the report by X. Liu et al., who found that the oxidation states of Co and Mn were unchanged in Ni-rich cathode with PEO-based SPE.<sup>41</sup>

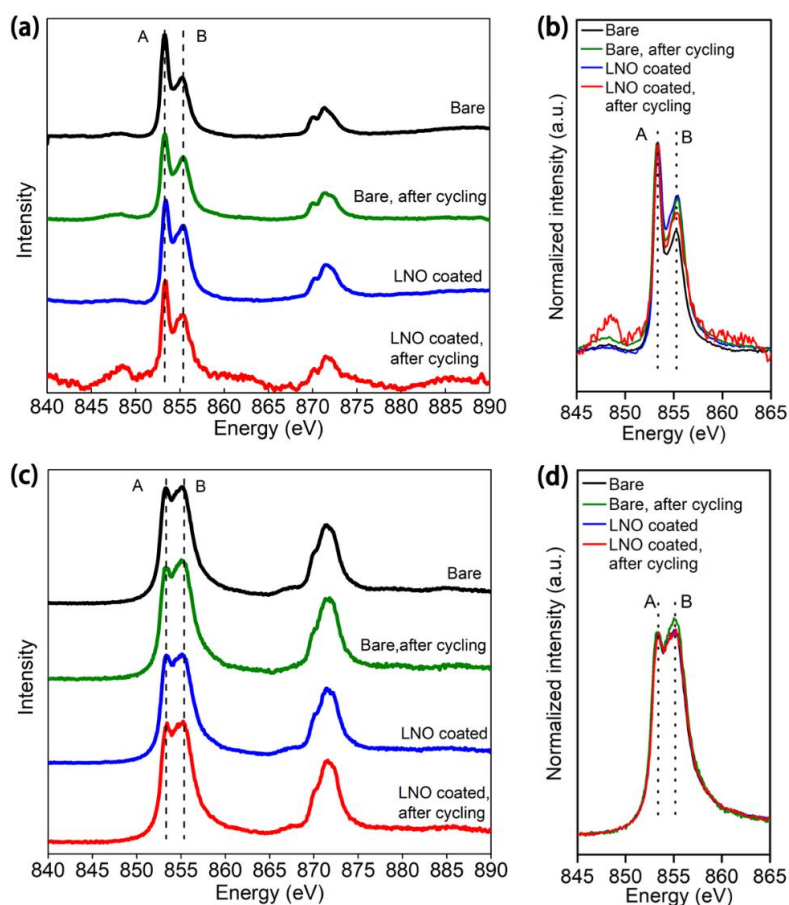


**Figure 5.4** Ni L<sub>3</sub>-edge synchrotron-based XAS at TEY mode (a, b) and FLY mode (c, d) for bare NMC811 and ALD-LNO coated NMC811 electrodes before/after 5 charge/discharge cycle at discharge state. (b), (d) Normalized peak A intensity in comparison with varied peak B intensity.



PEO-based SPE is known to be unstable under high voltage ( $> 3.8$  V).<sup>13</sup> Therefore, the effects of ALD-LNO coating on the interfacial stability between NMC811 electrode and SPE were analyzed by X-ray photoelectron spectroscopy (XPS) and electrochemical impedance spectroscopy (EIS). XPS C K-edge results of bare NMC811 electrode, and ALD-LNO coated NMC811 electrode before and after 5 cycles charge/discharge at discharge state are shown in **Figure 5.5a-c**, respectively. The C 1s XPS spectrum of bare NMC811 electrode (**Figure 5.5a**) showed the peaks of C=C at 284.3 eV, C-C(C-H) at 284.8 eV, C-OH (C-O-C) at 286.0 eV, and CF<sub>2</sub> at 290.5 eV.<sup>42,43</sup> An increase in the C-OH (C-O-C) (286.0 eV) peak intensity and area was observed in bare NMC811 electrode (**Figure 5.5b**) and ALD-LNO coating NMC811 electrode (**Figure 5.5c**) after being cycled in SPE-based SSBs, which was attributed the adhesion of PEO-based SPE on the surface of NMC811 electrode after SPE being peeled off from the electrodes. A new peak corresponding to O-C=O group (288.8 eV)<sup>42</sup> emerged in bare NMC811 electrode (**Figure 5.5b**). PEO has repeating units of  $-(\text{O}-\text{CH}_2-\text{CH}_2)-$ , where there was no O-C=O group in pristine PEO. This O-C=O peak can be attributed to the decomposition of SPE, as supported by the previous theoretical studies and the nuclear magnetic resonance (NMR) studies which showed that the decomposed products of PEO contain O-C=O group.<sup>44-46</sup> The decomposition of SPE at the NMC811 electrode/SPE interface can form an instable cathode electrolyte interface (CEI), and result in low coulombic efficiency (**Figure 5.2d**) and high cell internal resistance, which was consistent with the EIS results (**Figure S5.10a**). The overall cell resistance of bare NMC811 SSB was over 4 K $\Omega$  after 30 cycles of charge/discharge and increased to around 10 K $\Omega$  after 200 cycles of charge/discharge (**Figure S5.10a**). The continue increase of cell impedance is the result of accumulated decomposed products from SPE at the interface. With ALD-LNO coating, the C 1s spectrum shows no O-C=O peak, which means ALD-LNO coating on NMC811 electrode surface can effectively palliate the decomposition of PEO-based SPE. This is also supported by the EIS study of ALD-LNO coated NMC811 SSB after different cycling (**Figure S5.10b**). The over-all resistance of ALD-LNO coated NMC811 SSB after 30 cycles was about 1.5 k $\Omega$ , which was lower than half of the bare NMC811 SSB. After 200 cycles, the overall resistance was slightly increase to 2.8 k $\Omega$ , lower a quarter than that of the bare NMC811 SSB.

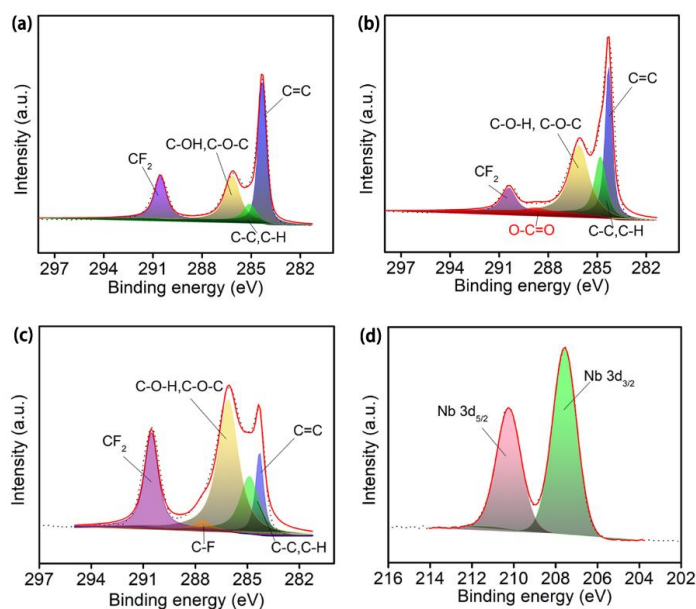


**Figure 5.5** XPS C 1s spectra of (a) bare NMC811 electrode, (b) bare NMC811 electrode after 5 charge/discharge cycles at the discharge state, and (c) ALD-LNO coated NMC811 electrode after 5 charge/discharge cycles at the discharge state. (d) XPS spectrum of Nb 3d of ALD-LNO coated NMC811 electrode after 5 charge/discharge cycles at discharge state.

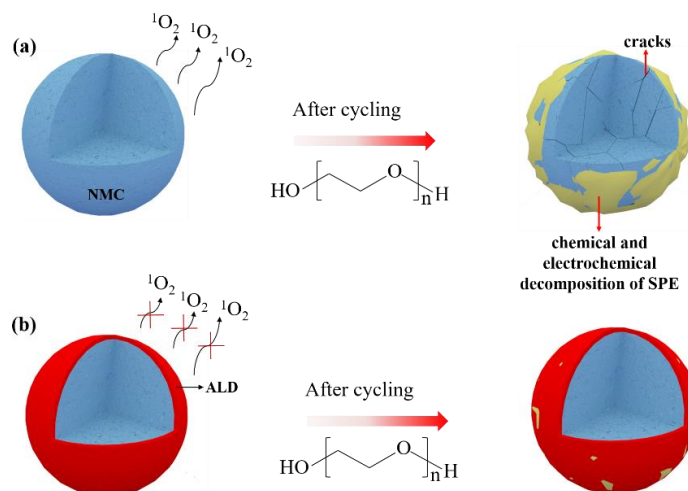


**Figure 5.6** Schematically showing the ALD-LNO coating effect on the NMC811 SSBs with PEO-based SPE. (a) bare NMC811 particle. Crack emerged in the NMC811 particle after cycling, along with oxygen released, triggering the severe chemical decomposition of SPE.<sup>46</sup> The decay of NMC811 particle, chemical decomposition of SPE and the electrochemical decomposition of SPE result in an unstable CEI in SSBs; (b) ALD-LNO

coated NMC811 particle. ALD-LNO coated NMC811 particle preserves structural integrity and without/with less oxygen release, and alleviated SPE decomposition.

Combining the XPS, STEM results and previous study,<sup>10,39,47</sup> bare Ni-rich NMC active material undergo phase transition of the layered structure to the rock-salt phase after charging/discharging, which will release peroxo-like oxygen species or singlet oxygen ( $^1\text{O}_2$ ),<sup>47,48</sup> which is in a quantum state where all electrons are spin paired and is kinetically unstable at ambient temperature. The singlet oxygen or peroxo-like oxygen is very strong oxidant for PEO-based SPE, they will trigger the decomposition of SPE similar to its effect to trigger the decomposition of liquid organic electrolyte.<sup>49,50</sup> Therefore, (1) the chemomechanical degradations of NMC811 active materials along with (2) the oxygen release triggering the chemical decomposition of PEO-based SPE,<sup>46</sup> (3) the electrochemical decomposition of PEO-based SPE at high voltage charge process SPE would be the three main reasons for the serious performance decay of Ni-rich NMC811 SSBs. The ALD-LNO coating can effectively inhibit the surface reconstruction of NMC811, thus reduce the oxygen release, creating a friendly operation environment for PEO-based SPE. Moreover, the low electronic LNO coating layer can reduce the electrochemical decomposition of PEO-based at high voltage. As a result of this, ALD-LNO coating helps the NMC811 SSBs achieve a stable long cycling performance. **Figure 5.6** schematically illustrate the ALD coating mechanism for improving the electrochemical performance of NMC811 SSBs.

## 5.4 Conclusions

In conclusion, ALD derived LNO was applied for enhancing the electrochemical performance of SSBs with PEO-based SPE and Ni-rich NMC811 cathode for high energy density. The role of ALD-LNO coating on NMC811 electrode surface was disclosed by STEM, SEM, XAS, and XPS. The results showed that ALD-LNO coating can (i) stabilize the NMC811 active materials by preventing them from chemomechanical degradation upon cycling, and inhibit the oxygen release, and (ii) minimize the chemical oxidation and electrochemical decomposition of PEO-based SPE under high voltage charge/discharge processes. The stabilized NMC811 active materials and SPE/cathode interface rendered a stable and high performance SSB. This study provides a strategy for stabilizing Ni-rich

cathode in solid polymer batteries and inhibiting/ameliorating the decomposition of SPE, lighting up the way toward next-generation safe and high energy density ASSLIBs.

## Acknowledgement

This work was supported by China Automotive Battery Research Institute, Natural Sciences and Engineering Research Council of Canada (NSERC), Canada Research Chair Program (CRC), the Canada Light Source (CLS) and University of Western Ontario. We also appreciate the helps from the beamline scientists of the Spherical Grating Monochromator (SGM) beamline at Canadian Light Source, Dr. Tom Regier, Dr. James Dynes and Dr. Zechary Arthur. Electron microscopy work is performed by the Center for Functional Nanomaterials, which is a U.S. DOE Office of Science Facility, at Brookhaven National Laboratory under Contract No. DE-SC0012704.

## References

1. J. W. Choi and D. Aurbach, *Nat. Rev. Mater.*, 2016, 1, 16013.
2. X.-B. Cheng, R. Zhang, C.-Z. Zhao and Q. Zhang, *Chem. Rev.*, 2017, 117, 10403-10473.
3. P. G. Bruce, S. A. Freunberger, L. J. Hardwick and J.-M. Tarascon, *Nat. Mater.*, 2012, 11, 19.
4. Z. Xue, D. He and X. Xie, *J. Mater. Chem. A*, 2015, 3, 19218-19253.
5. J. W. Fergus, *J. Power Sources*, 2010, 195, 939-954.
6. H. Yoshizawa and T. Ohzuku, *J. Power Sources*, 2007, 174, 813-817.
7. B. Xiao, H. Liu, J. Liu, Q. Sun, B. Wang, K. Kaliyappan, Y. Zhao, M. N. Banis, Y. Liu, R. Li, T.-K. Sham, G. A. Botton, M. Cai and X. Sun, *Adv. Mater.*, 2017, 29, 1703764.
8. N. Nitta, F. Wu, J. T. Lee and G. Yushin, *Mater. Today*, 2015, 18, 252-264.
9. S.-T. Myung, F. Maglia, K.-J. Park, C. S. Yoon, P. Lamp, S.-J. Kim and Y.-K. Sun, *ACS Energy Lett.*, 2016, 2, 196-223.
10. F. Lin, I. M. Markus, D. Nordlund, T.-C. Weng, M. D. Asta, H. L. Xin and M. M. Doeff, *Nat. Commun.*, 2014, 5, 3529.
11. P. Rozier and J. M. Tarascon, *J. Electrochem. Soc.*, 2015, 162, A2490-A2499.

12. P. Yan, J. Zheng, J. Liu, B. Wang, X. Cheng, Y. Zhang, X. Sun, C. Wang and J.-G. Zhang, *Nat. Energy*, 2018, 3, 600-605.
13. Y. Xia, T. Fujieda, K. Tatsumi, P. P. Prosini and T. Sakai, *J. Power Sources*, 2001, 92, 234-243.
14. P. Hovington, M. Lagacé, A. Guerfi, P. Bouchard, A. Mauger, C. M. Julien, M. Armand and K. Zaghib, *Nano Lett.*, 2015, 15, 2671-2678.
15. H. Miyashiro, Y. Kobayashi, S. Seki, Y. Mita, A. Usami, M. Nakayama and M. Wakihara, *Chem. Mater.*, 2005, 17, 5603-5605.
16. M. n. M. Besli, S. Xia, S. Kuppan, Y. Huang, M. Metzger, A. K. Shukla, G. Schneider, S. Hellstrom, J. Christensen and M. M. Doeff, *Chem. Mater.*, 2018, 31, 491-501.
17. B. Xiao and X. Sun, *Adv. Energy Mater.*, 2018, 8, 1802057.
18. W. Zhao, J. Zheng, L. Zou, H. Jia, B. Liu, H. Wang, M. H. Engelhard, C. Wang, W. Xu and Y. Yang, *Adv. Energy Mater.*, 2018, 1800297.
19. F. Lin, D. Nordlund, Y. Li, M. K. Quan, L. Cheng, T.-C. Weng, Y. Liu, H. L. Xin and M. M. Doeff, *Nat. Energy*, 2016, 1, 15004.
20. S. Seki, Y. Kobayashi, H. Miyashiro, Y. Mita and T. Iwahori, *Chem. Mater.*, 2005, 17, 2041-2045.
21. J. Ma, Z. Liu, B. Chen, L. Wang, L. Yue, H. Liu, J. Zhang, Z. Liu and G. Cui, *J. Electrochem. Soc.*, 2017, 164, A3454-A3461.
22. J. Liang, Y. Sun, Y. Zhao, Q. Sun, J. Luo, F. Zhao, X. Lin, X. Li, R. Li, L. Zhang, S. Lu, H. Huang and X. Sun, *J. Mater. Chem. A*, 2020, 8, 2769-2776.
23. Y. Kobayashi, K. Shono, T. Kobayashi, Y. Ohno, M. Tabuchi, Y. Oka, T. Nakamura and H. Miyashiro, *J. Power Sources*, 2017, 341, 257-263.
24. C. Wang, T. Wang, L. Wang, Z. Hu, Z. Cui, J. Li, S. Dong, X. Zhou and G. Cui, *Adv. Sci.*, 2019, 6, 1901036.
25. J. Xie, A. D. Sendek, E. D. Cubuk, X. Zhang, Z. Lu, Y. Gong, T. Wu, F. Shi, W. Liu and E. J. Reed, *ACS nano*, 2017, 11, 7019-7027.
26. M. Chen, E. Zhao, D. Chen, M. Wu, S. Han, Q. Huang, L. Yang, X. Xiao and Z. Hu, *Inorg. Chem.*, 2017, 56, 8355-8362.
27. W. Cho, Y. J. Lim, S.-M. Lee, J. H. Kim, J.-H. Song, J.-S. Yu, Y.-J. Kim and M.-S. Park, *ACS Appl. Mater. Interfaces*, 2018, 10, 38915-38921.

28. B. Wang, Y. Zhao, M. N. Banis, Q. Sun, K. R. Adair, R. Li, T.-K. Sham and X. Sun, *ACS Appl. Mater. Interfaces*, 2018, 10, 1654-1661.
29. D. Zhang, H. Yan, Z. Zhu, H. Zhang, J. Wang and Qilu, *J. Power Sources*, 2011, 196, 10120-10125.
30. T. Kobayashi, Y. Kobayashi, M. Tabuchi, K. Shono, Y. Ohno, Y. Mita and H. Miyashiro, *ACS Appl. Mater. Interfaces*, 2013, 5, 12387-12393.
31. K. Chen, Y. Shen, J. Jiang, Y. Zhang, Y. Lin and C.-W. Nan, *J. Mater. Chem. A*, 2014, 2, 13332-13337.
32. J.-H. Choi, C.-H. Lee, J.-H. Yu, C.-H. Doh and S.-M. Lee, *J. Power Sources*, 2015, 274, 458-463.
33. J. Zhang, N. Zhao, M. Zhang, Y. Li, P. K. Chu, X. Guo, Z. Di, X. Wang and H. Li, *Nano Energy*, 2016, 28, 447-454.
34. S. Seki, *ChemistrySelect*, 2017, 2, 3848-3853.
35. Y. Lin, Y. Cheng, J. Li, J. D. Miller, J. Liu and X. Wang, *RSC Adv.*, 2017, 7, 24856-24863.
36. Q. Yang, J. Huang, Y. Li, Y. Wang, J. Qiu, J. Zhang, H. Yu, X. Yu, H. Li and L. Chen, *J. Power Sources*, 2018, 388, 65-70.
37. K. Karthik and R. Murugan, *J. Solid State Electrochem.*, 2018, 22, 2989-2998.
38. Y. Makimura, S. Zheng, Y. Ikuhara and Y. Ukyo, *J. Electrochem. Soc.*, 2012, 159, A1070-A1073.
39. P. Yan, J. Zheng, T. Chen, L. Luo, Y. Jiang, K. Wang, M. Sui, J.-G. Zhang, S. Zhang and C. Wang, *Nat. Commun.*, 2018, 9, 2437.
40. J. Xu, E. Hu, D. Nordlund, A. Mehta, S. N. Ehrlich, X.-Q. Yang and W. Tong, *ACS Appl. Mater. Interfaces*, 2016, 8, 31677-31683.
41. X. Liu, D. Wang, G. Liu, V. Srinivasan, Z. Liu, Z. Hussain and W. Yang, *Nat. Commun.*, 2013, 4, 2568.
42. T. Dong, J. Zhang, G. Xu, J. Chai, H. Du, L. Wang, H. Wen, X. Zang, A. Du, Q. Jia, X. Zhou and G. Cui, *Energy Environ. Sci.*, 2018, 11, 1197-1203.
43. J. Lee and W. Choi, *J. Electrochem. Soc.*, 2015, 162, A743-A748.
44. O. A. Mkhatresh and F. Heatley, *Macromol. Chem. Phys.*, 2002, 203, 2273-2280.
45. O. A. Mkhatresh and F. Heatley, *Polym. Int.*, 2004, 53, 1336-1342.

46. P. de Sainte Claire, *Macromolecules*, 2009, 42, 3469-3482.
47. J. Wandt, A. T. S. Freiberg, A. Ogrodnik and H. A. Gasteiger, *Mater. Today*, 2018, 21, 825-833.
48. H. Wang, E. Rus, T. Sakuraba, J. Kikuchi, Y. Kiya and H. D. Abruña, *Anal. Chem.*, 2014, 86, 6197-6201.
49. R. Jung, M. Metzger, F. Maglia, C. Stinner and H. A. Gasteiger, *J. Electrochem. Soc.*, 2017, 164, A1361-A1377.
50. A. T. S. Freiberg, M. K. Roos, J. Wandt, R. de Vivie-Riedle and H. A. Gasteiger, *J. Phys. Chem. A*, 2018, 122, 8828-8839.

## Supporting information

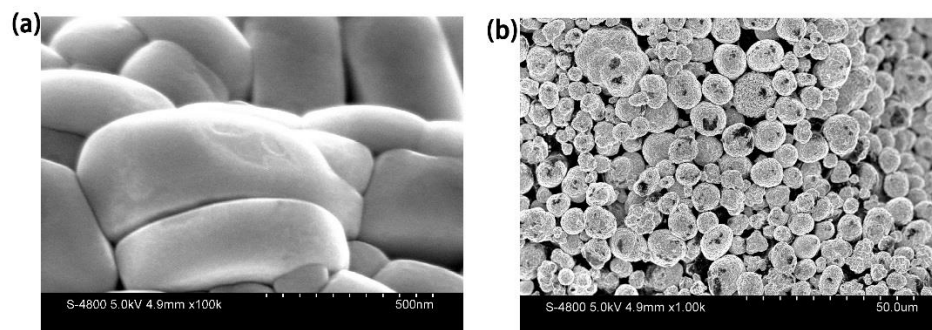


**Figure S5.1** SEM images of pristine (a) NMC811 primary particles and (b) secondary particles

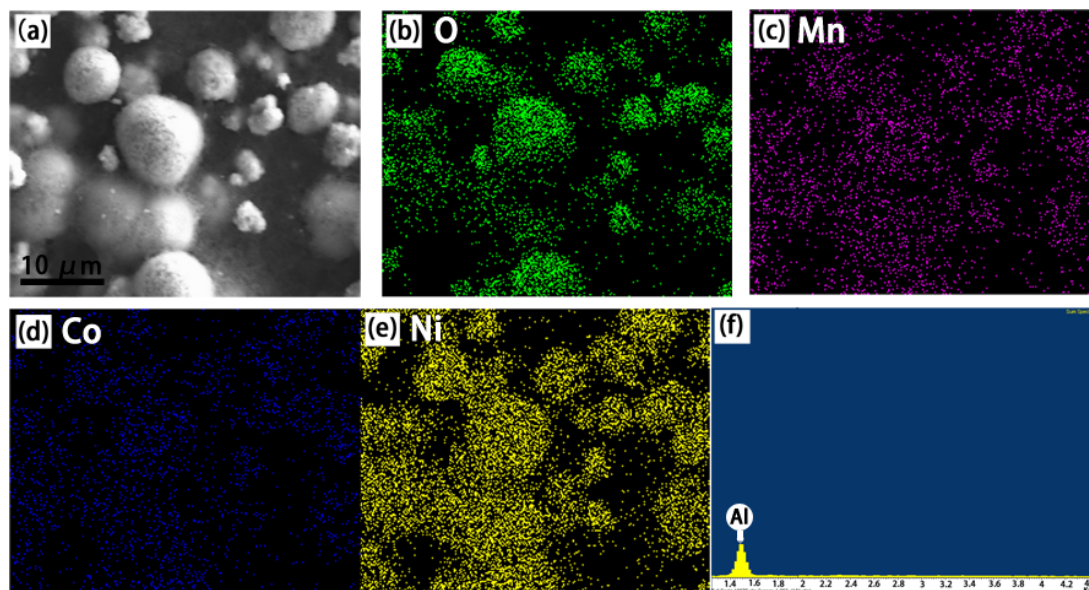


**Figure S5.2** Characterization of bare NMC811 electrode (a) SEM image of NMC811 particles and (b)-(e) O, Mn, Co, Ni EDX mapping. (f) EDX spectrum on selected energy area. Al signal is originated from a Al foil working as a current collector.



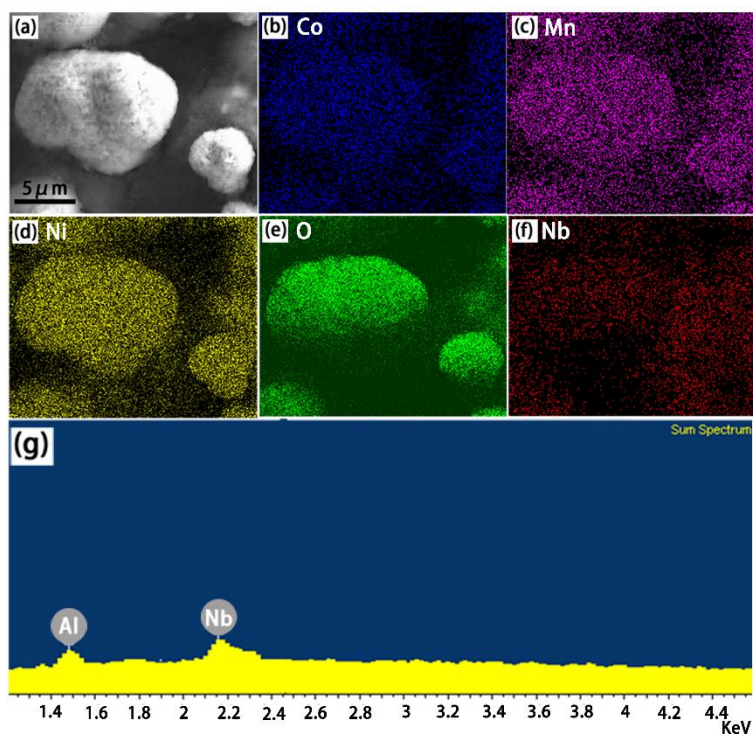


**Figure S5.3** Characterization of LNO coating on NMC811 electrode (a) SEM image of NMC811 particles with 50 cycles ALD-LNO coating and (b)-(f) Co, Mn, Ni, O and Nb EDX mapping, and (g) EDX spectrum on selected energy area.

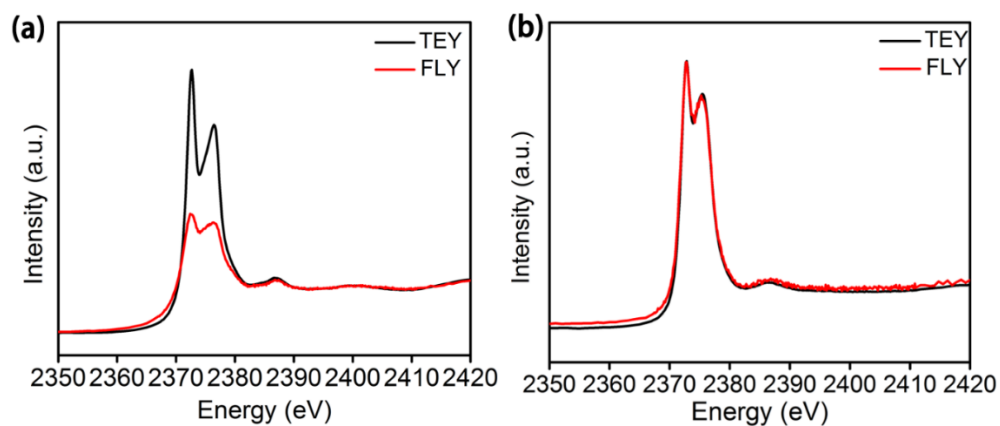


**Figure S5.4** XAS in TEY and FLY mode of (a) standard  $\text{LiNbO}_3$ ; (b) ALD-LNO.

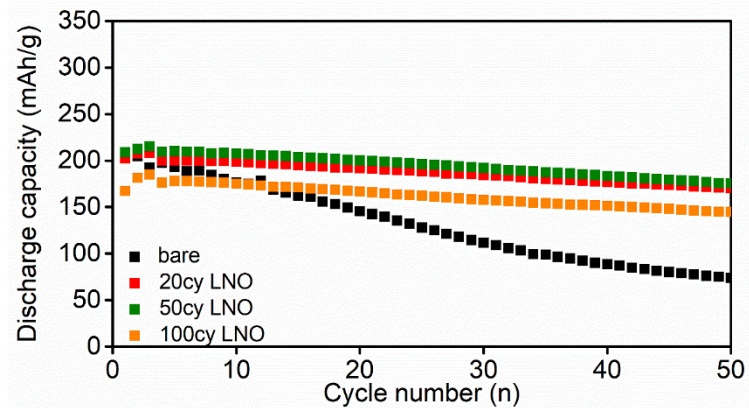


**Figure S5.5** The effects of ALD-LNO coating thickness on the performance of NMC811 SSBs.

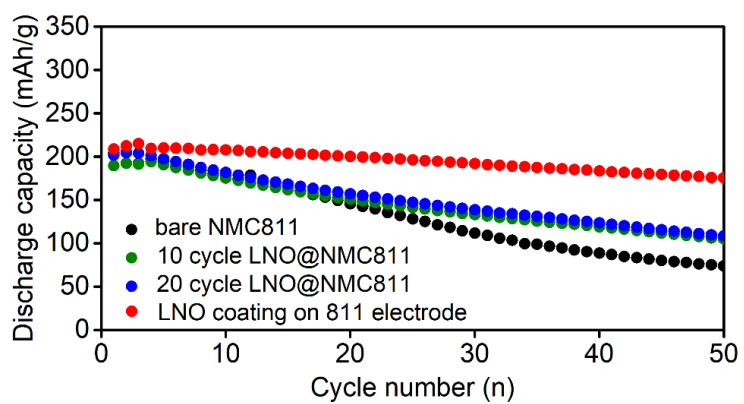


**Figure S5.6** The effects of ALD-LNO coating on particles and on electrode.

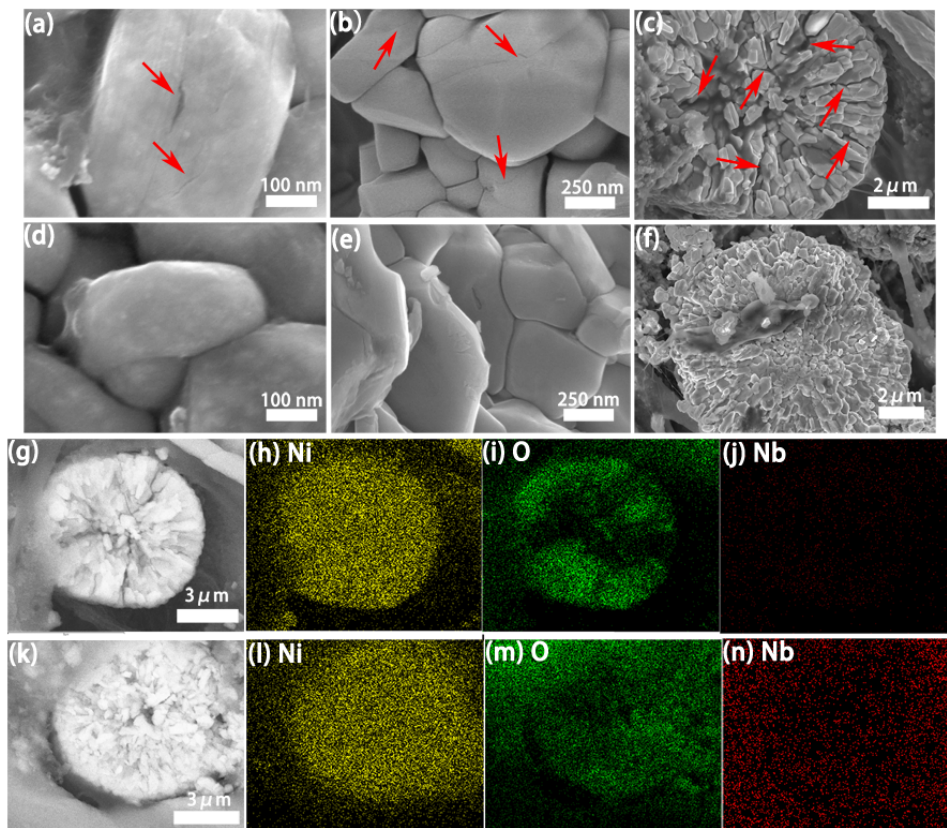


**Figure S5.7** SEM images and EDX mapping of NMC811 particles after 200 cycles of charge/discharge at solid-state batteries (SSBs) with PEO-based solid polymer electrolyte (SPE). (a)-(b) High magnitude SEM image of NMC811 primary particle and (c) low magnitude SEM image of NMC811 secondary particle after 200 cycles of charge/discharge at SSBs. (d)-(e) High magnitude SEM image of LNO coating NMC811 primary particle and (f) low magnitude SEM image of NMC811 secondary particle after 200 cycles of charge/discharge at SSBs. (The SEM images are obtained under 5 KV, 15 mA). (g) SEM image of NMC811 secondary particle after 200 cycles of charge/discharge at SSBs. (The SEM image is obtained under 20 KV, 15 mA), and its corresponding EDX mapping of (h)Ni, (i)O, (j)Nb. (k) SEM image of LNO coating NMC811 secondary particle after 200 cycles of charge/discharge at SSBs. (The SEM image is obtained under 20 KV, 15 mA), and its corresponding EDX mapping of (h)Ni, (i)O, (j)Nb.

SEM images of NMC811 particles after 200 cycles charge/discharge show obviously cracked particles (Figure S5.7a-c, g), which is consistent with the reported results.<sup>16</sup> The

reason for the crack is not fully clear. It is suggested that the lattice breathing, anisotropic volume change during cycling, the release of the oxygen, the phase transformation and surface reconstruction may be possibly responsible to the crack arise. Surprisingly, the NMC811 in the electrode with ALD-LNO coating show almost not cracking in the particles (Figure S5.7d-f, k), indicating the LNO can enhance the stability of NMC811 cathode particles.

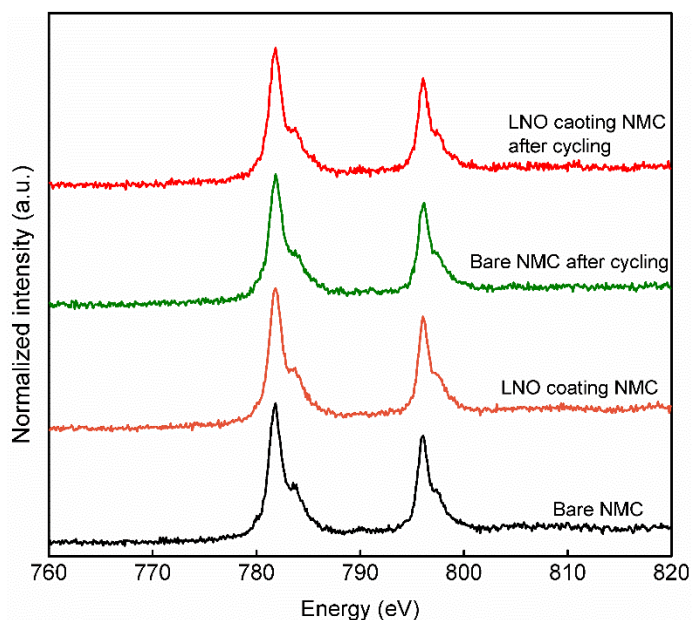


**Figure S5.8** Co XAS under FLY mode of bare NMC 811 electrode, LNO coating NMC811 electrode, bare NMC811 electrode after 5 cycles of charge/discharge at discharge state and LNO coating NMC811 electrode after 5 cycles of charge/discharge at discharge state.

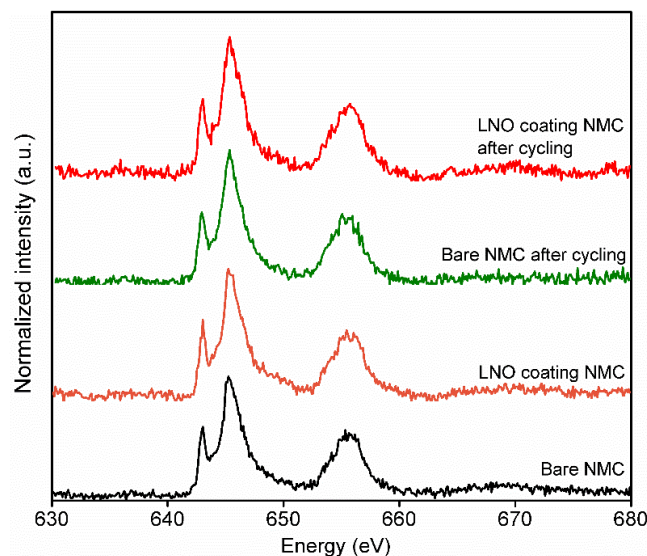


**Figure S5.9** Mn XAS under FLY mode of bare NMC 811 electrode, LNO coating NMC811 electrode, bare NMC811 electrode after 5 cycles of charge/discharge at discharge state and LNO coating NMC811 electrode after 5 cycles of charge/discharge at discharge state.

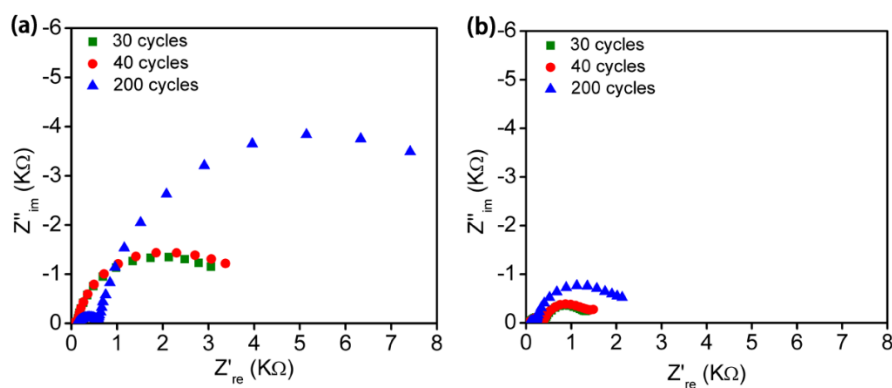


**Figure S5.10** Comparisons of the cell overall resistance at after 30, 40 and 200 cycles of charge/discharge at 60 °C. (a) bare NMC811 SSB. (b) ALD LNO coating NMC811 SSB.

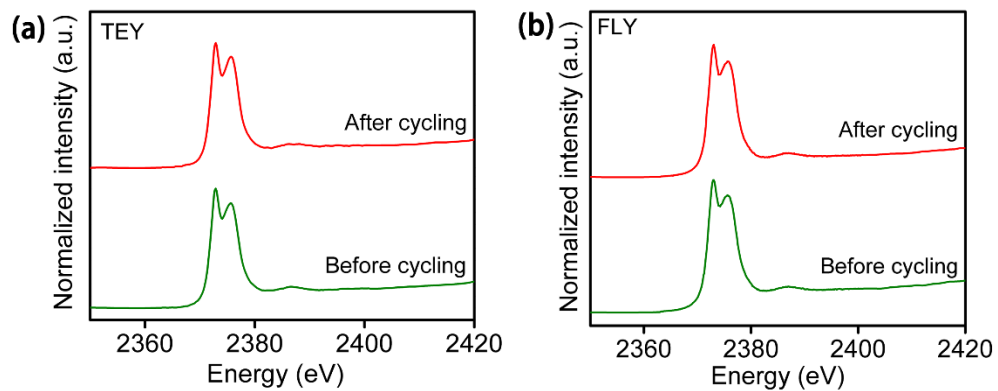


**Figure S5.11** Nb synchrotron based XAS at  $L_3$  edge at (a) TEY mode and (FLY) mode.

## Chapter 6

### 6 A facile method for enhancing the electrochemical oxidation window of PEO-based solid-polymer electrolytes

In the previous two chapters, the interfacial engineering by ALD derived materials was conducted to enhance the performance of ASSLIBs. However, the intrinsic problem, the low electrochemical oxidation window of PEO-based SPEs, is not solved if only interfacial engineering is used.

In this study, PEO-based SPEs are prepared by dimethylformamide (DMF) and acetonitrile (AN) solvent, respectively, for ASSLIBs with a 4 V class cathode. The PEO-based SPE prepared by DMF coupling with LiCoO<sub>2</sub> ASSLIBs deliver excellent cycling performance with 84 % capacity retention after 150 cycles. NMR spectrum of PEO-based SPEs prepared by DMF and AN indicates these SPEs have different end group in PEO chain. Via (DFT) calculation, it is disclosed that DMF modified end group of PEO has higher stability than that of regular OH end group PEO, consistent well which is consistent with the electrochemical stability testing results from LSV. Synchrotron-based XAS results and EIS studies indicate that PEO-based SPEs prepared by DMF have a more stable interface with LiCoO<sub>2</sub>, compared to PEO-based SPEs prepared by AN, due to their higher electrochemical stability at high voltage. This study provides a novel strategy for enhancing the electrochemical oxidation window of PEO-based SPEs, paving the way for developing high performance, high energy density solid polymer batteries.

---

**J. Liang**<sup>#</sup>, Andreas J. Achazi<sup>#</sup>, Q. Sun, K. Adair, Liam Israels, Y. Sun, R. Li, L. Zhang, S. Lu, H. Huang, P. Kaghazchi\*, and X. Sun\*, to be submitted.

<sup>#</sup> J. Liang and Andreas J. Achazi contributed equally to this work.

## 6.1 Introduction

The pursuit of safe and high energy density lithium ion batteries (LIBs) are receiving more and more research concerns due to the global energy risks, environmental pollution and the rapid increase in energy consumption and also because LIBs are green energy storage systems and they are promising candidates for replacing fossil fuels for the application in electric vehicles (EVs). However, current liquid-based LIB technologies suffer from serious safety issues related to the existence of liquid organic electrolyte, which is flammable and could potentially leak, resulting in safety concerns such as fire and explosion. Therefore, developing all-solid-state LIBs (ASSLIBs) is urgent and is regarded as the ultimate solution for safe and high energy density LIB systems. To realize ASSLIBs, many solid-state electrolytes (SSEs) including polymer-, oxide-, sulfide-, and halide-based ionic conductors have been heavily investigated as the separators in ASSLIBs.<sup>1-7</sup>

Among all the SSEs, polymer-based SSEs consisting of polyethylene oxide (PEO) complexing with lithium salt is one of the most promising SSEs for ASSLIBs. It has been commercialized in practical EVs with  $\text{LiFePO}_4$  as the cathode and lithium metal as the anode.<sup>8</sup> Therefore, PEO-based solid polymer electrolytes (SPEs) receive tremendous research concerns due to their capacity for EV applications.<sup>1-3,9,10</sup> PEO-based SPEs have many advantages such as a facile preparation process, low interfacial resistance towards electrode, low cost, and are environmentally-friendly. Unfortunately, the low ionic conductivity at room temperature and the low electrochemical oxidation window of PEO significantly limits its application in 4 V class high energy density cathodes, such as  $\text{LiCoO}_2$ , layer structure lithium nickel manganese cobalt oxide (NMC), and lithium nickel cobalt aluminum oxide.<sup>11-13</sup>

The low ionic conductivity at room temperature problem has received tremendous research interests and the approaches for addressing this challenge include (i) making hybrid electrolytes, (ii) adding plasticizer and (iii) searching for new polymer systems.<sup>2,9,14-16</sup> However, a few works were done to address the low electrochemical oxidation window problem for high voltage cathodes. To stabilize the SPE in 4 V class cathode systems, protecting the active materials with an inert coating layer is one of the promising strategies. The coating materials such as  $\text{Al}_2\text{O}_3$ ,  $\text{Li}_3\text{PO}_4$ , poly(ethylcyanoacrylate) and SSE



$\text{Li}_{1.4}\text{Al}_{0.4}\text{Ti}_{1.6}(\text{PO}_4)_3$ , have been studied for protecting  $\text{LiCoO}_2$  for the application in solid polymer batteries (SPBs).<sup>13, 17-19</sup> They showed that the coating method can improve the electrochemical performance of  $\text{LiCoO}_2$  SPBs to some extent. Our previous study showed that the conductive carbon in the  $\text{LiCoO}_2$  electrode is detrimental to the cycling performance of SPBs, because conductive carbon can accelerate the decomposition of the SPE at high voltage. By applying atomic layer deposition, a thin layer of lithium tantalite was coated on conductive carbon to protect the SPE/carbon interface. As a result of this, an enhanced cycling performance was achieved in all-solid-state  $\text{LiCoO}_2$  batteries.<sup>20</sup> Another strategy for stabilizing 4 V class SPBs is to pursue high voltage stable SPEs. As a good example, W. Zhou et al. develop a poly(N-methyl-malonic amide)-based SPE for high performance 4 V class SPBs by using this SPE at the cathode interface, and a PEO-based SPE at the anode interface. The poly(N-methyl-malonic amide)-based SPE is stable at high voltage to again electrochemical oxidation, but it is not stable toward the lithium anode, while the PEO-based SPE is stable toward the lithium anode but its electrochemical oxidation window is low. Therefore, the double layer structure SPE renders a high-performance SPB with a  $\text{LiCoO}_2$  cathode.<sup>21</sup> Even though these approaches can improve the performance of SPBs to some extent, the intrinsic problem, the low electrochemical oxidation window problem of PEO-based SPEs, does not change in all the cases.

Herein, a facile method for enhancing the electrochemical oxidation window of PEO-based SPEs was proposed. PEO-based SPEs prepared by DMF and AN (referred to as DMF-PEOSPE and AN-PEOSPE, respectively) are studied and applied in ASSLIBs. PEO-based SPEs prepared by DMF show very stable electrochemical performance in ASSLIBs with  $\text{LiCoO}_2$  as the cathode. After 150 charge/discharge cycles, the capacity retention for DMF-PEOSPE is 84 %, while only 50 % is achieved for AN-PEOSPE. The linear scan voltammetry (LSV) studies illustrated that DMF-PEOSPE has a higher oxidation window compared to AN-PEOSPE. By studying the structure of PEO polymer using  $^1\text{H}$  NMR, it is found that, when DMF is used as the solvent, the  $\text{CH}_3$  end-group of PEO is replaced by the dimethylamine group. This replacement makes the C-C bonds in PEO polymer more stable as indicated by the theoretical calculation result. The higher stability of DMF-PEOSPE could be the reason for the 4 V class ASSLIB's performance enhancement. The synchrotron-based X-ray absorption spectroscopy (XAS) results and electrochemical

impedance spectroscopy (EIS) studies indicate the DMF-PEOSPE/cathode interface is more stable than the AN-PEOSPE/cathode interface, which is consistent with the electrochemical performance results and LSV results. This facile approach shall give new insights about tailoring the chemical structure of PEO polymer for enhancing its electrochemical stability window for high performance, high energy density ASSLIBs.

## 6.2 Experimental

### 6.2.1 Preparation of PEO-based SPEs with different solvents

PEO (M.W. 1000,000) was firstly dried at 50 °C before use. The 0.6 g of PEO and 0.10 g of LiClO<sub>4</sub> (purity, 99.9 % stored in glovebox) were then added in to either 25 mL acetonitrile (AN) solvent or dimethylformamide (DMF) solvent and stirred at 70 °C for overnight. The mixtures were then cast in a Teflon substrate and the solvent slowly evaporated room temperature firstly for over-night, following by transferring to a 60 °C vacuum oven for 3 days. The obtain PEO-LiClO<sub>4</sub> SPEs membranes (label as AN-PEOSPE and DMF-PEOSPE) were then immediately transferred to an Ar-protected glovebox and left to rest for 3 days or longer before usage. For PEO-LITFSI SPEs, the same procedure was conducted but just replacing the LiClO<sub>4</sub> by LITFSI.

### 6.2.2 LiCoO<sub>2</sub> electrodes preparation

LiCoO<sub>2</sub> electrodes were prepared by mixing 90wt. % LiCoO<sub>2</sub> particles, 6 wt. % carbon-black (Acetylene Black), 6 wt.% binder polyvinylidene fluoride (PVDF) and N-Methyl-2-pyrrolidone (NMP) solvent to form a slurry. Then the slurry was cast on Al foil by doctor blade method. The sample was then dried at 100 °C in a vacuum oven for 12 h to obtain the LiCoO<sub>2</sub> cathode electrode.

### 6.2.3 Electrochemical performance testing

ASSLIBs were assembled in 2032 type coin cells in an Ar-protected glove box (Vacuum Atmosphere Company, moisture and oxygen level less than 1 ppm). LiCoO<sub>2</sub> electrode and lithium foils were used as the working electrode and the counter electrode, respectively. The AN-PEOSPE or DMF-PEOSPE were used as both ionic conductor and separator in different ASSLIBs. No additional solvent or liquid electrolyte was used in the LiCoO<sub>2</sub>

ASSLIBs. Galvanostatic charge/discharge testing was performed between 2.7 and 4.2 V (or 4.3 V) in a 60 °C oven, using a LAND Battery Tester. All ASSLIBs were rested for over 30 h before testing at 60 °C. Cyclic Voltammetry of the ASSLIBs was performed between 2.7 and 4.2 V (vs. Li/Li<sup>+</sup>) in a 60 °C oven. Electrochemical impedance spectroscopy (EIS) was performed on a versatile multichannel potentiostat 3/Z (VMP3) by applying an AC voltage with 10 mV amplitude in the frequency range from 500 kHz to 0.01 Hz.

#### 6.2.4 Material characterizations

A Hitachi S-4800 field emission scanning electronic microscope (FE-SEM) equipped with energy dispersive X-ray spectroscopy (EDX) was used to characterize the morphology and element distribution in samples. Raman spectra were obtained using a HORIBA Scientific LabRAM HR Raman spectrometer system equipped with a 532.4 nm laser. X-ray diffraction (XRD) was performed in Bruker D8 Advance Diffractometer. Co L-edge X-ray absorption spectroscopy (XAS) measurements using total electron yield (TEY) and fluorescence yield (FLY) modes were collected at the Canadian light source (CLS). <sup>1</sup>H NMR spectrum was obtained in Mercury 400 NMR equipment by using CDCl<sub>3</sub> as the solvent at 25 °C.

### 6.3 Results and discussion

DMF-PEOSPE based SPE is prepared by dissolving the PEO polymer, and LiClO<sub>4</sub> in DMF solvent and stirring it at 70 °C overnight. In comparison, AN-PEOSPE is prepared by dissolving the PEO polymer, and LiClO<sub>4</sub> in acetonitrile (AN) solvent and stirring it at 70 °C overnight. The obtained mixture is cast on Teflon dishes to evaporate the solvent in a 60 °C vacuum oven for 3 days. Thermogravimetric analysis (TGA) was applied to check the remaining solvent in both SPEs. The result in **Figure 6.1a** shows that there is no residue of solvent in either SPE. The electrochemical and physical properties of DMF-PEOSPE and AN-PEOSPE are studied by impedance spectroscopy, Raman, X-ray diffraction (XRD) (Supporting information) and scanning electron microscopes (SEM). Interestingly, the physical properties of AN-PEOSPE and DMF-PEOSPE behave differently. The thicknesses of SPEs prepared with the same mass of PEO and the same mass of LiClO<sub>4</sub>

salt casting, in the same size of evaporating dish, are different. A 90  $\mu\text{m}$  thickness of AN-PEOSPE is obtained, while its thickness is only 68  $\mu\text{m}$  for DMF-PEOSPE (**Figure 6.1b,c**). The optical colors of these two SPEs are also different, AN-PEOSPE is white color with half transparent, while DMF-PEOSPE exhibits orange color with half transparent (**Figure 6.1e,f**). **Figure 6.1d** presents the temperature dependent ionic conductivity of DMF-PEOSPE and ANPEOSPE. They have similar ionic conductivity values at room temperature and high temperature areas, but different ionic conductivities in the 50 - 60  $^{\circ}\text{C}$  region, which should be the reason that DMFPEOSPE and AN-PEOSPE have different chain movement. At 60  $^{\circ}\text{C}$ , the ionic conductivity of AN-PEOSPE is  $3.3 \times 10^{-4}$  S/cm and it is  $1.1 \times 10^{-4}$  S/cm for DMF-PEOSPE; both are sufficient for the application in ASSLIBs.

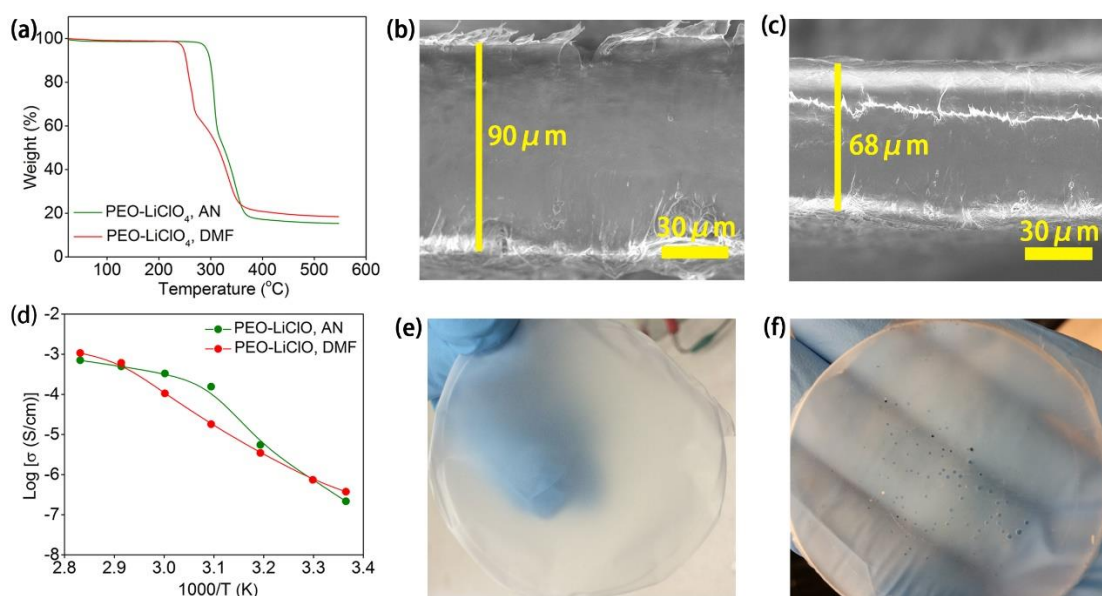


**Figure 6.1** (a) Comparison of TGA for DMF-PEOSPE and AN-PEOSPE. (b), (c) The comparison of thicknesses of AN-PEOSPE (b) and DMF-PEOSPE (c) with the same weight and same size. (d) Temperature dependent ionic conductivity of DMF-PEOSPE and AN-PEOSPE. (e) and (f) The optical images of AN-PEOSPE (e) and DMF-PEOSPE (f).

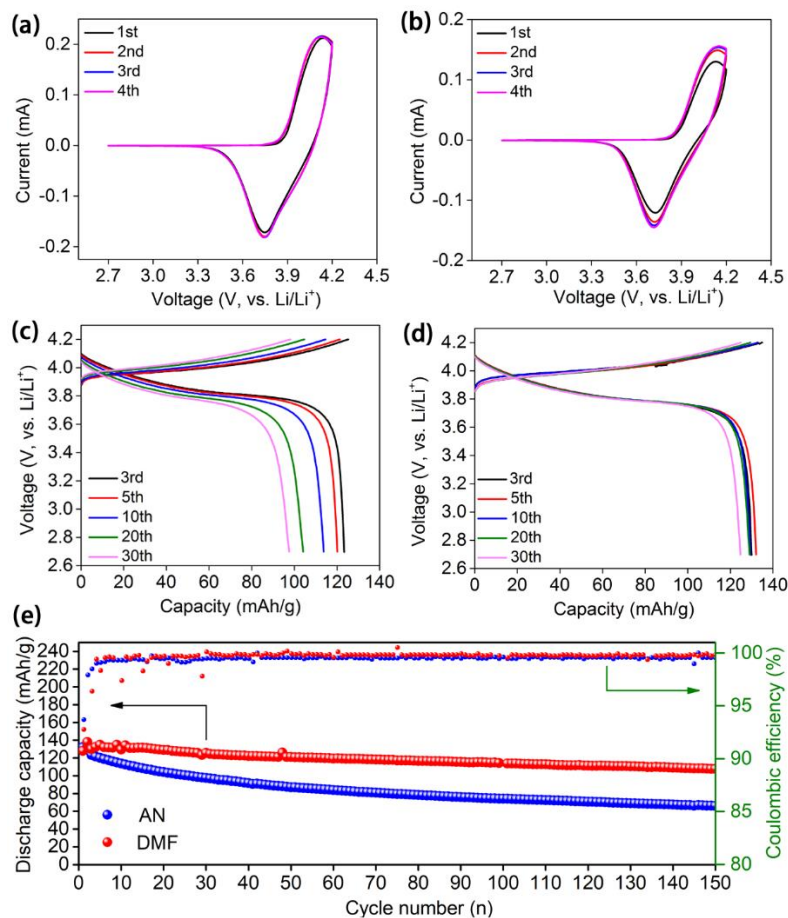


**Figure 6.2** CV cures of (a) Li/SPE/LiCoO<sub>2</sub> ASSLIBs with AN-PEOSPE, and (b) Li/SPE/LiCoO<sub>2</sub> ASSLIBs with DMF-PEOSPE, Charge/discharge profiles of (c) Li/SPE/LiCoO<sub>2</sub> ASSLIBs with AN-PEOSPE and (d) Li/SPE/LiCoO<sub>2</sub> ASSLIBs with DMF-PEOSPE and (e) the comparison of long cycling performance of Li/SPE/LiCoO<sub>2</sub> ASSLIBs with AN-PEOSPE and DMF-PEOSPE. All Li/SPE/LiCoO<sub>2</sub> ASSLIBs were tested at 60 °C.

The electrochemical performances of ASSLIBs with DMF-PEOSPE or AN-PEOSPE and LiCoO<sub>2</sub> as the cathode are evaluated and the results are presented in **Figure 6.2**. Firstly, the CV cures of ASSLIBs with AN-PEOSPE and DMF-PEOSPE are illustrated in **Figure 6.2a, b**. Both CV cures display very similar cathodic/anodic processes with an anodic peak voltage at 4.12 V and a cathodic peak voltage at 3.73 V, corresponding to that of the conversion between Co<sup>3+</sup> and Co<sup>4+</sup>. The long cycling performance of ASSLIBs with LiCoO<sub>2</sub> were evaluated by galvanostatic testing at 60 °C, with the first two cycles in 0.1 C current density and the rest at 0.4 C current density. **Figure 6.2c, d** compared the

charge/discharge voltage profiles for the ASSLIBs with AN-PEOSPE and DMF-PEOSPE. It is clear that the ASSLIBs with AN-PEOSPE show obvious capacity fading within 30 cycles of charge/discharge, along with an obvious increase in the overpotential of the cell. In great contrast, the ASSLIBs with DMF-PEOSPE show almost no increase in the cell overpotential and the capacity fading is very small, which means DMF-PEOSPE has better electrochemical performance in 4 V class LiCoO<sub>2</sub> ASSLIBs. The long cycling performance of the ASSLIBs are compared in **Figure 6.2e**. The ASSLIBs with AN-PEOSPE deliver an initial discharge capacity of 132.1 mAh/g at 0.1 C; it dramatically decreases to 66.2 mAh/g after 150 cycles. For the ASSLIBs with DMF-PEOSPE, an initial discharge capacity of 128 mAh/g is disclosed, after 150 cycles, its discharge capacity still maintains at 107.7 mAh/g (corresponding to a capacity retention of 84 %), almost two times higher than that of the ASSLIBs with AN-PEOSPE. For the average coulombic efficiency within 150 cycles, it is 99.3 % for the ASSLIBs with AN-PEOSPE and 99.8 % for the ASSLIBs with DMFPEOSPE. The higher average coulombic efficiency of the SPBs with DMF-PEOSPE indicates there is less decomposition of DMF-PEOSPE at LiCoO<sub>2</sub> ASSLIB.

To understand the insight mechanism for the electrochemical performance enhancement of the LiCoO<sub>2</sub> ASSLIBs, the electrochemical oxidation window of these SPEs were studied by the LSV method. The results are presented in **Figure 6.3a**. The on-set oxidation potential of DMF-PEOSPE is around 0.2 V higher than that of AN-PEOSPE, clearly demonstrating again that DMF-PEOSPE has higher capacity to electrochemical oxidation at high voltage. <sup>1</sup>H nuclear magnetic resonance (NMR) was performed to study the molecule structures of DMF-PEOSPE and AN-PEOSPE. The results are presented in **Figure 6.3b,c** below. The main shift at 3.67 ppm for both SPE samples are from the main chain of ethylene oxide. Differently, the chemical shift at 2.97 ppm for AN-PEOSPE is the H from the end methyl (CH<sub>3</sub>) group of PEO, which is supported by the reported data.<sup>22, 23</sup> For DMF-PEOSPE, a chemical shift at 2.38 ppm, and a minor shift at 2.77 ppm are outstanding, which could be the H in dimethylamine group and the adjacent methylene, respectively. Similar data is reported by Y. Want et al. and C. Mu et al.<sup>22, 24</sup> It is believed that the dimethylamine group for DMF-PEOSPE comes from the reaction between DMF and original PEO. The possible chemical reactions between DMF and PEO is proposed in **Figure SI6.5**. DMF is an active solvent; it has great potential to react with PEO. Similar

reaction between DMF and polymers have been studied by D. DrHgan,<sup>25</sup> Y. Wang et. al.<sup>24</sup> and C. Subramanian et al.<sup>26</sup> After being replaced, the polymer structure may become more stable. Therefore, the electrochemical oxidation resistance of SPE is increased. In order to confirm this proposal, the Gibbs energies for the breaking of a C-C bond in a  $[\text{H}_3\text{CO}-[-\text{CH}_2-\text{CH}_2-\text{O}-]_4-\text{CH}_3]^+$  cation and in a  $[(\text{H}_3\text{C})_2\text{N}-[-\text{CH}_2-\text{CH}_2-\text{O}-]_4-\text{CH}_2-\text{CH}_2-\text{N}(\text{CH}_3)_2]^+$  cation are calculated. The results in **Figure 6.3d,e** illustrate that a  $[(\text{H}_3\text{C})_2\text{N}-[-\text{CH}_2-\text{CH}_2-\text{O}-]_4-\text{CH}_2-\text{CH}_2-\text{N}(\text{CH}_3)_2]^+$  cation has a higher Gibbs energy for the breaking of a C-C bond, which is +176.4 kJ/mol compared to +58.7 kJ/mol for a  $[\text{H}_3\text{CO}-[-\text{CH}_2-\text{CH}_2-\text{O}-]_4-\text{CH}_3]^+$  cation. The higher Gibbs energy means it requires higher energy to break the C-C bond, which means it is more stable. This result supports that the replacement of the methyl group end group of PEO can enhance the stability of the polymer, which could be the reason why DMF-PEOSPE exhibits better electrochemical performance in ASSLIBs.

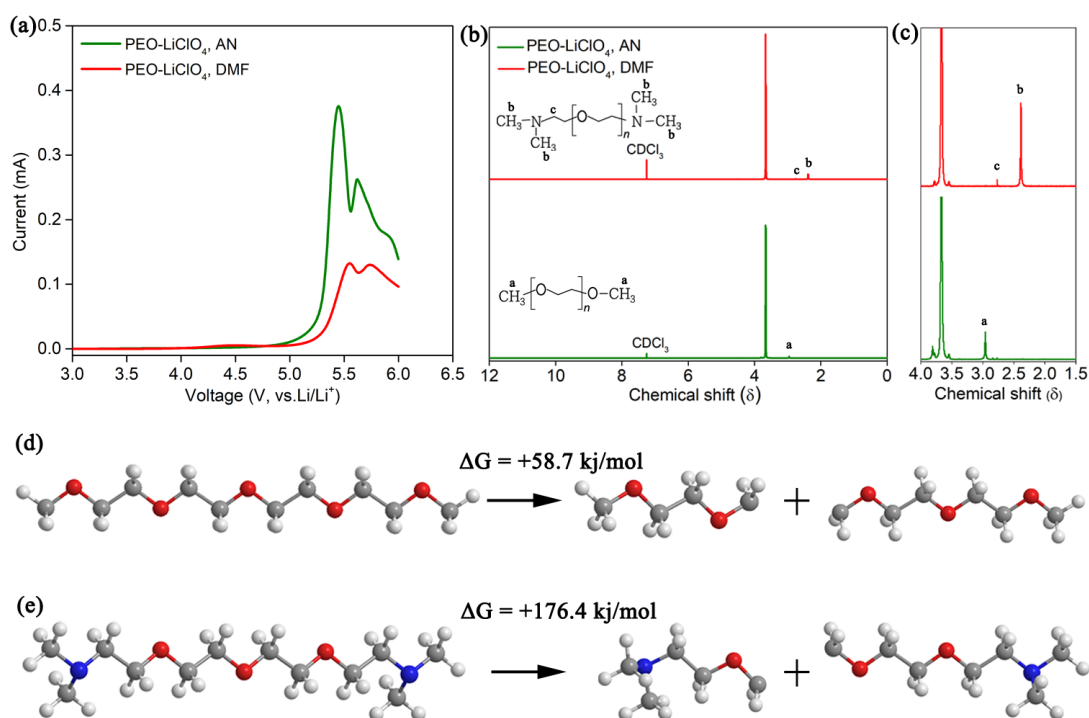


**Figure 6.3** (a) LSV studies of DMF-PEOSPE and AN-PEOSPE (from OCV to 6 V vs. Li/Li<sup>+</sup>). (b) <sup>1</sup>H NMR spectrum for DMF-PEOSPE and AN-PEOSPE and (c) the enlarged area of <sup>1</sup>H NMR spectrum from 1.5 to 4 ppm. Schematic diagram and Gibbs energies for breaking the C-C bond in (d)  $[\text{H}_3\text{CO}-[-\text{CH}_2-\text{CH}_2-\text{O}-]_4-\text{CH}_3]^+$  cation and (e)  $[(\text{H}_3\text{C})_2\text{N}-[-\text{CH}_2-\text{CH}_2-\text{O}-]_4-\text{CH}_2-\text{CH}_2-\text{N}(\text{CH}_3)_2]^+$  cation.

$\text{CH}_2\text{-CH}_2\text{-O-}]_4\text{-CH}_2\text{-CH}_2\text{-N(CH}_3)_2]^+$  cation. White sphere: H; grey sphere: C; red sphere: O and blue sphere: N.

The interfacial properties between  $\text{LiCoO}_2$  cathodes and SPEs were studied by synchrotron based XAS at Co L-edge and EIS.  $\text{LiCoO}_2$  electrodes were cycled in ASSLIBs for 5 times and stopped at discharge state, with different SPEs and then they were peeled off from the SPEs for XAS studies. The results are shown in **Figure 6.4a,b**. XAS at Co L-edge were collected at two different modes, which are total electron yield (TEY) and fluorescence yield models (FYL) modes, respectively, for each sample. The TEY mode collected the information from the top few nanometers of the surface of the samples, while FLY collected the information from the more inside of the samples, which is bulk sensitive. For the TEY mode (**Figure 6.4a**), the  $\text{LiCoO}_2$  in the ASSLIBs with ANPEOSPE shows a clear increase in the  $L_3$  peak shoulder, which means there is a decrease in the unoccupied high energy Co 3d state, suggesting that Co is reduced.<sup>27, 28</sup> The reduction of Co is possibly due to the interaction/reaction between the PEO and  $\text{LiCoO}_2$  particle surface. This interaction/reaction between the PEO and  $\text{LiCoO}_2$  particle surface can refer to the interaction/reaction between liquid organic electrolytes and  $\text{LiCoO}_2$ , as reported by D. Takamatsu et al.<sup>29</sup> The reduction of Co means there is oxidation of AN-PEOSPE in ASSLIBs. And this result suggests that the AN-PEOSPE/ $\text{LiCoO}_2$  electrode interface is not stable, which is detrimental for the electrochemical performance of ASSLIBs. In contrast, the Co  $L_3$  edge of the  $\text{LiCoO}_2$  in the ASSLIBs with DMF-PEOSPE, after cycling, has very good reversibility compared to pristine  $\text{LiCoO}_2$ , which indicates that the DMF-PEOSPE/ $\text{LiCoO}_2$  interface is stable. For FLY information (**Figure 6.4b**), all the Co XAS from these three samples have similar spectra, which indicates the bulk of the  $\text{LiCoO}_2$  are highly reversible and the interaction/reaction between SPEs and  $\text{LiCoO}_2$  only happens on the surface of  $\text{LiCoO}_2$ , within 5 cycles of charge/discharge.



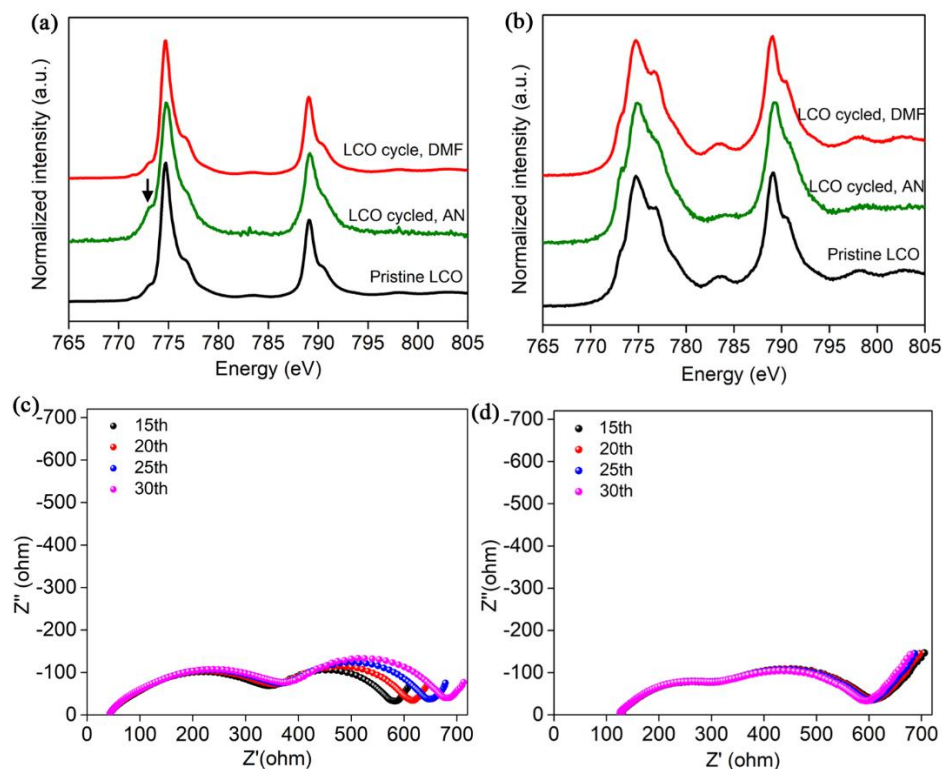


**Figure 6.4** Co L-edge XAS in (a) TEY and (b) FLY modes. EIS spectra for Li/SPE/LiCoO<sub>2</sub> ASSLIBs with SPE prepared by (c) AN and (d)DMF. EIS spectra were collected at a 4.2 V charging state.

Furthermore, in order to investigate how the interfacial resistances of the cell evolve during different charge/discharge cycles, EIS measurements were conducted to study the interfacial impedance of the ASSLIBs. The interfacial impedance is a comprehensive physical quantity that represents the interface stability of the batteries. For ASSLIBs with AN-PEOSPE, EIS spectra have represented two semicircles, one at a high frequency region and the other at a low frequency region. The high frequency semicircle is corresponding to the SPE/Li anode interface, and the low frequency semicircle is corresponding to the SPE/LiCoO<sub>2</sub> cathode interface, as proposed by S. Seki et al.<sup>18</sup> The overall impedance of the cell shows an obvious increase trend within 30 cycles of charge/discharge, from around 580  $\Omega$  at the 15<sup>th</sup> cycle, growing to 680  $\Omega$  at the 30<sup>th</sup> cycle. More importantly, the increase of the overall cell resistance is mainly due to the enlargement of the low frequency semicircle (SPE/LiCoO<sub>2</sub> cathode interfacial resistance), which suggests that the AN-PEOSPE/LiCoO<sub>2</sub> cathode interface is not stable. The accumulated decomposed products

from AN-PEOSPE on the AN-PEOSPE/LiCoO<sub>2</sub> cathode interface, with the long cycling number, will dramatically increase the resistance ASSLIBs. Differently, the overall impedance of ASSLIBs with DMF-PEOSPE is quite stable at 600  $\Omega$ , within 30 cycles. This stable impedance evaluation of ASSLIBs with DMF-PEOSPE demonstrates that DMFPEOSPE has better electrochemical stability compared to AN-PEOSPE in ASSLIBs during cycling. The XAS and EIS results are quite consistent with the cycling performance results (**Figure 6.2**) and the LSV, Gibbs energy calculation results (**Figure 6.3**).

## 6.4 Conclusion

In summary, a facile method to increase the electrochemical oxidation window of PEO-based SPEs is reported. PEO-based SPEs prepared by DMF have a dimethylamine end group, which is different from the common PEO having an active end group. This dimethylamine end group PEO has an enhanced electrochemical oxidation window and better cycling performance in 4 V class LiCoO<sub>2</sub> ASSLIBs. After 150 charge/discharge cycles, the capacity retention for DMF-PEOSPE was 84 %, while only 50 % was achieved for AN-PEOSPE. The Co L-edge XAS and EIS studies also supported the better interfacial stability between the DMF-PEOSPE/cathode interface. This study discloses a novel approach for improving the electrochemical performance of 4 V class ASSLIBs with PEO-based SPEs, paving the way for developing high energy density ASSLIBs for practical electric vehicle application.

## Acknowledgements

This work was supported by the China Automotive Battery Research Institute, Natural Sciences and Engineering Research Council of Canada (NSERC), Canada Research Chair Program (CRC), and University of Western Ontario. We also appreciate the help from the beamline scientists of the Spherical Grating Monochromator (SGM) beamline at Canadian Light Source, Dr. Tom Regier, Dr. James Dynes and Dr. Zechary Arthur. Jianneng Liang greatly appreciates the China Scholarship Council (CSC) for the support of PhD study.

## References

1. F. Croce, G. B. Appetecchi, L. Persi and B. Scrosati, *Nature*, 1998, 394, 456-458.

2. J. Liang, J. Luo, Q. Sun, X. Yang, R. Li and X. Sun, *Energy Storage Mater.*, 2019, 21, 308-334.
3. J. Liang, Q. Sun, Y. Zhao, Y. Sun, C. Wang, W. Li, M. Li, D. Wang, X. Li, Y. Liu, K. Adair, R. Li, L. Zhang, R. Yang, S. Lu, H. Huang and X. Sun, *J. Mater. Chem. A*, 2018, 6, 23712-23719.
4. R. Murugan, V. Thangadurai and W. Weppner, *Angew. Chem. Int. Ed.*, 2007, 46, 7778-7781.
5. Y. Liu, J. Liu, Q. Sun, D. Wang, K. R. Adair, J. Liang, C. Zhang, L. Zhang, S. Lu, H. Huang, X. Song and X. Sun, *ACS Appl. Mater. Interfaces*, 2019, 11, 27890-27896.
6. N. Kamaya, K. Homma, Y. Yamakawa, M. Hirayama, R. Kanno, M. Yonemura, T. Kamiyama, Y. Kato, S. Hama, K. Kawamoto and A. Mitsui, *Nat. Mater.*, 2011, 10, 682-686.
7. X. Li, J. Liang, N. Chen, J. Luo, K. R. Adair, C. Wang, M. N. Banis, T.-K. Sham, L. Zhang, S. Zhao, S. Lu, H. Huang, R. Li and X. Sun, *Angew. Chem. Int. Ed.*, 2019, 58, 16427-16432.
8. P. Hovington, M. Lagacé, A. Guerfi, P. Bouchard, A. Mauger, C. M. Julien, M. Armand and K. Zaghib, *Nano Lett.*, 2015, 15, 2671-2678.
9. K. Fu, Y. Gong, J. Dai, A. Gong, X. Han, Y. Yao, C. Wang, Y. Wang, Y. Chen, C. Yan, Y. Li, E. D. Wachsman and L. Hu, *Proc. Natl. Acad. Sci. U.S.A.*, 2016, 113, 7094-7099.
10. J. Wan, J. Xie, X. Kong, Z. Liu, K. Liu, F. Shi, A. Pei, H. Chen, W. Chen, J. Chen, X. Zhang, L. Zong, J. Wang, L.-Q. Chen, J. Qin and Y. Cui, *Nat. Nanotechnol.*, 2019, 14, 705-711.
11. Y. Xia, T. Fujieda, K. Tatsumi, P. P. Prosini and T. Sakai, *J. Power Sources*, 2001, 92, 234-243.
12. M. M. Besli, S. Xia, S. Kuppam, Y. Huang, M. Metzger, A. K. Shukla, G. Schneider, S. Hellstrom, J. Christensen, M. M. Doeff and Y. Liu, *Chem. Mater.*, 2019, 31, 491-501.
13. J. Ma, Z. Liu, B. Chen, L. Wang, L. Yue, H. Liu, J. Zhang, Z. Liu and G. Cui, *J. Electrochem. Soc.*, 2017, 164, A3454-A3461.

14. J. Zhang, N. Zhao, M. Zhang, Y. Li, P. K. Chu, X. Guo, Z. Di, X. Wang and H. Li, *Nano Energy*, 2016, 28, 447-454.
15. T. Kwon, I. Choi and M. J. Park, *ACS Appl. Mater. Interfaces*, 2017, 9, 24250-24258.
16. Y. Lin, J. Li, K. Liu, Y. Liu, J. Liu and X. Wang, *Green Chem.*, 2016, 18, 3796-3803.
17. H. Miyashiro, Y. Kobayashi, S. Seki, Y. Mita, A. Usami, M. Nakayama and M. Wakihara, *Chem. Mater.*, 2005, 17, 5603-5605.
18. S. Seki, Y. Kobayashi, H. Miyashiro, Y. Mita and T. Iwahori, *Chem. Mater.*, 2005, 17, 2041-2045.
19. Q. Yang, J. Huang, Y. Li, Y. Wang, J. Qiu, J. Zhang, H. Yu, X. Yu, H. Li and L. Chen, *J. Power Sources*, 2018, 388, 65-70.
20. J. Liang, Y. Sun, Y. Zhao, Q. Sun, J. Luo, F. Zhao, X. Lin, X. Li, R. Li, L. Zhang, S. Lu, H. Huang and X. Sun, *J. Mater. Chem. A*, 2020, 8, 2769-2776.
21. W. Zhou, Z. Wang, Y. Pu, Y. Li, S. Xin, X. Li, J. Chen and J. B. Goodenough, *Adv. Mater.*, 2019, 31, 1805574.
22. Q. Luo, H. Gao, L. Peng, G. Liu and Z. Zhang, *J. Appl. Polym. Sci.*, 2016, 133, 43465
23. X.-A. Chen, L.-J. Zhang, Z.-J. He, W.-W. Wang, B. Xu, Q. Zhong, X.-T. Shuai, L.-Q. Yang and Y.-B. Deng, *Int. J. Nanomedicine*, 2011, 6, 843-853.
24. Y. Wang, S. Chen and J. Huang, *Macromolecules*, 1999, 32, 2480-2483.
25. D. Drăgan, *Angew. Makromol. Chem.*, 1996, 236, 85-95.
26. C. Subramanian, M. Giotto, R. A. Weiss and M. T. Shaw, *Macromolecules*, 2012, 45, 3104-3111.
27. F. Lin, I. M. Markus, D. Nordlund, T.-C. Weng, M. D. Asta, H. L. Xin and M. M. Doeff, *Nat. Commun.*, 2014, 5, 3529.
28. F. Lin, D. Nordlund, Y. Li, M. K. Quan, L. Cheng, T.-C. Weng, Y. Liu, H. L. Xin and M. M. Doeff, *Nat. Energy*, 2016, 1, 15004.
29. D. Takamatsu, Y. Koyama, Y. Orikasa, S. Mori, T. Nakatsutsumi, T. Hirano, H. Tanida, H. Arai, Y. Uchimoto and Z. Ogumi, *Angew. Chem. Int. Ed.*, 2012, 51, 11597-11601.

## Supporting information

Supporting images:

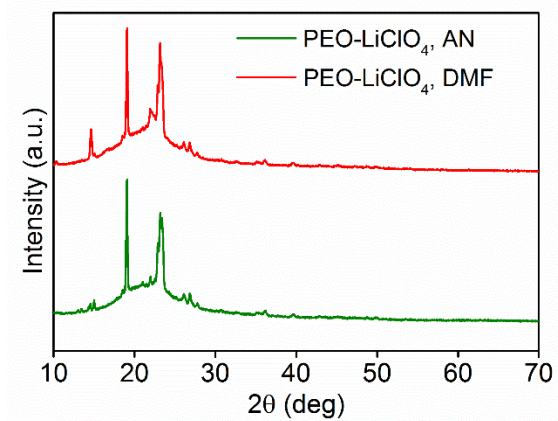


**Figure S6.1** XRD of PEO-based SPE prepared by AN and DMF.

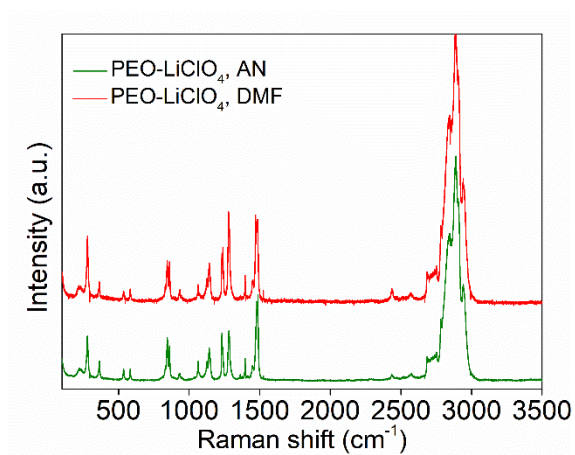


**Figure S6.2** Raman spectra of PEO-based SPE prepared by AN and DMF.

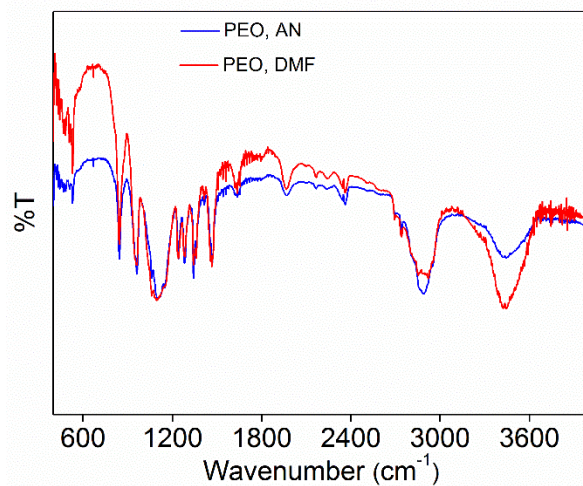


**Figure S6.3** FTIR spectra of PEO-based SPE prepared by AN and DMF.

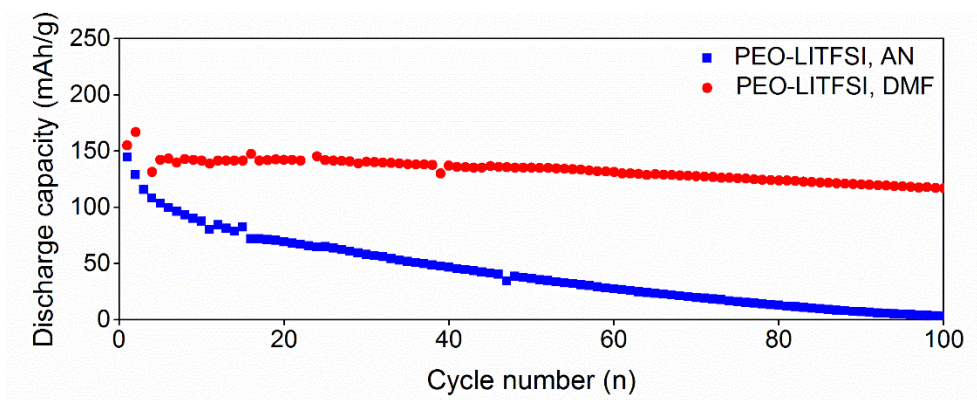


**Figure S6.4** Comparison of electrochemical performance for ASSLIBs with PEO-LITFSI SPEs prepared by AN and DMF. The charge/discharge voltage range is 2.7 – 4.3 V. Temperature: 60 °C. Current density: 0.4C.

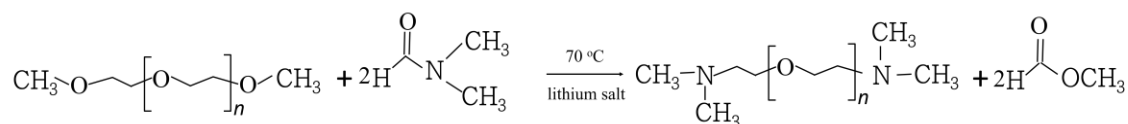


**Figure S6.5** Proposed chemical reaction between methyl group end group PEO, with DMF solvent at 70 °C.

## Modeling of Gibbs energy:

All systems were optimized at the B3LYP-D3(BJ)/def2-TZVP level in Gaussian 16.<sup>1-7</sup> Solvent effects were included by simulating an acetone solvent (relative permittivity = 20.493) with the polarizable continuum model (PCM).<sup>8</sup> Acetone is chosen because most Li-based batteries use a 7:3 mixture of linear and cyclic carbonates with a relative permittivity of about 20.<sup>9</sup> Analytic computations of vibrational frequencies verified all structures as minima and gave the ro-vibrational contributions to the Gibbs energy.

## Supporting reference:

1. Gaussian 16, Revision A.03, M. J. Frisch, G. W. Trucks, H. B. Schlegel, G. E. Scuseria, M. A. Robb, J. R. Cheeseman, G. Scalmani, V. Barone, G. A. Petersson, H. Nakatsuji, X. Li, M. Caricato, A. V. Marenich, J. Bloino, B. G. Janesko, R. Gomperts, B. Mennucci, H. P. Hratchian, J. V. Ortiz, A. F. Izmaylov, J. L. Sonnenberg, D. Williams-Young, F. Ding, F. Lipparini, F. Egidi, J. Goings, B. Peng, A. Petrone, T. Henderson, D. Ranasinghe, V. G. Zakrzewski, J. Gao, N. Rega, G. Zheng, W. Liang, M. Hada, M. Ehara, K. Toyota, R. Fukuda, J. Hasegawa, M. Ishida, T. Nakajima, Y. Honda, O. Kitao, H. Nakai, T. Vreven, K. Throssell, J. A. Montgomery, Jr., J. E. Peralta, F. Ogliaro, M. J. Bearpark, J. J. Heyd, E. N. Brothers, K. N. Kudin, V. N. Staroverov, T. A. Keith, R. Kobayashi, J. Normand, K. Raghavachari, A. P. Rendell, J. C. Burant, S. S. Iyengar, J. Tomasi, M. Cossi, J. M. Millam, M. Klene, C. Adamo, R. Cammi, J. W. Ochterski, R. L. Martin, K. Morokuma, O. Farkas, J. B. Foresman, and D. J. Fox, Gaussian, Inc., Wallingford CT, 2016.
2. A. D. Becke, "Density-functional thermochemistry. III. The role of exact exchange," *J. Chem. Phys.*, 98 (1993) 5648-52
3. S. H. Vosko, L. Wilk, and M. Nusair, "Accurate spin-dependent electron liquid correlation energies for local spin density calculations: A critical analysis," *Can. J. Phys.*, 58 (1980) 1200-11
4. C. Lee, W. Yang, and R. G. Parr, "Development of the Colle-Salvetti correlation-energy formula into a functional of the electron density," *Phys. Rev. B*, 37 (1988) 785-89

5. B. Miehlich, A. Savin, H. Stoll, and H. Preuss, "Results obtained with the correlation-energy density functionals of Becke and Lee, Yang and Parr," *Chem. Phys. Lett.*, 157 (1989) 200-06
6. S. Grimme, S. Ehrlich and L. Goerigk, "Effect of the damping function in dispersion corrected density functional theory," *J. Comp. Chem.* 32 (2011) 1456-65
7. F. Weigend and R. Ahlrichs, "Balanced basis sets of split valence, triple zeta valence and quadruple zeta valence quality for H to Rn: Design and assessment of accuracy," *Phys. Chem. Chem. Phys.*, 7 (2005) 3297-305
8. J. Tomasi, B. Mennucci, and R. Cammi, "Quantum mechanical continuum solvation models," *Chem. Rev.*, 105 (2005) 2999-3093
9. L. Xing, O. Borodin, G. D. Smith and W. Li, "Density Functional Theory Study of the Role of Anions on the Oxidative Decomposition Reaction of Propylene Carbonate," *J. Phys. Chem. A*, 115 (2011), 13896-13905



## Chapter 7

### 7 Dramatically prolonged cycling life of 4 V all solid-state polymer batteries by alternating high voltage compatible binders

In previous three chapters, interfacial engineering by ALD between SPE and cathodes interfaces as well as the modification of PEO polymer structure are studied to enhance the electrochemical performance of ASSLIBs. However, the cathode component design has not yet been studied and the cathode component has great influence on the interface stability. The components' physical/chemical properties may be critical for the electrochemical performance of ASSLIBs.

Previous reported studies had mainly focused on the approaches including interface engineering and developing high voltage stable SPEs, while the binder effect of cathode electrode is ignored. In many reported studies, the most used binders were the low electrochemically stable PEO or EO containing polymers. In this work, four binders including commonly used binders PEO, PVDF, and carboxyl-rich polymer (CRP) binders such as sodium alginate (Na-alginate) and sodium carboxymethyl cellulose (CMC) were studied for the application in 4 V class all-state polymer batteries (ASSPBs). The results show ASSPBs with CRP binders exhibit superior cycling performance up to 1000 cycles (60 % capacity retention, almost 10 times higher than those of PEO and PVDF). Mechanism studies indicate that CRP binders are more stable at high voltage and they can not only strongly bind electrode materials together for maintaining the structure stability, but also work as a coating like material to avoid the detrimental effect of carbon in accelerating the decomposition of PEO-based SPE. This work shall give new insights on the facile and highly effective method of the alternation towards stable binders to realize high-performance long cycle life of 4 V class ASSPBs.

---

**J. Liang**,<sup>#</sup> D. Chen,<sup>#</sup> K. Adair, Q. Sun,<sup>a</sup> N. G. Holmes, Y. Zhao, Y. Sun, J. Luo, R. Li, L. Zhang, S. Zhao, S. Lu, H. Huang, X. Zhang, C. V. Singh,<sup>\*</sup> and X. Sun<sup>\*</sup> to be submitted.

<sup>#</sup> J. Liang and D. Chen contributed equally to this work.

## 7.1 Introduction

Lithium-ion batteries (LIBs) play an integral role in our daily life, with a wide variety of applications extending from portable electronic devices to electric vehicles (EVs). However, the organic liquid electrolyte used in conventional LIBs presents serious safety concerns due to its flammability and low flash point.<sup>1</sup> The development of solid-state batteries (SSBs) is a promising direction for addressing these safety issues. One of the key components of high-performance SSBs is the solid-state electrolyte (SSE). Oxide-based SSEs,<sup>2, 3</sup> sulfide-based SSEs,<sup>4, 5</sup> halide-based SSEs<sup>6-8</sup> and polymer-based SSEs<sup>9</sup> are regarded as the most encouraging candidates for applications in SSBs. Among them, polyethylene oxide (PEO) solid polymer electrolyte (SPE) shows great promise due to its high ionic conductivity at elevated temperature, low interfacial resistance towards electrodes and simple fabrication process.<sup>10</sup> More importantly, all-solid-state polymer batteries (ASSPBs) with lithium metal anodes, SPE and LiFePO<sub>4</sub> cathodes have been commercialized and are used in the Bolloré Bluecar,<sup>9</sup> which clearly demonstrates the great capability of SPE for SSBs.

However, it has been widely found that the state-of-the-art PEO-based SPEs developed so far deliver poor electrochemical performance when coupling with high energy density cathodes such as lithium cobalt oxide (LiCoO<sub>2</sub>) and layer structure lithium nickel manganese cobalt oxide (NMC). This is because PEO-based SPEs have a relatively low electrochemical oxidation potential - less than 3.8 V vs. Li/Li<sup>+</sup>.<sup>11</sup> These high energy density cathodes typically require charging voltages up to 4.2 V or higher to achieve a high specific capacity. At these voltages, PEO-based SPEs undergo electrochemical decomposition.<sup>11,12</sup> In order to address this serious limitation, significant research efforts have been dedicated to stabilizing the SPE when coupled with 4 V class cathodes and they can be classified to the following strategies: (i) the first approach is coating the cathode particles with inert materials which are stable at high voltage, such as Al<sub>2</sub>O<sub>3</sub>,<sup>13</sup> Li<sub>3</sub>PO<sub>4</sub>,<sup>14</sup> polymer materials (including PECA<sup>15</sup> and CMC<sup>16</sup>), and NASICON SSE (LATP).<sup>17</sup> (ii) the second method is coating the cathode electrode using techniques like atomic layer deposition to deposit materials such as lithium tantalite, to reduce the electrochemical decomposition of SPE.<sup>18</sup> (iii) third strategy involves making double layer SPEs with a SPE stable at high voltage on

the cathode side and a SPE stable at low voltage adjacent to the Li metal anode,<sup>19</sup> or using the same polymer matrix with different lithium salt at different layer.<sup>20</sup> Nonetheless, although many of the above-mentioned methods can enhance the cycling stability and increase the cycling life of ASSPBs using 4 V cathodes, they usually require additional treatment steps, and they still cannot be satisfactory for long cycling performance.

The cathode binder plays an important role in not only liquid-based LIBs but also SSBs. Binder effects in silicon anode-based LIBs and high-voltage cathode-based LIBs with liquid electrolyte have received tremendous research attention.<sup>21-25</sup> Binders for high performance SSBs with sulfide-based SSEs are also being studied and developed.<sup>26-30</sup> Unfortunately, in ASSPBs, the ionic conductivity of the binder is overemphasized, since the ionic conductivity of the cathode is poor without liquid electrolyte infiltration. Thus, the most commonly used binders in ASSPBs are PEO or ethylene oxide (EO)-containing polymers which have good ionic conductivity.<sup>3,9,13,15,31</sup> However, PEO and EO-containing polymers have a low electrochemical oxidation potential, which makes them unsuitable for 4 V class ASSPBs. It is therefore necessary to pursue a suitable binder for long cycle life, high performance, 4 V class ASSPBs.

Herein, we will introduce a facile and highly effective method by simply adopting the high voltage tolerant binders to significantly prolong the cycling lives of 4 V class ASSPBs based on PEO-based SPE. We conducted a careful study which examined the suitability of different binders including PEO, polyvinylidene fluoride (PVDF), and carboxyl-rich polymer (CRP) binders (including sodium alginate (Na-alginate) and sodium carboxymethyl cellulose (CMC)) for making 4 V class LiCoO<sub>2</sub> electrodes which were then coupled with a PEO-based SPE in ASSPBs. The electrochemical performance of these ASSPBs were evaluated and the mechanism were investigated by cyclic voltammetry (CV), X-ray photoelectron spectroscopy (XPS), synchrotron-based X-ray absorption spectroscopy (XAS) and first principles calculations. The initial discharge capacity of these 4 V class ASSPBs with different binders is approximately 131-135 mAh/g. After 300 cycles, 40.1 % capacity retention is achieved with PEO binder, 46 % capacity retention with PVDF binder, and 85% with CRP binder (CMC). After 1000 cycles, the ASSPB with PEO binder retains only 6.7 % capacity, while 59.7 % capacity is retained with the CRP

binder. CV results indicates CRPs have better electrochemical stability at high voltage compared to PEO and PVDF. O K-edge XAS and morphologies studies shows that CRPs can strongly bind the electrode materials together and also work as a coating material. XPS and Co L-edge XAS results demonstrate that a stable SPE/cathode interface is achieved with the CRP binder, while obvious PEO decomposition products are observed in the LiCoO<sub>2</sub> electrode surface with PEO as the binder. First principles calculations are consistent with electrochemical performance, XPS and XAS results, and they also show that CRP binders are better than PEO and PVDF binders. The stability and physical property of CRP binders in 4 V class cathodes throughout the charge and discharge processes is an important step on the road to high-performance, long cycle life, 4 V class ASSPBs.

## 7.2 Experimental

### 7.2.1 LiCoO<sub>2</sub> electrodes and binder-AB composite electrode preparation

LiCoO<sub>2</sub> electrodes were prepared by mixing 80 wt. % LiCoO<sub>2</sub> particles, 10 wt. % carbon-black (Acetylene Black), 10 wt.% binder (PEO, PVDF, Na-alginate, CMC,) and solvent to form a slurry. The solvent, acetonitrile, was used for the PEO binder, N-methylpyrrolidinone (NMP) for PVDF, and water for Na-alginate and CMC. A doctor blade casting method was used to coat the slurry on the carbon coated Al foil. The electrodes with different binder are referred as binder-LCO. The PEO-LCO, Na-alginate-LCO, and CMO-LCO electrodes were dried at 60 °C in a vacuum oven for 12 h and the PVDF-LCO electrode was dried at 100 °C in a vacuum oven for 12 h to obtain the LCO electrodes.

### 7.2.2 Electrochemical performance testing

All solid-state polymer batteries (ASSPBs) were assembled in 2032 type coin cells in an Ar-protected glove box (Vacuum Atmosphere Company, moisture and oxygen level less than 1 ppm). LiCoO<sub>2</sub> electrodes with different binders and lithium foils were used as the working electrodes and the counter electrodes. The PEO-LiClO<sub>4</sub>-LLZO SPEs were used as both ionic conductor and separator. No additional solvent or liquid electrolyte was used in

the LiCoO<sub>2</sub> ASSPBs. Galvanostatic charge/discharge testing was performed between 2.7 and 4.2 V (or 4.3 V) in a 60 °C oven using a LAND Battery Tester. All ASSPBs were rested for over 30 h before testing. For liquid based LiCoO<sub>2</sub> batteries, a liquid electrolyte containing 1 M LiPF<sub>6</sub> in ethylene carbonate (EC), ethylmethyl carbonate (EMC), and diethyl carbonate (DEC) solvents with a 1:1:1 volume ratio was used and Celgard 2400 was used as the separator. Cyclic voltammetry of the ASSPBs was performed between 2.7 and 4.2 V (vs. Li/Li<sup>+</sup>) in a 60 °C oven. Cyclic voltammetry of the Li/SPE/binder-carbon cell was performed between OCV and 4.3 V (vs. Li/Li<sup>+</sup>) in a 60 °C oven.

### 7.2.3 Material characterizations

A Hitachi S-4800 field emission scanning electronic microscope (FE-SEM) equipped with energy dispersive X-ray spectroscopy (EDX) was used to characterize the morphology and element distribution in samples. X-ray photoelectron spectroscopy (XPS) was conducted with a Thermo Scientific K-Alpha instrument at the University of Toronto. X-ray absorption spectroscopy (XAS) measurements using total electron yield (TEY) and fluorescence yield (FLY) modes at the Co K-edge were collected at the Canadian light source (CLS).

### 7.2.4 Theoretical method

All first principles calculations were performed using the Vienna Ab-initio Simulation Package (VASP) code<sup>32-34</sup>. The generalized gradient approximation (GGA) realized by the Perdew-Burke-Ernzerhof function (PBE) was adopted considering the electron exchange and correlation.<sup>35</sup> The Projected augmented wave (PAW)<sup>33,34</sup> was used to solve the electron orbitals and ground states. In view of the van der Waals interactions between the adsorption species and the substrate, the DFTD3 method with Becke-Jonson damping<sup>36</sup> was set in this study. The calculations of LiCoO<sub>2</sub>(001) surface and adsorption configurations were solved with a 400eV energy cut off, a 3×3×1 K-point sample<sup>37</sup> and an iteration convergence of 10<sup>-5</sup> eV in energy and 0.02 eV/Å in force. Due to the larger expansion of (001) in LiCoO<sub>2</sub> nanoflakes in this experiment and the high surface thermodynamic stability from theoretical evaluation<sup>38-40</sup> LiCoO<sub>2</sub>(001) was chosen in this study and was built using a 5×5×1 super cell with a unit cell of bulk structure: a=b=2.81 Å and c=14.05 Å. The surface

was built containing a 20 Å vacuum layer with a=b=14.05. The adsorption energy was calculated using the following equation:

$$E_{ads} = E_{Adsorption\ structure} - E_{LiCoO_2(001)} - E_{Polymer\ monomer/dimer} \quad (1)$$

Where  $E_{Polymer\ monomer/dimer}$  and  $E_{LiCoO_2(001)}$  are the total energy of the chosen polymer, monomer or dimer or pure LiCoO<sub>2</sub>(001) surface. The  $E_{adsorption\ structure}$  structure is the total energy of the whole structure of the polymer, monomer or dimer adsorbed on the LiCoO<sub>2</sub>(001) surface. The structure of these two adsorption species was fully optimized in a 15Å×15Å×15Å vacuum unit cell, as shown in Figure SI10(a) and (b). For the PEO dipolymer, the C-O and C-H bond lengths are 1.42 Å and 1.11 Å. The length of the Na-O bonds in the CMC is 2.19 Å. For the surface of LiCoO<sub>2</sub>(001), every Li atom locates between three adjacent O atoms at a distance of 1.89 Å. The Co-O bond length is about 2.05 Å. In this study, one layer of LiCoO<sub>2</sub> is used to build the surface to improve the calculation efficiency. The stoichiometric ratio does not conform with the bulk LiCoO<sub>2</sub>, but due to the distance between the adsorbed species and the lower atoms in the substrate, the interactions remain mainly within the upper layer.

### 7.3 Results and discussion

LiCoO<sub>2</sub> (LCO) electrodes with different binders were all prepared by a traditional slurry doctor blade method with an active material, binder and acetylene black (AB) ratio of 8:1:1 by weight. The cycle life of these ASSPBs was evaluated by galvanostatic charge-discharge cycling at 60 °C. The results are presented in **Figure 7.1**. The initial discharge capacity delivered by PEO-LCO is 135.3 mAh/g at 0.1 C, slightly higher than the 134.4 mAh/g, 130.9 mAh/g and 131.8 mAh/g delivered by PVDF-LCO, Na-alginate-LCO and CMC-LCO, respectively. The discharge capacity delivered by these ASSPBs is comparable to that obtained from liquid-based LCO batteries (**Figure S7.8**), and the cycling performance of liquid-based LCO batteries is observed to be quite stable. **Figure 7.1a,b** shows the charge/discharge profiles for these ASSPBs with PEO and CRP (CMC) as the binders at different charge/discharge cycles (from 3 - 100). For PEO-LCO, a significant decrease in the charge/discharge capacity and an obvious increase in the overpotential in later cycles is observed.

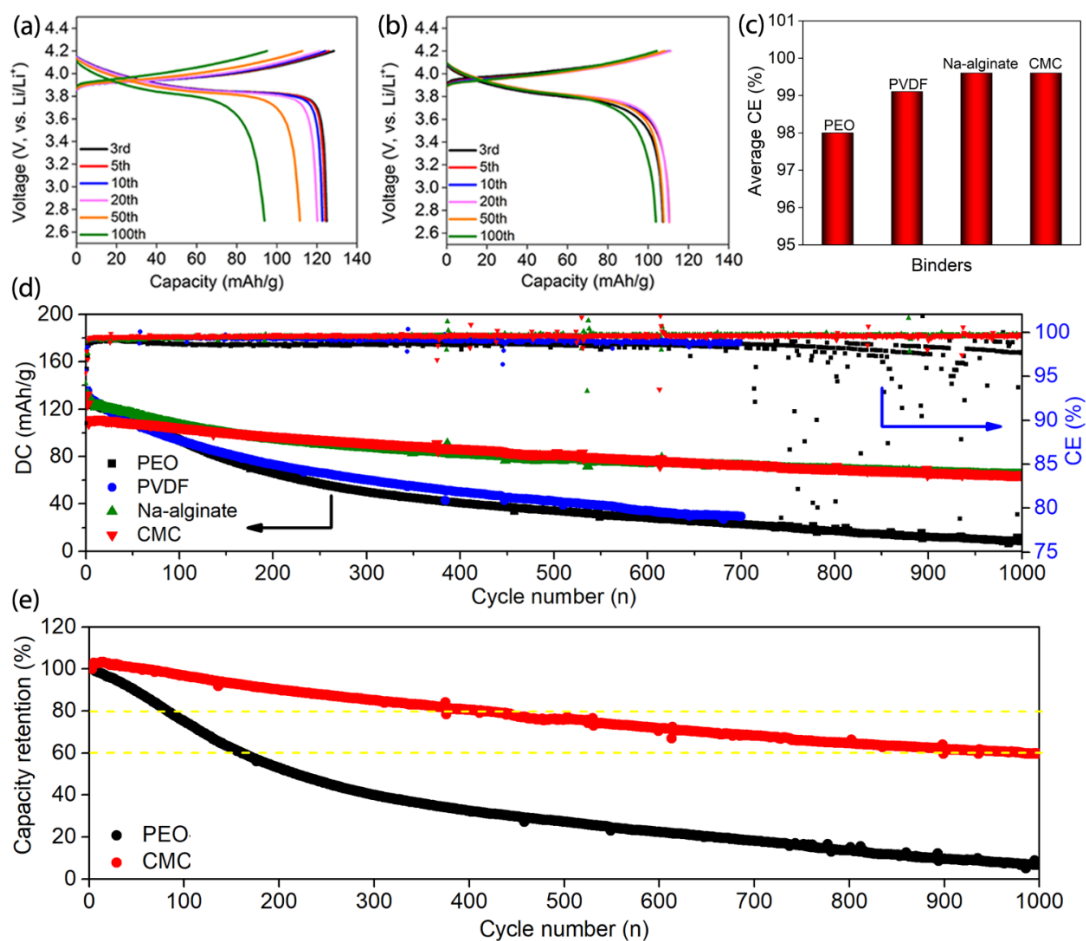


**Figure 7.1** Electrochemical performance of ASSPBs. The charge/discharge voltage profiles of (a) PEO-LCO, (b) CMC-LCO within the first 100 cycles. (c) The average coulombic efficiency of ASSPBs with different binders after 1000 cycles. (d) Cycle performance of ASSPBs with different binders. (e) Capacity retention of ASSPBs with PEO and CMC as the binders after 1000 cycles. Capacity retention is calculated as a percentage of the capacity over the third cycle discharge capacity. (DC: Discharge Capacity, CE: Coulombic Efficiency) All batteries were tested at 60 °C with a voltage cut off of 2.7 - 4.2 V, and a current density of 0.1 C for the first two cycles and 0.4 C for the remainder of the cycling.

However, for CMC-LCO, no decrease in the charge/discharge capacity or increase in the overpotential is observed, indicating that the ASSPBs fabricated with CMC binder are more stable than those fabricated with PEO binder. As shown in **Figure 7.1e,f**, after 300 cycles, 40.1 % capacity is retained with the PEO-LCO ASSPB, 46 % with the PVDF-LCO

ASSPB, and 85% with the CMC-LCO ASSPB. After 1000 cycles, the capacity retention of PEO-LCO batteries is only 6.7 %, while 59.7 % capacity remains for the CMC-LCO ASSPB. Compared to CMC-LCO, similar performance was achieved for Na-alginate-LCO ASSPBs, clearly demonstrating the improved electrochemical performances of CRPs binder-based LCO ASSPBs. The initial and average Coulombic efficiency of these ASSPBs after 1000 cycles is compared in **Figure S19** and **Figure 7.1c** respectively. After 1000 charge/discharge cycles, the average Coulombic efficiency for PEO-LCO, PVDF-LCO (700 cycles), Na-alginate-LCO, and CMC-LCO is 98.0 %, 99.1 %, 99.6 % and 99.6 % respectively. The lower average coulombic efficiency of PEO-LCO and PVDF-LCO indicates significant decomposition of the binders or PEO-based SPE in these ASSPBs systems and less decomposition in ASSPBs with CRP binders. The charge voltage up to 4.3 V were also investigated and similar performance enhancement with Na-alginate and CMC binders is also observed (**Figure S7.10**).

To investigate the underlying mechanism responsible for the performance enhancement associated with different binders in ASSPBs, CV, X-ray photoelectron spectroscopy (XPS), synchrotron-based soft X-ray absorption spectroscopy (XAS) and the density functional theory (DFT) calculation were performed to characterize the electrochemical properties of CRP binders and PEO, PVDF binder and the interfacial properties between LiCoO<sub>2</sub> and different binders.

The electrochemical stabilities of PEO, PVDF, Na-alginate and CMC were evaluated and compared using CV method. The results are shown in **Figure S7.12**. The cell contains lithium metal anode as the counter electrode, PEO-based SPE as the lithium ion conductor and separator, and 70 wt.% binder + 30 wt.% AB composite electrode as the working electrode. CV were conducted at 60 °C with 0.2 mV/s scan rate, scanning from OCV to 4.3 V and then back to 3 V. A outstanding CV anodic current intensity from PEO binder cell compared to the PVDF, Na-alginate and CMC cells means a significant decomposition of PEO binder may happen if the cell was charged to over 4 V. PVDF binder also shows a very high anodic current intensity compared to CRP binders. The electrochemical decomposition process is not reversible since not a corresponding cathodic peak in CV curve is observed, which means the decomposition reaction is irreversible and the decomposed



products will accumulate, resulting in thicker CEI layer in electrode/SPE interface, which is detrimental to the ASSPBs' performance. The trend of CV anodic current intensity for different binders is consistent with the long cycling performance shown in **Figure 7.1d**, which means the decomposition of binder is the key reason for the performance fading in 4 V class ASSPBs. A stable binder can help to achieve a high performance and long cycling life 4 V class ASSPB.

XAS at the O K-edge was performed for studying the chemical state of LCO electrodes with different binders and the results are shown in **Figure 7.2**. Spectra were collected with two detection modes, total electron yield (TEY) and fluorescence yield (FLY). TEY mode collected information to a depth of a few nanometers (2 - 10 nm) from the sample surface while FLY is more bulk sensitive, collecting information deeper (over 100 nm) into the sample.<sup>41</sup> For TEY information (**Figure 7.2a**), the spectrum of PEO-LCO is almost the same to that of pristine LCO. However, For CRP binders, quietly different spectra are illustrated, where the strong peaks related to oxygen in C-O and C=O structure are outstanding.<sup>42,43</sup> This feature of spectra indicates there are CRP binders cover the surfaces of LCO electrode. For FLY information (**Figure 7.2b**), all the spectra present similar structure to that of pristine LCO, but a minor shoulder at 535.5 eV corresponding to C-O arise for PEO-LCO, CMC-LCO and Na-alginate-LCO. There is also a shoulder corresponding to C=O arise for CRP binders based LCO electrodes. The morphologies of these electrodes are characterized by SEM. PEO-LCO (**Figure 7.2c**) shows very loose and porous structure. The surface of the top LCO particles is clear with few carbon particles adhesive, which indicate PEO binder just randomly/linearly binds the particles together. However, for CMC-LCO and Na-alginate-LCO, the morphologies of these electrodes seem less porous. These binders can disperse the particles and strongly stick the carbon and LCO particles together (**Figure 7.2d,e**). The SEM images are consistent well with the TEY O K-edge results and discussion. The binding effect for PEO and CRPs binders is then schematically illustrated in **Figure 7.2f** and **Figure 7.2g**. It is suggested that the CRPs binders can not only strongly stick the carbon and LCO particles together for maintaining the structure stability of electrodes, but also work as a coating like material to avoid the detrimental effects of electronic conductive carbon in accelerating the decomposition of

PEO-based SPE at high voltage, therefore, rendering a ultra-stable high performance 4 V class ASSPB.

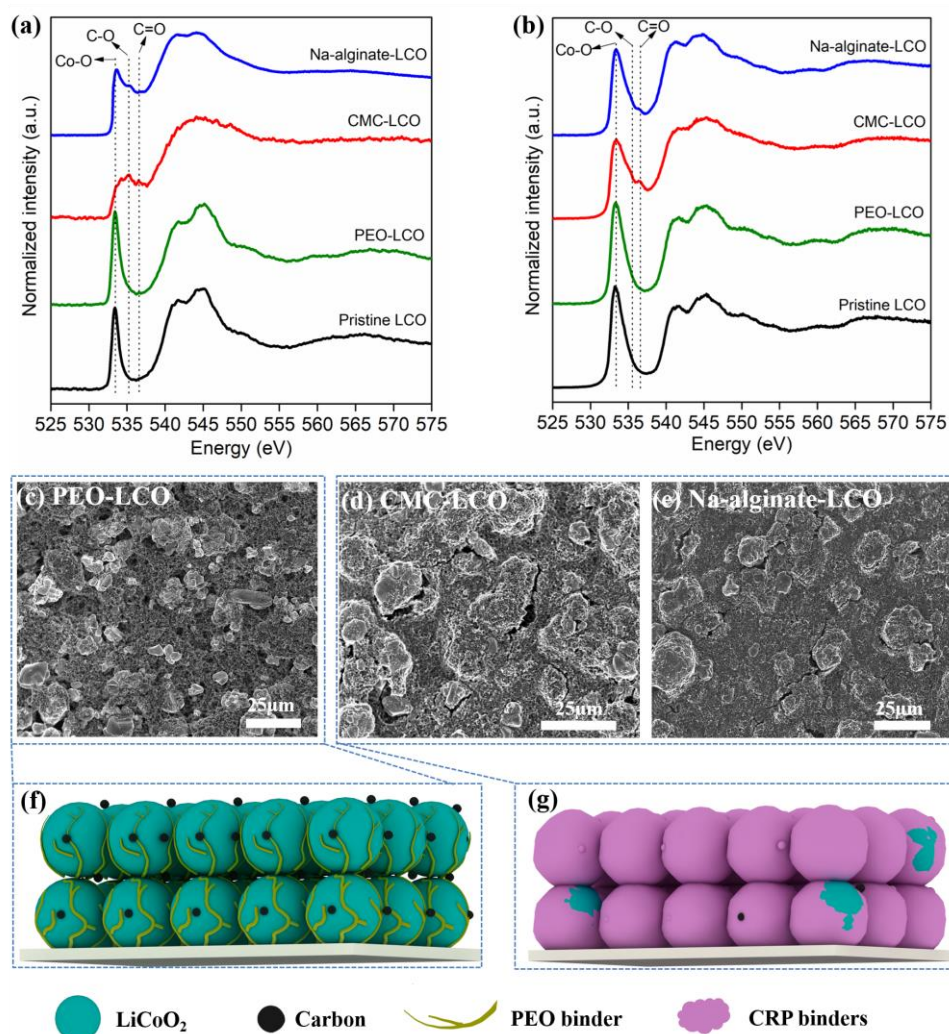


**Figure 7.2** (a) O K-edge XAS at TEY mode and (b) FLY mode for different LCO electrode samples. SEM images for (c) PEO-LCO, (d) CMC-LCO and (e) Na-alginate-LCO electrode. (f) Schematic diagrams for the binding capability of PEO (f) and CRP binders (g).

The interfacial properties between LCO electrodes and PEO-based SPE were investigated by XPS and XAS. The C1s and O1s XPS results at LCO electrodes surfaces are shown in **Figure 7.3a-d**. Before and after cycling, PEO-LCO have similar XPS C1s spectrum, which were fitted to C-C (~284.7 eV), R-C-O (~285.9 eV), R-C=O (~287.2 eV), O-C=O

( $\sim 288.9\text{eV}$ ).<sup>44-46</sup> The C-C peak at 284.5 eV can be assigned to the conductive carbon AB. The R-C-O peak can be assigned to PEO binder in PEO-LCO electrode before cycling, since the PEO molecular structure consists of  $\text{HO}[\text{CH}_2\text{-CH}_2\text{-O}]_n\text{-H}$  molecular fragments. However, the XPS spectrum intensity at R-C-O peak decreases significantly after cycling for the PEO-LCO electrode. The R-C=O peak in PEO-LCO electrode before cycling could come from the defects of the conductive carbon. However, this peak's intensity increases significantly after cycling. The intensity at another peak of O-C=O is also increased after cycling. This is because the decomposition products of PEO containing R-C=O and O-C=O,<sup>47,48</sup> the increase of intensities at R-C=O and O-C=O peaks after cycling for PEO-LCO electrode means the decomposed products of PEO are detected, which is supported by the O 1s results (**Figure 7.3c**) where the O-C=O peak intensity increases obviously after cycling in PEO-LCO. ROLi is also detected by O1s in PEO-LCO both before and after cycling. The formation of ROLi may arise from the interaction between PEO and  $\text{LiCoO}_2$  during electrode making process. This peak increased in intensity after cycling, which means the decomposition of PEO results in Li-containing products such as LiOH or other RO-Li-type polymeric-organic species.<sup>46</sup> All these results indicate serious decomposition of PEO at the interface of the PEO-LCO electrode and SPE, resulting in an unstable cathodic electrolyte interphase (CEI).

XPS C1s and O1s results of CMC-LCO electrodes before and after cycling are shown in **Figure 7.3b, d**. Similar peak-assignments were used for fitting the spectra as detailed before. For C1s of CMC-LCO electrode before cycling, the R-C-O, R-C=O, O-C=O peaks arise from the defect of AB and CMC binder. Moreover, the R-C-O peak increases greatly after cycling, which is possibly because of the residue of PEO-based SPE on the electrode surface (after the electrode is peeled off from the SPB). The R-C-O peak in O1s spectrum is also increased, which is consistent with the C1s result. No increase in R-C=O, O-C=O peaks are observed in both C1s and O1s results after cycling, which suggests better stability between the SPE and the binder at high potentials. Minor ROLi peak arises in the CMC-LCO electrode after cycling is possibly due to the interaction between PEO-based SPE and  $\text{LiCoO}_2$ . Not/less decomposed products of PEO-based SPE at the CMC-LCO electrode surface was detected, which could be due to the reason that CRPs binders work as a coating

like materials to eliminate the detrimental effect of carbon in accelerating the electrochemical decomposition of PEO-based SPE.

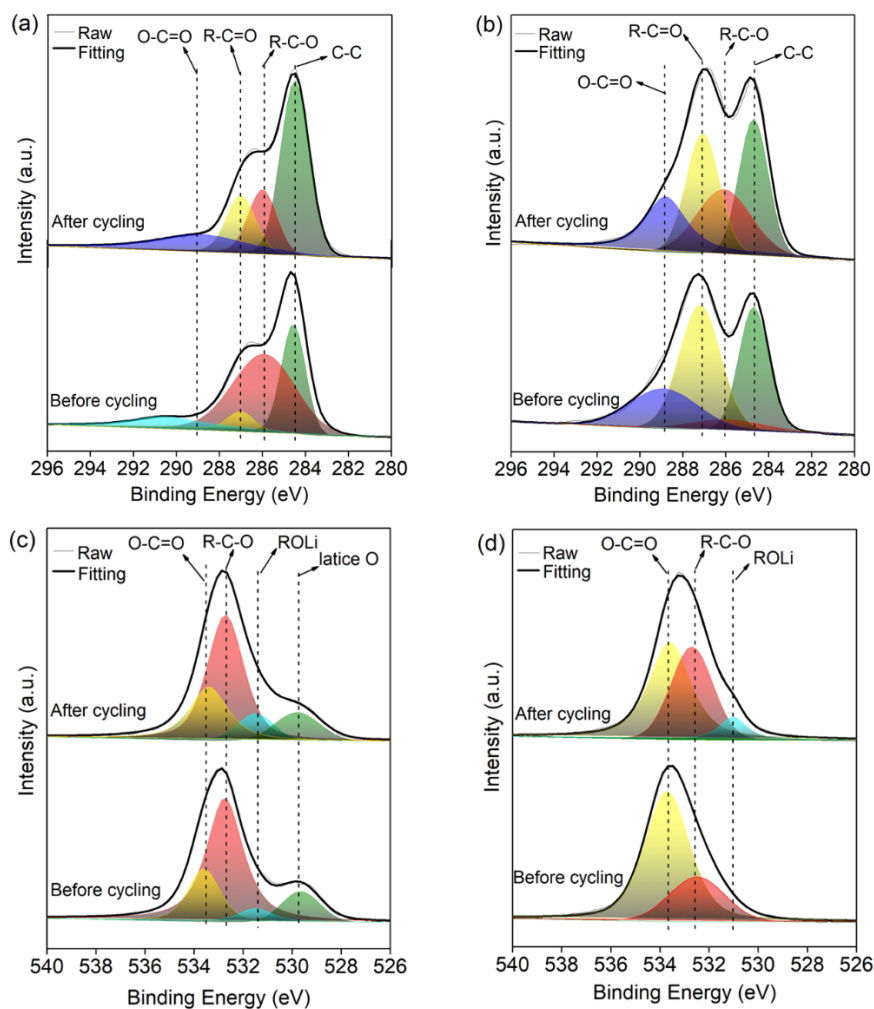


**Figure 7.3** XPS results of C1s from (a) PEO-LCO electrode surface and (b) CMC-LCO electrode surface before and after cycling in SPB for 5 cycling (discharge state); XPS results of O1s from (a) PEO-LCO electrode surface and (b) CMC-LCO electrode surface before and after cycling in SPB for 5 cycling (discharge state).

XAS at the Co L-edge was conducted to study the variation in surface chemical properties of LCO before and after charging. The results are presented in Figure 4. The Co L<sub>3,2</sub> edge XAS spectrum (**Figure 7.4**) consists of two main peaks corresponding to the transitions of Co 2p<sub>3/2</sub> and 2p<sub>1/2</sub> to unoccupied 3d states, respectively.<sup>49</sup> The TEY measurements of both the PEO-LCO and CMC-LCO electrodes exhibit similar Co L edge features compared to

that of pristine LCO particles. The Co L edge XAS spectrum of pristine LCO particles confirms the oxidation state of Co is 3+, as expected.<sup>50</sup> However, an obvious difference is detected at the low energy shoulder (778.5 eV) of the L<sub>3</sub> peak for PEO-LCO and CMC-LCO compared to pristine LCO. The increase in the shoulder peak intensity means a decrease in the unoccupied high-energy Co 3d state, indicating that Co is reduced.<sup>51-53</sup> In **Figure 7.4a**, both the PEO-LCO and CMC-LCO electrodes have a higher L<sub>3</sub> lower energy shoulder compared to that of a pristine LCO particle. This is possibly due to the interaction/reaction between the PEO or CMC binder with the LCO surface, resulting in the reduction of surficial Co, similar to how liquid electrolytes react with LCO.<sup>54,55</sup> However, after cycling, the L<sub>3</sub> lower energy shoulder intensity increases significantly for PEO-LCO, indicating that surficial reduction of the LCO by PEO is propagating during the charge/discharge process, leading to an unstable PEO/LCO interface. In contrast, after cycling, the L<sub>3</sub> lower energy shoulder of the CMC-LCO electrode decreases in intensity, indicating that the surface interaction/reaction between the LCO and CMC binder is reversible. This result illustrates that CMC-LCO has a more stable CEI than a PEO-LCO electrode in ASSPBs. From the FLY measurements (**Figure 7.4b**), no obvious difference was found in the Co XAS spectra, which suggests the reactions are isolated to the near-surface regions and the bulk of the LCO is unaffected by these parasitic side reactions.

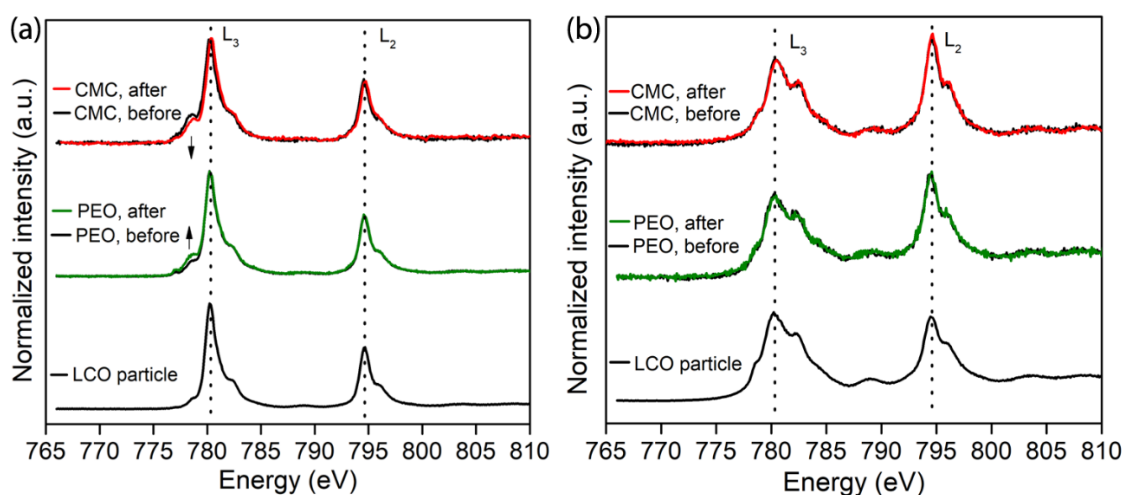


**Figure 7.4** Synchrotron-based XAS of the Co L-edge at discharge state with (a) TEY detection and (b) FLY detection for LCO particles, PEO-LCO electrodes and CMC-LCO electrodes before and after 5 cycles at full discharge state.

To determine the atomic mechanism behind the improved performance of CRPs binders over PEO and PVDF binders, the interface properties between binders and LiCoO<sub>2</sub> were further investigated by density functional theory (DFT). The details of the DFT study are listed in the supporting information. The adsorption energy and the structure of the binders adsorbed on the surface of LiCoO<sub>2</sub> (001) are shown in **Figure 7.5c-f**. For the CMC monomer and Na-alginate, the adsorption energies of -68.26 and -77.85 kcal/mol respectively, are computed to be much larger than the same amount of PEO and PVDF dipolymers (**Figure 7.5a**). Although the CMC and Na-alginate show much larger adsorption energies, their molar mass varies greatly. We therefore normalized the adsorption energy. The normalized adsorption energy (kcal/g) comparison is shown in **Figure 7.5b**, also demonstrating that the CMC and Na-alginate have stronger chemical interactions with the LiCoO<sub>2</sub> (001) surface compared to PEO and PVDF. The charge density difference (CDD) configurations of PEO and CMC adsorption are shown in **Figure S7.14**. Electron accumulation is found to occur between the carboxyl Na atom in CMC and the LCO surface. At the same time, the O atoms in PEO and CMC show electron accumulation around them, but to a lower degree than around carboxyl Na atom. The total density of states of the entire structures and the partial density of states of the adsorbed PEO and CMC are shown in **Figure S7.15**. The states from -17.5 eV to -7.5 eV are mainly from the adsorbed species, with a small contribution from the surface, indicating orbital overlapping in this energy range. The DFT simulation results suggest that stronger chemical interactions exist between the surface and CRPs binders, demonstrating better stability of CRPs binders in 4 V class ASSPBs compared to PEO and PVDF. These results are well consistent with the O K-edge XAS results in **Figure 7.2** and cycling performance results in **Figure 7.1**.

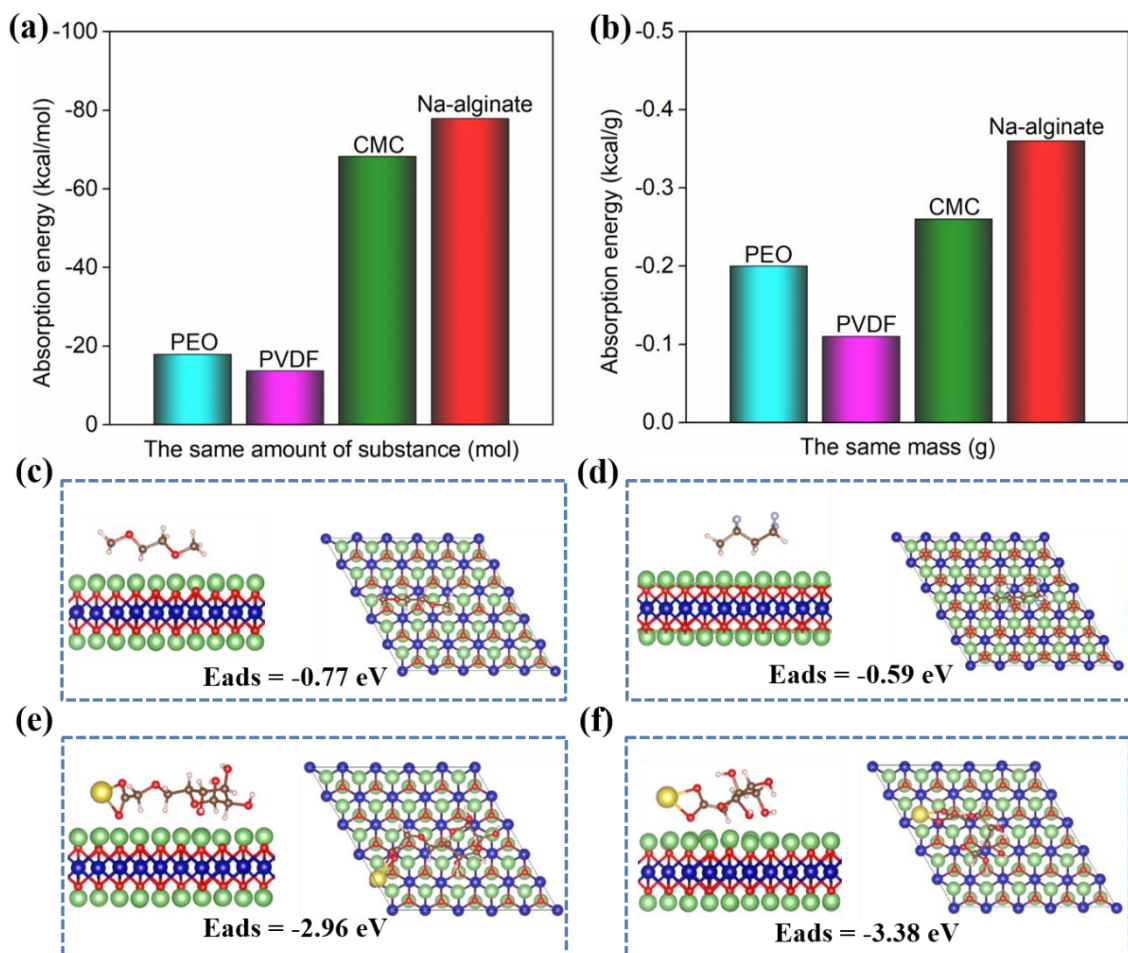


**Figure 7.5** (a) Adsorption energy comparison with the same molar quantity and (b) mass quantity (g). Optimized geometric structure and adsorption energy comparison (c) PEO dipolymer, (d) PVDF (dipolymer), (e) CMC monomer and (f) Sodium alginate monomer on LiCoO<sub>2</sub> (001).

## 7.4 Conclusion

Overall, we show that the alternation of binders can dramatically improve the cycling stability of PEO based ASSPBs. To demonstrate, four different binders including PEO, PVDF, and CRP binders (including Na-alginate and CMC) have been studied for the applications in 4 V class ASSPBs with LCO cathodes, lithium metal anodes and PEO-based SPEs. Results show that carboxyl-rich polymers are better binders for high performance and long cycle life. Mechanism studies indicate that PEO binders are highly reactive and electrochemically decomposed at high voltage, while CRP are more stable in

the same operating window. The strong chemical interactions between CRP and the LCO make these binders can not only strongly bind the carbon and LCO particles together for maintaining the structure stability of electrodes, but also work as a coating like material to avoid the detrimental effects of electronic conductive carbon for accelerating the decomposition of PEO-based SPE. Therefore, CRP binders can dramatically improve the performance of 4 V class ASSPBs. This study provides new insight for developing high-performance, long cycle life, 4V class solid polymer batteries, paving the way for high energy density SSBs for electric vehicle applications.

## Acknowledgement

This work was supported by China Automotive Battery Research Institute, Natural Sciences and Engineering Research Council of Canada (NSERC), Canada Research Chair Program (CRC), University of Western Ontario and University of Toronto. We also appreciate the helps from the beamline scientists of the Spherical Grating Monochromator (SGM) beamline at Canadian Light Source, Dr. Tom Regier, Dr. James Dynes and Dr. Zechary Arthur. D. Chen greatly appreciates China Scholarship Council (CSC) for the support of PhD study.

## References

1. K. Liu, Y. Liu, D. Lin, A. Pei and Y. Cui, *Sci. Adv.*, 2018, 4, eaas9820.
2. V. Thangadurai, S. Narayanan and D. Pinzaru, *Chem. Soc. Rev.*, 2014, 43, 4714-4727.
3. R. Murugan, V. Thangadurai and W. Weppner, *Angew. Chem. Int. Ed.*, 2007, 46, 7778-7781.
4. N. Kamaya, K. Homma, Y. Yamakawa, M. Hirayama, R. Kanno, M. Yonemura, T. Kamiyama, Y. Kato, S. Hama, K. Kawamoto and A. Mitsui, *Nat. Mater.*, 2011, 10, 682-686.
5. Y. Kato, S. Hori, T. Saito, K. Suzuki, M. Hirayama, A. Mitsui, M. Yonemura, H. Iba and R. Kanno, *Nat. Energy*, 2016, 1, 16030.
6. T. Asano, A. Sakai, S. Ouchi, M. Sakaida, A. Miyazaki and S. Hasegawa, *Adv. Mater.*, 2018, 30, 1803075.



7. X. Li, J. Liang, N. Chen, J. Luo, K. R. Adair, C. Wang, M. N. Banis, T.-K. Sham, L. Zhang, S. Zhao, S. Lu, H. Huang, R. Li and X. Sun, *Angew. Chem. Int. Ed.*, 2019, 58, 16427-16432.
8. X. Li, J. Liang, J. Luo, M. Norouzi Banis, C. Wang, W. Li, S. Deng, C. Yu, F. Zhao, Y. Hu, T.-K. Sham, L. Zhang, S. Zhao, S. Lu, H. Huang, R. Li, K. R. Adair and X. Sun, *Energy Environ. Sci.*, 2019, 12, 2665-2671.
9. P. Hovington, M. Lagacé, A. Guerfi, P. Bouchard, A. Mauger, C. M. Julien, M. Armand and K. Zaghib, *Nano Lett.*, 2015, 15, 2671-2678.
10. Z. Xue, D. He and X. Xie, *J. Mater. Chem. A*, 2015, 3, 19218-19253.
11. Y. Xia, T. Fujieda, K. Tatsumi, P. P. Prosini and T. Sakai, *J. Power Sources*, 2001, 92, 234-243.
12. K. Nie, X. Wang, J. Qiu, Y. Wang, Q. Yang, J. Xu, X. Yu, H. Li, X. Huang and L. Chen, *ACS Energy Lett.*, 2020, DOI: 10.1021/acsenerylett.9b02739.
13. H. Miyashiro, Y. Kobayashi, S. Seki, Y. Mita, A. Usami, M. Nakayama and M. Wakihara, *Chem. Mater.*, 2005, 17, 5603-5605.
14. S. Seki, Y. Kobayashi, H. Miyashiro, Y. Mita and T. Iwahori, *Chem. Mater.*, 2005, 17, 2041-2045.
15. J. Ma, Z. Liu, B. Chen, L. Wang, L. Yue, H. Liu, J. Zhang, Z. Liu and G. Cui, *J. Electrochem. Soc.*, 2017, 164, A3454-A3461.
16. T. Kobayashi, Y. Kobayashi, M. Tabuchi, K. Shono, Y. Ohno, Y. Mita and H. Miyashiro, *ACS Appl. Mater. Interfaces*, 2013, 5, 12387-12393.
17. Q. Yang, J. Huang, Y. Li, Y. Wang, J. Qiu, J. Zhang, H. Yu, X. Yu, H. Li and L. Chen, *J. Power Sources*, 2018, 388, 65-70.
18. J. Liang, Y. Sun, Y. Zhao, Q. Sun, J. Luo, F. Zhao, X. Lin, X. Li, R. Li, L. Zhang, S. Lu, H. Huang and X. Sun, *J. Mater. Chem. A*, 2020, 8, 2769-2776.
19. W. Zhou, Z. Wang, Y. Pu, Y. Li, S. Xin, X. Li, J. Chen and J. B. Goodenough, *Adv. Mater.*, 2019, 31, 1805574.
20. C. Wang, T. Wang, L. Wang, Z. Hu, Z. Cui, J. Li, S. Dong, X. Zhou and G. Cui, *Adv. Sci.*, 2019, 6, 1901036.

21. N. P. W. Pieczonka, V. Borgel, B. Ziv, N. Leifer, V. Dargel, D. Aurbach, J.-H. Kim, Z. Liu, X. Huang, S. A. Krachkovskiy, G. R. Goward, I. Halalay, B. R. Powell and A. Manthiram, *Adv. Energy Mater.*, 2015, 5, 1501008.
22. Y. Shi, X. Zhou and G. Yu, *Accounts of Chemical Research*, 2017, 50, 2642-2652.
23. S. Zhang, H. Gu, H. Pan, S. Yang, W. Du, X. Li, M. Gao, Y. Liu, M. Zhu, L. Ouyang, D. Jian and F. Pan, *Adv. Energy Mater.*, 2017, 7, 1601066.
24. T. Zhang, J.-t. Li, J. Liu, Y.-p. Deng, Z.-g. Wu, Z.-w. Yin, D. Guo, L. Huang and S.-g. Sun, *Chem. Commun.*, 2016, 52, 4683-4686.
25. H. Chen, M. Ling, L. Hencz, H. Y. Ling, G. Li, Z. Lin, G. Liu and S. Zhang, *Chem. Rev.*, 2018, 118, 8936-8982.
26. K. Lee, J. Lee, S. Choi, K. Char and J. W. Choi, *ACS Energy Lett.*, 2019, 4, 94-101.
27. K. Lee, S. Kim, J. Park, S. H. Park, A. Coskun, D. S. Jung, W. Cho and J. W. Choi, *J. Electrochem. Soc.*, 2017, 164, A2075-A2081.
28. J. Zhang, H. Zhong, C. Zheng, Y. Xia, C. Liang, H. Huang, Y. Gan, X. Tao and W. Zhang, *J. Power Sources*, 2018, 391, 73-79.
29. N. C. Rosero-Navarro, T. Kinoshita, A. Miura, M. Higuchi and K. Tadanaga, *Ionics*, 2017, 23, 1619-1624.
30. K. H. Park, Q. Bai, D. H. Kim, D. Y. Oh, Y. Zhu, Y. Mo and Y. S. Jung, *Adv. Energy Mater.*, 2018, 8, 1800035.
31. X. Yang, Q. Sun, C. Zhao, X. Gao, K. R. Adair, Y. Liu, J. Luo, X. Lin, J. Liang, H. Huang, L. Zhang, R. Yang, S. Lu, R. Li and X. Sun, *Nano Energy*, 2019, 61, 567-575.
32. G. Kresse and J. Furthmüller, *Comput. Mater. Sci.*, 1996, 6(1), 15-50.
33. P. E. Blöchl, *Phys. Rev. B*, 1994, 50(24), 17953.
34. G. Kresse, D. Joubert, *Phys. Rev. B*, 1999, 59(3), 1758.
35. J. P. Perdew, K. Burke, M. Ernzerhof, *Phys. Rev. Lett.*, 1996, 77(18), 3865.
36. S. Grimme, S. Ehrlich, L. Goerigk, *J. Comput. Chem.*, 2011, 32(7), 1456-1465.
37. H. J. Monkhorst, J. D. Pack, *Phys. Rev. B*, 1976, 13(12), 5188.
38. M. Dogangun, M. N. Hang, J. M. Troiano, A. C. McGeachy, E. S. Melby, J. A. Pedersen, R. J. Hamers, F. M. Geiger, *ACS nano*, 2015, 9(9), 8755-8765.
39. D. Kramer, G. Ceder, *Chem. Mater.*, 2009, 21(16), 3799-3809.

40. X. Huang, J. W. Bennett, M. N. Hang, E. D. Laudadio, R. J. Hamers, S. E. Mason, J. Phys. Chem. C, 2017, 121(9), 5069-5080.
41. J. Xu, E. Hu, D. Nordlund, A. Mehta, S. N. Ehrlich, X.-Q. Yang and W. Tong, ACS Appl. Mater. Interfaces, 2016, 8, 31677-31683.
42. J. Ren, F. Weber, F. Weigert, Y. Wang, S. Choudhury, J. Xiao, I. Lauermann, U. Resch-Genger, A. Bande and T. Petit, Nanoscale, 2019, 11, 2056-2064.
43. N. Bonnet-Mercier, R. A. Wong, M. L. Thomas, A. Dutta, K. Yamanaka, C. Yogi, T. Ohta and H. R. Byon, Sci. Rep., 2014, 4, 7127.
44. A. N. Mansour, D. G. Kwabi, R. A. Quinlan, Y.-C. Lu and Y. Shao-Horn, J. Electrochem. Soc., 2016, 163, A2911-A2918.
45. R. Tataru, P. Karayaylali, Y. Yu, Y. Zhang, L. Giordano, F. Maglia, R. Jung, J. P. Schmidt, I. Lund and Y. Shao-Horn, J. Electrochem. Soc., 2019, 166, A5090-A5098.
46. D. J. Xiong, R. Petibon, L. Madec, D. S. Hall and J. R. Dahn, J. Electrochem. Soc., 2016, 163, A1678-A1685.
47. L. Yang, F. Heatley, T. G. Blease and R. I. G. Thompson, Eur. Polym. J., 1996, 32, 535-547.
48. P. de Sainte Claire, Macromolecules, 2009, 42, 3469-3482.
49. W.-S. Yoon, K.-B. Kim, M.-G. Kim, M.-K. Lee, H.-J. Shin, J.-M. Lee, J.-S. Lee and C.-H. Yo, J. Phys. Chem. B, 2002, 106, 2526-2532.
50. Y. Ma, Y. Zhou, C. Du, P. Zuo, X. Cheng, L. Han, D. Nordlund, Y. Gao, G. Yin, H. L. Xin, M. M. Doeff, F. Lin and G. Chen, Chem. Mater., 2017, 29, 2141-2149.
51. F. Lin, I. M. Markus, D. Nordlund, T.-C. Weng, M. D. Asta, H. L. Xin and M. M. Doeff, Nat. Commun., 2014, 5, 3529.
52. F. Lin, D. Nordlund, T. Pan, I. M. Markus, T.-C. Weng, H. L. Xin and M. M. Doeff, J. Mater. Chem. A, 2014, 2, 19833-19840.
53. F. Lin, D. Nordlund, Y. Li, M. K. Quan, L. Cheng, T.-C. Weng, Y. Liu, H. L. Xin and M. M. Doeff, Nat. Energy, 2016, 1, 15004.
54. D. Takamatsu, Y. Koyama, Y. Orikasa, S. Mori, T. Nakatsutsumi, T. Hirano, H. Tanida, H. Arai, Y. Uchimoto and Z. Ogumi, Angew. Chem. Int. Ed., 2012, 51, 11597-11601.

55. Y. Oriksa, D. Takamatsu, K. Yamamoto, Y. Koyama, S. Mori, T. Masese, T. Mori, T. Minato, H. Tanida, T. Uruga, Z. Ogumi and Y. Uchimoto, *Adv. Mater. Interfaces*, 2014, 1, 1400195.

## Supporting information

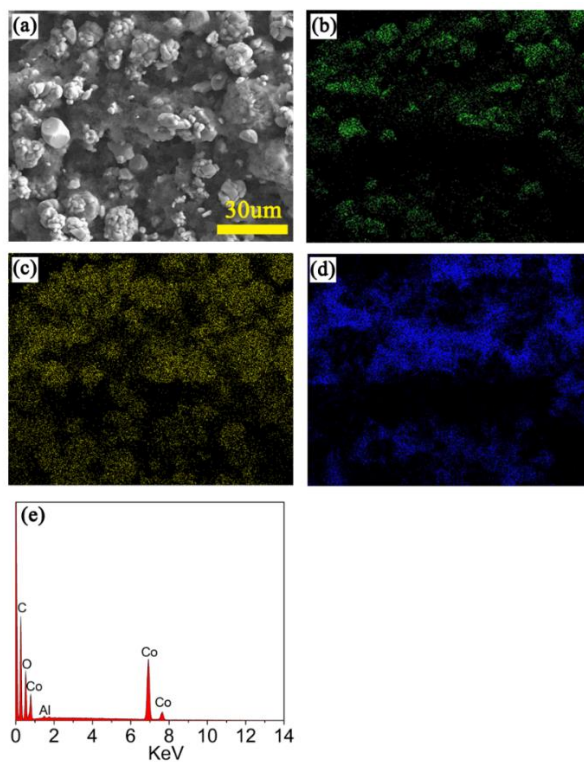


**Figure S7.1** (a) SEM image of PEO-LCO electrode surface, and its corresponding element mapping of (b) O, (c) Co, (d) C and (e) EDX spectra.

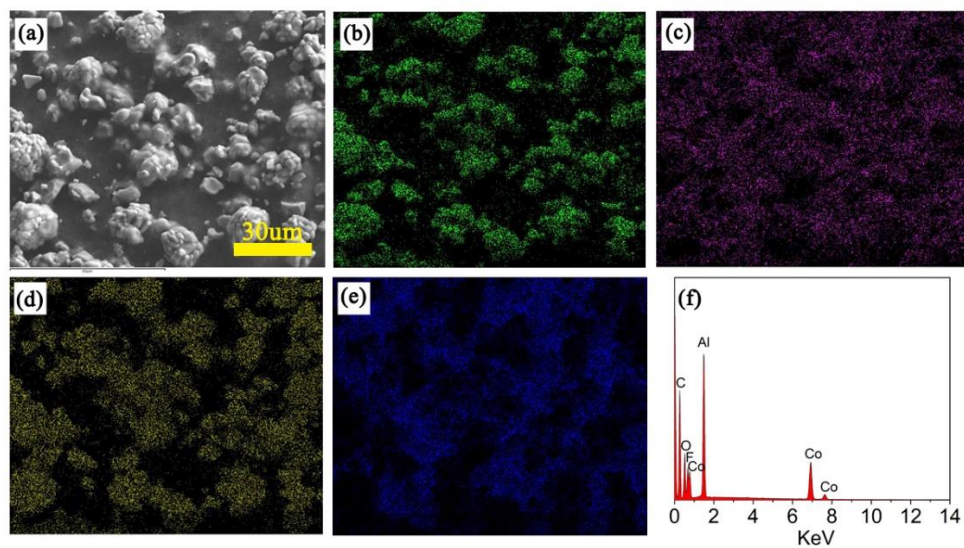


**Figure S7.2** (a) SEM image of the PVDF-LCO electrode surface, and its corresponding element mapping of (b) O, (c) F, (d) Co, (e) C and (e) EDX spectra.

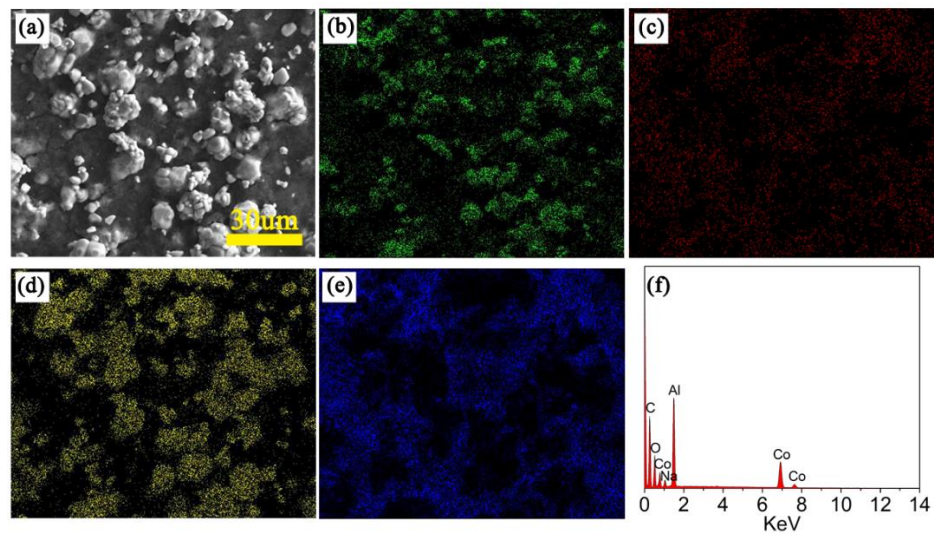


**Figure S7.3** (a) SEM image of Na-LCO electrode surface, and its corresponding element mapping of (b) O, (c) Na, (d) Co, (e) C and (e) EDX spectra.

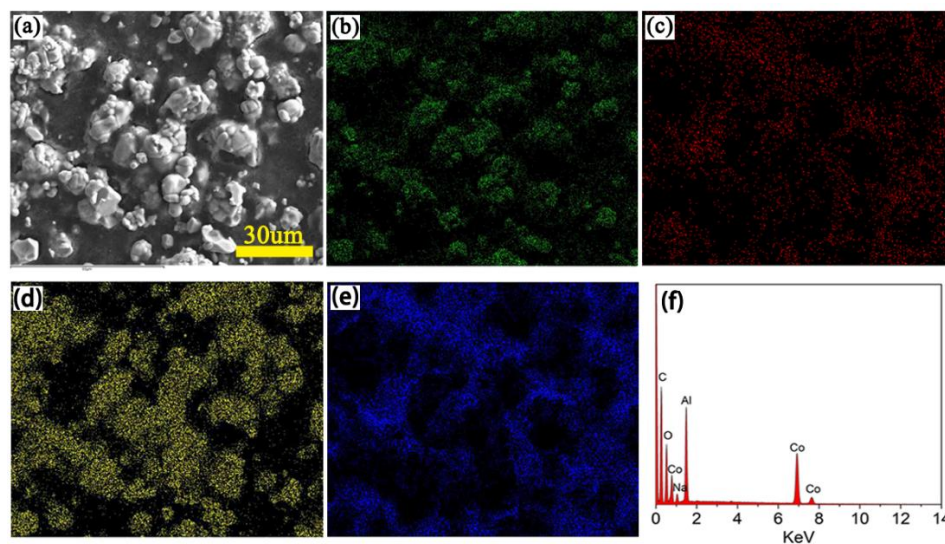


**Figure S7.4** (a) SEM image of CMC-LCO electrode surface, and its corresponding element mapping of (b) O, (c) Na, (d) Co, (e) C and (e) EDX spectra.

All binders have very good dispersion capacities for slurries with LCO particles and AB particles. Energy-dispersive X-ray spectroscopy (EDX) mapping was conducted to characterize the electrodes with different binders. EDX mapping shows that PEO-LCO has C, O, Al, Co (**Figure S7.1**), PVDF-LCO has C, O, F, Al, Co (**Figure S7.2**), and both Na-alginate-LCO and CMC-LCO have C, O, Al, Na, Co (**Figure S7.3** and **Figure S7.4**). The Al signal is a result of the carbon-coated aluminum current collector.

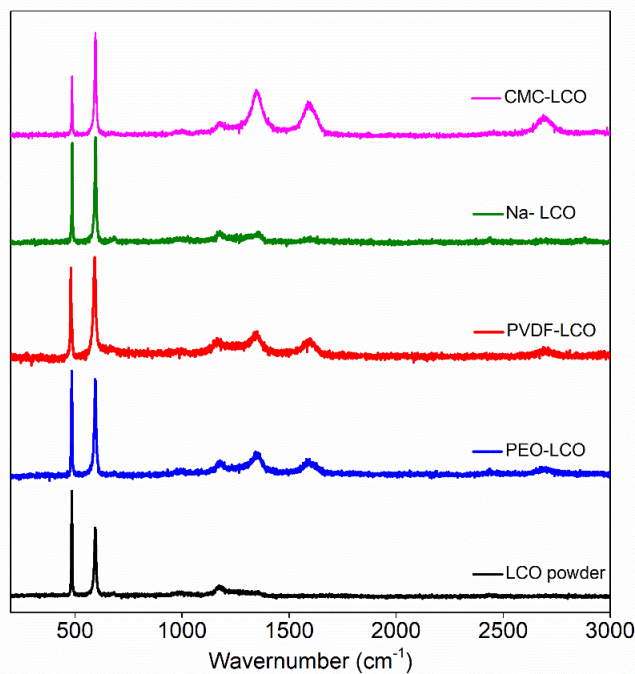


**Figure S7.5** The Raman spectrum of LCO powder, PEO-LCO, PVDF-LCO, Na-alginate-LCO, CMC-LCO.

The Raman spectra for these electrodes are shown in **Figure S7.5**. All the electrodes have prominent Raman peaks associated with LiCoO<sub>2</sub> at 485 cm<sup>-1</sup>, 595 cm<sup>-1</sup> and 1175 cm<sup>-1</sup>. The peaks at 1350 cm<sup>-1</sup>, 1590 cm<sup>-1</sup> and 2690 cm<sup>-1</sup> correspond to carbon (AB).

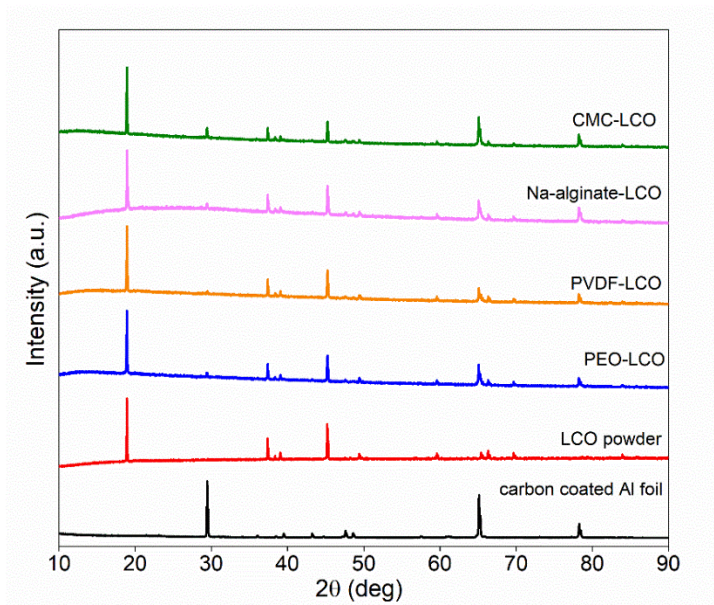


**Figure S7.6** The Raman spectrum of LCO powder, PEO-LCO, PVDF-LCO, Na-alginate-LCO, CMC-LCO.

X-ray diffraction (XRD) was conducted to characterize the phase structure of these electrodes. All electrodes show XRD patterns almost identical to the  $\text{LiCoO}_2$  powder pattern. No additional peaks attributable to impurities were found, indicating all binders and solvents are stable toward LCO powder.



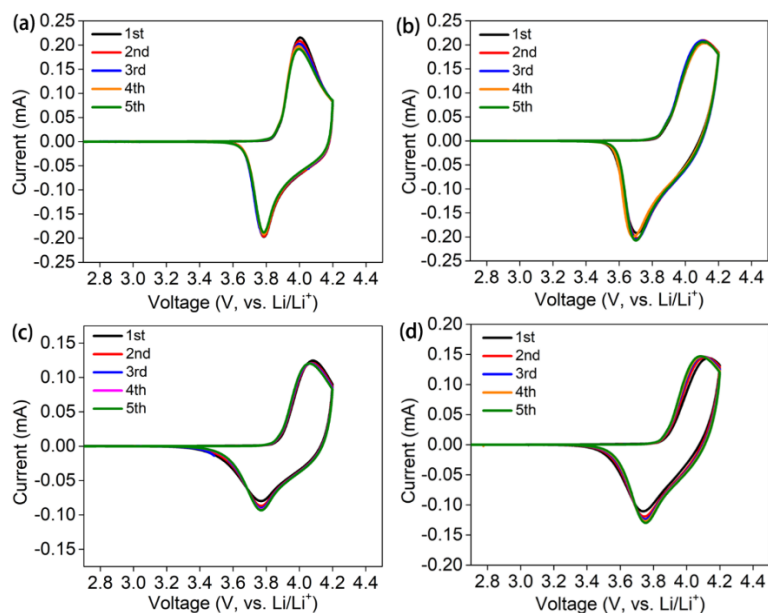


**Figure S7.7** Cyclic voltammetry of solid polymer batteries with different binders (a) PEO binder, (b) PVDF binder, (c) sodium alginate, (d) sodium carboxymethyl cellulose.

ASSPBs with LCO cathodes using different binders were assembled with PEO-based SPE and lithium metal as the anode. Electrochemical performance testing was conducted at 60 °C. Cyclic voltammetry (CV) results for these ASSPBs are shown in **Figure S7.7**. All ASSPBs show similar CV behavior, with an anodic peak corresponding to the  $\text{Li}^+$  extraction from LCO, and a cathodic peak that attributed to the  $\text{Li}^+$  insertion process into LCO. These redox pairs are the result of the conversion between  $\text{Co}^{3+}$  and  $\text{Co}^{4+}$  for the first-order phase transformation between two hexagonal phases of LCO.

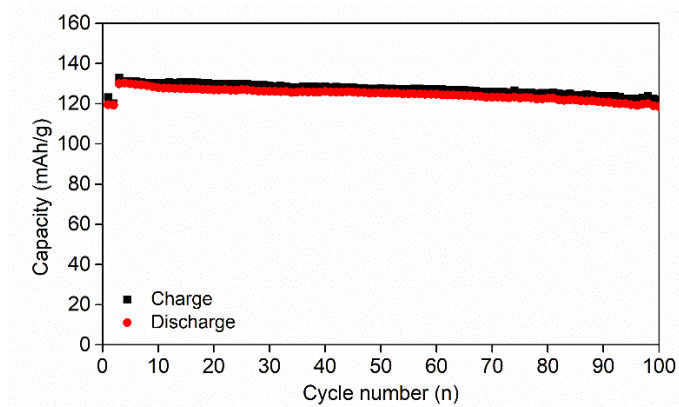


**Figure S7.8** Cycling performance of liquid based  $\text{LiCoO}_2$  batteries at room temperature with a voltage cut off of 2.7 – 4.2 V.

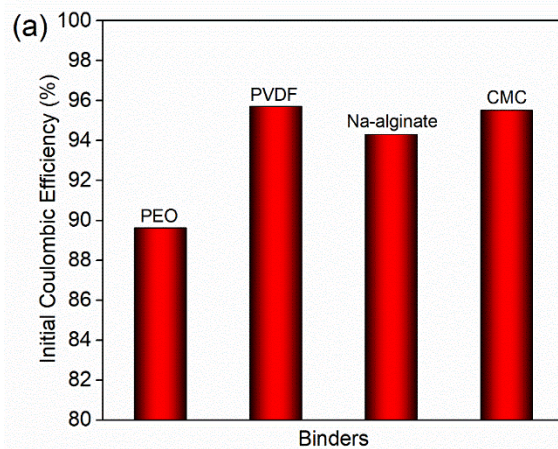


**Figure S7.9** (a) Initial coulombic efficiency of ASSPBs with different binders

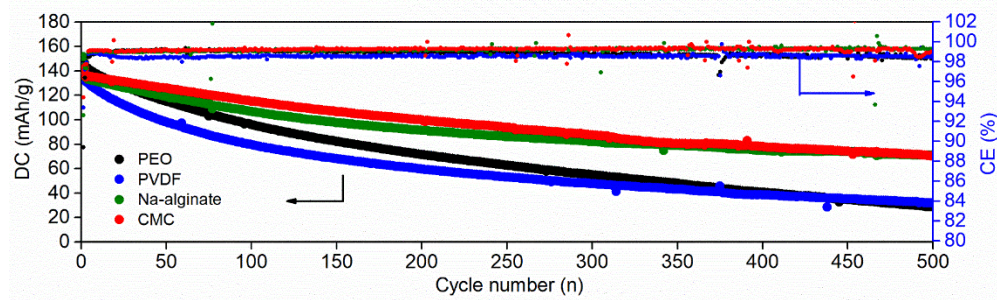


**Figure S7.10** Cycling performance of solid polymer batteries with different binders. (DC: Discharge Capacity, CE: Coulombic Efficiency) All batteries tested at 60 °C with a voltage cut off of 2.7- 4.3 V at 0.4 C current density.

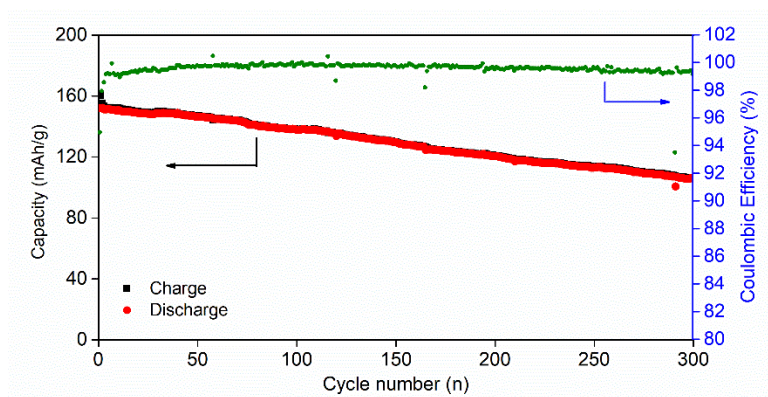


**Figure S7.11** Cycling performance of liquid based  $\text{LiCoO}_2$  batteries at room temperature with a voltage cut off of 2.7 - 4.3 V.

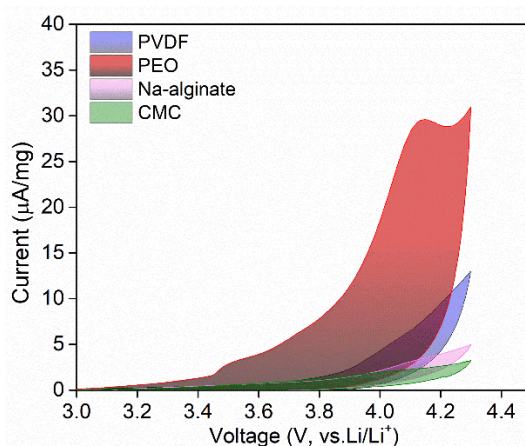


**Figure S7.12** The CV curves of  $\text{Li/SPE/binder+AB}$  cells. CV were conducted from OCV to 4.3 V vs.  $\text{Li/Li}^+$  and then back to 3 V at 60 °C.

**Table S11.** Summary of adsorption energy with the same molar quantity; and the same mass quantity

Adsorption species	$E_{\text{ads}}$ (kcal/mol)	$E_{\text{ads}}$ (kcal/g)
PVDF (dipolymer)	-13.69	-0.11
PEO (dipolymer)	-17.85	-0.20
Sodium alginate (monomer)	-77.85	-0.36
CMC-Na (monomer)	-68.26	-0.26

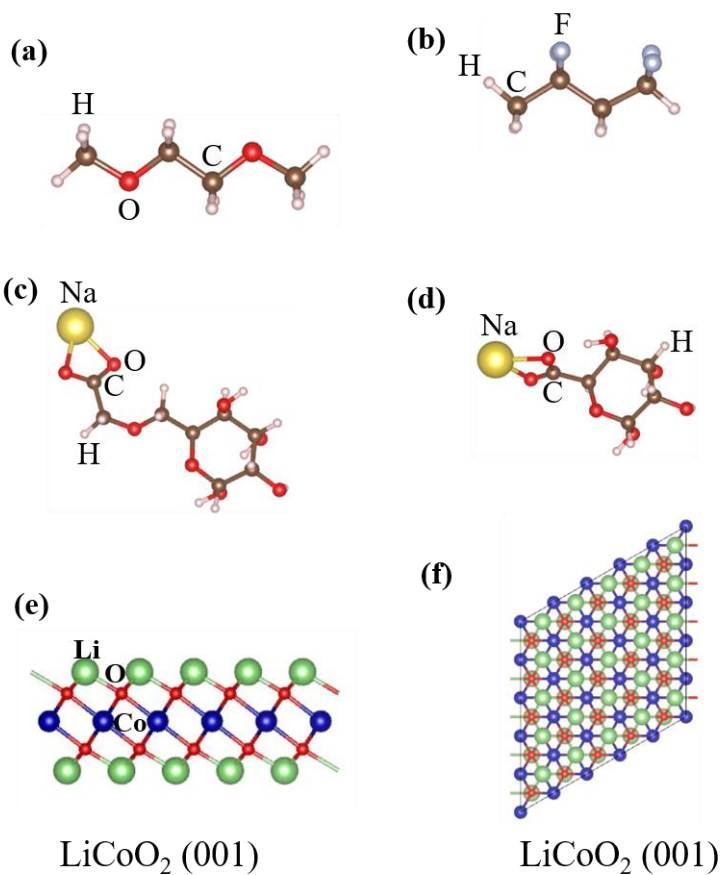


**Figure S7.13** Geometric structure of several adsorption species on a LiCoO<sub>2</sub> (001) surface, (a) PEO dipolymer; (b) PVDF (dipolymer); (c) CMC monomer; (d) Na-alginate monomer; (e) LiCoO<sub>2</sub> (001) surface (front view) and (f) LiCoO<sub>2</sub> (001) surface (top view)

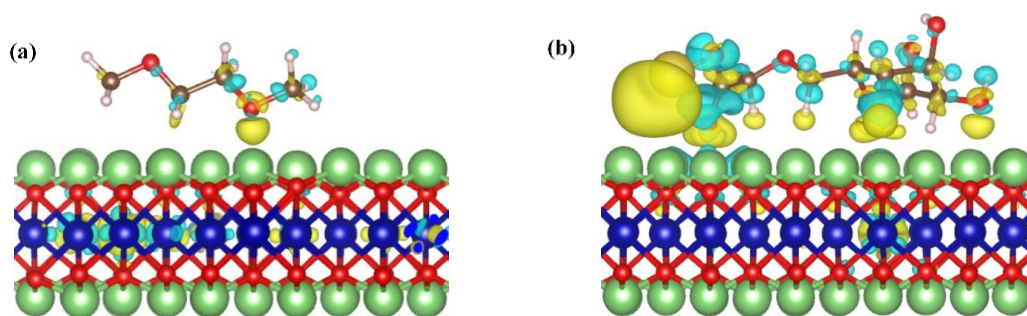


**Figure S7.14** Charge density difference (CDD) of the structure after adsorption, (a) PEO (dipolymer) adsorption, (b) CMC monomer (G unit) adsorption (the isosurface is  $0.002 \text{ e}\text{\AA}^{-3}$ )

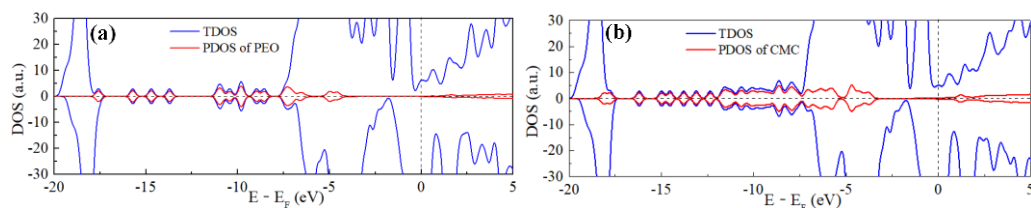


**Figure S7.15** Total density of states (TDOS) and partial density of states (PDOS) of the structure after adsorption, (a) PEO (dipolymer) adsorption, (b) CMC monomer (G unit) adsorption

## Chapter 8

### 8 In-situ synthesis of $\text{Li}_3\text{InCl}_6$ halide solid-state electrolyte for addressing interfacial challenge in $\text{LiCoO}_2$ /garnet solid-state batteries

In previous chapters, ASSLIBs with SPEs were studied. However, SPEs suffer from low ionic conductivity and low electrochemical oxidation window problems, which limit their wide application in ASSLIBs. Compared to SPEs, oxide-based SSEs have higher oxidation window and higher ionic conductivity. In the next two chapters, SSBs with oxide ceramic solid-state electrolytes, which have high ion conductivities at RT and a high electrochemical oxidation window will be studied.

However, due to their rigid properties, oxide-based SSEs have poor capacity to maintain intimate contact with powder electrode materials. To address this challenge,  $\text{Li}_3\text{BO}_3$  as a co-sintering assistance, is the most popular material for building all ceramic batteries. However,  $\text{Li}_3\text{BO}_3$  has lower ionic conductivity and a high melting point, which limit the release capacity and the loading of active materials. In this study, in-situ synthesis of  $\text{Li}_3\text{InCl}_6$  halide SSE, which has ionic conductivity over  $10^{-3}$  S/cm, at the oxide-based garnet SSE and  $\text{LiCoO}_2$  interface, was achieved by solution synthesis method. The solution method helps  $\text{Li}_3\text{InCl}_6$  uniformly distribute at the garnet SSE and  $\text{LiCoO}_2$  interface, resulting in a continuous  $\text{Li}^+$  ion channel within the thick electrode. Therefore, with such a  $\text{Li}_3\text{InCl}_6$ - $\text{LiCoO}_2$  composite cathode, ASSLIBs with garnet SSEs can operate at 0.1 C, with a discharge capacity of 129.2 mAh/g, which is comparable to that of liquid organic electrolyte-based LIBs. This study provides a new approach to build ASSLIBs with garnet oxide SSEs, paving the way for developing high energy density and safe ASSLIBs for practical application.

---

**J. Liang**,<sup>#</sup> Jing Luo,<sup>#</sup> Weihan Li, Junjie Li, Jiamin Fu, Liam Israels, Jianwen Liang, Qian Sun, Ruying Li, Shangqian Zhao, Li Zhang, Shigang Lu, Huan Huang, and Xueliang Sun\*

<sup>#</sup> J. Liang and J. Luo contributed equally to this work.

## 8.1 Introduction

Lithium ion batteries (LIBs) with liquid organic electrolytes are potentially unsafe due to the flammability of the liquid organic electrolyte. Therefore, developing all-solid-state lithium ion batteries (ASSLIBs) with an inorganic solid-state electrolyte (SSE) have been considered as the ultimate solution for addressing the safety issue of LIBs. To obtain high performance ASSLIBs, many types of inorganic SSEs have been developed, including sulfide-based SSEs,<sup>1-3</sup> oxide-based SSEs<sup>4,5</sup> and halide-based SSEs,<sup>6-8</sup> etc. Sulfide-based SSEs, such as  $\text{Li}_{10}\text{GeP}_2\text{S}_{12}$  (LGPS) and  $\text{Li}_6\text{PS}_5\text{Cl}$  (LPSC), have received plenty of research attention in ASSLIBs due to their high ionic conductivity at room temperature (RT) and relatively soft mechanical property, which enable them to achieve good contact with electrodes. Unfortunately, sulfide-based SSEs are unstable to moisture,<sup>9,10</sup> and they have a narrow electrochemical stability window,<sup>11,12</sup> which make them incompatible with cathode materials and lithium metal anodes, seriously limiting the energy density of ASSLIBs. Halide-based SSEs also have high ionic conductivity at RT; over  $10^{-3}$  S/cm.<sup>6-8</sup> Halide-based SSEs have excellent compatibility with cathode materials, which have made them attract more and more research interests in recent years. However, the problems including instability toward moisture and incompatibility with anode materials still seriously limit their wide application in ASSLIBs.<sup>6-8</sup>

Oxide-based SSEs, such as garnet type SSE  $\text{Li}_7\text{La}_3\text{Zr}_2\text{O}_{12}$  (LLZO) and its derivatives with Ta and Al doping, attracted increasing attention due to its higher air stability and electrochemical stability, as well as high ionic conductivity at RT.<sup>13</sup> It has excellent compatibility with lithium metal anodes.<sup>11</sup> However, the mismatch problem between electrode and SSE is still the main challenge for oxide-based SSEs. To tackle the mismatch problem, several strategies have been developed. For LLZO and lithium metal anode interface, melting lithium metal on the surface of LLZO and then solidifying lithium metal is the most popular way to address the interfacial mismatch problem.<sup>14</sup> Melted lithium has good fluidity that can fill the uneven surface of the SSE. However, LLZO SSEs may behave ‘lithiumphobically’, still leading to poor contact.<sup>14</sup> To turn the ‘lithiumphobic’ surface of LLZO to a ‘lithiumphilic’ surface, coating with an ‘lithiumphilic’ material, such as Al,  $\text{Al}_2\text{O}_3$ , ZnO, Ge, Au etc. is a facile method to realize intimate contact and low interfacial

resistance of the LLZO/Li interface.<sup>14-18</sup> Another opinion is that the reason why pristine LLZO is not ‘lithiophobic’ is because of the formation of  $\text{Li}_2\text{CO}_3$  and  $\text{LiOH}$  on the surface of LLZO, which behaves ‘lithiophobically’. Therefore, by removing the  $\text{Li}_2\text{CO}_3$  and  $\text{LiOH}$  impurities of LLZO, it will behave ‘lithiophilically’.<sup>19,20</sup>

The LLZO/Li interface issues have been reasonably addressed by the above-mentioned approaches. However, the LLZO/cathode interface is still the most challenging for oxide based ASSLIBs. Firstly, melting strategy cannot be applied to reduce the LLZO/cathode interfacial resistance, since both LLZO and cathode materials have very high melting points. Secondly, cathode materials usually are dispersed particles with micrometer or nanometer size. The dispersed particles have great difficulty in achieving continuous  $\text{Li}^+$  ion pathways with the point to point contact property. To address the oxide-based SSE/cathode interface challenge and realize practical ASSLIBs, several strategies have been studied. Firstly, applying liquid organic electrolyte to fill the gaps between oxide-based SSE and cathode particles to provide a continuous lithium flux.<sup>21</sup> However, the usage of liquid organic electrolyte may still pose safety issues for battery application. Secondly, applying solid polymer electrolyte (SPE) as the buffer layer for connecting oxide-based SSE and cathode materials by taking the advantage of the intimate contact between polymer and rigid particles.<sup>22</sup> Unfortunately, SPEs have low ionic conductivity and high interfacial resistance with oxide-based SSE and cathode materials at RT. Thirdly, creating a 3D porous SSE structure for enlarging the contact area between SSE and active materials, to enhance the usage percentage of active materials.<sup>23</sup> However, the interfacial resistance is still too high for practical ASSLIBs. Fourthly, in-situ depositing cathode materials directly on the surface of the SSE to realize intimate contact.<sup>24</sup> However, such a method can only deposit a thin film of cathode material, thereafter, the loading of active material is low. Last but not least, applying a low melting point of SSE as a co-sintering assistant to bridge the SSE and cathode interface. This low melting point SSE, such as  $\text{Li}_3\text{BO}_3$ , has been widely used in the fabrication of ASSLIBs.<sup>25-27</sup>  $\text{Li}_3\text{BO}_3$  is one of the most popular low melting point SSEs for building oxide based ASSLIBs due to its relatively low melting point (700 °C) and relatively high ionic conductivity at RT.<sup>28</sup>



However, the melting point of  $\text{Li}_3\text{BO}_3$  is still high, which will possibly result in the elemental diffusion between cathode and SSE. Moreover, the ionic conductivity of  $\text{Li}_3\text{BO}_3$  is at the range of  $10^{-6}$  -  $10^{-5}$  S/cm,<sup>28</sup> which limit the rate performance and current density of ASSLIBs. Therefore, most of the oxide based ASSLIBs built by  $\text{Li}_3\text{BO}_3$  can only run below 0.05 C. In the study, in great contrast to  $\text{Li}_3\text{BO}_3$ , halide-based SSEs, which have low sintering temperature (200 °C) and high ionic conductivity ( $10^{-3}$  S/cm), and good compatibility with the cathode,<sup>6,7</sup> are used as a co-sintering assistance for building oxide based ASSLIBs. ASSLIBs, with a LLZO SSE and  $\text{LiCoO}_2$  cathode, are fabricated with the help of in-situ formation of a  $\text{Li}_3\text{InCl}_6$  halide SSE at the interface between the LLZO SSE and  $\text{LiCoO}_2$ , by solution method. These ASSLIBs can deliver a discharge capacity of 129.2 mAh/g, which is comparable to that of liquid organic electrolyte-based LIBs, at 0.1 C, at the same voltage range. Moreover, even with as high as 13 mg/cm<sup>2</sup> active material loading, ASSLIBs can still operate at 0.1 C, which is a benefit from the high ionic conductivity of the  $\text{Li}_3\text{InCl}_6$  halide SSE. The superior electrochemical performance of oxide based ASSLIBs demonstrates that halide SSEs are a good interfacial engineering medium for addressing the mismatch problem between oxide-based SSEs and cathodes.

## 8.2 Experimental

### 8.2.1 Preparation of LLZO solid-state electrolyte

LLZO ( $\text{Li}_{6.4}\text{La}_3\text{Zr}_{1.4}\text{Ta}_{0.6}\text{O}_{12}$ ) powders were mixed with Polyvinyl alcohol (PVA) binder and then pressed into green pellets with 12 mm diameter and 1 mm thickness. These green pellets were then transferred into a Muffle furnace for sintering. The temperature was first set to 500 °C for 1 h to decompose the PVA binder and was then shifted to 1200 °C, at the rate of 1 °C/min for 6 h. LLZO SSE pellets were then obtained after the temperature cooled down. The obtained LLZO pellets were polished with sandpaper before they were used for building all-solid-state lithium ion batteries.

### 8.2.2 Preparation of LIC-LCO-AB composite cathode on the surface of LLZO SSE.

The LIC-LCO-AB composite cathode was prepared by dissolving 12.72 mg LiCl and 29.38 mg  $\text{InCl}_3 \cdot 4\text{H}_2\text{O}$  in a certain volume of water-ethanol (1:1) solution, which resulted in 34.83

mg of  $\text{Li}_3\text{InCl}_6$ . Then LCO powders and Acetylene black (AB) powders were added into the solution. The weight ratio of LIC:LCO:AB were set at 30: 70: 0, 30: 65:5, 30:60:10, 30:55:15 and 40:50:10, 50:40:10 for different composite electrodes. Then, the mixture was dropped on the surface of the LLZO SSE by using a Pipette. The loading of LCO was controlled by the volume of mixture using a Pipette. After evaporating the solvent at RT, the samples were transferred to a high vacuum oven at 80 °C for 12 h. Then, the temperature was shifted to 200 °C for 5 h and then cooled down to RT. After the temperature reached RT, the samples were taken out and transferred into a glovebox for battery assembly. The loading of LCO was further confirmed by the balance before battery assembly.

### 8.2.3 ASSLIB assembly

The ASSLIBs consisting of a LLZO SSE, LIC-LCO-AB composite cathode and lithium metal anode were assembled in the Ar-filled glovebox. For the lithium metal/LLZO interface, a thin layer of PEO-based solid polymer electrolyte (SPE) or 2 $\mu\text{l}$  liquid organic electrolyte was used to reduce the interface resistance. ASSLIBs were tested at 60 °C with a current density of 0.1 C (1 C = 140 mAh/g) for ASSLIBs with SPE and they were tested at room temperature for ASSLIBs with a liquid organic electrolyte modified Li/LLZO interface. The voltage range was 3 - 4.2 V for all the ASSLIB testing.

### 8.2.4 Material characterizations

A Hitachi S-4800 field emission scanning electronic microscope (FE-SEM), equipped with energy dispersive X-ray spectroscopy (EDX), was used to characterize the morphology and element distribution in samples. X-ray absorption spectroscopy (XAS) measurements were collected at the Soft X-ray Microcharacterization Beamline (SXRMB) and Hard X-ray Micro-Analysis (HXMA) in the Canadian light source (CLS). Raman spectra were collected in Renishaw via Raman microscope; laser wavelength = 514.5 nm. XRD were collected in the Bruker D8 Advance Diffractometer XRD system.

## 8.3 Results and discussion

The procedures for building the ASSLIBs are illustrated in **Figure 8.1**. Stoichiometric quantities of  $\text{LiCl}$  and  $\text{InCl}_3 \cdot 4\text{H}_2\text{O}$  were first dissolved in a certain amount of water-ethanol

(1:1) solvent. Then, a certain amount of  $\text{LiCoO}_2$  (LCO) powders and acetylene black (AB) were added into the mixture solvent. The mixture was then drawn by a Pipette, with controllable volume and dropped on the surface of the LLZO SSE pellet. The dropped mixture dispersed spontaneously on the surface of the LLZO surface. The LLZO SSEs with this composite cathode were then transferred into a high vacuum oven at  $80\text{ }^\circ\text{C}$  for 12 h, followed by shifting the temperature to  $200\text{ }^\circ\text{C}$  for 5 h, to obtain  $\text{Li}_3\text{InCl}_6$  (LIC). After that, the temperature of the oven spontaneously cooled down to RT (without shutting down the vacuum). The obtained LLZO SSEs with composite cathodes were transferred to gloveboxes for further use. By using the solution base synthesis method, a  $\text{Li}_3\text{InCl}_6$  halide SSE is uniformly distributed on the  $\text{LiCoO}_2$  particles' surface and bind with LLZO to build intimate contact. This is very helpful for building intimate contact between SSE and electrode and providing continuous lithium flux within the cathode electrode. Therefore, it is expected that such a composite cathode system (LIC-LCO-AB) can achieve high rate performance and high percent usage of active materials (high charge/discharge capacity).

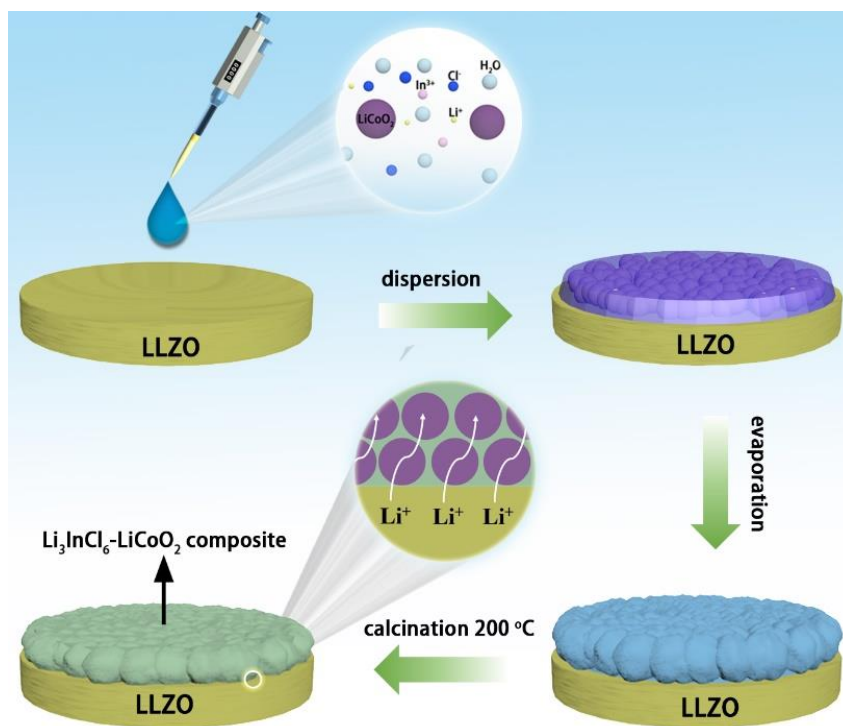


**Figure 8.1** Schematic diagram shows processes of making a LIC-LCO-AB composite cathode at the surface of a garnet LLZO SSE surface. The acetylene black powders are omitted.

The LIC-LCO-AB composite cathode was characterized by XRD, Raman and the synchrotron-based hard X-ray absorption spectroscopy (XAS) at In K-edge studies. As shown in **Figure SI8.1**, XRD spectra of LIC-LCO-AB has no impurity phase formation, meaning there is not side-reaction between the LLZO, LCO and  $\text{Li}_3\text{InCl}_6$ . For the Raman spectra of LIC-LCO-AB (**Figure SI8.2**), a peak at  $280\text{ cm}^{-1}$  corresponding to  $\text{Li}_3\text{InCl}_6$  arise, which means the success of the synthesis of  $\text{Li}_3\text{InCl}_6$ . The successfully synthesis of  $\text{Li}_3\text{InCl}_6$  in the LIC-LCO-AB composite cathode is further confirmed by the In K-edge XAS spectra (**Figure SI8.3**). The In K-edge XAS spectra of LIC-LCO-AB present the same as that of  $\text{Li}_3\text{InCl}_6$ .

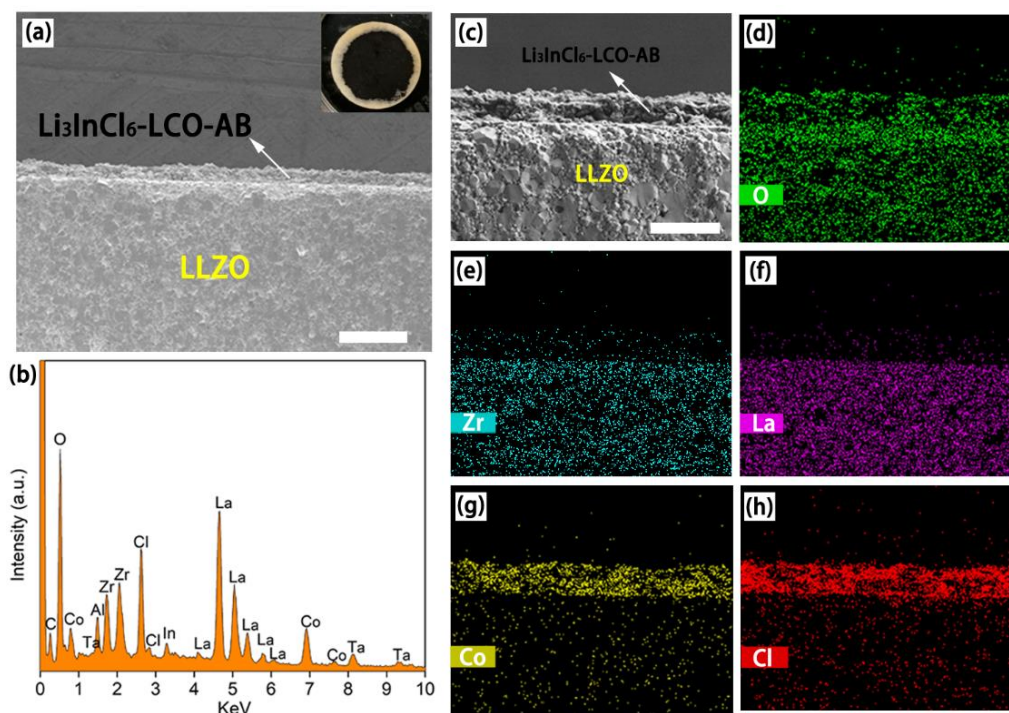


**Figure 8.2** SEM images of cross-section of (a) LIC-LCO-AB composite electrode on the surface of LLZO at low magnification (b) EDX spectrum of cross-section LIC-LCO-AB composite electrode at low magnification (c). (d)-(h) elemental EDX mapping of O, Zr, La, Co, and Cl, respectively. Scale bare:  $100\mu\text{m}$  for (a),  $50\mu\text{m}$  for (c).

**Figure 8.2a** shows the cross-section SEM image of a LLZO SSE with the LIC-LCO-AB composite cathode, where the composite cathode has intimate contact with the LLZO SSE. The insert is the photo image of the top view of a LIC-LCO-AB composite cathode on a

LLZO surface. EDX was conducted to study the distribution of elements. The EDX spectrum is shown in **Figure 8.2b**. The SEM image with its corresponding elemental distributions of O, Zr, La, Co, and Cl are presented in **Figure 8.2c-h**. The thickness of cathode is around 35  $\mu\text{m}$ , as we can see from the SEM image. Co and Cl elements coming from  $\text{LiCoO}_2$  and  $\text{Li}_3\text{InCl}_6$  respectively, are uniformly distributed on the top of the LLZO SSE. The uniformly distributed  $\text{Li}_3\text{InCl}_6$  in the composite cathode is the key for building a continuous  $\text{Li}^+$  flux channel for the thick electrode.

The influence of the content of  $\text{Li}_3\text{InCl}_6$  and AB in the composite cathode were systematically studied. For a certain content of  $\text{Li}_3\text{InCl}_6$ , different contents of AB ranging from 0% to 15% were first studied. The initial charge/discharge capacities, shown in **Figure SI8.4**, indicate that 10% of AB can release better charge/discharge capacity compared to other contents of AB additive. A low content of AB (5% or 0%) cannot provide sufficient electronic conductivity, while a high content of AB will result in poor electrode bonding, due to the high surface area of AB accommodating a big amount of  $\text{Li}_3\text{InCl}_6$ . The content of  $\text{Li}_3\text{InCl}_6$  at the same amount of AB (10%) was then studied. As shown in **Figure 8.3a,b**, with the increase in the content of  $\text{Li}_3\text{InCl}_6$ , there is a decrease in the overall cell resistance and an increase in the charge/discharge capacity. The over cell resistance, for 30% content of  $\text{Li}_3\text{InCl}_6$ , is around 2100  $\Omega$ ; it decreases to around 1000  $\Omega$  with 50% content of  $\text{Li}_3\text{InCl}_6$ . For the released discharge capacity, it is 84.7 mAh/g for 30%  $\text{Li}_3\text{InCl}_6$ , and 120.7 mAh/g for 40%  $\text{Li}_3\text{InCl}_6$ , increasing to 129.2 mAh/g for 50%  $\text{Li}_3\text{InCl}_6$ , which means a higher content of  $\text{Li}_3\text{InCl}_6$  lead to better electrochemical performance. However, a higher content of  $\text{Li}_3\text{InCl}_6$  sacrifices the loading of active materials. Therefore, 40% of  $\text{Li}_3\text{InCl}_6$ , 10% of AB and 50%  $\text{LiCoO}_2$ , as the composite cathode, was used for further battery testing and studies. ASSLIBs with different loading of  $\text{LiCoO}_2$  was also investigated from 2  $\text{mg}/\text{cm}^2$  to 13  $\text{mg}/\text{cm}^2$ . Their charge/discharge voltage-capacity profiles at 0.1 C are compared in **Figure 8.3c**. A discharge capacity of 120.7 mAh/g for 2  $\text{mg}/\text{cm}^2$  is obtained. When the loading increases to 4  $\text{mg}/\text{cm}^2$ , although the overpotential increase a little bit, the discharge capacity can still maintain at 116 mAh/g. The discharge capacity of 58 mAh/g is achieved for the loading of 8  $\text{mg}/\text{cm}^2$ . If the loading increased to 13  $\text{mg}/\text{cm}^2$ , the delivered capacity still has 16 mAh/g at 0.1 C. Such a good, high loading performance of the ASSLIBs indicates  $\text{Li}_3\text{InCl}_6$  halide SSE is a

good co-sintering medium for building lithium ion channels within the thick electrode, in oxide based ASSLIBs. **Figure 8.3d** shows the long cycling performance of ASSLIBs with  $4 \text{ mg/cm}^2$  of active materials loading. This stable cycling performance indicates the high interfacial stability between the LIC-LCO-AB composite cathode and LLZO SSE.

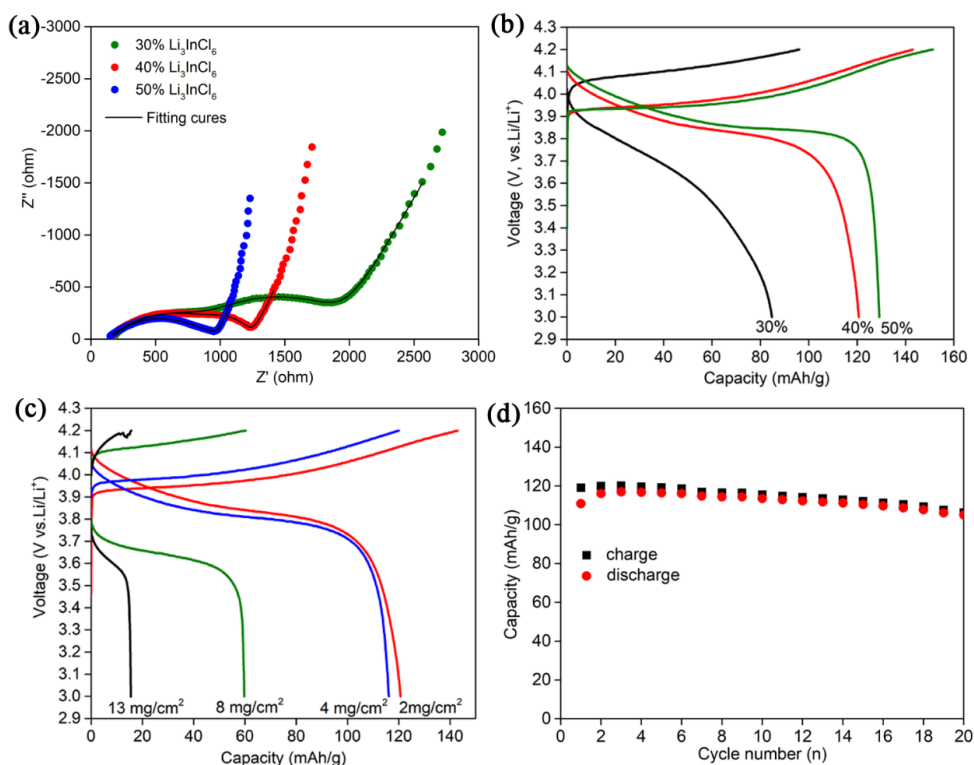


**Figure 8.3** (a) EIS spectrum of ASSLIBs with 30 %, 40 % and 50 %  $\text{Li}_3\text{InCl}_6$  in LCO composite electrode. (b) charge/discharge profiles of ASSLIBs with 30 %, 40 % and 50 %  $\text{Li}_3\text{InCl}_6$  in LCO composite electrode at 0.1 C. (c) charge/discharge profiles of ASSLIBs with 40 %  $\text{Li}_3\text{InCl}_6$  in LCO composite cathode with different LCO active materials loading at 0.1 C. (d) Cycling performance of ASSLIB with  $4 \text{ mg/cm}^2$  loading of LCO at 0.1 C. All the batteries were tested at  $60^\circ\text{C}$  because a dry PEO-based SPE was used at the lithium anode side for reducing the interface resistance between the lithium and garnet SSE.

The interfacial stability between  $\text{LiCoO}_2$  and  $\text{Li}_3\text{InCl}_6$  have been comprehensively studied by X. Li et al.<sup>6</sup> They concluded that the  $\text{LiCoO}_2$  and  $\text{Li}_3\text{InCl}_6$  interface is quite stable. There is not necessary for further study the stability between  $\text{LiCoO}_2$  and  $\text{Li}_3\text{InCl}_6$  in here. However, in this study, the interface between LLZO and  $\text{Li}_3\text{InCl}_6$  also matters since

$\text{Li}_3\text{InCl}_6$  bridges the  $\text{Li}^+$  ion flux from LLZO to  $\text{LiCoO}_2$ . Therefore, the stability of LLZO and  $\text{Li}_3\text{InCl}_6$  is investigated by synchrotron based XAS. The results are shown in **Figure 8.4**. For comprehensive studies, five samples, including pristine LLZO powders, pristine  $\text{Li}_3\text{InCl}_6$  powders, LLZO- $\text{Li}_3\text{InCl}_6$  mixture powders, LLZO- $\text{Li}_3\text{InCl}_6$  mixture powders with 200 °C treatment and in-situ synthesis of  $\text{Li}_3\text{InCl}_6$  on the LLZO powders, are studied and compared. **Figure 8.4a, b** shows the La and Zr  $L_3$ -edge XAS spectra, respectively. For La  $L_3$ -edge XAS, the white line feature A is corresponding to the direct transition from core p electrons to partial empty d states, peak C results from the contributions of multiple scattering; the so-called shape resonances.<sup>29</sup> For these four samples with LLZO powders, all La  $L_3$ -edge XAS spectra exhibit almost the same feature, which mean LLZO is stable towards  $\text{Li}_3\text{InCl}_6$ , either by simply the mixing of powders or the in-situ synthesis process. In Zr  $L_3$ -edge XAS, two identical peaks, A' and B' appear. Peaks A' and B' result from the transitions of 2p to  $e_g$  and 2p to  $t_{2g}$ , respectively. The peak ratio A'/B' reflects the difference in the compositions of  $4d_{2/3}$  ( $4d_{5/2}$ ) in  $e_g$  and  $t_{2g}$  states.<sup>30</sup> For these four samples with LLZO powders, all Zr  $L_3$ -edge XAS spectra also exhibit the same feature, which again supports that LLZO is stable towards  $\text{Li}_3\text{InCl}_6$ .

The stability of  $\text{Li}_3\text{InCl}_6$  was studied by In  $L_3$ -edge XAS and Cl K-edge XAS. For In  $L_3$ -edge XAS (**Figure 8.4c**), a white line at 3732 eV is the result of the transition from 2p to localized s state.<sup>31</sup> Another peak at 3740 eV is possibly the result of the electronic transitions from 2p to unoccupied d state, or 2p to 5s electronic transition enhanced by s-d orbital hybridization.<sup>31</sup> These four  $\text{Li}_3\text{InCl}_6$  containing samples have similar In  $L_3$ -edge XAS spectra. However, for these samples with 200 °C treatment, the intensity of the peaks at 3732 eV and 3740 eV decrease. But the spectra for these two samples behave almost the same, which means it is the temperature treatment that influences the change of spectra, not the mixing process. The in-situ synthesis  $\text{Li}_3\text{InCl}_6$  with LLZO powders behaves the same as the LLZO- $\text{Li}_3\text{InCl}_6$  powder mixture after 200 °C treatment, which means the existence of LLZO powders will not influence the phase formation of in-situ synthesis  $\text{Li}_3\text{InCl}_6$ . For Cl K-edge XAS spectra, the peak at 2822.5 eV is attributed to the transitions from Cl 1s shell to unoccupied orbitals with localized p character. There are also another two peaks at 2827 and 2829 eV for Cl K-edge XAS spectra. All these  $\text{Li}_3\text{InCl}_6$  containing samples have similar Cl K-edge XAS spectra, however, similar to the behavior of In  $L_3$ -

edge XAS, after 200 °C treatment, the intensity of the peaks at 2822.5 eV decrease, which again supports that the existence of LLZO powders will not influence the phase formation of in-situ synthesis  $\text{Li}_3\text{InCl}_6$ . The intensity difference might be the result of distorted octahedral structure with different bond angles in  $\text{Li}_3\text{InCl}_6$ , due to the vacancies of In or Cl after 200 °C treatment with the existence of LLZO powders. This is probably due to the interphase formation between LLZO and  $\text{Li}_3\text{InCl}_6$  at 200 °C. This interphase formation may be helpful for enhancing the  $\text{Li}^+$  ion transportation from LLZO to  $\text{Li}_3\text{InCl}_6$ .

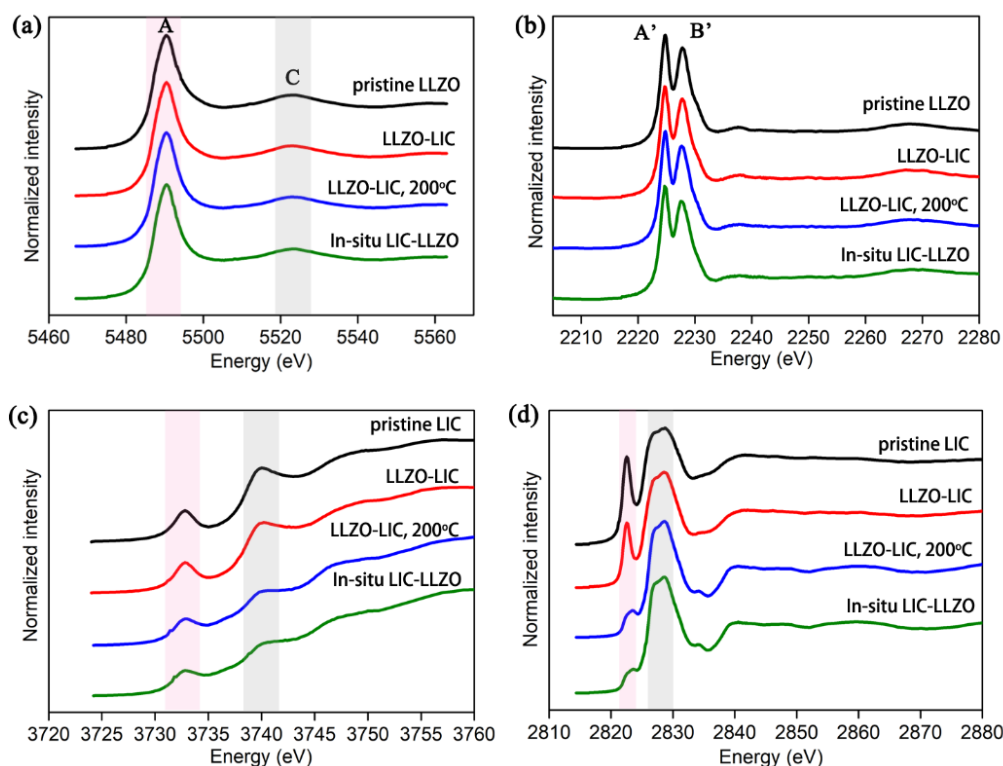


**Figure 8.4** Synchrotron based XAS results from five samples including pristine LLZO powders, pristine  $\text{Li}_3\text{InCl}_6$  powders, LLZO- $\text{Li}_3\text{InCl}_6$  mixture powders, LLZO- $\text{Li}_3\text{InCl}_6$  mixture powders with 200 °C treatment and in-situ synthesis of  $\text{Li}_3\text{InCl}_6$  on the LLZO powders at 200 °C. (a) La  $L_3$ -edge XAS spectra; (b) Zr  $L_3$ -edge XAS spectra; (c) In  $L_3$ -edge XAS spectra and (d) Cl K-edge XAS spectra.

## 8.4 Conclusion

In summary, ASSLIBs with a LLZO oxide-based SSE and  $\text{LiCoO}_2$  cathode, are built by interfacial engineering, with an in-situ synthesis of  $\text{Li}_3\text{InCl}_6$  using solution method.



$\text{Li}_3\text{InCl}_6$  works as an intermediate for bridging the  $\text{Li}^+$  ion channel between the LLZO oxide-based SSE and  $\text{LiCoO}_2$ . Due to the high ionic conductivity and good distribution of  $\text{Li}_3\text{InCl}_6$ , ASSLIBs have a low interfacial resistance and they can deliver a discharge capacity which is comparable to that of liquid-based LIBs at 0.1 C. Moreover, the loading of the active materials in these ASSLIBs can reach as high as  $13 \text{ mg/cm}^2$ . The synchrotron soft XAS studies disclose that LLZO and  $\text{Li}_3\text{InCl}_6$  are stable during the synthesis process. There is interphase formation between LLZO and  $\text{Li}_3\text{InCl}_6$ , which is good for  $\text{Li}^+$  ion transportation at the interface, therefore rendering a high performance ASSLIB with an oxide-based SSE. This study provides a new strategy for addressing the interfacial challenge between oxide-based SSEs and cathode electrodes, paving the way for developing high energy density ASSLIBs for practical applications.

## 8.5 Acknowledgement

This work was supported by the China Automotive Battery Research Institute, Natural Sciences and Engineering Research Council of Canada (NSERC), Canada Research Chair Program (CRC), the Canada Light Source (CLS), and the University of Western Ontario. J. Liang greatly appreciates the China Scholarship Council (CSC) and MITACS Elevate PhD program for the support of his PhD study.

## References

10. N. Kamaya, K. Homma, Y. Yamakawa, M. Hirayama, R. Kanno, M. Yonemura, T. Kamiyama, Y. Kato, S. Hama, K. Kawamoto and A. Mitsui, *Nat. Mater.*, 2011, 10, 682-686.
11. Y. Kato, S. Hori, T. Saito, K. Suzuki, M. Hirayama, A. Mitsui, M. Yonemura, H. Iba and R. Kanno, *Nat. Energy*, 2016, 1, 16030.
12. D. H. Kim, D. Y. Oh, K. H. Park, Y. E. Choi, Y. J. Nam, H. A. Lee, S.-M. Lee and Y. S. Jung, *Nano Lett.*, 2017, 17, 3013-3020.
13. R. Murugan, V. Thangadurai and W. Weppner, *Angew. Chem. Int. Ed.*, 2007, 46, 7778-7781.
14. H. Morimoto, H. Awano, J. Terashima, Y. Shindo, S. Nakanishi, N. Ito, K. Ishikawa and S.-i. Tobishima, *J. Power Sources*, 2013, 240, 636-643.

15. X. Li, J. Liang, N. Chen, J. Luo, K. R. Adair, C. Wang, M. N. Banis, T.-K. Sham, L. Zhang, S. Zhao, S. Lu, H. Huang, R. Li and X. Sun, *Angew. Chem. Int. Ed.*, 2019, 58, 16427-16432.
16. K.-H. Park, K. Kaup, A. Assoud, Q. Zhang, X. Wu and L. F. Nazar, *ACS Energy Lett.*, 2020, 5, 533-539.
17. T. Asano, A. Sakai, S. Ouchi, M. Sakaida, A. Miyazaki and S. Hasegawa, *Adv. Mater.*, 2018, 30, 1803075.
18. T. Ohtomo, A. Hayashi, M. Tatsumisago and K. Kawamoto, *J. Solid State Electrochem.*, 2013, 17, 2551-2557.
19. P.-J. Lian, B.-S. Zhao, L.-Q. Zhang, N. Xu, M.-T. Wu and X.-P. Gao, *J. Mater. Chem. A*, 2019, 7, 20540-20557.
20. F. Han, Y. Zhu, X. He, Y. Mo and C. Wang, *Adv. Energy Mater.*, 2016, 6, 1501590.
21. Y. Zhu, X. He and Y. Mo, *ACS Appl. Mater. Interfaces*, 2015, 7, 23685-23693.
22. V. Thangadurai, S. Narayanan and D. Pinzarú, *Chem. Soc. Rev.*, 2014, 43, 4714-4727.
23. X. Han, Y. Gong, K. Fu, X. He, G. T. Hitz, J. Dai, A. Pearse, B. Liu, H. Wang, G. Rubloff, Y. Mo, V. Thangadurai, E. D. Wachsman and L. Hu, *Nat. Mater.*, 2017, 16, 572-579.
24. K. Fu, Y. Gong, B. Liu, Y. Zhu, S. Xu, Y. Yao, W. Luo, C. Wang, S. D. Lacey, J. Dai, Y. Chen, Y. Mo, E. Wachsman and L. Hu, *Sci. Adv.*, 2017, 3, e1601659.
25. C. Wang, Y. Gong, B. Liu, K. Fu, Y. Yao, E. Hitz, Y. Li, J. Dai, S. Xu, W. Luo, E. D. Wachsman and L. Hu, *Nano Lett.*, 2017, 17, 565-571.
26. W. Luo, Y. Gong, Y. Zhu, Y. Li, Y. Yao, Y. Zhang, K. Fu, G. Pastel, C.-F. Lin, Y. Mo, E. D. Wachsman and L. Hu, *Adv. Mater.*, 2017, 29, 1606042.
27. J. Wang, H. Wang, J. Xie, A. Yang, A. Pei, C.-L. Wu, F. Shi, Y. Liu, D. Lin, Y. Gong and Y. Cui, *Energy Storage Mater.*, 2018, 14, 345-350.
28. A. Sharafi, E. Kazyak, A. L. Davis, S. Yu, T. Thompson, D. J. Siegel, N. P. Dasgupta and J. Sakamoto, *Chem. Mater.*, 2017, 29, 7961-7968.
29. H. Huo, Y. Chen, N. Zhao, X. Lin, J. Luo, X. Yang, Y. Liu, X. Guo and X. Sun, *Nano Energy*, 2019, 61, 119-125.

30. C. Wang, Q. Sun, Y. Liu, Y. Zhao, X. Li, X. Lin, M. N. Banis, M. Li, W. Li, K. R. Adair, D. Wang, J. Liang, R. Li, L. Zhang, R. Yang, S. Lu and X. Sun, *Nano Energy*, 2018, 48, 35-43.
31. W. Zhou, S. Wang, Y. Li, S. Xin, A. Manthiram and J. B. Goodenough, *J. Am. Chem. Soc.*, 2016, 138, 9385-9388.
32. J. van den Broek, S. Afyon and J. L. M. Rupp, *Adv. Energy Mater.*, 2016, 6, 1600736.
33. H.-S. Kim, Y. Oh, K. H. Kang, J. H. Kim, J. Kim and C. S. Yoon, *ACS Appl. Mater. Interfaces*, 2017, 9, 16063-16070.
34. F. Han, J. Yue, C. Chen, N. Zhao, X. Fan, Z. Ma, T. Gao, F. Wang, X. Guo and C. Wang, *Joule*, 2018, 2, 497-508.
35. T. Liu, Y. Ren, Y. Shen, S.-X. Zhao, Y. Lin and C.-W. Nan, *J. Power Sources*, 2016, 324, 349-357.
36. S. Ohta, J. Seki, Y. Yagi, Y. Kihira, T. Tani and T. Asaoka, *J. Power Sources*, 2014, 265, 40-44.
37. K. Nagao, A. Sakuda, A. Hayashi and M. Tatsumisago, *J. Power Sources*, 2019, 424, 215-219.
38. W. Xu, A. Marcelli, B. Joseph, A. Iadecola, W. S. Chu, D. Di Gioacchino, A. Bianconi, Z. Y. Wu and N. L. Saini, *J. Phys.: Condens. Matter*, 2010, 22, 125701.
39. H. Ikeno, M. Krause, T. Höche, C. Patzig, Y. Hu, A. Gawronski, I. Tanaka and C. Rüssel, *J. Phys.: Condens. Matter*, 2013, 25, 165505.
40. X. Li, J. Liang, J. Luo, M. Norouzi Banis, C. Wang, W. Li, S. Deng, C. Yu, F. Zhao, Y. Hu, T.-K. Sham, L. Zhang, S. Zhao, S. Lu, H. Huang, R. Li, K. R. Adair and X. Sun, *Energy Environ. Sci.*, 2019, 12, 2665-2671.

## Supporting information

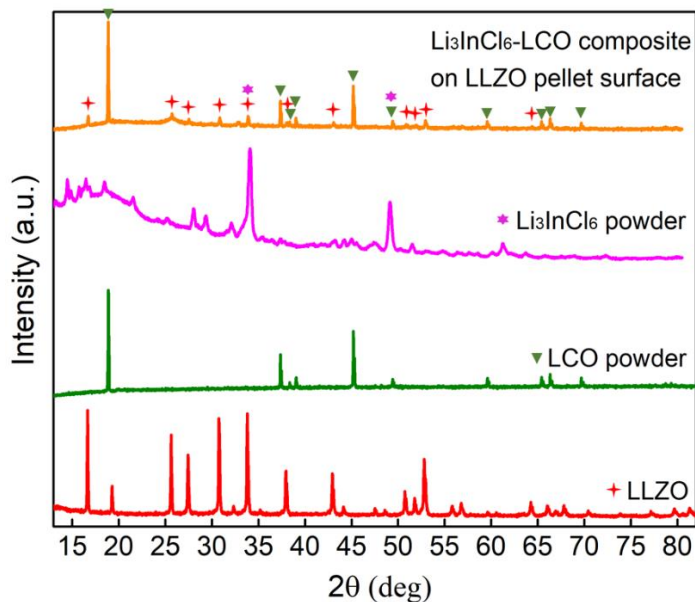


**Figure S8.1** Comparison of XRD spectra for LLZO SSE pellet, LiCoO<sub>2</sub> powders, Li<sub>3</sub>InCl<sub>6</sub> powders, and the LIC-LCO-AB composite cathode.

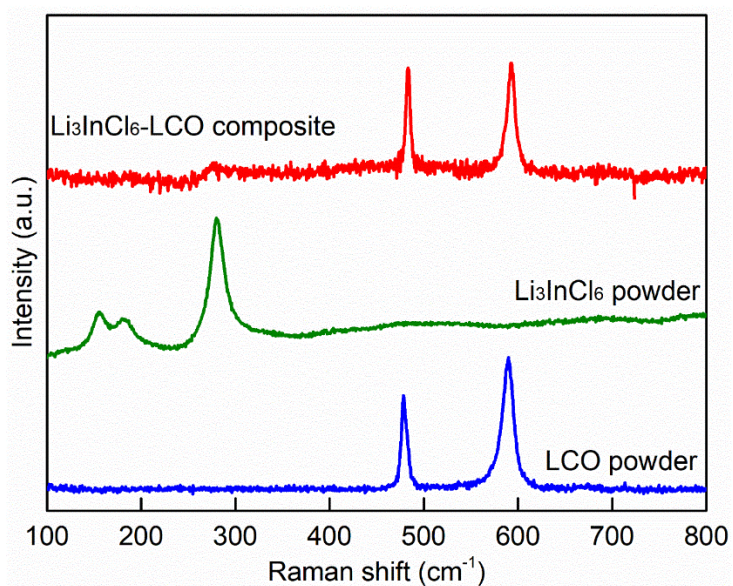


**Figure S8.2** Comparison of Raman spectra for LiCoO<sub>2</sub> powders, Li<sub>3</sub>InCl<sub>6</sub> powders, and the LIC-LCO-AB composite cathode.

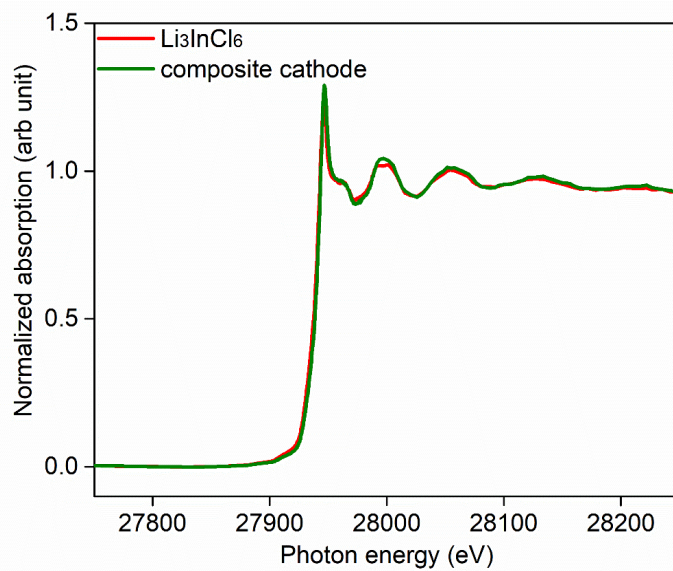


**Figure S8.3** Comparison of In K-edge XAS for  $\text{Li}_3\text{InCl}_6$  powders and LIC-LCO-AB composite cathode.

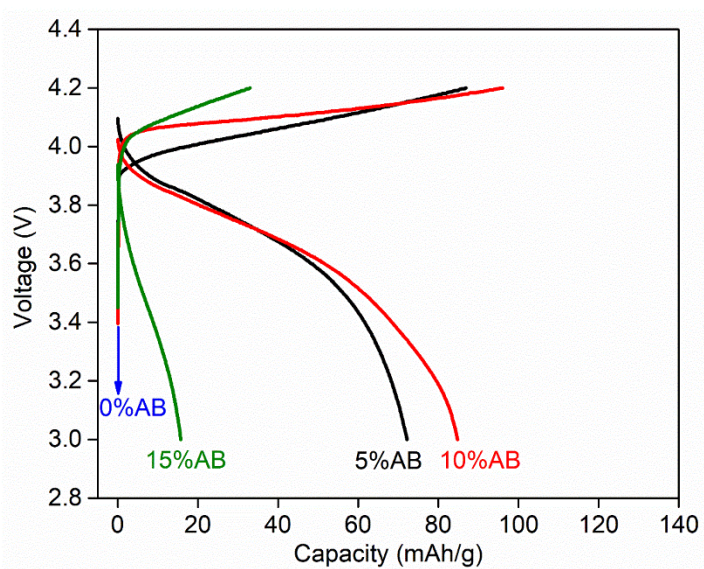


**Figure S8.4** The effect of AB content in the LIC-LCO-AB composite cathode for ASSLIBs.

## Chapter 9

### 9 Stabilization of all-solid-state Li-S batteries with a polymer-ceramic sandwich electrolyte by atomic layer deposition

In previous chapter, ASSLIB with  $\text{LiCoO}_2$  cathode is studied. However, to obtain a higher energy density all-solid-state lithium batteries (ASSLBs), alternative cathode such as sulfur, which is abundant in the earth and cheap and who has a specific capacity of 1670 mAh/g, almost 10 times higher than that of  $\text{LiCoO}_2$ , should be used in ASSLB. In this chapter, All-solid-state lithium-sulfur batteries (ASSLSBs) will be studied.

ASSLSBs are promising candidates as the power source for future electric vehicles due to their high energy density and superior safety properties. However, one of the major challenges of state-of-the-art ASSLSBs is related to the high interfacial resistance resulting from the instability between the solid-state electrolyte (SSE) and electrodes and/or the side reactions between polysulfides and SSE. Herein, we propose and demonstrate the significant enhancement of the cycling stability of an ASSLSB through atomic layer deposition interfacial engineering on the polymer/oxide ceramic/polymer sandwich-structured SSE. The results show that as few as 10 cycles (1 nm) of ALD  $\text{Al}_2\text{O}_3$  on the LATP can endow ASSLSBs with a discharge capacity of 823 mAh/g after 100 charge/discharge cycles, which is almost two times higher than that of the ASSLSB without an ALD coating and that of a Li-S battery with a liquid-based electrolyte. Such improvement is attributed not only to the blocking of the polysulfide shuttling effect via the use of a sandwich SSE but also the significant reduction of the side reaction between the polysulfide and oxide ceramic SSE, which introduces high interfacial resistance and degrades the electrochemical performance. The protection role and mechanism of the ALD layer is also confirmed and revealed by XRD, SEM and XPS measurements.

---

Note: this work has been published.

**J. Liang**, Q. Sun, Y. Zhao, Y. Sun, C. Wang, W. Li, M. Li, D. Wang, X. Li, Y. Liu, K. Adair, R. Li, L. Zhang, R. Yang, S. Lu, H. Huang and X. Sun\*, **J. Mater. Chem. A**, 2018, 6, 23712-23719

## 9.1 Introduction

Lithium-sulfur (Li-S) batteries are promising candidates for application in portable electronics and electric vehicles (EVs) and have received significant attention due to the natural abundance, low cost and environmental friendliness of sulfur. In addition, sulfur possesses high theoretical specific capacities and energy densities which are up to 1675 Ah/kg and 2500 Wh/kg,<sup>1,2</sup> respectively, i.e. a 6-fold increase in specific energy density over that of the LiCoO<sub>2</sub> cathode in conventional LIBs.<sup>3</sup> However, several critical obstacles have hindered conventional Li-S batteries using liquid electrolyte from achieving practical application. One of the major challenges is that polysulfide intermediates are soluble in liquid electrolyte, resulting in the polysulfide shuttle effect,<sup>4,5</sup> which induces rapid capacity fading during cycling and results in low coulombic efficiency.<sup>1,6,7</sup> Meanwhile, a liquid-based electrolyte contains flammable and volatile solvents, leading to serious safety concerns. Accordingly, the development of all-solid-state Li-S batteries (ASSLSBs) is regarded as a potential strategy to solve these problems in Li-S batteries.<sup>7,8</sup> The application of a non-flammable solid-state electrolyte (SSE) is expected to eliminate the possibilities of polysulfide shuttling to realize safe and long-life ASSLSBs as a desirable candidate for application in future EVs.

Various choices of SSEs for ASSLSBs have previously been reported, such as poly(ethylene oxide) (PEO) based solid polymer electrolytes (SPEs),<sup>9,10</sup> oxide-based SSEs,<sup>11</sup> sulfide-based SSEs<sup>12-14</sup> and sandwich-type hybrid electrolytes.<sup>15</sup> In particular, the application of sandwich-type hybrid electrolytes in ASSLSBs has received significant attention due to their high ionic conductivity, ability to prevent lithium dendrite formation and good electrode wetting properties. All of the above-mentioned merits can contribute to improved cycling performance.<sup>16-18</sup>

However, the development of ASSLSBs based on all-solid-state hybrid SSEs has been hindered due to several challenges, including: (i) low ionic conductivity at room temperature; (ii) instability between the SSE and electrode materials; (iii) high interfacial resistance. The instability between the SSE and electrodes comes from the side reactions between the SSE and electrode materials, resulting in degradation of the SSE and thus lowered ionic conductivity. For example, the reduction of Ti-containing SSEs such as

NASICON-type  $\text{Li}_{3-2x}(\text{Al}_{1-x}\text{Ti}_x)_2(\text{PO}_4)_3$  (LATP) and perovskite-type  $\text{Li}_{3x}\text{La}_{2/3-x}\text{TiO}_3$  (LLTO) is observed when placed in contact with a lithium anode<sup>16,19</sup> or other reductant species such as polysulfides.<sup>20</sup> LATP is one of the most studied oxide-based SSEs that has already been used in quasi-solid-state Li-S batteries.<sup>20,21</sup> However, there is a critical problem that needs to be addressed when using LATP in Li-S batteries, which is the instability of LATP against polysulfide species. Manthiram's group used SEM, XRD and XPS to study the reduction of LATP by polysulfides and the results indicate that polysulfides can deteriorate the performance of the LATP SSE, which results in degradation of Li-S battery performance.<sup>20</sup>

Therefore, the protection of LATP from reduction by polysulfides is critical to build long-life ASSLSBs. The properties of the protection layer should meet two primary requirements: (i) chemical stability in a reducing environment and (ii) enabling diffusion of  $\text{Li}^+$  ions through the protection layer. As a promising protection technique, atomic layer deposition (ALD) is a unique technology that can realize conformal thin film deposition with excellent coverage and controllable deposition thickness at the nanoscale due to the use of self-limiting reactions.<sup>22-24</sup> More importantly, the deposition temperature of ALD can be low enough to avoid side reactions between the deposited material and the substrate. Accordingly, it is expected that ALD  $\text{Al}_2\text{O}_3$  can be a promising candidate for LATP protection against polysulfide species due to its thin film nature that can allow  $\text{Li}^+$  ions to diffuse through and inherent chemical and electrochemical stability.<sup>25-27</sup>

Herein, we demonstrate the successful application of ALD to create an ultrathin protective coating layer on LATP for ASSLSBs with a polymer/ceramic/polymer sandwich-type (PEO/LATP/PEO) hybrid electrolyte operating at 60 °C. Compared to the pristine PEO/bare-LATP/PEO (PLP) SSE, the PEO/ALD-coated LATP/PEO (ALD-PLP) SSE presents significantly enhanced cycling performance. The results show that as few as 10 cycles of ALD  $\text{Al}_2\text{O}_3$  coating on the LATP can endow ASSLSBs with discharge capacities of 1035 mAh/g at the initial cycle and 823 mAh/g after 100 charge/discharge cycles, which is almost two times higher than that of the ASSLSB without ALD coating. The improved electrochemical performance is attributed to the protection of LATP by ALD  $\text{Al}_2\text{O}_3$ . FE-SEM studies show that bare LATP is pulverized after long-term cycling, due to the



reduction of LATP by polysulfide, whereas with ALD coating, the LATP stability is greatly improved. XRD and XPS studies indicate that ALD coating can effectively prevent the reduction of Ti in LATP by polysulfides. This investigation discloses a new avenue to tackle the instability problem between the SSE and electrodes for the development of all-solid-state lithium batteries.

## 9.2 Experimental

### 9.2.1 Preparation of NASICON-type solid-state electrolyte LATP for ALD coating

NASICON-type SSE  $\text{Li}_{1.4}\text{Al}_{0.4}\text{Ti}_{1.6}(\text{PO}_4)_3$  (LATP) was synthesized by a solid-state reaction method.<sup>28</sup> Stoichiometric amounts of  $\text{Li}_2\text{CO}_3$ ,  $\text{Al}_2\text{O}_3$ ,  $\text{TiO}_2$ , and  $\text{NH}_4\text{H}_2\text{PO}_4$  were first mixed using a ball milling method at 300 rpm for 5 h in a zirconia vessel with zirconia balls. Then the mixed powders were calcined at 700 °C for 2 h. The obtained powders were ground with polyvinyl alcohol (PVA) as the binder before being pressed into 12 mm diameter pellets at 250 MPa. The as-pressed pellets were calcined at 900 °C for 6 h. The obtained LATP SSE pellets were polished using sandpaper down to a thickness of  $500 \pm 30$   $\mu\text{m}$ . The polished LATP pellets were coated with an  $\text{Al}_2\text{O}_3$  layer by atomic layer deposition (ALD). Then one surface of this ALD coated LATP was polished again to remove the ALD coating. LATP with one ALD coated surface was assembled into ASSLSB with the ALD coated surface toward the sulfur cathode. Different thicknesses of ALD  $\text{Al}_2\text{O}_3$  were directly coated on the surfaces of LATP pellets in an ALD reactor (Gemstar-8 ALD system) by controlling the ALD cycle number. Trimethylaluminum (TMA) and water ( $\text{H}_2\text{O}$ ) were used as the precursors and the deposition temperature was set as 120 °C. The growth rate of ALD  $\text{Al}_2\text{O}_3$  at 120 °C is 0.1 nm per cycle.<sup>29,30</sup>

### 9.2.2 Preparation of the sulfur electrode

Commercial carbon black (Ketjenblack EC-600, US) and sulfur powder (99.5%, Sigma-Aldrich) were dried at 70 °C overnight in a vacuum oven. Then carbon black and a certain amount of sulfur were mixed together and transferred to a sealed steel reactor. The reactor was heated at 150 °C for 10 h and then at 300 °C for 3 h. The obtained carbon-sulfur composites (C-S) maintained a 65 wt% sulfur loading (**Figure S9.1**). The electrodes were

prepared by slurry casting on carbon-coated aluminum foil. The slurry mass ratio of C-S composites, acetylene black, and polyvinylidene fluoride (PVDF) is 8:1:1. The as-prepared electrodes were finally dried at 60 °C overnight in a vacuum oven. The final loading of sulfur in the cathode electrode is 0.6 - 1 mg/cm<sup>2</sup>.

### 9.2.3 Preparation of fully reduced-LATP

Fully reduced LATP was prepared by soaking pristine LATP pellets in a polysulfide solution containing 1 M Li<sub>2</sub>S<sub>6</sub> for 1 week. The reduced LATP was used for XRD and XPS study.

### 9.2.4 Electrochemical characterization

PEO-based SPE membranes were cut into a circular shape for electrochemical impedance spectroscopy (EIS) testing using stainless steel as the blocking electrode. For the EIS testing of LATP SSE pellets, a layer of gold was deposited on the surface of pellets using sputtering and used as blocking electrodes. The stainless steel was also applied in the EIS testing of the PEO/LATP/PEO (PLP) sandwich-type hybrid electrolyte because PEO-based SPE has good contact ability with stainless steel and LATP. EIS was performed on the versatile multichannel potentiostat 3/Z (VMP3) by applying an AC voltage of 10 mV amplitude in the 500 kHz to 0.01 Hz frequency range. The EIS of the PEO-based SPE and PLP sandwich-type hybrid electrolyte were measured using stainless steel as the blocking electrode and the electrolytes were preheated to 80 °C for over 2 h before measurement.

CR-2032 type coin cells were assembled in an argon-filled glovebox. The first type of coin cells consisted of a C-S cathode, commercial liquid electrolyte (containing 1 M LiTFSI salt dissolved in dioxolane (DOL) : dimethoxyethane (DME) of a 1: 1 volume ratio and LiNO<sub>3</sub> as an additive), and lithium metal anode. The second type of coin cells consisted of a C-S cathode, PEO-based SPE, and lithium metal anode. The third type of coin cells consisted of a C-S cathode, PLP (or ALD-LATP) sandwich-type hybrid electrolyte, and lithium metal anode. A detailed illustration of the battery configurations is presented in **Figure S9.2**. Cyclic voltammograms were collected on a versatile multichannel potentiostat 3/Z (VMP3) at a scan rate of 0.1 mV/s between 1.5 V and 3.0 V (vs. Li/Li<sup>+</sup>) for the liquid electrolyte Li-S battery and 1.0-3.0 V for the all solid-state Li-S battery. All of the batteries

were tested by holding at 60 °C after assembling for 24 h. Charge/discharge characteristics were galvanostatically tested in the range of 1.5-3.0 V for the liquid electrolyte Li-S battery and 1.0-3.0 V for the all solid-state Li-S battery at 60 °C using LAND Battery Test equipment with a current density of 0.1C.

### 9.2.5 Physical characterization

The morphologies of the samples were characterized using a Hitachi S-4800 field emission scanning electron microscope (FE-SEM) equipped with energy dispersive spectroscopy (EDS). Thermogravimetric analysis (TGA) was carried out in a nitrogen atmosphere from room temperature to 700 °C at a heating rate of 10 °C/min on a SDT Q600 (TA Instruments). Phase analysis was performed by X-ray diffraction (XRD) (Bruker D8 Advance, Cu K $\alpha$  X-ray source). X-ray photoelectron spectroscopy was conducted on a Kratos AXIS Ultra Spectrometer system. High energy X-ray photoelectron spectroscopy (HEXPS) measurements at Ti 1s were performed at the Soft X-Ray Microcharacterization Beamline (SXRMB) at the Canadian Light Source (CLS) located at the University of Saskatoon, Saskatoon, Canada. The photon energy used for HEXPS is 8 keV with a probing depth of around 4 nm.

## 9.3 Results and discussion

SSE LATP was prepared by a solid-state reaction method,<sup>28</sup> and the surface modification was carried out by depositing ALD Al<sub>2</sub>O<sub>3</sub> onto LATP pellets before ASSLSB assembly (**Figure 9.1** shows the schematic diagram of a LATP pellet, an ALD coated LATP pellet and the configurations of ASSLSBs). One of the surfaces of the LATP pellet (facing anode) was polished after the ALD process to remove the ALD coating. The phase of LATP after ALD coating was evaluated by XRD (**Figure 9.1b**), where the results clearly indicate that there are no impurities introduced by the ALD process. On the other hand, the PEO-based SPE was prepared by a solution casting method.<sup>31</sup> The sandwich type polymer/ceramic/polymer SSE is assembled by stacking PEO, a LATP pellet, and another layer of PEO. The detailed configurations of the ASSLSBs are presented in **Figure 9.1a**.

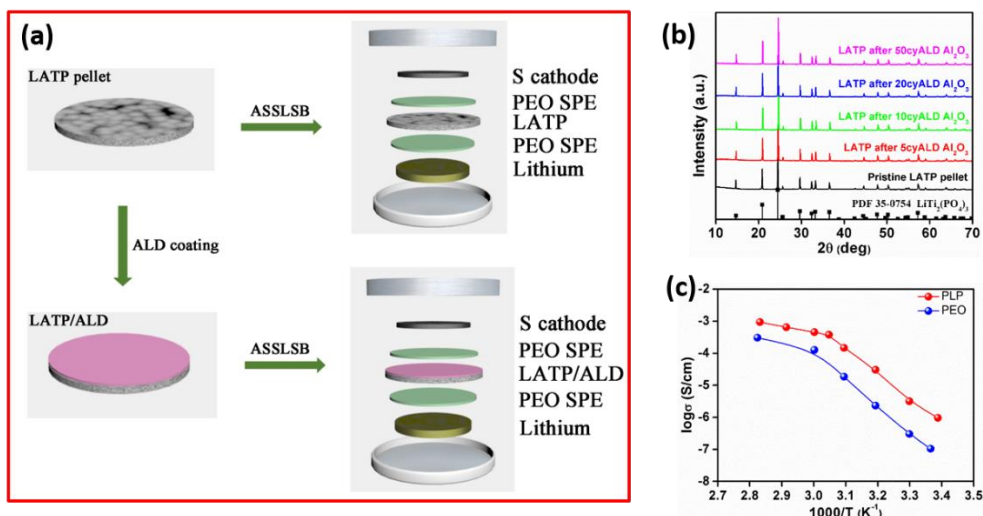


**Figure 9.1** (a) A schematic diagram showing the preparation of an ALD coated LAMP SSE and the configuration of ASSLSBs. (b) XRD patterns of LAMP with different numbers of ALD coating cycles. (c) Temperature dependent ionic conductivity of the PEO-based SPE and PLP sandwich-type hybrid electrolyte.

The ionic conductivities of the PEO-based SPE and PLP SSE were evaluated by electrochemical impedance spectroscopy (EIS). Temperature dependent ionic conductivities of different SSEs are illustrated in **Figure 9.1c**. PEO-based SPE has a low ionic conductivity on the order of  $\sim 10^{-8}$  S/cm at room temperature (RT), which is similar to a previously reported result.<sup>31</sup> At an elevated temperature of  $\sim 60$  °C, the ionic conductivity increases to the order of  $10^{-4}$  S/cm. The ionic conductivity of the PLP SSE is higher than that of the SPE, which is  $4.8 \times 10^{-4}$  S/cm at 60 °C, due to the existence of the LAMP ceramic SSE.

Cyclic voltammetry (CV) measurements have been conducted to analyze the electrochemical reaction mechanism of the ASSLSBs with the PEO-based SPE and PLP with or without ALD modification at 60 °C. **Figure 9.2a-c** illustrate the CV curves of Li-S batteries with the PEO-based SPE, PLP and ALD-PLP SSEs. A conventional Li-S battery with commercialized ether-based liquid electrolyte was also assembled using the same S/C cathode to make a fair comparison (**Figure S9.8**). For the liquid-based Li-S battery, two well defined cathodic peaks at 2.3 V and 2.1 V (vs. Li/Li<sup>+</sup>), and one anodic peak at 2.4 V are present (**Figure S9.8a**). Similarly, two cathodic peaks are present at 2.4 V and 1.9 V in

the ASSLSBs with PEO SPE and PLP SSEs (**Figure 9.2a** and **b**), and 2.3 V and 1.7 V in the ASSLSB with the ALD-PLP SSE (**Figure 9.2c**). The two cathodic peaks in the CV curves of the ASSLSBs indicate that the electrochemical reactions are similar to that in the liquid-based Li-S battery. During the cathodic processes, sulfur is first reduced into long chain polysulfide species such as  $S_8^{2-}$  and  $S_6^{2-}$ , followed by the stepwise reduction into short chain polysulfides ( $S_4^{2-}$ ,  $S_2^{2-}$ , and  $S^{2-}$ ) at relatively lower voltages.<sup>32,33</sup> The anodic peaks of the ASSLSB with PEO SPE show strong current and fluctuation, indicating that the polysulfide intermediates dissolve and migrate through the SPE. The dissolution and migration of the polysulfide in the PEO-based SPE had been observed using in operando SEM and ultraviolet-visible spectroscopy studies by K. Zaghib et al.<sup>9</sup> So, the polysulfide species can migrate through the PEO SPE layer and reach the PEO/LATP interface in the PLP, and cause the reduction of  $Ti^{4+}$  in LATP, leading to the deterioration of the cycling performance of ASSLSBs. In order to protect the SSE and improve the cycling performance, ALD-derived  $Al_2O_3$  has been applied to enhance the stability of LATP against the reduction by polysulfide species. The insulating nature of the ALD coating leads to an increase in the overall impedance (**Figure S9.9a**), in agreement with the two cathodic peaks of the ALD-PLP ASSLSB shifting to lower voltages and the anodic peak shifting to higher voltages compared to the uncoated PLP. After the initial CV scan, these two cathodic peaks shift to relatively higher voltages (**Figure 9.2c**), which is possibly due to the lithiation of ALD coating layer resulting in an enhancement of the ionic conductivity and a decrease of the overall cell impedance. The lithiation of  $Al_2O_3$  was confirmed by XPS study and the results are presented in Figure S11. There is no Li 1s signal for the 50 cycle ALD coated LATP before charge/discharge cycling. This is because there is no Li element in the ALD  $Al_2O_3$  coating layer. This is Al 2p signal is related to  $Al_2O_3$  in the same sample. After the PLP SSE was charged/discharged for 10 cycles in the ASSLSB, XPS was performed on the ALD coated surface of the LATP, and a strong Li 1s peak was observed. Also, we found a shift of the Al 2p to a lower binding energy, which confirms the lithiation of  $Al_2O_3$  to  $LiAlO_x$  after battery cycling. Similar results had been reported by X. Xiao et al. and Y. S. Jung et al.<sup>34,35</sup>

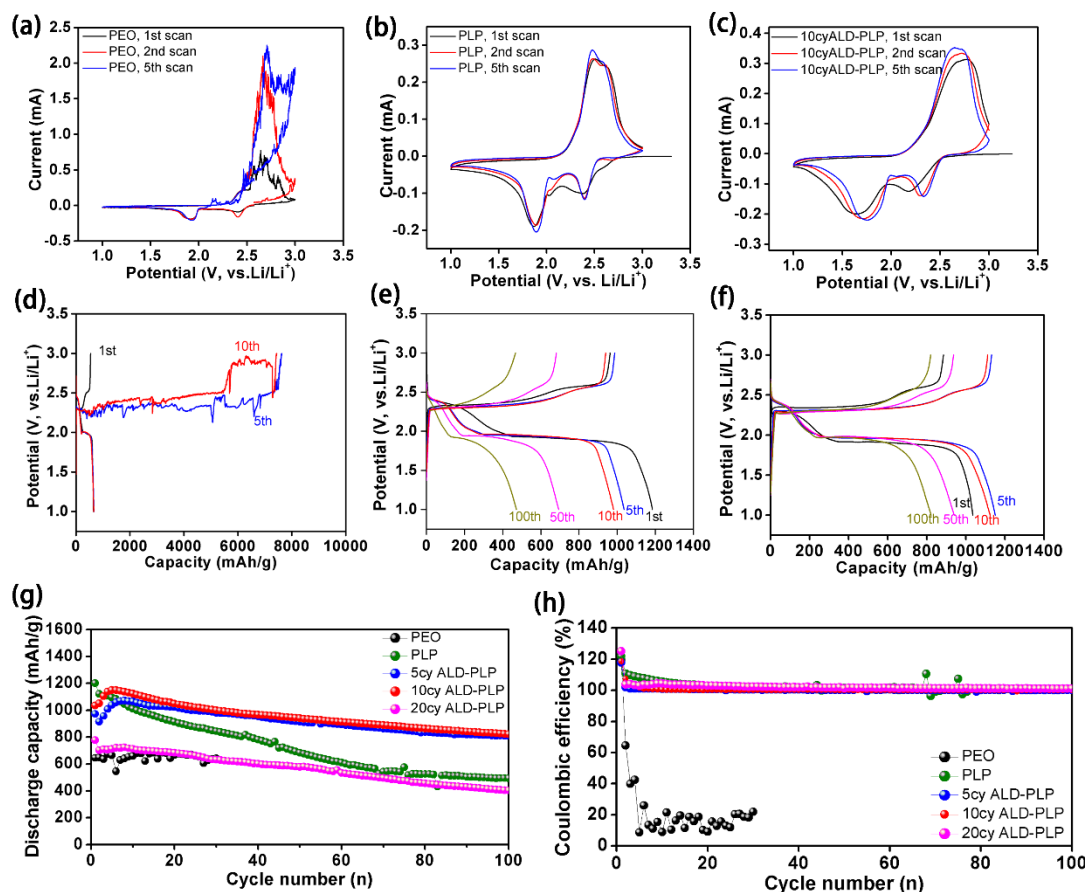


**Figure 9.2** Cyclic voltammety curves of a (a) PEO SPE Li-S battery, (b) ASSLSB with a PLP sandwich electrolyte and (c) ASSLSB with 10 cycles of ALD-PLP. Charge/discharge potential profiles of ASSLSB (d) with a PEO SPE, (e) with a PLP SSE and (f) with 10 cycles of ALD-PLP SSE; (g) cycling performance of Li-S batteries with different electrolytes and its corresponding coulombic efficiency (h). All cycling was performed at a current density of 0.1C (1C = 1670 mAh/g) and 60 °C.

To evaluate the electrochemical performance and stability of Li-S batteries, galvanostatic charge/discharge testing was performed at high temperature (60 °C). The Li-S battery with a liquid-based electrolyte has two discharge plateaus, one at 2.3 V and another at 2.1 V, in addition to a charge plateau at 2.2 V (**Figure S9.8b**). Similar behaviors are observed in ASSLSBs with PEO, PLP and ALD-PLP SSEs where two discharge plateaus are present (**Figure 9.2d-f**). For ASSLSBs with PLP and ALD-PLP SSEs, two charge potential plateaus are well defined, indicating clear stepwise oxidation of short chain polysulfide

species. In contrast, the stepwise oxidation process is not obvious in the liquid-based Li-S battery. The reason behind this phenomenon is possibly related to the high viscosity of the SPE, which can effectively limit the diffusion rate of polysulfides compared to their fast transport in liquid electrolyte.

The long-term cycling performance of the liquid-based Li-S batteries and ASSLSBs is displayed in **Figure S9.8c** and **Figure 9.2g**, respectively. The Li-S batteries were first discharged then charged, and the coulombic efficiency was calculated from the ratio of discharge capacity to charge capacity. From **Figure S9.8c**, it can be seen that the liquid-based Li-S battery delivers an initial discharge capacity of 1134 mAh/g which then rapidly decays to 295 mAh/g after 100 charge/discharge cycles. The coulombic efficiency of the liquid-based Li-S battery is very low during the first 30 cycles, which can be attributed to the polysulfide shuttle effect. In comparison, the ASSLSB with PEO can yield a discharge capacity around 645 mAh/g with a very low coulombic efficiency fluctuating between 0 and 30% and a severe overcharging problem is observed (**Figure 9.2d**), which is consistent with the result reported by M. Lécuyer et al.<sup>36</sup> Similar to the liquid-based system, this poor coulombic efficiency can also be attributed to the polysulfide shuttle effect. However, the ASSLSB with the PLP SSE displays an initial discharge capacity of 1201 mAh/g with a coulombic efficiency of 122% in the first cycle. The coulombic efficiency values of over 100% indicate that some of the discharged active material is irreversibly lost. This is possibly because of the dissolution of the polysulfides in the PEO-based SPE and the reduction of the LATP consuming polysulfides. However, after 5 charge/discharge cycles, the ASSLSBs with PLP and ALD-PLP show stabilization of the coulombic efficiencies at around 100% for 100 cycles, which indicates the inhibition of polysulfide shuttling and good retention of the active material. After 100 charge/discharge cycles, the ASSLSB with the PLP SSE has a discharge capacity of 494 mAh/g, which is higher than that of the liquid-based system. However, the battery still shows dramatic capacity fade over extended cycling. The cycling performance of the lithium symmetric cell with a PLP SSE is illustrated in **Figure S9.12**. This shows that with an ultra-long cycling time and increased cycling numbers, there is no voltage drop or over-potential increase, which indicates that PLP is ultra-stable in lithium symmetric cells without lithium dendrite formation and reduction of LATP. However, in the ASSLSB with the PLP SSE, there are

charge/discharge intermediate products, polysulfides, which are dissolvable in PEO-based SPEs and thus they can transfer to the PEO/LATP interface to react with LATP causing the reduction of LATP. With extensive cycling of the ASSLSB, the degradation of LATP is progressive. With the degradation of LATP, polarization in the charge/discharge curves of ASSLSB with PLP (as shown in **Figure 9.2e**) increases. Therefore, the capacity fading of the ASSLSB is caused by the degradation of PLP. The degradation of PLP is caused by the reduction of LATP by polysulfides. Thus, the protection of PLP from reduction is extremely important for the enhancement of ASSLSBs' performance.

Therefore, an ultra-thin  $\text{Al}_2\text{O}_3$  was deposited on LATP by ALD to inhibit the reduction by the polysulfide. An optimization of the  $\text{Al}_2\text{O}_3$  thickness was done and the results are presented in **Figure 9.2g**. With 10 cycles of ALD coating, the best cycling performance could be achieved. A thicker coating layer will result in higher overall resistance (**Figure S9.9**) and lower the discharge capacity significantly. With 10 cycles of ALD coating, the increase of the overall resistance is not significant compared to the ASSLSB with the PLP electrolyte (**Figure S9.9a**). The initial discharge capacity of the ASSLSB with 10 cycles of ALD ALD-PLP SSE is 1035 mAh/g, which is comparable to that of liquid-based Li-S and PLP ASSLSBs. After several initial cycles, the discharge capacity increases to 1150.5 mAh/g. This is because the ALD  $\text{Al}_2\text{O}_3$  coating was lithiated after several charge/discharge cycles and the resistance of the ASSLSB therefore decreases, resulting in increased capacity (as supported by the XPS results shown in **Figure S9.11b**). From the EIS results (**Figure S9.9**) we can find that the impedance of the ASSLSB with ALD coating decreased after charge/discharge, which also supports this hypothesis. A similar phenomenon had been reported in  $\text{Al}_2\text{O}_3$  coated  $\text{LiCoO}_2$  batteries.<sup>35</sup> After 100 charge/discharge cycles, the ALD-PLP ASSLSB can still deliver a capacity of 823 mAh/g, which is almost twice of liquid-based and PLP-based Li-S batteries. This result is much better than the previous reported all-solid-state Li-S battery performances. (**Table S9.1**).



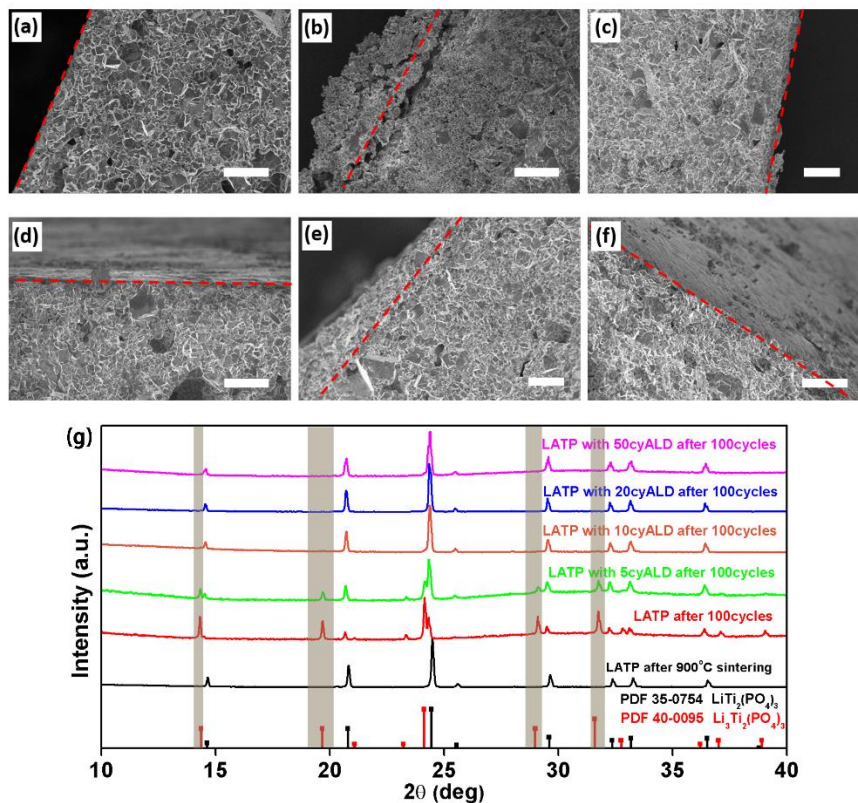


**Figure 9.3** Cross sectional SEM images of (a) pristine LATP, (b) bare LATP after 100 charge/discharge cycles, (c) 5 cycles of ALD coated LATP after 100 charge/discharge cycles, (d) 10 cycles of ALD coated LATP after 100 charge/discharge cycles, (e) 20 cycles of ALD coated LATP after 100 charge/discharge cycles, and (f) 50 cycles of ALD coated LATP after 100 charge/discharge cycles. The red dotted lines indicate the cross section of the LATP side at the cathode interface. Scale bar: 20  $\mu\text{m}$ . (g) Comparison of the XRD patterns of LATP after sintering and LATP with different cycle numbers of ALD coating after 100 charge/discharge cycles in ASSLSBs. The XRD peaks corresponding to the reduced LATP phase are highlighted.

To investigate the decomposition of the SSE by the polysulfide and to study the effect of ALD coating on the protection of LATP in ASSLSBs, cross-sectional SEM of LATP facing the sulfur cathode is conducted. **Figure 9.3a** illustrates the cross-sectional image of the pristine LATP after sintering and polishing. The LATP pellet presents a flat surface and has a grain size of approximately 5  $\mu\text{m}$  with good intergranular contact. However, after 100 charge/discharge cycles, the LATP interface on the sulfur cathode side shows grain

pulverization and structural collapse (**Figure 9.3b**). The pulverized LATP particles range in size of 100 - 500 nm (**Figure S9.13**). Furthermore, the pulverization can be observed to occur as deep as 50  $\mu\text{m}$  into the LATP pellet (**Figure 9.3b**). The destruction of the LATP structure indicates severe reduction of LATP by polysulfide species, which is the reason for the rapid capacity fading. By applying 5 cycles of ALD, the deterioration of the interface can be effectively inhibited. As a matter of fact, the formation of small secondary particles is rarely observed and the surface of the ALD-protected LATP is much flatter (**Figure 9.3c**) compared to that of the bare LATP after cycling. With a thicker ALD coating, the formation of secondary particles is almost completely inhibited and the cycled LATP can retain a uniform grain size similar to the pristine sample (**Figure 9.3d-f**). The crystal phase structure of LATP facing the sulfur cathode side after cycling was characterized by XRD (**Figure 9.3g**). Pristine LATP after sintering exhibits a pure  $\text{LiTi}_2(\text{PO}_4)_3$  phase where Ti exists as  $\text{Ti}^{4+}$ . In contrast, the LATP after 100 cycles shows strong peaks related to the  $\text{Li}_3\text{Ti}_2(\text{PO}_4)_3$  phase, in which Ti is reduced to  $\text{Ti}^{3+}$ . Upon protecting the interface with ALD, the intensities of the peaks associated with the  $\text{Li}_3\text{Ti}_2(\text{PO}_4)_3$  phase decrease with the use of 5 ALD cycles, and further disappears with thicker coatings of 10, 20, and 50 ALD cycles. The prevention of Ti reduction indicates the excellent protection effect of the ALD  $\text{Al}_2\text{O}_3$  coating.

To study the chemical states of Ti in LATP before and after cycling, synchrotron-based high energy X-ray photoelectron spectroscopy (HEXPS) was utilized to study the LATP interface. The Ti 1s XPS of pristine LATP is shown in **Figure S9.14a**, where a single peak at 4970 eV is presented. This peak can be indexed to  $\text{Ti}^{4+}$  of the  $\text{LiTi}_2(\text{PO}_4)_3$  phase in the pristine LATP. After complete reduction by polysulfides, the Ti 1s spectrum shows a decrease in binding energy to 4969 eV (**Figure S9.14b**), which is indexed as reduced-Ti. To calculate the content of  $\text{Ti}^{4+}$  and reduced-Ti in the LATP SSE after 100 charge/discharge cycles in ASSLSBs, XPS peaks of 4970 and 4969 eV were used to fit the spectrum and the results are presented in **Figure 9.4** and **Table S9.2**. Bare LATP after cycling has a strong Ti 1s peak related to the reduced-Ti and a weak peak corresponding to  $\text{Ti}^{4+}$ , which indicates significant reduction of LATP by polysulfides. With the presence of ALD protection, the peak associated with reduced-Ti species decreased significantly. The contents of  $\text{Ti}^{4+}$  and reduced-Ti for bare LATP after 100 charge/discharge cycles are 28.7% and 71.3%,

respectively. With ALD coating, the content of reduced-Ti decreases to 43.2% for 5 cycles of ALD-LATP, 37.4% for 10 cycles ALD-LATP and 29.2% for 20 cycles of ALD-LATP. **Table S9.2** summarizes the fitting results of the XPS spectra. Clearly, a thicker ALD coating is more effective in preventing the reduction of LATP by polysulfide species.

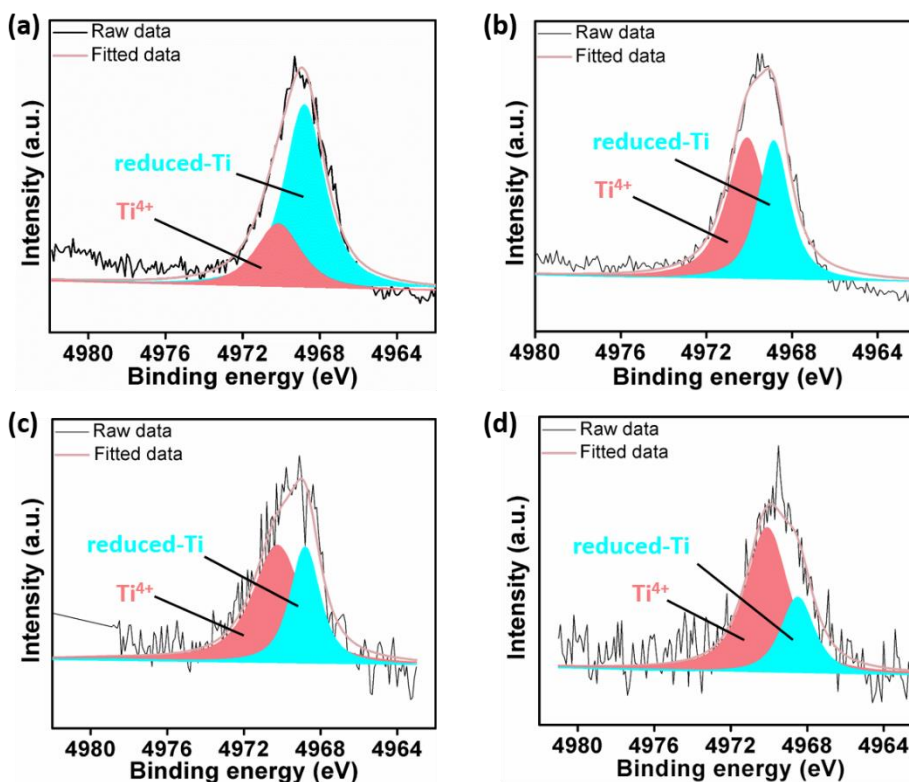


**Figure 9.4** Ti 1s XPS of (a) bare LATP, (b) 5 cycles ALD-LATP, (c) 10 cycles of ALD-LATP and (d) 20 cycles of ALD-LATP after 100 charge/discharge cycles in ASSLSBs. All XPS studies were conducted on the LATP surface facing the sulfur cathode.

To summarize the aforementioned results with respect to their cell configurations, the schematic diagrams of the tested ASSLSB systems and the role of the ALD Al<sub>2</sub>O<sub>3</sub> coating are illustrated in **Figure 9.5**. In the ASSLSB with the PLP SSE, a serious reduction of LATP by polysulfides happens and a very thick layer of reduced-LATP (r-LATP) is formed on the surface of LATP (toward the sulfur cathode side) accompanied by degradation of structural features after being charged/discharged for 100 cycles (**Figure 9.5a** and **d** (bottom)). However, with 10 cycles of ALD coating, the reduction of LATP is significantly reduced and a very thin layer of r-LATP is formed on the LATP surface (**Figure 9.5b** and

e (bottom)). Thus, with ALD protection, LATP can maintain its electrochemical properties and endow the ASSLSB with stable, long cycle performance.

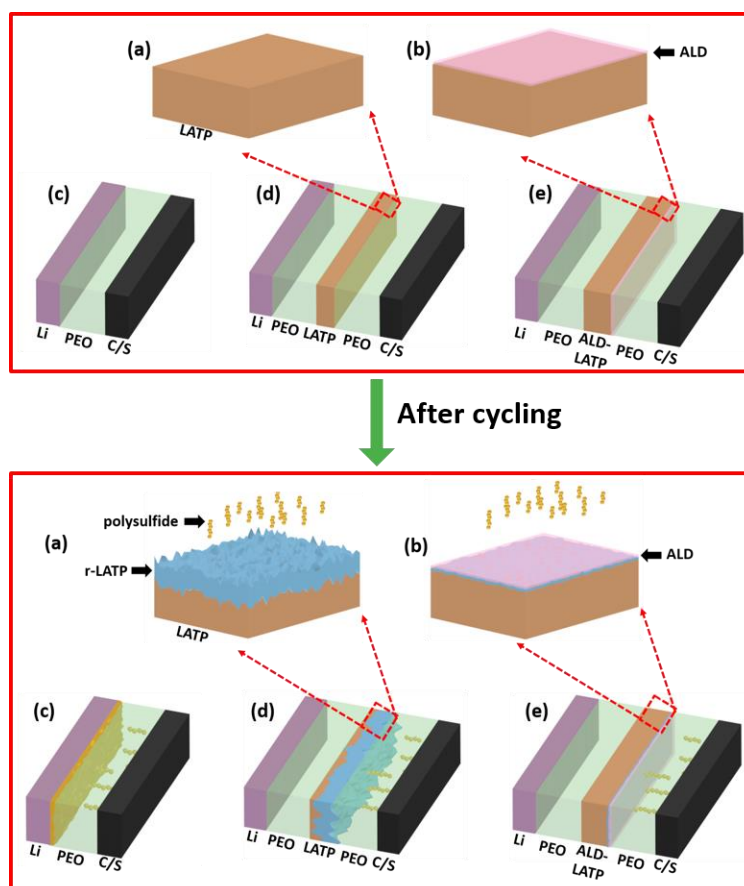


**Figure 9.5** Magnified schematic diagram showing (a) bare LATP (top) and the reduction of LATP upon cycling (bottom), and (b) protection of the bulk LATP by ALD before (top) and after (bottom) cycling. The cell configurations of (c) Li/PEO/S ASSLSB, (d) Li/PLP/S ASSLSB, and (e) Li/ALD-PLP/S ASSLSB.

## 9.4 Conclusions

In conclusion, we report an innovative and effective strategy to enhance the cycling stability of ASSLSBs via solving the instability between the SSE and polysulfide species. By preventing the reduction of polysulfides toward LATP during battery operation using ALD surface engineering on the LATP SSE, the rapid capacity fading of the ASSLSB can be avoided. Using ALD-derived  $\text{Al}_2\text{O}_3$ -coated LATP, the reduction of LATP by polysulfide species can be effectively eliminated and the electrochemical performance of

ASSLSBs can be significantly enhanced. As a result, the ASSLSB with ALD-PLP shows a stable cycling performance with a discharge capacity of 823 mAh/g after 100 charge/discharge cycles, which is two times higher than that of the unprotected SSE and Li-S battery with a liquid-based electrolyte. This work sheds light on addressing the major challenge of the instability problem between the LATP SSE and sulfur cathode, paving the way to develop a high energy density ASSLSB.

## Acknowledgements

This work was supported by the China Automotive Battery Research Institute-Western University Joint Laboratory, Natural Sciences and Engineering Research Council of Canada (NSERC), Canada Research Chair (CRC) Program, Ontario Research Fund, Canada Light Source (CLS), University of Western Ontario, and China Scholarship Council (CSC).

## References

1. X. Liang, C. Hart, Q. Pang, A. Garsuch, T. Weiss and L. F. Nazar, *Nat. Commun.*, 2015, 6, 5682.
2. Y. Yang, G. Zheng and Y. Cui, *Chem. Soc. Rev.*, 2013, 42, 3018-3032.
3. X. Tao, Y. Liu, W. Liu, G. Zhou, J. Zhao, D. Lin, C. Zu, O. Sheng, W. Zhang, H.-W. Lee and Y. Cui, *Nano Lett.*, 2017, 17, 2967-2972.
4. H. J. Peng, J. Q. Huang, X. B. Cheng and Q. Zhang, *Adv. Energy Mater.*, 2017, 7, 1700260.
5. Xiong, M. Regula, D. Wang and J. Song, *Electrochem. Energy Rev.*, 2018, 1, 388-402.
6. Y. V. Mikhaylik and J. R. Akridge, *J. Electrochem. Soc.*, 2004, 151, A1969-A1976.
7. J. Yue, M. Yan, Y. X. Yin and Y. G. Guo, *Adv. Funct. Mater.*, 2018, 1707533.
8. Y.-Z. Sun, J.-Q. Huang, C.-Z. Zhao and Q. Zhang, *Sci. China Chem.*, 2017, 60, 1508-1526.
9. H. Marceau, C.-S. Kim, A. Paoletta, S. Ladouceur, M. Lagacé, M. Chaker, A. Vijh, A. Guerfi, C. M. Julien, A. Mauger, M. Armand, P. Hovington and K. Zaghib, *J. Power Sources*, 2016, 319, 247-254.

10. B. H. Jeon, J. H. Yeon, K. M. Kim and I. J. Chung, *J. Power Sources*, 2002, 109, 89-97.
11. K. K. Fu, Y. Gong, G. T. Hitz, D. W. McOwen, Y. Li, S. Xu, Y. Wen, L. Zhang, C. Wang and G. Pastel, *Energy Environ. Sci.*, 2017, 10, 1568-1575.
12. Z. Lin, Z. Liu, N. J. Dudney and C. Liang, *ACS Nano*, 2013, 7, 2829-2833.
13. R.-c. Xu, X.-h. Xia, S.-h. Li, S.-z. Zhang, X.-l. Wang and J.-p. Tu, *J. Mater. Chem. A*, 2017, 5, 6310-6317.
14. F. Han, J. Yue, X. Fan, T. Gao, C. Luo, Z. Ma, L. Suo and C. Wang, *Nano Lett.*, 2016, 16, 4521-4527.
15. Q. Wang, Z. Wen, J. Jin, J. Guo, X. Huang, J. Yang and C. Chen, *Chem. Commun.*, 2016, 52, 1637-1640.
16. W. Zhou, S. Wang, Y. Li, S. Xin, A. Manthiram and J. B. Goodenough, *J. Am. Chem. Soc.*, 2016, 138, 9385-9388.
17. B. Liu, Y. Gong, K. Fu, X. Han, Y. Yao, G. Pastel, C. Yang, H. Xie, E. D. Wachsman and L. Hu, *ACS Appl. Mater. Interfaces*, 2017, 9, 18809-18815.
18. P. R. Chinnam and S. L. Wunder, *ACS Energy Lett.*, 2016, 2, 134-138.
19. R. Chen, W. Qu, X. Guo, L. Li and F. Wu, *Mater. Horiz.*, 2016, 3, 487-516.
20. S. Wang, Y. Ding, G. Zhou, G. Yu and A. Manthiram, *ACS Energy Lett.*, 2016, 1, 1080-1085.
21. L. Wang, Y. Wang and Y. Xia, *Energy Environ. Sci.*, 2015, 8, 1551-1558.
22. X. Meng, X. Q. Yang and X. Sun, *Adv. Mater.*, 2012, 24, 3589-3615.
23. J. Liu and X. Sun, *Nanotechnology*, 2014, 26, 024001.
24. Y. Zhao and X. Sun, *ACS Energy Lett.*, 2018, 3, 899-914.
25. D. Wang, J. Yang, J. Liu, X. Li, R. Li, M. Cai, T.-K. Sham and X. Sun, *J. Mater. Chem. A*, 2014, 2, 2306-2312.
26. X. Li, J. Liu, M. N. Banis, A. Lushington, R. Li, M. Cai and X. Sun, *Energy Environ. Sci.*, 2014, 7, 768-778.
27. X. Li, J. Liu, X. Meng, Y. Tang, M. N. Banis, J. Yang, Y. Hu, R. Li, M. Cai and X. Sun, *J. Power Sources*, 2014, 247, 57-69.

28. C. Wang, Q. Sun, Y. Liu, Y. Zhao, X. Li, X. Lin, M. N. Banis, M. Li, W. Li, K. R. Adair, D. Wang, J. Liang, R. Li, L. Zhang, R. Yang, S. Lu and X. Sun, *Nano Energy*, 2018, 48, 35-43.
29. J. Ferguson, A. Weimer and S. George, *Chem. Mater.*, 2004, 16, 5602-5609.
30. M. Groner, F. Fabreguette, J. Elam and S. George, *Chem. Mater.*, 2004, 16, 639-645.
31. F. Croce, G. Appetecchi, L. Persi and B. Scrosati, *Nature*, 1998, 394, 456.
32. X. Li, X. Li, M. N. Banis, B. Wang, A. Lushington, X. Cui, R. Li, T.-K. Sham and X. Sun, *J. Mater. Chem. A*, 2014, 2, 12866-12872.
33. D. Zheng, D. Liu, J. B. Harris, T. Ding, J. Si, S. Andrew, D. Qu, X.-Q. Yang and D. Qu, *ACS Appl. Mater. Interfaces*, 2016, 9, 4326-4332.
34. X. Xiao, P. Lu and D. Ahn, *Adv. Mater.*, 2011, 23, 3911-3915.
35. Y. S. Jung, P. Lu, A. S. Cavanagh, C. Ban, G. H. Kim, S. H. Lee, S. M. George, S. J. Harris and A. C. Dillon, *Adv. Energy Mater.*, 2013, 3, 213-219.
36. M. Lécuyer, J. Gaubicher, M. Deschamps, B. Lestriez, T. Brousse and D. Guyomard, *J. Power Sources*, 2013, 241, 249-254.
37. L. Carbone and J. Hassoun, *Ionics*, 2016, 22, 2341-2346.
38. O. Garcia-Calvo, N. Lago, S. Devaraj and M. Armand, *Electrochim. Acta*, 2016, 220, 587-594.
39. K. Liu, Y. Lin, J. D. Miller, J. Liu and X. Wang, *J. Electrochem. Soc.*, 2017, 164, A447-A452.
40. X. Judez, H. Zhang, C. Li, J. A. González-Marcos, Z. Zhou, M. Armand and L. M. Rodríguez-Martinez, *J. Phys. Chem. Lett.*, 2017, 8, 1956-1960.
41. J. Hassoun and B. Scrosati, *Adv. Mater.*, 2010, 22, 5198-5201.
42. X. Liang, Z. Wen, Y. Liu, H. Zhang, L. Huang and J. Jin, *J. Power Sources*, 2011, 196, 3655-3658.
43. X. Zhu, Z. Wen, Z. Gu and Z. Lin, *J. Power Sources*, 2005, 139, 269-273.

## Supporting information

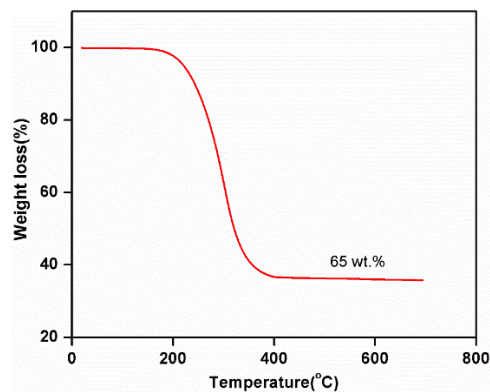


**Figure S9.1** TGA analysis of C-S composite

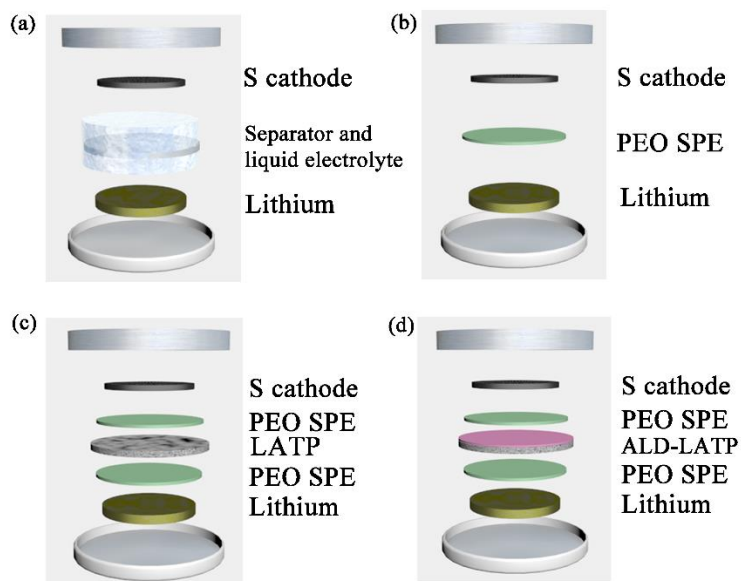


**Figure S9.2** Schematic diagram shows the configurations of Li-S batteries in our studies.

(a) Liquid-based Li-S battery; (b) All-solid-state Li-S battery with PEO SPE; (c) All-solid-state Li-S battery with PLP SSE; (d) All-solid-state Li-S battery with ALD-PLP SSE



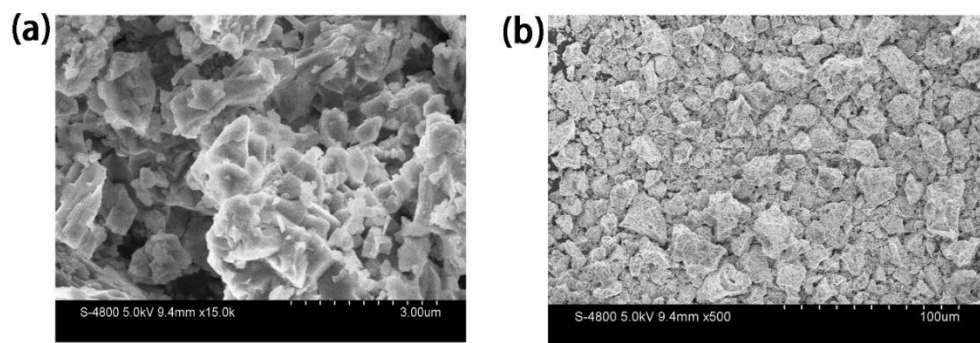


**Figure S9.3** SEM images of LATP precursor after calcinating at 700 °C for 2 h. (a) high magnification, (b) low magnification.

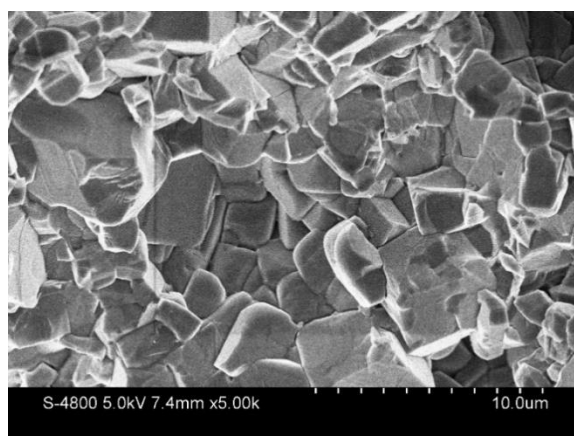


**Figure S9.4** Cross section SEM image of LATP SSE after sintering at 900 °C, 6 h.

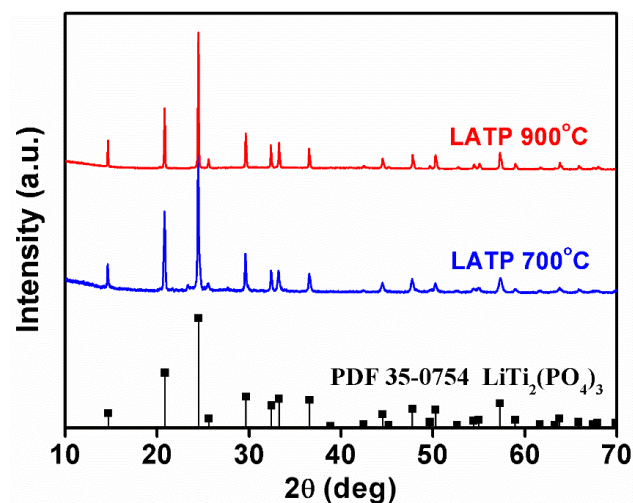


**Figure S9.5** XRD patterns of LATP after calcinating at 700 °C and after sintering at 900 °C.

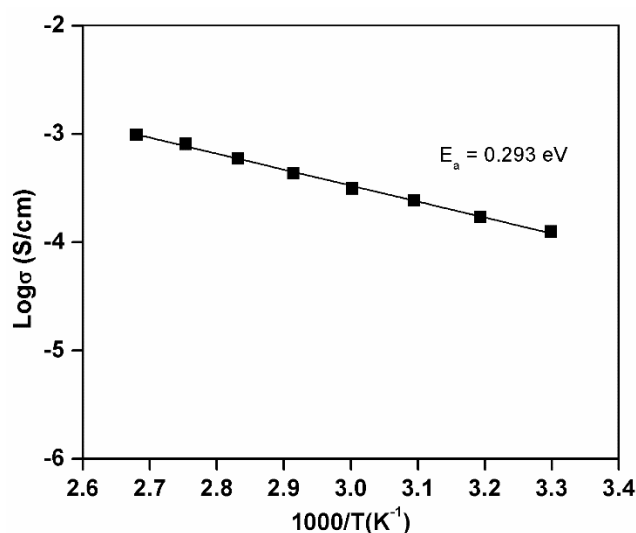


**Figure S9.6** Temperature dependent ionic conductivity of LATP SSE after sintering at 900 °C.

LATP pellets were polished to a thickness of around 500 μm before ALD Al<sub>2</sub>O<sub>3</sub> coating process. The morphology of LATP after calcination are presented in Figure S9.3a, b. The particle size of the LATP precursor is around 200-500 nm with secondary aggregates ranging from 10 to 50 μm in dimension (Figure S9.3b). After sintering at 900 °C, LATP particles are well bonded to each other and a dense structure can be obtained (Figure S9.4). Both LATP powder and LATP pellet are found to exhibit the same phase as parent crystal

structure  $\text{LiTi}_2(\text{PO}_4)_3$  (PDF 35-0754) phase structure (Figure S9.5). The ionic conductivity of LATP is  $1.6 \times 10^{-4} \text{ S/cm}$  at RT with an activation energy ( $E_a$ ) of 0.293 eV (Figure S9.6),

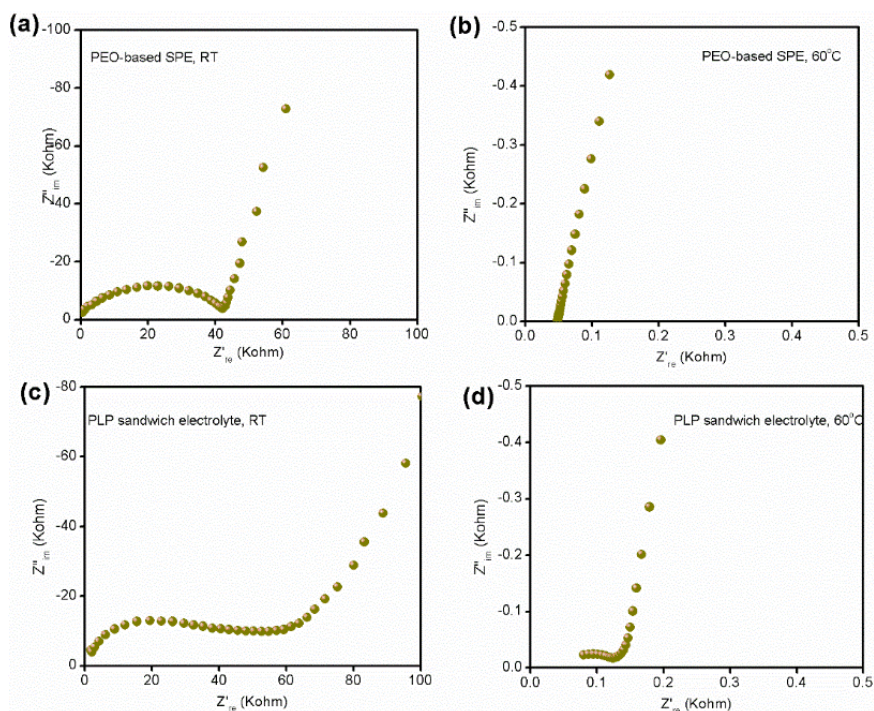


**Figure S9.7** EIS of (a) PEO-based SPE at RT, (b) PEO-based SPE at 60 °C, (c) PLP sandwich-type hybrid electrolyte at RT and (d) 60 °C.

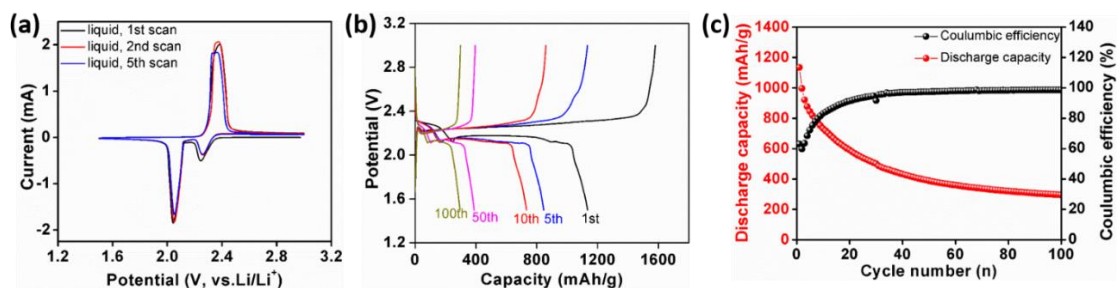


**Figure S9.8** (a) CV curve of liquid-based Li-S battery, (b) charge/discharge profile of liquid-based Li-S battery, (c) discharge capacity and coulombic efficiency of liquid-based Li-S battery. All testing is performed at 60 °C.

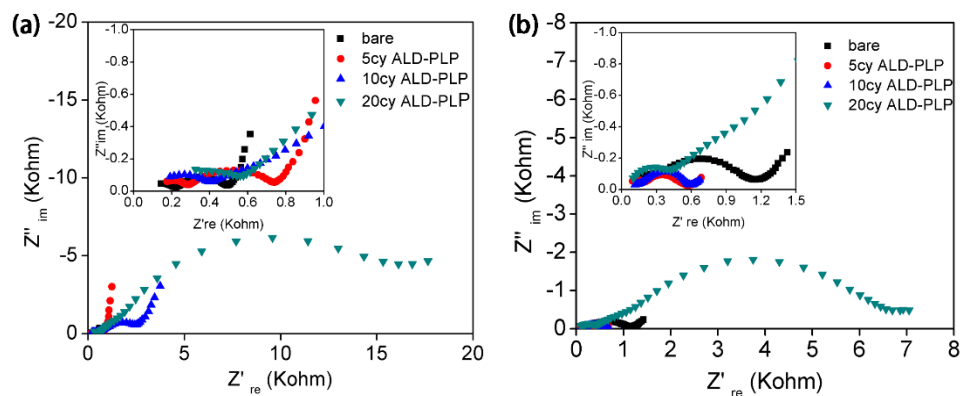


**Figure S9.9** EIS of ASSLSBs with different cycles ALD coating PLP sandwich-type hybrid electrolyte at 60 °C (a) before charge/discharge testing and (b) after 100 charge/discharge cycles.

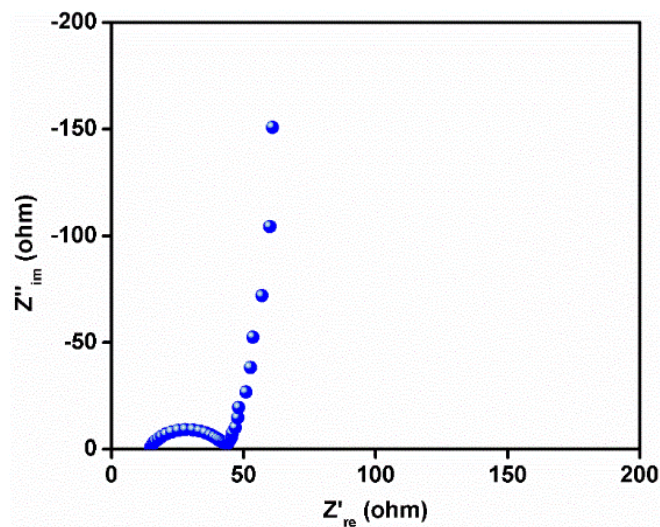


**Figure S9.10** EIS of Liquid-based Li-S battery at 60 °C before charge/discharge testing. The overall impedance of liquid-based Li-S battery is 44  $\Omega$ , much smaller than that of ASSLSBs with PLP electrolyte ( $\sim 500 \Omega$ ).

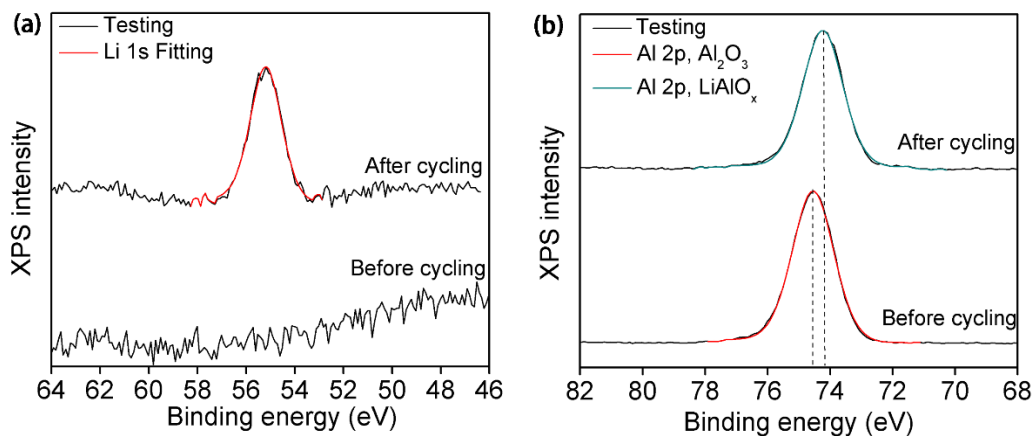


**Figure S9.11** Comparisons of Li 1s and Al 2p XPS on 50cy ALD coating LATP surface before charge/discharge and after 10 cycles charge/discharge.

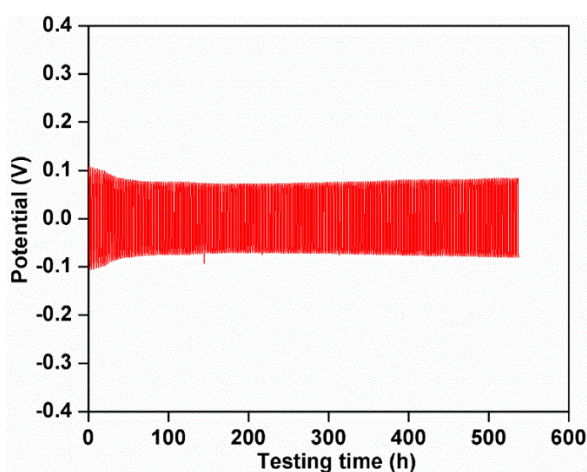


**Figure S9.12** Potential profile of lithium symmetric cell with PLP SSE at 60 °C, current density 0.1 mA/cm<sup>2</sup>, with a cut-off capacity 0.1 mAh/cm<sup>2</sup>.

The LATP SSE is known to suffer from chemical instability against the lithium metal anode where the Ti<sup>4+</sup> is reduced. However, SPEs can be applied between the LATP SSE and lithium anode, leading to the formation of a stable interface that can inhibit dendrite growth. Figure S9.12 shows the lithium plating/stripping process of lithium symmetric cell with PLP sandwich-type hybrid electrolyte at a current density of 0.1 mA/cm<sup>2</sup>. Over 500 h testing period, no short circuit or overpotential growth could be observed, which indicates

a stable plating/stripping process with no dendrite formation. This result eliminates the possibility of the reduction of LATP in ASSLSBs by lithium anode.

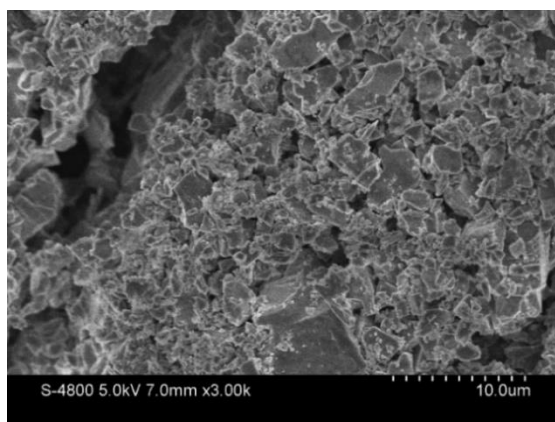


**Figure S9.13** Bare LATP after 100 charge/discharge cycles in ASSLSB. The formation of the small particles indicates the decomposition of LATP by polysulfide.

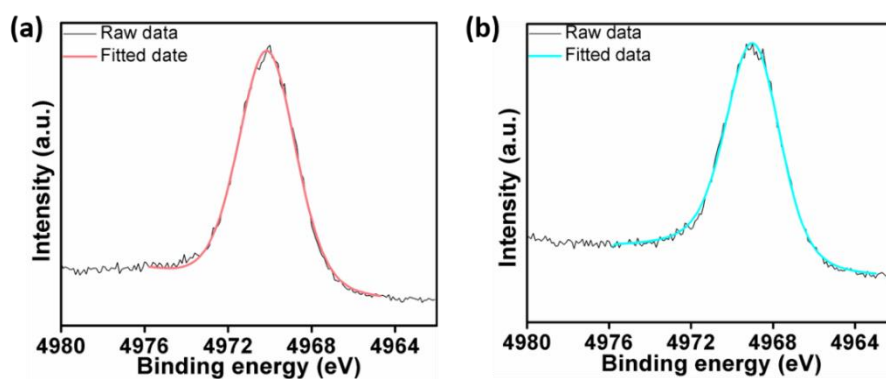


**Figure S9.14** (a) Ti 1s XPS of pristine LATP and (b) Ti 1s XPS of reduced-LATP by polysulfide solution.

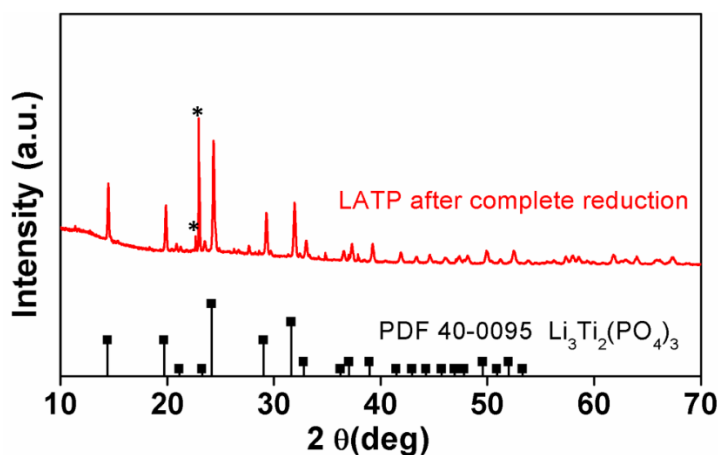


**Figure S9.15** XRD of completely reduced-LATP. (\* sulfur) The existence of sulfur peaks is due to the oxidation of  $\text{Li}_2\text{S}_6$  by LATP.

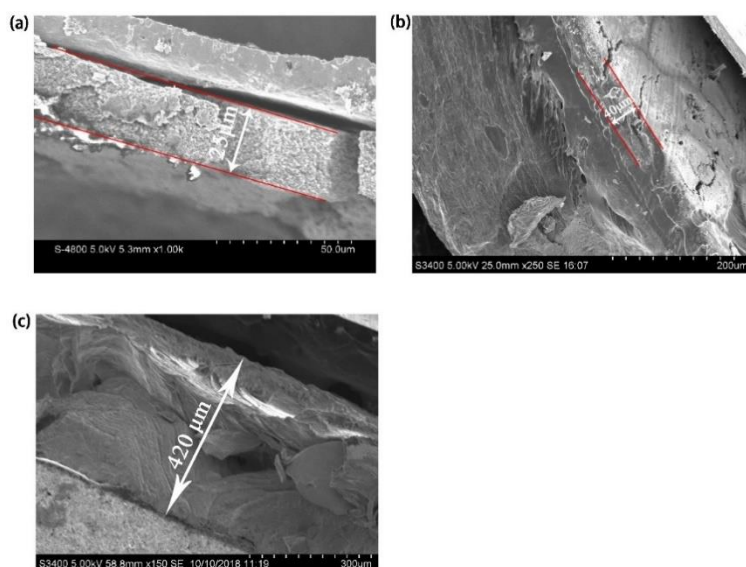


**Figure S9.16** Cross-section SEM images of (a) C-S cathode; (b) C-S cathode after 100 cycles charge/discharge. (c) Lithium anode after 100 cycles charge/discharge.

**Figure S9.16a** is the cross-section SEM image of a C-S cathode with current collector. The thickness of the cathode layer is 25  $\mu\text{m}$ . After the cathode was charge/discharge for 100 times, the thickness of the cathode is 40  $\mu\text{m}$ . The volume expansion is 60 % which is significant large. For the anode part, the SEM image of lithium anode after 100 cycles was

obtained, whose thickness is 420  $\mu\text{m}$ . 10  $\mu\text{m}$  thicker than the original lithium anode (410  $\mu\text{m}$ ).

**Table S9.1** A comparison of the all-solid-state Li-S batteries performances

Solid-state electrolyte	Sulfur loading ( $\text{mg}/\text{cm}^2$ )	Initial capacity ( $\text{mAh}/\text{g}$ )	Cycling ( $\text{mAh}/\text{g}$ )	performance	Refs.
PEO-LiCF <sub>3</sub> SO <sub>3</sub>	/	520 (0.05C)	300 (Second cycles, 0.05C)		37
PEO-PEGDA-DVB cross-linking polymer- LITFSI	/	375 (0.05C)	175 (50 <sup>th</sup> cycles, 0.05C)		38
Polyether-based polymer-LiClO <sub>4</sub> -SiO <sub>2</sub>	0.34	1131	About 965 (first charge)		9
Sucrose-boron polymer- PEO-LITFSI	About 0.8 (PAN-S)	1302 (0.1C)	About 620 (100 <sup>th</sup> cycles, 0.1C)		39
PEO-LITFSI	/	900 (0.05C)	About 700(50 <sup>th</sup> cycles, 0.05C)		40
PEO-LiCF <sub>3</sub> SO <sub>3</sub> -ZrO <sub>2</sub>	/	About 170	About 172 (50 <sup>th</sup> cycles)		41
PEO-LiTFSI-SiO <sub>2</sub>	/	1265	800 (25 <sup>th</sup> cycles)		42
PEO-LiTFSI-LiAlO <sub>2</sub>		609	280 (10 <sup>th</sup> cycles)		43
PEO/ALD-LATP/PEO	0.6~1	1035 (0.1C)	823 (100 <sup>th</sup> cycles, 0.1C)		<b>This work</b>

**Table S9.2** XPS fitting results

Sample name	Bare LATP	5 ALD-LATP	10 ALD-LATP	20ALD-LATP
Content of Ti <sup>4+</sup> (%)	28.7	56.8	62.6	70.8
Content of reduced-Ti (%)	71.3	43.2	37.4	29.2



## Chapter 10

### 10 Conclusions and perspectives

In this chapter, the results and contributions of this thesis and personal suggestions of the future directions for developing high performance all solid-state batteries (ASSBs) will be summarized.

## 10.1 Conclusion

LIBs have become dominating energy storage systems for the applications in portable devices and electric vehicles in modern society. However, using liquid organic electrolyte in LIBs makes the batteries unsafe, thus ASSLIBs are regarded as the ultimate solution for safe energy storage systems. For achieving high performance ASSLIBs, SSEs are the key factor. This thesis focused on two popular SSEs including SPE and oxide-based SSEs, which are the most promising SSEs for building ASSBs. PEO-based SPEs have high ionic conductivity at elevated temperature, low interfacial resistance towards electrodes and a facile preparation process. With these advantages, PEO-based SPEs received tremendous research attentions. However, the low electrochemical oxidation window of PEO-based SPEs seriously limit their application in high energy density ASSLIBs. Even though PEO-based SPEs have been commercialized in the Bolloré Bluecar, with a lithium metal anode and  $\text{LiFePO}_4$  cathode, their electrochemical performance with high energy density cathodes such as  $\text{LiCoO}_2$ , Ni-rich NMC, etc. is still very poor. Oxide-based SSEs are relatively stable at ambient environment and they have high ionic conductivity at RT, which has made them also attracting many research interests. However, the mismatch problem due to the rigid property and the reduction of  $\text{Ti}^{4+}$  still inhibit their wide application.

In order to break the limitation of PEO-based SPE coupling with high energy density cathode materials, interfacial engineering between the SPE and cathode, as well as developing high voltage stable SPEs are reported to be the effective approaches. To address the mismatch problem in the oxide-based SSE, co-sintering the oxide-based SSE and cathode, with a low melting point of SSE, is an effective strategy. To prevent the reduction of  $\text{Ti}^{4+}$ , surface coating to prevent direct contact between the SSE and reductant is a practical solution.

One of the main objectives of this thesis is to develop different approaches including interface engineering, SPE modification and electrode designs for coupling PEO-based SPEs with high voltage, high energy density cathode materials, to get high performance, long cycling life of ASSLIBs. Another main objective is to understand how these approaches achieve better performance by combining the results from synchrotron

radiation technique, XPS and TEM, etc. studies. One more objective of this thesis is to tackle the mismatch problem of oxide-based SSE by using halide SSE as a co-sintering material and  $\text{Ti}^{4+}$  reduction problem of LATP SSEs by interface protection approach. More details about each part is described as follows:

1). Interface engineering between the cathode electrode and SPE by ALD derived lithium tantalate was studied. The effects of ALD derived lithium tantalate coating on the  $\text{LiCoO}_2$  cathode electrode surface (coating on both  $\text{LiCoO}_2$  particles and AB particles),  $\text{LiCoO}_2$  particles only, and AB particles only were studied. There is a significant enhancement in the electrochemical performance of  $\text{LiCoO}_2$  cathode electrode surface coating and AB particles coating, while no positive effect was seen for the  $\text{LiCoO}_2$  particles coating. This indicates that the stability of the AB/SPE interface is very important for high voltage ASSLIBs. LSV studies show that AB can accelerate the electrochemical decomposition of the SPE, while the low electronic conductive lithium tantalate coating layer can effectively reduce the electrochemical decomposition at high voltage. XAS studies disclosed that  $\text{LiCoO}_2$  particles are stable during charge/discharge cycling and that further coating with ALD does not show positive effects of enhancing their performance.

2). In order to further increase the energy density of ASSLIBs, a Ni-rich NMC811 cathode, which has higher energy density compared to  $\text{LiFePO}_4$  and  $\text{LiCoO}_2$ , must be used. Therefore, applying NMC811 in the ASSLIBs is important for achieving high energy density. However, not only the electrochemical decomposition of PEO-based SPEs but also the instability of NMC811 during cycling process, attribute to the poor cycling performance of the ASSLIBs. To enhance the performance of NMC811 ASSLIBs, inspired by previous work, ALD derived LNO was coated on the NMC811 electrode surface. The mechanism studies by STEM, XAS and XPS disclosed that LNO coating can not only enhance the stability of the NMC811 cathode, but also inhibit the chemical/electrochemical decomposition of the PEO-based SPE, therefore, rendering a stable performance of high energy density ASSLIBs.

3). Different from the interfacial engineering strategy, a facile method for enhancing the electrochemical oxidation window of PEO-based solid-polymer electrolytes was disclosed

by simply tailoring the end functional group of the PEO polymer chain. Traditionally, PEO based SPEs were prepared by AN solvent. In contrast, by using DMF as the preparation solvent, we found that ASSLIBs, with DMF prepared SPEs have better electrochemical cycling performance compared to AN prepared SPEs. NMR studies illustrated that the methyl end group of PEO was replaced by a dimethylamine group. The Gibbs energy for breaking the C-C bond in dimethylamine end group PEO is 3 times higher than that of methyl end group PEO, which disclosed the reason why DMF prepared PEO-based SPEs have higher electrochemical stability.

4). Another factor that influences the performance of 4 V class ASSLIBs was studied in this thesis, which is the binder effect. By comparing the performance of different binders including common used PEO, PVDF binder and two kinds of carboxyl-rich polymer (CRP) binders which are Na-alginate or CMC, it is found that CRP binders are better binders for 4 V class ASSLIBs. After 1000 cycles, the ASSLIBs can maintain a capacity retention of 60%, 10 times high than that of PEO binder based ASSLIBs. CV studies shows CRP binders have less electrochemical decomposition at high voltage. Mechanism studies by XAS and DFT calculation show that carboxyl in CRP has a strong attraction capacity on the surface of  $\text{LiCoO}_2$  and CRP works as a coating like material for the stabilizing cathode/SPE interface.

5). Oxide-based SSEs are promising for the application in ASSLIBs. However, the mismatch problem significantly hinders the performance of ASSLIBs that use oxide-based SSEs. To address this challenge, a high ionic conductive halide SSE,  $\text{Li}_3\text{InCl}_6$ , was in-situ synthesized at the SSE/electrode interface to ensure the intimate contact between LLZO oxide-based SSE and  $\text{LiCoO}_2$  cathode. With the in-situ synthesized  $\text{Li}_3\text{InCl}_6$ , ASSLIBs can operate at 0.1C and deliver a discharge capacity of 129.2 mAh/g, which is comparable to that delivered from liquid based LIBs. And the loading of the active materials can be as high as 13 mg/cm<sup>2</sup>. Such a good electrochemical performance indicates that applying a low melting point, high ionic conductivity halide SSE as the co-sintering assistance for building practical oxide based ASSLIBs is possible. This provides a new approach for developing high performance oxide based ASSLIBs.

6). Li-S batteries are regarded as the next generation lithium batteries due to their ultra-high energy density. However, the polysulfide shuttle effect, the low ionic and electronic conductivity of the sulfur cathode and the huge volume change of the cathode, limit the development of Li-S batteries. In the last of this thesis, an ASSLSB with a polymer-ceramic sandwich structure SSE was studied. SPEs work as an interlayer for intimate contact between the oxide-based SSE and sulfur cathode. However, the charge intermediate products, polysulfides, will reduce the  $Ti^{4+}$  in the LATP SSE. To stabilize the LATP SSE, an ultra-thin and uniform ALD derived  $Al_2O_3$  thin film was coated on the surface of the LATP towards sulfur cathode side. With the  $Al_2O_3$  protection, the stability of the LATP was greatly improved as confirmed by the SEM, XPS and XRD results. Due to the enhanced the stability of the LATP, the performance of ASSLSBs was greatly enhanced.

## 10.2 Contributions to this field

1. Developing ultrathin film as a protective layer for coupling high voltage cathodes with SPEs. In this thesis, we developed ALD derived materials to act as the protective layer for stabilizing the cathode/SPE interface. ALD is a low temperature process, which makes it a friendly process for depositing thin film coating materials. Moreover, the thin film and controllable thickness of ALD will not inhibit the transportation of ions. In this thesis, the details for coating on electrode or cathode particles were also disclosed, providing a guide for future work on coating strategy for enhancing the performance of ASSLIBs.

2. Developing a new approach for enhancing the electrochemical oxidation window of PEO-based SPEs. In chapter 6, we disclosed that the end functional group of the PEO polymer chain has great influence on the stability of PEO. Gibbs energy for breaking the C-C bond in the dimethylamine end group of PEO is almost 3 times higher than that of methyl end group PEO. With the dimethylamine end group PEO-based SPE, the cycling performance of 4 V class ASSLIBs was significantly improved.

3. New insight for understanding the binder effects on the performance of 4 V class ASSLIBs. In most of the reported studies, the binder for ASSLIBs with a SPE is PEO or EO containing polymer, for enhancing the ionic conductivity of the electrode. However, PEO and EO containing polymer has a low electrochemical oxidation window, which

means it is a good binder for 4 V ASSLIBs. To pursue a high-performance binder for 4 V class ASSLIBs, carboxyl-rich polymers were studied. With carboxyl-rich polymer CMC as the binder, the capacity retention of 4 V ASSLIBs, after 1000 cycles, is maintain at 60%; 10 times high than that of PEO binders.

4. Developing a new strategy for building practical oxide based ASSLIBs. Oxide based ASSLIBs suffer from the mismatch problem due to their rigid property. Up to now, the developed methods for building oxide based ASSLIBs include adding liquid electrolyte, applying a SPE interlayer, and using  $\text{Li}_3\text{BO}_3$  as the co-sintering assistance. In chapter 8, we applied a new approach, which is in-situ synthesis of halide SSE  $\text{Li}_3\text{InCl}_6$  at the SSE/cathode interface to ensure intimate contact between the SSE and cathode. In-situ synthesis  $\text{Li}_3\text{InCl}_6$  was conducted by a solution-based method at 200 °C. The solution-based method helps to create an even distribution of  $\text{Li}_3\text{InCl}_6$  at the interface and provide continuous  $\text{Li}^+$  ion change within the thick electrode. With the  $\text{Li}_3\text{InCl}_6$ , ASSLIBs with LLZO and  $\text{LiCoO}_2$  were built and delivered excellent electrochemical performance.

5. Deep understanding of the interface properties between the cathode and SSE. The surface and interface chemistries of cathodes, including  $\text{LiCoO}_2$ , Ni-rich NMC811 and sulfur, as well as the SSE, have been deeply investigated by different techniques, including X-ray photoelectron spectroscopy (XPS), the synchrotron based XAS technique, STEM and SEM.

### 10.3 Perspectives

Although there have been some progresses related to the development of high energy density ASSBs, there are still significant challenges to be overcome. Herein, I propose potential directions and perspectives for this field:

1. Developing high voltage stable SPEs for high energy density ASSLIBs. PEO-based SPEs are popular SSEs for ASSLIBs, however, their electrochemical stability window is limited, which means they cannot be used in high voltage battery systems (over 4.5 V vs. $\text{Li}/\text{Li}^+$ ), even though a coating layer is applied. Therefore, developing high voltage stable SPEs is very important for the development of high energy density ASSLIBs.

Tailoring the end functional group of the PEO polymer chain would be a good strategy, as proposed in chapter 6. The stabilities of different end functional groups of PEO-based SPEs can be calculated and summarized to provide a guide for developing high voltage stable PEO-based SPEs. Other polymer systems are also worth trying for high voltage stable SPEs.

**2. Developing high voltage stable coating materials for enhancing the cycling performance of 4 V class ASSLIBs.**

F containing materials such as LiF, AlF<sub>3</sub> etc. are calculated to be stable at higher voltages (up to 6 V vs. Li/Li<sup>+</sup>). Applying such materials as the coating layer for protecting the interface between high voltage cathodes and SSEs is one of the most promising directions.

**3. Developing high performance binders for high energy density ASSLIBs.**

In chapter 7, for the first time we disclosed that binders have a very important impact on the performance of 4 V class ASSLIBs. The carboxyl-rich polymer binders present better performance in ASSLIBs. However, carboxyl-rich polymer binders have poor ionic conductivity, and this will sacrifice the rate performance of ASSLIBs. It is believed that there must be other better binders for high rate, long cycling life of ASSLIBs. To pursue a high ionic conductivity, high performance polymer binder is a future research direction.

**4. Better fundamental understating between the high voltage cathode and SPE interface by advanced characterization techniques.**

A well accepted opinion is that SPEs will electrochemically decompose at high voltage. However, the electrochemical decomposition process (electrochemical reaction), the decomposed products and their influence on the solid electrolyte interphase have not yet been fully studied. Moreover, the layer structure cathode materials such as LiCoO<sub>2</sub>, NMC have the oxygen release problem. The influence of the released oxygen on the decomposition of SPEs is still not clear. Therefore, fundamental studies on these fields are important for further development of high energy density ASSLIBs. Advanced characterization techniques, including MS, cryo-TEM, STXM, resonant inelastic X-ray scattering (RIXS) etc. are important techniques for better understanding the decomposition of SPEs and the related oxygen release effect.

**5. Next generation all-solid-state Li-S batteries.**

In chapter 9, ASSLBs with a PEO-LATP sandwich structure SSE was fabricated. LATP is unstable toward polysulfide

species. In future studies, other oxide-based SSEs such as LLZO and LAGP can be used in ASSLSBs. To address the interface mismatch issue, using halide SSEs as the co-sintering assistance can be a potential solution for replacing the SPE interlayer. The application of other SSEs, such as sulfide-based, halide SSEs and SPEs, in ASSLSBs are potential future directions in this field.

**6. Practical application.** To realize the practical application of ASSBs, the cycling performance and the energy density of the ASSBs are two main factors that need to be seriously considered. The cycling performance of the batteries relies on the chemical/electrochemical stability of the battery's components, including the cathode, anode, electrolyte, current collector and the interface. The energy density of the batteries is related to the capacity of the electrodes and the weight percentage of each component. To get a higher energy density battery, each component of the battery should be minimized. Therefore, developing ultra-thin SSEs for reducing the weight of SSE can improve the energy density of SSBs for practical application.

In conclusion, different approaches including interface engineering, electrolyte modification, and electrode design have been developed in this thesis for enhancing the performance of ASSLIBs. The mismatch problem and the instability problem in oxide SSE based ASSBs were also addressed. However, there is still a long way to go for developing ASSBs for practical applications. A deep understanding of the interface chemicals in ASSBs is necessary and the energy density for practical battery application need to be considered. It is expected that with continued efforts, a high energy density and high performance ASSB for practical electric vehicle application can be achieved.



## Appendices

### Appendix A: Permission from Royal Society of Chemistry (RSC) For Published Article on **Journal of Materials Chemistry A**.

Published papers:

1. **Jianneng Liang**, Qian Sun, Yang Zhao, Yipeng Sun, Changhong Wang, Weihan Li, Minsi Li, Dawei Wang, Xia Li, Yulong Liu, Keegan Adair, Ruying Li, Li Zhang, Rong Yang, Shigang Lu, Huan Huang, Xueliang Sun, Stabilization of all-solid-state Li-S batteries with a polymer-ceramic sandwich electrolyte by atomic layer deposition, **J. Mater. Chem. A**, 2018, 6, 23712-23719.

2. **Jianneng Liang**, Yipeng Sun, Yang Zhao, Qian Sun, Jing Luo, Feipeng Zhao, Xiaoting Lin, Xia Li, Ruying Li, Li Zhang, Shigang Lu, Huan Huang, Xueliang Sun, Engineering the conductive carbon/PEO interface to stabilize solid polymer electrolytes for all-solid-state high voltage LiCoO<sub>2</sub> batteries, **J. Mater. Chem. A**, 2020, 8, 2769-2776.

**RSC Copyright Policy:** <https://www.rsc.org/journals-books-databases/journal-authors-reviewers/licences-copyright-permissions/#deposition-sharing>

## Re-use permission requests

Material published by the Royal Society of Chemistry and other publishers is subject to all applicable copyright, database protection, and other rights. Therefore, for any publication, whether printed or electronic, permission must be obtained to use material for which the author(s) does not already own the copyright. This material may be, for example, a figure, diagram, table, photo or some other image.

---

### Author reusing their own work published by the Royal Society of Chemistry

You do not need to request permission to reuse your own figures, diagrams, etc, that were originally published in a Royal Society of Chemistry publication. However, permission should be requested for use of the whole article or chapter except if reusing it in a thesis. If you are including an article or book chapter published by us in your thesis please ensure that your co-authors are aware of this.

Reuse of material that was published originally by the Royal Society of Chemistry must be accompanied by the appropriate acknowledgement of the publication. The form of the acknowledgement is dependent on the journal in which it was published originally, as detailed in 'Acknowledgements'.

## Appendix B: Permission from Elsevier for Published Article on **Energy Storage Materials**

**RightsLink**Home?Email SupportSign inCreate Account



**Recent progress on solid-state hybrid electrolytes for solid-state lithium batteries**  
Author: Jianneng Liang, Jing Luo, Qian Sun, Xiaofei Yang, Ruying Li, Xueliang Sun  
Publication: Energy Storage Materials  
Publisher: Elsevier  
Date: September 2019  
© 2019 Elsevier B.V. All rights reserved.

Please note that, as the author of this Elsevier article, you retain the right to include it in a thesis or dissertation, provided it is not published commercially. Permission is not required, but please ensure that you reference the journal as the original source. For more information on this and on your other retained rights, please visit: <https://www.elsevier.com/about/our-business/policies/copyright#Author-rights>


[BACK](#) [CLOSE WINDOW](#)

© 2020 Copyright - All Rights Reserved | Copyright Clearance Center, Inc. | Privacy statement | Terms and Conditions  
Comments? We would like to hear from you. E-mail us at [customer@copyright.com](mailto:customer@copyright.com)

Published papers:


**Jianneng Liang, Jing Luo, Qian Sun, Xiaofei Yang, Ruying Li, Xueliang Sun, Recent progress on solid-state hybrid electrolytes for solid-state lithium batteries, *Energy Storage Materials*, 2019, 21, 308-334.**

## Appendix C: Permission from Elsevier for Published Article on **Nano Energy**.



# RightsLink®

Home
Help
Email Support
Sign in
Create Account



**Stabilizing and understanding the interface between nickel-rich cathode and PEO-based electrolyte by lithium niobium oxide coating for high-performance all-solid-state batteries**

**Author:**  
 Jianneng Liang, Sooyeon Hwang, Shuang Li, Jing Luo, Yipeng Sun, Yang Zhao, Qian Sun, Weihan Li, Minsi Li, Mohammad Norouzi Banis, Xia Li, Ruying Li, Li Zhang, Shangqian Zhao, Shigang Lu, Huan Huang, Dong Su, Xueliang Sun

**Publication:** Nano Energy  
**Publisher:** Elsevier  
**Date:** December 2020

© 2020 Elsevier Ltd. All rights reserved.

Please note that, as the author of this Elsevier article, you retain the right to include it in a thesis or dissertation, provided it is not published commercially. Permission is not required, but please ensure that you reference the journal as the original source. For more information on this and on your other retained rights, please visit: <https://www.elsevier.com/about/our-business/policies/copyright#Author-rights>

BACK
CLOSE WINDOW

© 2020 Copyright - All Rights Reserved | [Copyright Clearance Center, Inc.](#) | [Privacy statement](#) | [Terms and Conditions](#)  
 Comments? We would like to hear from you. E-mail us at [customer@copyright.com](mailto:customer@copyright.com)

### Published papers:

**Jianneng Liang**, Sooyeon Hwang, Shuang Li, Jing Luo, Yipeng Sun, Yang Zhao, Qian Sun, Weihan Li, Minsi Li, Mohammad Norouzi Banis, Xia Li, Ruying Li, Li Zhang, Shangqian Zhao, Shigang Lu, Huan Huang, Dong Su, Xueliang Sun, Stabilizing and understanding the interface between nickel-rich cathode and PEO-based electrolyte by lithium niobium oxide coating for high-performance all-solid-state batteries, **Nano Energy**, 2020, 105107.

## Curriculum Vitae

<b>Name:</b>	Jianneng Liang
<b>Post-secondary Education and Degrees:</b>	Central South University Changsha, Hunan, China 2011-2015 B.A.
	The University of Western Ontario London, Ontario, Canada 2015-2020 Ph.D.
<b>Honours and Awards:</b>	China Scholarship Council 2015-2019,
	Mitacs Interns award 2020. 03-2020. 05
<b>Related Work Experience</b>	Research Assistant The University of Western Ontario 2015-2020

### Publications:

(A) Peer-reviewed Journal Papers Based on This Thesis (First Author)

1. **J. Liang**, Y. Sun, Y. Zhao, Q. Sun, J. Luo, F. Zhao, X. Lin, X. Li, R. Li, L. Zhang, S. Lu, H. Huang, and X. Sun, Engineering the Conductive Carbon/PEO Interface to Stabilize Solid Polymer Electrolytes for All-Solid-State High Voltage LiCoO<sub>2</sub> Batteries, **J. Mater. Chem. A**, 2020, 8, 2769-2776.
2. **J. Liang**, J. Luo, Q. Sun, X. Yang, R. Li, X. Sun, Recent progress on solid-state hybrid electrolytes for solid-state lithium batteries, **Energy Storage Mater.**, 2019, 21, 308-334.
3. **J. Liang**, Q. Sun, Y. Zhao, Y. Sun, C. Wang, W. Li, M. Li, D. Wang, X. Li, Y. Liu, K. Adair, R. Li, L. Zhang, R. Yang, S. Lu, H. Huang, X. Sun, Stabilization of all-solid-state Li-S batteries with a polymer–ceramic sandwich electrolyte by atomic layer deposition, **J. Mater. Chem. A**, 2018, 6 (46), 23712-23719.
4. **J. Liang**, S. Hwang, S. Li, J. Luo, Y. Sun, Y. Zhao, Q. Sun, W. Li, M. Li, M. N. Banis, X. Li, R. Li, L. Zhang, S. Zhao, S. Lu, H. Huang, D. Su, and X. Sun, Stabilizing

and understanding the interface between Nickel-rich cathode and PEO-based electrolyte by lithium niobium oxide coating for high-performance all-solid-state batteries, **Nano Energy**, 2020, Accepted.

5. **J. Liang**, D. Chen, K. Adair, Q. Sun, N. G. Holmes, Y. Zhao, Y. Sun, J. Luo, R. Li, S. Zhao, S. Lu, H. Huang, X. Zhang, C. V. Singh, X. Sun\*, Dramatically prolonged cycling life of 4 V all solid-state polymer batteries by alternating high voltage compatible binders, to be submitted, 2020.
6. **J. Liang**, A. J. Achazi, . Sun, K. Adair, Y. Sun, R. Li, L. Zhang, S.Lu, H. Huang, P. Kaghazchi, X. Sun\*, A facile method for enhancing the electrochemical oxidation window of PEO-based solid polymer electrolytes, to be submitted, 2020.
7. **J. Liang**, J. Luo, W. Li, J. Li, J. Fu, J. Liang, Q. Sun, R. Li, S. Zhao, L. Zhang, S. Lu, H. Huang, X. Sun\*, In-situ synthesis of Li<sub>3</sub>InCl<sub>6</sub> halide-based solid electrolyte for addressing the interfacial challenge between cathode and garnet solid electrolyte, to be submitted, 2020

(B) Peer-reviewed Journal Papers Related to This Thesis (Co-author)

1. S. Deng, X. Lia, Z. Ren, W. Li, J. Luo, J. Liang, **J. Liang**, M. N. Banis, M. Li, Y. Zhao, X. Li, C. Wang, Y. Sun, Q. Sun, R. Li, Y. Hu, H. Huang, L. Zhang, S. Lu, J. Luo, X. Sun, Dual-functional interfaces for highly stable Ni-rich layered cathodes in sulfide all-solid-state batteries, **Energy Storage Mater.**, 2020, 27, 117-123
2. X. Yang, X. Gao, C. Zhao, Q. Sun, Y. Zhao, K. Adair, J. Luo, X. Lin, **J. Liang**, H. Huang, L. Zhang, S. Lu, R. Li, X. Sun, Suppressed dendrite formation realized by selective Li deposition in all-solid-state lithium batteries, *Energy Storage Mater.*, 2020, 27, 198-204;
3. H. Huo, X. Li, Y. Chen, **J. Liang**, S. Deng, X. Gao, K. D. Davis, R. Li, X. Guo, Y. Shen, C. Nan, X. Sun, Bifunctional composite separator with a solid-state-battery strategy for dendrite-free lithium metal batteries, **Energy Storage Mater.**, 2020, in press;
4. X. Yang, X. Gao, Q. Sun, S. P. Jand, Y. Yu, Y. Zhao, X. Li, K. Adair, L.Y. Kuo, J. Rohrer, **J. Liang**, X. Lin, M. N. Banis, Y. Hu, H. Zhang, X. Li, R.Li, H. Zhang, P. Kaghazchi, T.K. Sham, X. Sun, Promoting the Transformation of Li<sub>2</sub>S<sub>2</sub> to Li<sub>2</sub>S:

- Significantly Increasing Utilization of Active Materials for High-Sulfur-Loading Li-S Batteries, **Adv. Mater.** 2019, 31, 1901220
5. S. Deng, B. Wang, Y. Yuan, X. Li, Q. Sun, K. Davis, M. Banis, **J. Liang**, Y. Zhao, J. Li, R. Li, T. K. Sham, R. Yassar, H. Wang, M. Cai, J. Lu, X. Sun, Manipulation of an ionic and electronic conductive interface for highly-stable high-voltage cathodes, **Nano Energy**, 2019, 65, 103988;
  6. X. Yang, Q. Sun, C. Zhao, X. Gao, K. Adair, Y. Zhao, J. Luo, X. Lin, **J. Liang**, H. Huang, L. Zhang, S. Lu, R. Li, X. Sun, Self-healing electrostatic shield enabling uniform lithium deposition in all-solid-state lithium batteries, **Energy Storage Mater.**, 2019, 22, 194-199;
  7. F. Kong, S. Liu, J. Li, L. Du, M. Banis, L. Zhang, G. Chen, K. Davis, **J. Liang**, S. Wang, F. Zhao, R. Li, C. Du, G. Yin, Z. Zhao, X. Sun, Trimetallic Pt–Pd–Ni octahedral nanocages with subnanometer thick-wall towards high oxygen reduction reaction, **Nano Energy** 2019, 64, 103890;
  8. X. Gao, X. Yang, Q. Sun, J. Luo, **J. Liang**, W. Li, J. Wang, S. Wang, M. Li, R. Li, T. K. Sham, X. Sun, Converting a Thick Electrode into Vertically Aligned “Thin Electrodes” By 3D-Printing for Designing Thickness Independent Li-S Cathode, **Energy Storage Mater.**, 2020, 24, 682-688;
  9. W. Xiao, Q. Sun, M. Banis, B. Wang, **J. Liang**, A. Lushington, R. Li, X. Li, T. K. Sham, X. Sun, Unveiling the Interfacial Instability of the Phosphorus/Carbon Anode for Sodium-Ion Batteries, **ACS Appl. Mater. Interfaces**, 2019, 11, 34, 30763-30773;
  10. Y. Liu, J. Liu, Q. Sun, D. Wang, K. Adair, **J. Liang**, C. Zhang, L. Zhang, S. Lu, H. Huang, X. Song, X. Sun, Insight into the Microstructure and Ionic Conductivity of Cold Sintered NASICON Solid Electrolyte for Solid-State Batteries, **ACS Appl. Mater. Interfaces**, 2019, 11, 31, 27890-27896;
  11. X. Yang, Q. Sun, C. Zhao, X. Gao, K. Adair, Y. Liu, J. Luo, X. Lin, **J. Liang**, H. Huang, L. Zhang, R. Yang, S. Lu, R. Li, X. Sun, High-areal-capacity all-solid-state lithium batteries enabled by rational design of fast ion transport channels in vertically-aligned composite polymer electrodes, **Nano Energy**, 2019, 61, 567-575;

12. S. Wang, J. Liao, X. Yang, J. Liang, Q. Sun, **J. Liang**, F. Zhao, A. Koo, F. Kong, Y. Yao, X. Gao, M. Wu, S. Yang, R. Li, X. Sun, Designing a highly efficient polysulfide conversion catalyst with paramontroseite for high-performance and long-life lithium-sulfur batteries, **Nano Energy**, 2019, 57, 230-240;
13. X. Gao, X. Yang, M. Li, Q. Sun, J. Liang, J. Luo, J. Wang, W. Li, J. Liang, Y. Liu, S. Wang, Y. Hu, Q. Xiao, R. Li, T.K. Sham, X. Sun, Cobalt-Doped SnS<sub>2</sub> with Dual Active Centers of Synergistic Absorption-Catalysis Effect for High - S Loading Li - S Batteries, **Adv. Funct. Mater.**, 2019, 29, 1806724;
14. C. Zhao, **J. Liang**, Q. Sun, J. Luo, Y. Liu, X. Lin, Y. Zhao, H. Yadegari, M. Banis, R. Li, H. Huang, L. Zhang, R. Yang, S. Lu, X. Sun, Ultralong - Life Quasi - Solid - State Li - O<sub>2</sub> Batteries Enabled by Coupling Advanced Air Electrode Design with Li Metal Anode Protection, **Small Methods**, 2019, 3 (2), 1800437;
15. X. Gao, Q. Sun, X. Yang, J. Liang, A. Koo, W. Li, **J. Liang**, J. Wang, R. Li, F. B. Holness, A. Price, S. Yang, T.K. Sham, X. Sun, Toward a remarkable Li-S battery via 3D printing, **Nano Energy**, 2019, 56, 595-603;
16. D. Wang, Q. Sun, J. Luo, **J. Liang**, Y. Sun, R. Li, K. Adair, L. Zhang, R. Yang, S. Lu, H. Huang, X. Sun, Mitigating the Interfacial Degradation in Cathodes for High-Performance Oxide-Based Solid-State Lithium Batteries, **ACS Appl. Mater. Interfaces**, 2019, 11, 5, 4954-4961.
17. C. Zhao, **J. Liang**, Y. Zhao, J. Luo, Q. Sun, Y. Liu, X. Lin, X. Yang, H. Huang, L.Zhang, S. Zhao, S. Lu, X. Sun, Engineering a “nanonet”-reinforced polymer electrolyte for long-life Li–O<sub>2</sub> batteries, **J. Mater. Chem. A**, 2019, Accepted;
18. F. Kong, M. Banis, L. Du, L. Zhang, L. Zhang, J. Li, K.Davis, **J. Liang**, Q. Liu, X. Yang, R. Li, C. Du, G. Yin, X. Sun\*, Highly stable one-dimensional Pt nanowires with modulated structural disorder towards the oxygen reduction reaction, **J. Mater. Chem. A**, 2019, 7, 24830–24836.
19. Y. Sun, Y. Zhao, J. Wang, J. Liang, C. Wang, Q. Sun, X. Lin, K. Adair, J. Luo, D. Wang, R. Li, M. Cai, T. K. Sham, X. Sun, A Novel Organic “Polyurea”Thin Film for Ultralong-Life Lithium-Metal Anodes via Molecular-Layer Deposition, **Adv. Mater.**, 2019, 31 (4), 1806541.

20. Z. Song, M. Banis, L. Zhang, B. Wang, L. Yang, D. Banham, Y. Zhao, **J. Liang**, M. Zheng, R. Li, S. Ye, X. Sun, Origin of achieving the enhanced activity and stability of Pt electrocatalysts with strong metal-support interactions via atomic layer deposition, **Nano Energy**, 2018, 53, 716-725.
21. X. Lin, Q. Sun, H. Yadegari, X. Yang, Y. Zhao, C. Wang, **J. Liang**, A. Koo, R. Li, X. Sun, On the Cycling Performance of Na - O<sub>2</sub> Cells: Revealing the Impact of the Superoxide Crossover toward the Metallic Na Electrode, **Adv. Funct. Mater.**, 2018, 28(35), 181904;
22. Y. Liu, Q. Sun, D. Wang, K. Adair, **J. Liang**, X. Sun, Development of the cold sintering process and its application in solid-state lithium batteries, **J. Power Sources**, 2018, 393, 193-203;
23. C. Wang, Q. Sun, Y. Liu, Y. Zhao, X. Li, X. Lin, M. Banis, M. Li, W. Li, K. Adair, D. Wang, **J. Liang**, R. Li, L. Zhang, R. Yang, S. Lu, X. Sun, Boosting the performance of lithium batteries with solid-liquid hybrid electrolytes: Interfacial properties and effects of liquid electrolytes, **Nano Energy**, 2018, 48, 35-43;
24. Y. Liu, Q. Sun, X. Yang, **J. Liang**, B. Wang, A. Koo, R. Li, J. Li, X. Sun, High-performance and recyclable Al-air coin cells based on eco-friendly chitosan hydrogel membranes, **ACS Appl. Mater. Interfaces**, 2018, 10, 23, 19730-19738;
25. X. Yang, Y. Yu, X. Lin, **J. Liang**, K. Adair, Y. Zhao, C. Wang, X. Li, Q. Sun, H. Zhang, X. Li, R. Li, H. Zhang, X. Sun, Multi-functional nanowall arrays with unrestricted Li<sup>+</sup> transport channels and an integrated conductive network for high-area-capacity Li-S batteries, **J. Mater. Chem. A**, 2018, 6 (45), 22958-22965;
26. C. Zhao, C. Yu, M. Zhang, H. Huang, S. Li, X. Han, Z. Liu, J. Yang, W. Xiao, **J. Liang**, X. Sun, J. Qiu, Ultrafine MoO<sub>2</sub>-Carbon Microstructures Enable Ultralong-Life Power-Type Sodium Ion Storage by Enhanced Pseudocapacitance, **Adv. Energy Mater.**, 2017, 7 (15), 1602880;

(c) Conference presentation and abstracts

1. J. Liang, X. Sun, Stabilization of Solid-state Electrolyte by Atomic Layer Deposition for High Performance All-solid-state Li-S Battery, **Proceedings of The Joint**



**Canadian Society for Mechanical Engineering and CFD Society of Canada  
International Congress 2019.**

2. J. Liang, X Yang, X. Sun, Stabilizing Polymer-Based Solid-State Electrolytes with 4 V Class Cathodes: From Interface Modification to Electrode Designs, **ECS Meeting Abstracts**, 2020.